OPTIMISATION OF SCALE-UP OF CHROMATOGRAPHY

by

Christopher Brett Colby.

Thesis submitted for the degree of
Doctor of Philosophy

in

The University of Adelaide,
Department of Chemical Engineering,
Faculty of Engineering,

January, 1997.

This work contains no material which has been accepted for the award of any other degree or diploma in any university or any other tertiary institution, and to the best of my knowledge and belief, contains no material previously published or written by another person, except where due reference has been made in the text.

I give consent to this copy of my thesis, when deposited in the University Library, being available for loan and photocopying.

SIGNED ..... DATE: .....

ACKNOWLEDGMENTS

Several individuals and organisations deserve recognition for their contribution to this thesis. I would like to thank my supervisor, Dr Brian O'Neill, for his guidance and encouragement, and for taking time to edit this thesis and suggest useful changes. My thanks go to Dr Anton Middelberg for his personal support and valued input towards research conducted in this thesis. I am also grateful to the staff and students, in particular my post-graduate colleagues, in the Department of Chemical Engineering, The University of Adelaide. Their friendship and assistance have made my post-graduate studies an enjoyable experience.

This thesis investigates the scale-up of an ion-exchange system to manufacture a whey growth factor extract from cheese whey. In this regard, I am grateful to Dr Geoff Regester for providing background information and technical support. I would also like to acknowledge the work presented by Dr Eric James in his Ph.D. thesis which provides experimental data for simulation studies performed in this thesis.

I am indebted to the Dr William Kaggwa for his permission to use soil-testing facilities in the Department of Civil & Environmental Engineering, The University of Adelaide, without which many experimental tests conducted in this thesis would not have been possible.

The computational simulations presented in this thesis were performed on a CM-5 supercomputer at the South Australian Centre for Parallel Computing. I am grateful to Francis Vaughan for enthusiastically providing me with access to the CM-5, and more specifically, for helping me optimise various numerical algorithms encoded in C*.

Financial support for this work was granted by the Co-operative Research Centre for Tissue Growth and Repair. I am thankful for their award of a postgraduate scholarship and their contributions toward the operating expenses incurred.

Last, and by no means least, I am indebted to my wife, Verity. Her love and continual support and encouragement throughout the last two years have been my inspiration.

ABSTRACT

Chromatography has become an integral part of biotechnology. It plays an important role in the purification of biological compounds from natural sources, as well as those produced from recombinant DNA and hybridoma techniques. Unfortunately, it is widely regarded as difficult and uneconomic to scale-up from the laboratory, where it is employed for analytical and preparative purposes, to larger-scale systems, where cost-effective commercial-scale manufacture is important. While simulation is a common tool for scale-up of chromatographic systems in other industries, its application in biotechnology has been limited by the availability of protein properties capable of describing essential parameters in the complex mathematical models which must be used. Consequently, alternative scale-up methodologies for chromatographic systems have been developed. These employ a combination of heuristics and time consuming experimentation. A generic approach is to arbitrarily increase flowrate to maximise productivity (the product yield per unit resin volume per unit time). Normally, this is unsuccessful. It does not guarantee optimal cost during scale-up.

The optimal scale-up of an ion-exchange system is investigated in this thesis. The ion-exchange system is used to separate a whey growth factor extract (WGFE) from cheese whey. A laboratory-scale ion-exchange system has already been the subject of a scale-up study. A heuristic technique was employed to devise an industrial-scale design. Flowrate was arbitrarily increased to improve productivity (WGFE yield per unit resin volume per unit time).

Key scale-up problems in the ion-exchange system were identified. The impact of resin compressibility on pressure drop during scale-up was examined. Pressure drop is an important constraint to the successful scale-up of a chromatographic system. It restricts the combination of flowrates and bed heights that can be utilised. Sepharose Big-Beads SP Pharmacia, Uppsala, Sweden) is the chromatographic resin employed in the ion-exchange system. It is compressible. During scale-up, the pressure drop across a compressible packed bed will increase in larger (diameter) columns. This is a result of wall friction effects. The implications of such a change for the ion-exchange system are potentially

catastrophic. Some form of prediction is essential. However, existing models for pressure-drop prediction in compressible packed beds are inadequate. They cannot account for wall friction effects.

A new model for pressure-drop prediction in compressible packed beds of chromatographic resin is developed. It combines a common theoretical thread between the multiphase theory of filtration and the method of differential slices which predicts wall friction effects in hoppers. Its key parameters were determined for Sepharose Big-Beads SP. These were used to validate model predictions against experimental packed-bed pressure-drop data. The model can successfully predict packed-bed pressure drop during scale-up of the ion-exchange system. Furthermore, the model is a significant advance in analysis of fluid flow in particulate systems. It is the first to allow true *a priori* prediction of pressure drop for compressible packed beds where wall friction effects are significant.

The new model was used to investigate the packed-bed pressure-drop behaviour of Sepharose Big-Beads SP in a production-scale chromatographic column, namely, a Pharmacia (Uppsala, Sweden) BioProcess™ Glass (BPG) 450/500 column. The results were combined with column pressure-loss data to anticipate the pressure-drop behaviour of the ion-exchange system during scale-up. The possible combinations of superficial velocity and packed-bed height are restricted by a pressure constraint to a feasible region. The current operating conditions being considered for the ion-exchange system are a superficial velocity and packed-bed height of 8.5 cm/min and 21 cm, respectively. These do not compromise the pressure constraint. Furthermore, a proposed increase in superficial velocity to 14 cm/min can be sustained by the ion-exchange system during scale-up.

The impact of compression on porosity and resin particle properties in the packed bed of the ion-exchange system during scale-up was examined. Porosity can decrease in a production-scale column by up to 36% compared to 9% in a laboratory-scale column. Similarly, Sauter-mean particle diameter can also decrease by 5 and 2%, respectively. This increased compression during scale-up can deleteriously influence ion-exchange system behaviour and performance.

As a consequence, compression effects on the behaviour and performance of the ion-exchange system were investigated. A non-linear multicomponent rate-equation

chromatography model was modified. The modifications account for the variation in porosity and Sauter-mean particle diameter that can occur in a packed bed during compression. Two major whey proteins, namely, lactoperoxidase and lactoferrin, were used to simulate the ion-exchange system behaviour. The variation in porosity and Sauter-mean particle diameter during scale-up was estimated. An indirect technique using the new model for pressure-drop prediction described above was employed. Model simulations were performed. The results were compared. System behaviour was largely independent of compression for both frontal adsorption and step elution. Increasing compression generated only small and trivial variations in effluent concentration profiles. Compression effects on system behaviour and performance do not need to be considered during scale-up of the ion-exchange system.

The general non-linear multicomponent rate-equation chromatography model used to simulate compression effects in the ion-exchange system can be also be used as a tool to optimise its scale-up. Model simulations were employed to examine the sensitivity of system behaviour during frontal adsorption to superficial velocity and packed-bed height. Lactoperoxidase and lactoferrin were employed to imitate the two key fractions in the microfiltered whey: the WGFE product and lactoferrin. Intraparticle-diffusion limitations were found to play an important role in determining the whey volume that can be sustained by the packed bed during frontal adsorption. This has an important impact on the cyclic WGFE product yield of the ion-exchange system. An increase in superficial velocity can produce a dramatic decline in WGFE yield per cycle.

Simulation results were combined with pilot-plant data for other steps in the ion-exchange system to examine the impact of packed-bed height and frontal-adsorption superficial velocity on productivity. An optimal region of productivity exists. It corresponds to a band of superficial velocities and packed-bed heights which rise from 5 cm/min at a bed height of 10 cm to nearly 20 cm/min at 30 cm. There are multiple design scenarios for the superficial velocity in the frontal-adsorption step and the packed-bed height which will maximise productivity of the ion-exchange system. This is a direct result of intraparticle-diffusion limitations and the decline in cyclic WGFE yield it induces with an increase in superficial velocity. The proposed increase in superficial velocity to 14 cm/min for the ion-exchange system (at a packed-bed height of 21 cm) corresponds to an optimal region of productivity.

These results have important implications for scale-up of other chromatographic systems in biotechnology. Standard industry practice involves a heuristic technique which arbitrarily increases flowrate to increase productivity. However, this study shows increasing flowrate does not always necessarily improve productivity.

The frontal-adsorption superficial velocity and packed-bed height which will optimise the cost of the ion-exchange system during scale-up was investigated. A comprehensive design for the ion-exchange system in a proposed commercial-scale facility was developed. The design was correlated with an objective function describing annualised dimensionless cost. There is an optimal design for the ion-exchange system which will minimise cost. It is located at a superficial velocity and packed-bed height of 2 to 6 cm/min and 25 to 30 cm, respectively. While the cost of chromatographic resin and columns were important, the cost of the ion-exchange system was dominated by consumable costs, in particular, those for eluent and sanitisation solutions. This is an important observation. Maximising productivity to minimise resin volume in a chromatographic system will not always optimise cost. Furthermore, a heuristic of increasing flowrate inadvertently acts to increase consumable costs. This is a result of the rise in cycle frequency which inevitably accompany higher superficial velocities and increase the volumetric consumption of wash, buffer, eluent and/or sanitisation solutions. Existing heuristic techniques which rely on maximising productivity are not always suitable for chromatographic scale-up where optimal cost is the key objective.

Consequently, the current operating conditions considered for the ion-exchange system are sub-optimal. They will result in annual scale-up costs more than 15 to 20% greater than if a superficial velocity and packed-bed height in the optimal-cost region are employed. Furthermore, the proposed increase in superficial velocity to 14 cm/min should be avoided. While it will improve system productivity, it will lead to an annual scale-up cost that exceeds its optimal counterpart by more than 50%.

Further work to optimise scale-up of the ion-exchange system should be considered. In particular, the use of a perfusion chromatographic resin or smaller resin particle size to alleviate intraparticle-diffusion limitations may yield significant performance and cost benefits.

TABLE OF CONTENTS

Acknowledgments i

Abstract ii

Publications List xi

List of Figures xiii

List of Tables xx

1 Introduction 1

1.1 Objective - Thesis 1

1.2 Preamble - Thesis 1

1.3 Introduction 1

1.4 Thesis - Content and Organisation 5

1.5 Manufacture of WGFE by Ion-Exchange 7

1.5.1 Background 7

1.5.2 The WGFE Manufacturing Process 9

1.5.3 The Ion-Exchange Step Scale-Up Methodology 11

1.5.4 Scale-Up and Performance and Cost 15

1.5.5 Scale Up and the Pressure Constraint 17

1.5.6 Scale-Up and Compression Effects on Performance 19

PART I: PRESSURE-DROP PREDICTION

2 Model Development 22

2.1 Objective - Part I 22

2.2 Preamble - Chapter 2 22

2.3 Background Art - Compressible Chromatography Resins 22

2.4 Background Art - Other Compressible-Type Media 27

2.5 The Multiphase Theory of Filtration 28

2.6 Scope and Application 33

2.7 A Model for Compressible Systems at Steady State 34

2.8 Accounting for Wall Friction 36
2.8.1 Coulomb's Method of Wedges 36
2.8.2 The Method of Characteristics 37
2.8.3 The Method of Differential Slices 41
2.9 Porosity and Particle Deformation 44
2.10 Variation in Bed Height 46
2.11 Concluding Remarks 47

3 Experimental 48
3.1 Preamble 48
3.2 Initial Volume-Mean Particle Diameter 48
3.2.1 Introduction 48
3.2.2 Experimental Apparatus and Procedure 50
3.2.3 Results and Discussion 51
3.3 Pressure-Drop Data 54
3.3.1 Introduction 54
3.3.2 Experimental Apparatus 55
3.3.3 Experimental Procedure 56
3.3.4 Results and Discussion 58
3.4 Internal Angle of Friction 61
3.4.1 Introduction 61
3.4.2 Experimental Apparatus and Procedure 65
3.4.3 Results and Discussion 66
3.5 Angle of Wall Friction 69
3.5.1 Introduction 69
3.5.2 Experimental Apparatus and Procedure 72
3.5.3 Results and Discussion 73
3.6 Initial Shape Factor 74
3.7 Initial Porosity 74
3.7.1 Introduction 74
3.7.2 Experimental 75
3.7.3 Results and Discussion 75
3.8 Variation in Local Bed Height, $f_c(\tau^s_{zz})$ 76

3.8.1 Introduction 76
3.8.2 Experimental Apparatus 76
3.8.3 Experimental Procedure 77
3.8.4 Results and Discussion 78
3.9 Concluding Remarks 80

4 Validation & Prediction 82
4.1 Preamble 82
4.2 Determination of $\chi(\tau^{s}_{zz})$ 82
4.3 Model Validation 85
4.4 Model Prediction and Scale-Up 96
4.5 Concluding Remarks 107

PART II: COMPRESSION EFFECTS

5 A Mathematical Model 110
5.1 Objective - Part II 110
5.2 Preamble 110
5.3 Background Art - Mathematical Models 111
5.4 Rate Models 112
5.5 Accounting for Compression Effects 114
5.5 Key Model Parameters 115
5.6 Solving Model Equations - Numerical Strategy 116
5.7 Numerical Strategy - Validation 117
5.8 Simulating Compression Effects - A Hypothetical Study 118
5.9 Concluding Remarks 124

6 Model Parameters & Validation 125
6.1 Preamble 125
6.2 Selecting Indicator Compounds 125
6.3 System Model Parameters 127
6.3.1 Bed Porosity 127
6.3.2 Particle diameter 127

6.4 Species Model Parameters 128
6.4.1 Intraparticle-Diffusion Coefficient 128
6.4.2 Intraparticle Voidage 129
6.4.3 Damköhler Numbers and Adsorption Capacity 129
6.4.4 Dispersion Coefficient 132
6.4.5 External-Film Mass Transfer Coefficient 133
6.5 Model Validation 133
6.5.1 Experimental Data 133
6.5.2 Optimal Numerical Parameters 135
6.5.3 Model Validation - Frontal Adsorption 139
6.5.4 Model Validation - Step Elution 144
6.6 Concluding Remarks 147

7 Compression Effects 148
7.1 Preamble 148
7.2 Background Art - Porosity Variation in Compressed Beds 148
7.3 Methodology 150
7.4 Initial Sauter-Mean Particle Diameter and Internal Voidage 153
7.5 Prediction of Porosity and Particle-Deformation Profiles 154
7.6 Compression Effects on Model Parameters 159
7.7 Concluding Remarks 161

8 Simulation & Prediction **163**
8.1 Preamble 163
8.2 Evaluation of Optimal Numerical Parameters 163
8.3 Compression Effects during Frontal Adsorption 167
8.4 Compression Effects during Step Elution 175
8.5 Concluding Remarks 179

PART III: OPTIMISATION

9 Scale-Up & Optimisation **182**
9.1 Objective - Part III 182

9.2 Preamble 182
9.3 Background Art - Optimisation of Chromatography 183
9.4 Study Methodology 187
9.5 Scale-up Studies - Key Design Variables 188
9.6 Scale-up Studies - System Design 189
9.7 An Appropriate Objective Function 196
9.8 Evaluating Component Costs 196
9.8.1 Chromatographic Columns 197
9.8.2 Pump & Control System 198
9.8.3 Tanks 198
9.8.4 Ultrafiltration Unit 199
9.9 Principal Consumable Costs 199
9.9.1 Chromatographic Resin 200
9.9.2 Wash, Eluent & Sanitisation Costs 200
9.9.3 Ultrafiltration Membranes 201
9.10 The Characteristic Cost 201
9.11 Costing - Results and Discussion 201
9.12 The Pressure Constraint 204
9.13 Concluding Remarks 205

10 Summary & Final Remarks 207

Nomenclature 220

References 225

Appendix 1: BPG 100/500 Schematic & Parts List 231

Appendix 2: Literature Result of a Numerical Simulation 234

PUBLICATIONS LIST

Refereed Journals

Colby, C.B.; O'Neill, B.K.; Middelberg, A.P.J. 1996. A modified version of the volume-averaged continuum theory to predict pressure drop across compressible packed beds of Sepharose Big-Beads SP. *Biotech. Prog.*, **12**, 92-99.

Colby, C.B.; O'Neill, B.K.; Middelberg, A.P.J. 1996. Simulation of compression effects during scale-up of a commercial ion-exchange process. *Biotech. Prog.*, **12**, 662-681.

Refereed Conference Papers

Colby, C.B.; O'Neill, B.K.; Middelberg, A.P.J. 1996. Optimal scale-up of a commercial ion-exchange process. In *Proceedings, 24th Australian Chemical Engineering Conference, CHEMECA '96*, Vol. 4, pp 101-106.

Pelekani, C.; Colby, C.B.; James, T.; O'Neill, B.K. 1996. A comprehensive study of winery wastewater quality. In *Proceedings, 24th Australian Chemical Engineering Conference, CHEMECA '96*, Vol. 4, pp 7-12.

Querzoli, A.; Middelberg, A.P.J.; Bush, M.; Colby, C.B.; Baart, G. 1996. Insights into Electrical Field-Flow Fractionation by simulation. In *Proceedings, 24th Australian Chemical Engineering Conference, CHEMECA '96*, Vol. 5, pp 15-20.

Colby, C.B.; O'Neill, B.K.; Middelberg, A.P.J. 1995. Frontal adsorption and gradient elution in compressed packed beds of chromatography resin. In *Proceedings, 23rd Australian Chemical Engineering Conference, CHEMECA '95*, Vol. 3, pp 74-79.

Colby, C.B.; O'Neill, B.K.; Middelberg, A.P.J. 1994. Prediction of pressure drop across a compressible packed bed of chromatography resin. In *Proceedings, 22nd Australian Chemical Engineering Conference, CHEMECA '94,* pp 133-140.

Unrefereed Conference Papers

Colby, C.B.; O'Neill, B.K.; Middelberg, A.P.J. 1995. Prediction of pressure-drop/flow behaviour across compressible packed beds of chromatography resin. In *Proceedings, 4th Pacific Rim Biotechnology Conference, Melbourne*, pp 230-231.

LIST OF FIGURES

Figure	Title	Page
1.1	A simple schematic of the pilot-plant for manufacture of WGFE.	9
2.1	Pressure-drop data *vs.* model predictions for Sephadex G-100 Regular at varying lengths as reproduced from Mohammad *et al.* (1992).	23
2.2	Pressure-drop data *vs.* model predictions for Sephadex G-100 Regular at different column diameters as reproduced from Mohammad *et al.* (1992).	24
2.3	Compressible cake filtration.	28
2.4	A two-dimensional differential element in a hopper.	37
2.5	The Mohr Circle which defines the stress state of an ideal Coulomb material at incipient yield.	39
2.6	A differential slice of pulverulent material in a cylindrical hopper.	41
3.1	Malvern System 2600 Particle Sizer configuration for size measurement of particles dispersed in a fluid.	49
3.2	Light scattering and detection in the Malvern System 2600 Particle Sizer.	50
3.3	Volume particle-size distribution and cumulative undersize for Sepharose Big-Beads SP dispersed in water - pH 7.	52
3.4	Microscopy image of Sepharose Big-Beads SP in water - pH 7, at 20× magnification.	52
3.5	Experimental system employed to collect pressure-drop data.	55
3.6	Variation in bed height and pressure drop during cyclical and continuous loading.	59
3.7	Variation in steady-state pressure drop and bed height, at relaxation and compression, with flowrate.	59
3.8	Packed-bed pressure-drop behaviour as a function of test-column diameter.	60

3.9	Packed-bed pressure-drop behaviour for the Pharmacia XK 50/60 as a function of initial packed-bed height with 21% (by wt.) ethanol.	61
3.10	The tri-axial test apparatus.	62
3.11	The tri-axial test compression shear apparatus with specimen of Sepharose Big-Beads SP in its pre-test state.	63
3.12	Graphical depiction of a specimen at failure during a tri-axial compression test.	64
3.13	Specimen of Sepharose Big-Beads SP (as illustrated in Figure 3.11) at failure.	66
3.14	Variation of axial compressive stress during a tri-axial compression shear test, σ_{rr}=428 kPa.	67
3.15	Various Mohr circles determined at incipient failure of Sepharose Big-Beads SP *vs.* yield locus for an internal angle of friction of 10.3°.	68
3.16	Experimental Mohr-Coulomb failure criterion stress points for Sepharose Big-Beads SP *vs.* Mohr-Coulomb failure criterion at an internal angle of friction of 10.3°.	68
3.17	Prediction of major principal stress with *eq.* 2.31 at an internal angle of friction of 10.3° *vs.* experimental data.	69
3.18	Direct-shear test apparatus employed for determination of angle of wall friction.	70
3.19	The metal shear box of the direct-shear test apparatus.	71
3.20	Metal shear box in modified direct-shear test with glass insert.	72
3.21	Metal shear box in modified direct-shear test with Sepharose Big-Beads SP specimen ready for testing.	73
3.22	Variation of axial compressive stress during a modified direct-shear test.	73
3.23	Variation in shear stress with applied normal stress *vs.* yield locus at an angle of wall friction of 8.0° for modified direct-shear tests with Sepharose Big-Beads SP.	74

3.24	Experimental system employed to collect variation in local bed-height data.	76
3.25	Experimental fraction of initial bed height at compression and relaxation for Sepharose Big-Beads SP dispersed in water compared with *eq.s* 3.5 and 3.6 for $f_c(\tau^s_{zz})$ and $f_d(\tau^s_{zz})$, respectively.	79
4.1	Experimental pressure-drop, ΔP, and compressed bed-height, Z_c, data selected for determination of $\chi(\tau^s_{zz})$.	83
4.2	Model prediction of packed-bed pressure drop using *eq.* 4.1 to represent $\chi(\tau^s_{zz})$ *vs.* experimental data used for regression.	84
4.3	Variation in $\chi(\tau^s_{zz})$ and bed porosity with axial stress as predicted by *eq.* 4.1 and estimated from *eq.* 2.40, respectively.	85
4.4	Model predictions *vs.* experimental pressure-drop and bed-height data presented in Figure 3.7 - Chapter 3.	87
4.5	Model predictions *vs.* experimental pressure-drop and bed-height data, Pharmacia XK 16/40, 21% (by wt.) ethanol, L_i=20.2 cm.	88
4.6	Model predictions *vs.* experimental pressure-drop data presented in Figure 3.8 - Chapter 3.	89
4.7	Parity plot of model predictions, ΔP_{mod}, *vs.* experimental pressure drop, ΔP_{exp}, for all experimental data collected in Chapter 3.	90
4.8	Parity plot of model predictions, $Z_{c,mod}$, *vs.* experimental 'compressed' bed height, $Z_{c,exp}$, for all experimental data collected in Chapter 3.	91
4.9	Parity plot of model predictions, $Z_{e,mod}$, *vs.* experimental 'expanded' bed height, $Z_{e,exp}$, for all experimental data collected in Chapter 3.	91
4.10	Sensitivity of model predictions for pressure drop across a 25 cm packed bed to variation in bed height.	92
4.11	Sensitivity of model predictions for pressure drop at 1 cP to fluid viscosity.	95

4.12	Parity plot of model predictions *vs.* experimental pressure drop for all experimental data collected in Chapter 3 by test fluid.	96
4.13	Functional dependence of model prediction for pressure drop on column diameter at varying superficial velocities, v_{sup}.	97
4.14	Impact of wall friction effects on axial stress, τ^{s}_{zz}.	98
4.15	Contour plot of predicted packed-bed pressure drop for Sepharose Big-Beads SP in a Pharmacia BPG 100/500 column.	100
4.16	Column pressure losses in Pharmacia BPG columns for various fluids.	101
4.17	Contour plot of predicted system pressure drop for Sepharose Big-Beads SP in a BPG 100/500 column.	102
4.18	Column pressure-loss data for Sepharose Big-Beads SP in a Pharmacia BPG 300/500 column with water at 25°C (Pharmacia Bioprocess Technology, 1995).	105
4.19	Contour plot of WGFE ion-exchange system pressure drop in a Pharmacia BPG 450/500 production-scale column.	106
5.1	Model simulations of a single-component frontal adsorption for hypothetical model parameters presented in Table 5.1.	118
5.2	Breakthrough curves of a compressed and uncompressed bed for single-component frontal adsorption in a hypothetical packed bed system.	121
5.3	Breakthrough curves of a compressed and uncompressed bed for binary-component frontal adsorption in a hypothetical packed bed system.	122
5.4	Breakthrough curves of a compressed and uncompressed bed for binary-component gradient elution with modulator in a hypothetical packed bed system.	123
6.1	Multicomponent equilibria data (James, 1994) for lactoperoxidase and lactoferrin with multicomponent Langmuir isotherms for lactoperoxidase and lactoferrin.	130

6.2	Single-component equilibria data (James, 1994) for lactoperoxidase, 0 M and 0.2 M NaCl, and lactoferrin, 0 M and 0.6 M NaCl, with single-component extended Langmuir-Freundlich isotherms for lactoperoxidase and lactoferrin.	131
6.3	Experimental binary-component frontal-adsorption data (James, 1994) for lactoperoxidase and lactoferrin *vs.* model predictions using single-component extended Langmuir-Freundlich isotherms and multicomponent Langmuir isotherms.	134
6.4	Experimental binary-component step-elution data (James, 1994) for lactoperoxidase and lactoferrin *vs.* model predictions using single-component Extended Langmuir-Freundlich isotherms.	135
6.5	Model predictions using different combinations of numerical parameters.	136
6.6	Model predictions (Z=0 cm) of particle- (Figure 6.6a) and stationary-phase (Figure 6.6b) concentration profiles, respectively (N_e=10 and N_c=13).	137
7.1	Predicted variation in porosity with bed height in the laboratory- and production-scale column *vs.* correlation by empirical function.	155
7.2	Predicted variation in Sauter-mean particle diameter with bed height in the laboratory- and production-scale column *vs.* correlation by empirical function.	156
7.3	Predicted variation in internal particle voidage with bed height in the laboratory- and production-scale column *vs.* correlation by empirical function.	157
8.1	Single-component frontal-adsorption model predictions using different combinations of numerical parameters.	167
8.2	Compressed-bed simulations: frontal-adsorption model predictions with compression effects excluded and for compressed packed beds in the laboratory- and production-scale column.	169
8.3	Chronological development of bulk-phase concentration profiles for lactoperoxidase in a packed bed during a binary-component frontal-adsorption simulation (compression effects excluded).	172

8.4	Modified (resin particle size halved) frontal-adsorption model predictions with compression effects excluded and for compressed packed beds in the laboratory- and production-scale column.	174
8.5	Compressed-bed simulations: step-elution model predictions with compression effects excluded and for compressed packed beds in the laboratory- and production-scale column.	177
8.6	Modified (resin particle diameter halved) step-elution model predictions with compression effects excluded and for compressed packed beds in the laboratory- and production-scale column.	178
9.1	A simplified schematic of the WGFE ion-exchange system and associated equipment in the proposed production-scale facility.	188
9.2	Frontal-adsorption breakthrough curve for lactoperoxidase in the WGFE ion-exchange system at different combinations of bed height and superficial velocity.	191
9.3	Contour plot of dimensionless time at breakthrough during frontal-adsorption model simulations.	192
9.4	Contour plot of cycle time as a function of superficial velocity and packed-bed height.	193
9.5	Contour plot of productivity, Ψ, as a function of frontal-adsorption superficial velocity and packed-bed height.	194
9.6	Contour plot of non-dimensionalised direct-fixed-capital costs, ϕ^*_{dfc}, as a function of frontal-adsorption superficial velocity and packed-bed height.	202
9.7	Contour plot of non-dimensionalised consumable costs, ϕ^*_{cons}, as a function of frontal-adsorption superficial velocity and packed-bed height.	203
9.8	Contour plot of dimensionless costs, ϕ^*, as a function of frontal-adsorption superficial velocity and packed-bed height with predicted 300 kPa pressure-drop contour for the Pharmacia BPG 450/500 column.	203
10.1	Column pressure-loss data for Sepharose-Fast Flow SP in a BPG 450/500 column with water at 20°C.	218

A1.1	Photocopy of Schematic detailing parts and construction of Pharmacia BPG 100/500 column (Pharmacia Bioprocess Technology, 1996c).	232
A1.2	Photocopy of Table containing parts list (Pharmacia Bioprocess Technology, 1996c) for Schematic presented in Figure A1.1.	233
A2.1	Photocopy of general multicomponent rate-equation chromatography model single-component frontal adsorption simulation by Gu(1995).	235
A2.2	Photocopy of Table presented by Gu(1995) containing model parameters for model simulation in Figure A2.1.	235

LIST OF TABLES

Table	Title	Page
3.1	Particle size count and volume particle-size distribution for Sepharose Big-Beads SP determined from Figure 3.4.	53
3.2	Mean-volume particle diameter for Sepharose Big-Beads SP.	53
3.3	Initial height of packed beds in each column and test fluid during experiments to collect pressure-drop data.	57
4.1	Viscosity at 20°C of various fluids employed in the WGFE ion-exchange system.	103
5.1	Hypothetical model parameters used for the numerical solution of the non-linear multicomponent rate-equation model presented in Figure 5.1.	118
5.2	Model parameters for simulation of compression effects in three hypothetical compressed packed-bed systems.	121
6.1	Intraparticle diffusivity parameters for lactoperoxidase and lactoferrin during adsorption at 0 M sodium chloride and desorption in 0.4 and 1.0 M sodium chloride (James, 1994).	128
6.2	Multicomponent Langmuir and single-component extended Langmuir-Freundlich equilibrium parameters.	129
6.3	Maximum (experimental) adsorption capacities for lactoperoxidase and lactoferrin on a total stationary-phase basis (TSPB).	132
6.4	Important model parameters and values of key dimensionless groups employed for selection of optimal numerical parameters.	136
6.5	Important model parameters and values of key dimensionless groups employed for the binary-component frontal-adsorption simulation with lactoperoxidase and lactoferrin.	139
6.6	Important model parameters and values of key dimensionless groups employed for binary-component step-elution simulations with lactoperoxidase and lactoferrin.	145

7.1	Total particle stationary-phase volume (TPSV) and total particle volume (TPV) for compressed beds in laboratory- and production-scale columns compared to that prior to compression.	158
7.2	Modified (TSPB) maximum adsorption capacities of lactoperoxidase and lactoferrin for compressed-bed simulations.	161
8.1	Compressed-bed simulations: important model parameters and values of key dimensionless groups employed for selection of optimal numerical parameters.	164
8.2	Important component and system model parameters and values of key dimensionless groups employed for compressed-bed frontal-adsorption simulations.	168
8.3	Modified values of important system and component model parameters and key dimensionless groups for modified (resin particle size halved) frontal-adsorption simulations.	173
8.4	Important component model parameters and values of key dimensionless groups employed for step-elution simulations in laboratory- and production-scale columns.	176
8.5	Compressed-bed simulations: modified values of component model parameters and key dimensionless groups used in modified (resin particle halved) step-elution simulations.	178
9.1	Unit costs for wash, eluent and sanitisation solutions.	201

CHAPTER 1

INTRODUCTION

1.1 Objective - Thesis

The aim of this work is to investigate the optimal scale-up of a commercial ion-exchange process to manufacture a whey growth factor extract (WGFE) from cheese whey.

1.2 Preamble - Thesis

Chromatography is a key process in biotechnology for separation, purification and recovery of biological products. However, it is widely regarded as difficult and uneconomic to scale-up from the laboratory, where it is employed for analytical and preparative purposes, to larger-scale systems, where cost-effective commercial-scale manufacture is important. The complexity of this problem has generated a multitude of scale-up methodologies. Many attempt to design a larger-scale chromatographic system directly from their laboratory-scale counterparts by using a combination of experimental studies and heuristic scale-up rules. Normally, this approach is unsuccessful and does not result in optimal cost during scale-up, or even allow confident *a priori* prediction of chromatographic behaviour in larger-scale systems. Alternative scale-up methodologies to overcome these deficiencies are needed. This thesis investigates the scale-up of an ion-exchange chromatographic system to manufacture WGFE from cheese whey. Key scale-up problems are identified and discussed. Alternative scale-up methodologies required to overcome several of these problems are considered. The results will have wide application to scale-up and optimisation in other chromatographic systems.

1.3 Introduction

The recent advances in biotechnology have increased the need for large-scale production of many biological materials (Petrides, 1990). While products have traditionally been of high added value, this situation is changing as new products with potentially large markets

emerge (Middelberg, 1992). The key to success in bringing these types of bio-products to market is to have a well-integrated plan involving simultaneous activities in product development, process development and addressing regulatory issues (Petrides *et al.*, 1989). As a consequence, there is growing interest in formulating design methodologies which can facilitate the process design and development of large-scale biochemical processes. In particular, the development of cost-effective purification schemes has been the subject of considerable research and commercial activity in recent years (Sofer & Nyström, 1989; Knight, 1989; van Brakel & Kleizen, 1990; Spalding, 1991; Gupta & Mattiasson, 1994).

Of the most commonly applied laboratory techniques, liquid chromatography is the most widely used at moderate- and large-scale process levels for protein purification (Snoswell, 1990). A universal approach to process design and optimisation during scale-up is simulation. It relies on sophisticated mathematical models which can accurately describe the behaviour of a chemical or biochemical process. Advanced mathematical models of varying complexities have been formulated for chromatographic systems (Ruthven, 1984; Yu & Wang, 1988; Gu, 1995). These have been successfully employed to simulate chromatographic separations in a number of hypothetical and simplistic experimental systems (Ma & Guiochon, 1991; Gu *et al.*, 1991; Whitley *et al.*, 1993). However, real-life chromatographic separations involve complex multicomponent systems. Simulation is conditional on the availability of protein properties to describe model parameters. This has been a notable constraint in existing studies, and has impeded its wider-scale application.

Consequently, alternative scale-up methodologies for chromatographic systems have been developed. These employ a combination of heuristics and time consuming experimentation (Tsou & Graham, 1985). A set of scaling rules are used to guide the design and scale-up of an existing chromatographic separation based on the results of experimental investigations. Numerous studies on scale-up in a variety of chromatographic systems with different heuristic techniques have been reported (Tsou & Graham, 1985; Wankat & Koo, 1988; Mohammed *et al.*, 1992). While it is difficult to generalise, many techniques share a common heuristic of higher flowrate, and a common goal of maximising productivity (Gallant *et al.*, 1995). A simplistic example of a popular scale-up approach serves the purpose of illustration.

An existing analytical or preparative purification step to be scaled-up is replicated at a laboratory or pilot-plant scale. A sequence of steps are used to progressively improve its performance. The principal heuristic is to increase flowrate. New chromatographic supports which can replicate the required selectivity, resolution and yield for chromatographic separation are tested for higher flowrate. This either involves the use of a similar resin with an increased bead (particle) diameter, or if soft-gel resins based on dextran or agarose were used, their replacement with more rigid polymer-type resins constructed from polystyrene or polymethacrylate. Besides resolution and yield, pressure-drop limitations are the key constraint to increasing flowrate. If the desired flowrate cannot be achieved, a popular tactic is to decrease the height of the packed bed in the chromatographic column to satisfy this constraint.

The heuristic of increasing flowrate is designed to maximise the productivity of the chromatographic system. Productivity is synonymous with the yield of desired product per unit time per unit volume resin. To maximise productivity, is to minimise the volume of resin a chromatographic separation will require, and therefore, its cost. This reflects a widely held perception that resin volume is the principal cost driver in a chromatographic system during scale-up (Felinger & Guiochon, 1994). A higher flowrate should maximise productivity *per se*. A higher flowrate will lower cycle time (*ie* the time to load, wash, elute (or displace) and sanitise during a chromatographic cycle (run) will decrease). A shorter cycle time will increase cycle frequency. More cycles will increase total product yield for a defined volume of resin. The productivity of the chromatographic resin should rise. The reader should note that a critical assumption in this analysis is that product yield per cycle is independent of flowrate.

This simplistic type of scale-up strategy for a chromatographic system is widely adopted in the biotechnology industry. Some resin manufacturers, who act as de-facto consultants to the industry, actively promote it to their customers. However, despite its intuitive simplicity, a number of observations reveal that it is fundamentally flawed. First, chromatographic media and columns are not always the dominant cost driver in chromatographic systems during scale-up. For example, recurrent expenditure on chemical additives for wash, eluent and regeneration or sanitisation mixtures can be significant (Felinger & Guiochon, 1994). This can have a profound influence on the overall process

economics and cost of a large-scale chromatographic system. Maximising productivity is unlikely to generate a truly optimal, or even guarantee the most cost-effective, design.

Second, the impact of intraparticle-diffusion limitations on performance of chromatographic systems has been widely acknowledged (Spalding, 1991; Geisow, 1992; Gupta & Mattiasson, 1994; Li *et al.*, 1995). Intraparticle-diffusion limitations which emerge at higher flowrate can rapidly diminish product yields per cycle (Janson & Hedman, 1987; Hodgson, 1990). The tendency to increase particle diameter during scale-up exacerbates this problem. Bigger particles promote intraparticle-diffusion limitations. A higher flowrate, especially if bigger particles are employed to avoid a constraint on pressure drop, may not always necessarily increase the productivity of a chromatographic system as intended, despite an increase in cycle frequency. Evidently, there may be an absolute limit beyond which productivity will decline at higher flowrates.

Third, decreasing the packed-bed height in a chromatographic column will decrease the available working bed volume. This is unlikely to improve the product yield per cycle of a column, and thus its productivity, despite any increase in flowrate that may be gained.

Finally, compression of a packed bed in (larger-diameter) production-scale columns is a common phenomena if the chromatographic resin is compressible (Mohammad *et al.*, 1992). Compression can significantly alter the pressure drop across the packed bed, and thus, the production-scale chromatographic system. The implications of such a change during scale-up can be serious if pressure drop is a constraint in the final commercial-scale design. Flowrate restrictions may lead to a lower than design value severely limiting the capacity of a chromatographic system to meet its production goals (Janson & Hedman, 1987).

While these problems may discourage adherence to higher flowrate as the primary heuristic, without the benefits of simulation existing heuristic techniques and experimental programs used for scale-up of chromatographic systems are unlikely to be replaced. They therefore need to be adapted to seriously take into account the influence of these limitations. This would involve, at the very least, the development of a systematic attempt to carefully investigate multiple design scenarios (*ie* resin type and size, flowrate, bed height *etc*) for a proposed industrial-scale chromatographic system. A rigorous examination of the impact of

each scenario on productivity and overall cost would allow the optimal design to be identified. Careful consideration would also be need to be given to the impact of pressure-drop variations during scale-up if the chromatographic resin is compressible.

Such an approach, however, would require a considerable enlargement of the experimental effort presently exerted during scale-up given the large number of degrees of freedom that could be investigated. While additional efforts could be minimised by careful experimental design through the application of statistical (*ie* factorial) techniques, a significant investment in time, effort and money above that which is already expended would be necessary.

There are other problems that potentially present enormous impediments to pursuing this approach. The experimental design of such an investigation may be flawed without a clear understanding of the influence of the chosen variables on the process behaviour and cost of a chromatographic system. A truly optimal design for the industrial-scale process, or even an improved and more cost-effective design, as a final result is not guaranteed. Furthermore, the chronological demands of additional experimental work may disrupt other important functions that these experimental programs must fulfil. For example, to generate larger quantities of the desired product for clinical trials or market evaluation, or process validation for cGMP.

It is evident that in order to truly seek a successful and optimal design during the scale-up of a chromatographic system, an alternative approach must be considered. Such examples are easily found. In recent years, improved methodologies for scale-up and optimisation of chromatographic systems have been the topic of numerous publications.

1.4 Thesis - Content and Organisation

This thesis chronicles the research activities carried out by the author to optimise the scale-up of an ion-exchange chromatographic system. A whey growth factor extract (WGFE) is recovered from cheese whey. The chromatographic system is similar to many other commercial-scale chromatographic processes in the biotechnology industry. It provides some excellent examples of problems that exist in scaling-up chromatographic systems, and the need for improved scale-up methodologies.

An understanding of the purpose, design and operation of the commercial ion-exchange process to recover WGFE from cheese whey is necessary if attempts to optimise its scale-up are to be meaningfully discussed. It is therefore described in further detail in Section 1.5 of this Chapter. The compressibility of the ion-exchange chromatographic resin, pressure drop and a reliable technique for predicting the influence of physical and operational design characteristics (*ie* bed height, superficial velocity, particle diameter *etc*) on performance of the chromatographic system are identified as key impediments to developing an optimal commercial-scale design. It is shown that an existing heuristic scale-up methodology is inadequate. In particular, compression effects on pressure drop and system behaviour during scale-up cannot be predicted with certainty.

Subsequent chapters in the thesis are divided into three distinct sections: Parts I to III. Part I (Chapters 2 to 4) presents a new mathematical model developed by the author to predict the pressure drop across the compressible packed bed in the WGFE ion-exchange system. A modified version of an existing mathematical model that can simulate the performance of the ion-exchange chromatographic system is presented in Part II (Chapters 5 to 8). The modifications account for packed-bed compression effects, and it is therefore employed to predict their impact on behaviour of the WGFE ion-exchange system. The mathematical model presented in Part II can equally be used to simulate behaviour of the WGFE ion-exchange chromatographic system under the multiple design scenarios that may be considered during scale-up. Part III (Chapter 9) presents the results of such a study. An optimal packed-bed height and superficial velocity for a production-scale design of the ion-exchange system are identified. A final chapter, Chapter 10, will summarise the important findings presented in the thesis and consider the direction of further work which may be necessary.

The reader should note that the three parts in the thesis reflect the chronological progression of separate, but closely interrelated, research activities carried out by the author. Each individual part will present its own literature review of the subject matter it contains. Each part describes the author's attempts to overcome three problems regarded as key impediments to the successful scale-up of the WGFE ion-exchange system. This may initially appear disjointed, but corresponds to the historical evolution of the work contained in the thesis. I believe this presentation format captures the true spirit of the research

conducted. Each chapter comes as a natural advance on its predecessor, and serves as an inspiration for subsequent work.

1.5 Manufacture of WGFE by Ion-Exchange

1.5.1 Background

This purpose of this section is to provide a brief synopsis describing the origin of WGFE and the subsequent development of the process employed to manufacture it. It is only intended to provide the reader with an overview from a historical perspective, and in this respect, is by no means comprehensive. Some information is carefully guarded by confidentiality agreements. This contributes to the brevity of this Section (and subsequent Sections) in many places. Furthermore, it does not contain actual physical details of the design and operation of the process and the ion-exchange step employed to manufacture WGFE. These will be described subsequently in Section 1.5.2.

Whey is the yellow-green liquid that separates from the curd during the manufacture of cheese and acid casein (James, 1994). Whey has long been regarded as a waste by-product by the dairy industry and constitutes a considerable waste disposal problem. For example, in excess of one million tonnes (one billion kilolitres) of whey are generated each year in Victoria, Australia (CSIRO/DRL, 1990). Worldwide estimates of whey production exceed more than 80 million tonnes (CSIRO/DRL, 1990). Not surprisingly, the industry has considered a variety of methods for its disposal. Besides various direct waste treatment alternatives, this has included its commercial exploitation. Whey, for example, in a freeze-dried preparation is an important additive to processed foodstuffs as a flavour enhancer (CSIRO/DRL, 1990). Whey also contains a multitude of potentially valuable minor constituents (James, 1994). Many whey proteins and enzymes have a pharmaceutical or veterinary application. One such example is lactoferrin, which is employed in the formulation of human-infant milk preparations from bovine milk powder.

In 1990, a group of scientists at the Co-operative Research Centre (CRC) for Tissue Growth and Repair in Adelaide, Australia, discovered a protein extract recovered from cheese whey by ion-exchange chromatography contained a remarkable propensity to stimulate the growth of mammalian cells in culture (Francis *et al.*, 1995). This protein

extract became known as whey growth factor extract. Subsequent investigations have confirmed it contains a collection of low molecular weight (< 20,000) proteins which are potent growth factors (Francis *et al*, 1995). This includes the insulin-like growth factors (IGFs), epidermal growth factor (EGF) and transforming growth factor-β (TGF-β).

WGFE was quickly patented (PCT/AU91/00303, 1991) with the intention to commercialise it for a number of potentially valuable applications. These included a replacement or supplement to foetal bovine calf serum (FCS or FBS) in animal cell culture; a wound healing agent; and as a treatment for chemotherapy damage to the gut ('gut mucositis') in human cancer patients. Recent investigations have also indicated that WGFE may provide a commercial source for manufacture of individual growth factors it contains such as TGF-β (Rogers, 1996).

After its discovery, it was soon realised greater quantities of WGFE would be required to support ongoing research and development efforts required to realise its full potential. Subsequent development of the existing laboratory-scale WGFE process was commissioned. This took place initially in the CRC laboratories where it was first discovered, and then, under licence to Bonlac Pty Ltd (Australia's leading manufacturer of dairy products) at the Commonwealth Science and Industrial Research Organisation (CSIRO) Dairy Research Laboratories at Highett in Melbourne, Australia, where a pilot-scale plant was built in 1993. The establishment of a pilot-scale plant made available for the first time substantial quantities of WGFE and quickly led to the successful development of the first commercial WGFE-derived product. ACCEL gF (Gropep Pty Ltd, Adelaide, Australia) was launched in 1994 as an alternative growth preparation to FCS for cultured cells.

With the commercial availability of ACCEL gF and many new products in the pipeline, a decision was made in 1994 to develop a large-scale production plant permanently located at one of Bonlac's Victorian dairy processing and cheese manufacturing factories. A number options, ranging from an annual crude whey throughput of 5,000 kL to 40,000 kL, were considered. A prospectus for the commercial venture was commissioned. It indicated that potential viability of a large-scale production process depended in large part on the successful and cost effective scale-up of the pilot-plant (Davy John Brown Pty Ltd, 1993). In particular, a preliminary assessment of the capital and operating costs identified that the

ion-exchange step was a critical unit operation (Smithers, 1995). While it would only be a fractional contributor to capital costs (roughly 25%), the ion-exchange step would be the primary determinant of plant operating costs (approximately 40%).

1.5.2 The WGFE Manufacturing Process

The following description of the WGFE manufacturing process is based on the existing pilot-plant located at the CSIRO Dairy Research Laboratories. This information was provided by Geoff Regester, the Principal Research Scientist at the Division of Food Processing, Dairy Research Laboratory, CSIRO, Victoria, Australia. Particular attention is paid to describing in detail the design and operation of the ion-exchange step. Other unit operations in the process are only discussed in brief.

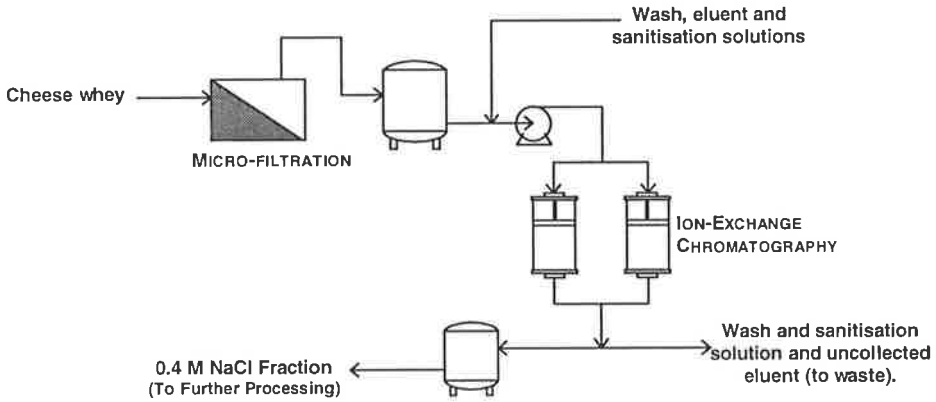

Figure 1.1: A simple schematic of the pilot-plant for manufacture of WGFE.

The process to manufacture WGFE consists of a number of steps. Figure 1.1 provides a simplified schematic of the unit operations which are employed. First, raw untreated cheese whey (pH 6 to 6.5) is microfiltered. The permeate is then directly loaded onto two 30 cm (internal) diameter Pharmacia (Uppsala, Sweden) BioProcess™ Glass (BPG) 300/500 chromatographic columns. Each column contains 18 L of Sepharose Big-Beads SP (Pharmacia, Uppsala, Sweden). The packed-bed height is approximately 21 cm. The flowrate of cheese whey applied to the two columns during the load step is 12 L/min or 6 L/min per column (a superficial velocity of 8.5 cm/min). A positive-displacement pump drives the microfiltration process and application of the microfiltered whey permeate to the BPG columns. It is also employed to pump all other process solutions used for subsequent steps (*ie* wash, elution, sanitisation *etc*).

The load step is terminated after 2300 L of whey is applied to the ion-exchange system and prior to breakthrough of any adsorbed species (as determined by a lactoperoxidase enzyme assay). The column is then washed with deionised water and subjected to a two-step elution protocol with sodium chloride at 0.4 M (or 0.5 M) and 1.0 M, respectively. All of these subsequent steps are carried out at an identical flowrate to the load step (*ie* a superficial velocity of 8.5 cm/min). The volume of process solutions employed in each step are approximately 310, 125 and 80 L, respectively.

The first fraction obtained during the step-elution protocol (at 0.4 M) represents the WGFE. It is collected, and sent for further processing at the CRC laboratories in Adelaide where it is subsequently diafiltered (with ammonium carbonate), sterile filtered, freeze dried and dispensed as the final product. The product yield obtained from the pilot-plant (under its current operating conditions) is approximately 40 to 60 grams of freeze-dried diafiltered WGFE per thousand litres of microfiltered cheese whey processed. This yield is variable and depends on whey type and quality. The second fraction (at 1.0 M) is a waste by-product and is discarded. The ion-exchange system is subsequently washed with deionised water, and then sanitised with 1.0 M sodium hydroxide to complete the chromatographic cycle. The wash step is conducted at an identical flowrate to load, wash and step-elution steps and uses 90 L of deionised water. The sanitisation step employs a combination of process solutions at varying flowrates. In the following sequence, these are 20 L of deionised water at 6 L/min; 20 L of 1.0 M sodium hydroxide at 4.5 L/min (a superficial velocity of 3.2 cm/min); and 40 L of deionised water at 20 L/min.

Analysis of the two step-elution fractions (James, 1994) indicate that the first consists predominantly of lactoperoxidase. Also present are a range of immunoglobulins and lactoglobulins, and the growth factors which provide the WGFE with its biological activity (Francis *et al.*, 1995). The second fraction consists mainly of lactoferrin. While this is at present regarded as a waste by-product, further investigations are underway to develop a process to purify the lactoferrin it contains for sale as a commercial product.

1.5.3 The Ion-Exchange Step Scale-Up Methodology

The ion-exchange step in the pilot plant described in Section 1.3.2 represents the culmination of a multitude of experimental studies, conducted at laboratory-scale, and at the pilot-plant itself, in the four years after WGFE was first discovered, to successfully optimise its scale-up. Physical and operational specifications that are currently employed will be the template for the design of the proposed production-scale ion-exchange system. This section provides a brief chronological review of scale-up methodology that led to their selection. It is based on informal discussions with key personnel at the CRC for Tissue Growth and Repair who were involved in development and scale-up of the WGFE ion-exchange system. It provides a fascinating reflection of the heuristic trial and error approach employed to scale-up chromatographic systems in the biotechnology industry.

It should be noted, however, that this review is not comprehensive. Four years is considerable period of time, and many activities have been summarised and chronologically condensed at the author's discretion. This is an attempt to consolidate the subject matter. The focus is placed on the broad scale-up methodology that was considered at the time, and with which, the author had no direct involvement. Furthermore, the scientists involved carried out many studies investigating numerous variations in design and operation of the ion-exchange step. One such example was the use of ammonium chloride instead of salt in the eluent (Francis *et al.*, 1995). Many of these variations had no direct bearing on the final design and operation of the pilot-plant and have not been considered in the following discussion.

When WGFE was first discovered, the ion-exchange chromatographic system consisted of an 10 cm (internal) diameter Pharmacia BPG 100/500 column packed with 500 mL of Sepharose Fast-Flow SP (Pharmacia, Uppsala, Sweden) and a peristaltic pump. Sepharose Fast-Flow SP is a strong cation-exchange (6%) cross-linked agarose chromatographic resin with an average (volume-mean) diameter of approximately 108 μm (James, 1994) and a particle size range between 45 to 165 μm (Pharmacia Bioprocess Technology, 1996a). The packed-bed height in the column was approximately 6 to 7 cm.

In an identical manner to the operation of the pilot-plant described above, microfiltered whey would be loaded onto the column to adsorb various constituents in the whey including

the growth factors. The flowrate employed in initial experiments during the load step was a 70 mL/min (a superficial velocity of 0.9 cm/min). The volume of whey applied was 5 L and the load step was terminated well before it was likely that breakthrough of any adsorbed species would occur. The resin in the column was then subsequently washed with (0.25 L of) 50 mM sodium citrate buffer solution, pH corrected to 6.5. A (0.25 L) single step-elution with 1.5 M sodium chloride was performed and the eluent collected. The resin was then sanitised with 1.0 M sodium hydroxide and washed again with 50 mM sodium citrate buffer solution, pH corrected to 6.5, to complete the chromatographic cycle. In all steps subsequent to the load step an identical flowrate was employed.

The (1.5 M) eluent was the predecessor of the WGFE - effectively a combination of the two step-elution fractions recovered from the existing pilot-plant (refer Section 1.5.2). Its propensity to enhance growth in number of mammalian cell lines *in vivo* resulted in further investigations to isolate its growth stimulating biological compounds. A sequence of experimental studies was performed. The single 1.5 M step-elution was replaced by a series of step elutions increasing in concentration from 0 M to 1.5 M. Various fractions during these experiments were collected and analysed for their mitogenic ability in a range of cell lines. It was finally decided that two-step elutions could be employed to recover the two most desirable fractions. A 0.4 M or 0.5 M step-elution would recover a fraction which contained a collection of whey proteins and growth factors which optimised its mitogenic properties. Major whey proteins present besides the growth factors included lactoperoxidase, immunoglobulins and lactoglobulin. This fraction would become the WGFE. A subsequent 1.0 M elution would recover a near-pure lactoferrin fraction.

Additional investigations were performed in an attempt to separate the growth factors from other whey proteins in the 0.4 M step-elution fraction. These involved, at first, further experiments to develop a refined step-elution protocol during the 0.4 M step elution. This consisted of a sequence of step-elutions increasing from 0 to 0.4 M sodium chloride. This strategy was unsuccessful. Secondly, further processing of the 0.4 M step-elution fraction by gel filtration. This additional step, while successful at removing immunoglobulins, was omitted from the proposed WGFE-production process, although, it has recently been re-considered in attempts develop a marketable purified version of WGFE.

With the step-elution protocol decided, subsequent investigations focussed on improving the productivity of the ion-exchange step. A three-pronged strategy was employed. First, the packed bed height in the column was increased to approximately 21 cm. This was designed to increase the total adsorption capacity of the packed bed allowing a larger whey volume to be applied in the load step of each cycle.

Second, flowrate was steadily increased to lower the cycle time. Pressure drop ultimately restricted the flowrate to a maximum value of approximately 250 mL/min (a superficial velocity of 3.2 cm/min). The constraint on flowrate was dictated by the maximum head the peristaltic pump could provide. This was two bar, beyond which any further increase in flowrate could not be reliably sustained. All flowrate increases were applied equally across all steps in the chromatographic cycle, except during sanitisation where the higher viscosity of the 1 M sodium hydroxide solution restricted the flowrate to a lower value of 90 mL/min (a superficial velocity of 1.1 cm/min).

Third, larger volumes of whey were applied during the load step to maximise the yield of WGFE per cycle while ensuring breakthrough was avoided. (Breakthrough was monitored by measuring lactoperoxidase enzyme activity in the column effluent.) These larger volumes of whey led to greater adsorption of whey proteins during the load step, and the volume of wash and eluent solutions required for recovery of the WGFE were also accordingly increased. A limit on whey feed volume was eventually reached at between 100-120 L. At this limit, and based on the maximum flowrate, the total time required to complete one (chromatographic) cycle was approximately 16.1 hours with the dominant step being the load step at nearly 13 hours.

A decision was made to replace Sepharose Fast-Flow SP with Sepharose Big-Beads SP. Sepharose Big-Beads SP is an identical ion-exchange resin to Sepharose Fast Flow, but with a larger average (volume-mean) particle diameter of 200 μm (James, 1994) and particle size range of 100 to 300 μm (Pharmacia Bioprocess Technology, 1995). This modification resulted in a decrease in pressure drop across the packed bed. The strategy of increasing flowrate was repeated. An increase in superficial velocity to approximately 8.5 cm/min was achieved before pressure drop again became a constraint. Once more, flowrate increases were applied equally across all steps in the chromatographic cycle, except during sanitisation where a superficial velocity of only 3.2 cm/min could be sustained. The time to

complete one cycle was now approximately 4.2 hours, of which, 3.2 hours was required for the load step.

The design and operation of this laboratory-scale system served as the template the pilot-plant at CSIRO's Dairy Research Laboratories which was subsequently built in 1993. After the initial pilot-plant trials, however, it was quickly realised that constraint on pressure drop encountered in the laboratory-scale system had disappeared. The positive-displacement pump could reliably pump a variety of larger flowrates than that currently employed in the ion-exchange system against heads of up to 60 bar. The Pharmacia BPG 300/500 column, unfortunately, could only sustain a maximum operational pressure of three bar (Pharmacia Bioprocess Technology, 1996b), although this was still much higher that two bar limit imposed by the peristaltic pump which was employed at laboratory-scale. In addition, it was discovered, that the pressure-drop across the ion-exchange system in the pilot-plant was much lower than in its laboratory-scale counterpart. The bed height of the packed bed was unchanged, and thus, the Pharmacia BPG 300/500 column displayed a lower pressure drop across the column and its peripherals (*ie* conduits, distributor, frits *etc*).

An increase in superficial velocity across the chromatographic system in the pilot-plant could be sustained. This led to a flurry of further investigations. WGFE yield per cycle was established as the determining factor for evaluating further increases in flowrate. In a surprising turn of events, it was discovered that despite the same volume of whey being applied during the load step, increases in flowrate beyond a certain limit resulted in a dramatic decline in yields of WGFE per cycle. This limit was 10 L/min per column (a superficial velocity of 14.5 cm/min). The pressure drop across the pilot-plant chromatographic system at this flowrate was less than 2 bar, well below the pressure constraint of 3 bar imposed on the system. Further increases in flowrate beyond this limit, even though they could be accommodated, would diminish the yield of WGFE per cycle. The reason for this remained a mystery and further variations in flowrate were not considered. The superficial velocity of 8.5 cm/min for load, wash and elution steps remains as the operating conditions for the pilot-plant at the time of this study. However, an increase to 14.5 cm/min will soon be implemented for further trials.

1.5.4 Scale-Up and Performance and Cost

At this point, it is worthwhile reflecting on the typical industry approach to chromatographic scale-up which was described in Section 1.3. Its fundamental premise can easily be recognised in the scale-up methodology employed for the ion-exchange step in the WGFE process. That is, higher flowrates will maximise system productivity, and thus, result in the optimal scale-up of a chromatographic system. Indeed, once the purification protocol with the Pharmacia BPG 100/500 column containing Sepharose Fast-Flow SP and an appropriate bed height (*ie* 21 cm) were selected, higher flowrates were mercilessly pursued to improve system productivity. When pressure drop became a constraint (*ie* the maximum head the peristaltic pump could provide), Sepharose Fast-Flow SP was replaced by a resin with a larger bead size: Sepharose Big-Beads SP. Flowrate was again increased until the pressure became a limiting factor. The resulting operating conditions were used as a template for the pilot-scale ion-exchange system. Even then, an increase in the flowrate was considered again when it was discovered the original pressure constraint no longer applied.

However, it is also interesting to note the deviations. The temptation to reduce bed height when pressure drop became constraint was avoided. Furthermore, a quantitative measure of product yield in the pilot-plant was used to guide the final selection of further increases in flowrate that were considered. With regard to this latter point, it appears quite plausible that additional increases in flowrate, subject to the prevailing pressure constraint, may well have been implemented if WGFE yield per cycle had not been monitored. But would this have been of great detriment to the performance of the pilot-scale ion-exchange system? Perhaps higher flowrates, and thus, shorter cycle times would have led to an overall increase in system productivity (the WGFE yield per unit time per unit volume of resin) despite a lower cyclic yield of WGFE. What would be the result of this variation on the cost of its large-scale counterpart for the bioprocessing facility being considered?

Many other possibilities can also be considered. Did the desire to increase the flowrate during initial laboratory-scale trials also lead to diminishing yields of WGFE per cycle? This is of course unknown because cyclic WGFE yield was not used as an indicator of system performance during initial experiments. Why was 21 cm arbitrarily selected as the bed height? Perhaps an alternative bed height should have been considered. For example, a

higher bed height would have increased the adsorption capacity of the packed bed. Although increased pressure-drop may have meant lower flowrates and longer cyclic times, higher cyclic WGFE yields would be the result. Would productivity rise? Likewise, a lower bed height would probably mean higher flowrates, shorter cycle times and lower cyclic WGFE yields. How would any of these changes affect the design and cost of the ion-exchange system?

These questions bring us back to the fundamental flaw of heuristic-type scale-up techniques. While they may have been successful for one type or group of systems, in which their origin can often be found, there can be no guarantee it will provide satisfactory results in others. Substantive and convincing accounts of the industry-standard scale-up strategy described in Section 1.3 are curiously absent in the published literature. In fact, this thesis will reveal considerable anecdotal evidence that contradict its utility for the purpose it was devised. It does not provide the answers we seek.

It is evident that an alternative and more reliable approach must be found to predict performance, and then, cost of the WGFE ion-exchange system during scale-up. The desirable attributes of such an approach have already been discussed. Ideally, it would involve the systemic examination of multiple design scenarios. Each scenario would include a different combination of the physical design or operational parameters that may be considered during scale-up. Re-consider the ion-exchange system pilot-plant, for example. Assuming the purification protocol and chromatographic resin were immune to further modification, this would probably include the packed-bed height, and flowrates and volumes of process solutions employed in each step of its chromatographic cycle. Such an approach would obviously improve the probability that a truly optimal design for a larger-scale ion-exchange system would be successfully identified.

Part III engages in further investigation of this problem. A non-linear multicomponent rate-equation chromatography model presented in Part II is employed to simulate the behaviour of the ion-exchange system at different packed-bed heights and superficial velocities during the frontal adsorption step. The results are used to analyse the process economics of a hypothetical large-scale ion-exchange system based on the pilot-plant. An optimal packed-bed height and superficial velocity for scale-up are identified.

1.5.5 Scale-Up and the Pressure Constraint

All of the questions in Section 1.5.4 were primarily concerned with the concept of performance and cost during scale-up of the WGFE ion-exchange system. However, it is quite clear that one important constraint limits the physical design and operational parameters that may be selected. It is pressure-drop. In the laboratory-scale ion-exchange system, the constraint on pressure drop was determined by the maximum head (*ie* 2 bar) the peristaltic pump could provide at laboratory-scale. In the pilot-plant, it was dictated by maximum operational pressure (*ie* 3 bar) of the Pharmacia BPG 300/500 column. For either case, the pressure drop was the limit on the flowrate and bed height which could be employed in the WGFE ion-exchange system, although these were different for type of chromatographic resin and fluid.

When the pilot-plant scale system was built, one can only regard it as serendipitious that the constraint on pressure drop increased while the actual pressure drop across the ion-exchange system decreased. However, consider an alternative scenario. What if, for example, the pressure constraint had decreased while the pressure drop increased? A lower flowrate would have been required for the pilot-plant. The implications of such a change would not have been serious. Quite simply, a lower flowrate would have been implemented. Now consider an identical scenario, but during the design and construction of large-scale ion-exchange system based on the pilot-plant. The implications of such a change are potentially catastrophic. The desired flowrate may not be attained. The simple remedy of decreasing flowrate in this case would not be acceptable. Flowrate would be restricted to a lower than design value severely limiting the capacity of the system to meet its production goals. Not a very successful scale-up!

It is therefore desirable to have prior knowledge of how pressure will limit the possible design scenarios that may be considered during scale-up of the WGFE ion-exchange system. The pressure constraint is nearly always known, and thus, it is the pressure drop of the WGFE ion-exchange system upon scale-up that must be estimated. Will it experience a similar decrease to that which was observed between the laboratory-scale system and the pilot-plant? This cannot be predicted with certainty for several reasons. To begin with, the pressure drop across the WGFE ion-exchange system depends on what can be regarded as two separate components. First, the pressure drop across the packed bed. Sepharose Big

Beads SP is an agarose based resin. These types of resins are compressible (Boyer & Hsu, 1992), and packed beds that contain them experience compression during fluid flow. This results in a non-linear parabolic relationship between flowrate and pressure drop (Mohammad *et al.*, 1992) in contrast to the linear behaviour of an incompressible type resin (*eg* polymethacrylate). Pressure drop across compressible packed beds also displays a significant functional dependence of column diameter (Janson & Hedman, 1987; Mohammad *et al.*, 1992). This is a result of friction effects between the packed bed (as it is compressed) and the walls of the column it contains. The pressure drop across a compressible packed bed in a smaller laboratory-scale column will be much lower than in a larger production-scale column (Janson & Hedman, 1987). While such behaviour was not explicitly observed during the laboratory and pilot-plant studies for the WGFE ion-exchange system, it has been identified in other experimental investigations using agarose-based resins (Janson & Hedman, 1987).

The second component of pressure losses across chromatographic systems is the pressure drop due to the column and its peripherals. This pressure drop is system dependent and will obviously be different for smaller laboratory-scale and larger pilot-plant or production-scale columns. This provides an explanation for the decrease in pressure drop across the ion-exchange system that was observed in the pilot-plant. While the pressure drop across the packed bed increased in the larger-sized column (due to compression), it was outweighed by a much larger decrease in the pressure drop across the column and its peripherals. However, there is no guarantee that such a decrease would occur in even larger-diameter columns that may be employed in a production-scale chromatographic system.

The contribution to pressure drop of both the packed bed and the column and its peripherals must be known in order to accurately predict the range of flowrates and bed heights that could be sustained in the WGFE ion-exchange system during scale-up. It is impossible to predict the pressure drop of the column. This information must be provided by the manufacturer, or alternatively by experimental measurement. Information regarding pressure drop across packed beds of chromatographic resin is usually unavailable, although some resin manufacturers provide experimental data for pressure drop in chromatographic systems containing the resin of interest. These combine the pressure drop of the packed bed with that of column and peripherals, and are therefore, useless in this respect. If a resin is incompressible, the pressure drop can be estimated from a plethora of predictive semi-

empirical and theoretical correlations that are available for incompressible-type packed beds (Foust *et al.*, 1980; Perry & Green, 1984). Unfortunately, if the resin is compressible, as is Sepharose Big-Beads SP, accurate and predictive correlations of this nature are rare. Some existing heuristic scale-up methodologies have employed such correlations in an attempt to account for the compressibility of chromatographic resins, and estimate the variation in pressure drop across the packed bed, during scale-up (Mohammad *et al.*, 1992).

Existing theoretical and predictive correlations for pressure-drop prediction in compressible packed beds are reviewed in Part I. It is shown that they are inadequate and cannot account for the combined influence of compressibility and wall friction effects that lead to variations in pressure drop during scale-up. A new model which overcomes both of these problems is developed by modifying the volume-averaged continuum theory. It is used to predict pressure drop across the compressible packed beds of Sepharose Big-Beads SP in the ion-exchange system. The increase in pressure drop that will occur in larger-diameter columns employed in the ion-exchange system of the proposed production-scale WGFE process is anticipated.

1.5.6 Scale-Up and Compression Effects on Performance

Clearly, increased compression of the packed bed in the ion-exchange system is likely to occur during scale-up. This gives rise to another important issue that must be considered. Would this increased compression be significant enough to alter the performance of the system? Could this impact on the physical design and operational conditions which would be regarded as optimal in the pilot-plant?

To put this in perspective, compression of a packed beds will inevitably decrease its voidage or porosity. It would obviously also lead to considerable deformation and compression of individual resin particles. Hypothetically, both of these changes could alter the system behaviour of protein separation during adsorption, elution or displacement in a variety of ways. The reduction in void space decreases the retention time of the system. The increase in interstitial velocity as voidage is reduced increases external-film mass transfer to, and from, resin particles. Deformation of particles during compression changes the surface area available for external-film mass transfer. Particle compression leads to reductions in intraparticle-pore space decreasing intraparticle diffusion. The effective resin adsorption

capacity is reduced as particle compression restricts access to intraparticle-pore space. All of these could potentially influence system performance during scale-up of the WGFE ion-exchange system.

However, does this concern have any basis? A number of studies have observed that compression impacts on chromatographic efficiency (Freitag *et al.*, 1994; Sarker & Guiochon, 1995), although a review of literature has revealed only two cases where such effects have been explicitly investigated. Both examined high-pressure liquid chromatography (HPLC) systems where a packing pressure was applied to the resin bed to artificially induce axial compression. Meyer and Hartwick (Freitag *et al.*, 1994) investigated the relationship between column efficiency and packing pressure for narrow-bore columns packed with silicaceous stationary-phase particles and found evidence for an optimal packing pressure. No attempt was made to explain this observation as a function of compression-induced changes in bed properties. Freitag *et al.* (1994) examined the influence of bed compression on the behaviour of a high-performance column packed with spherical gigaporous styrene-divinyl benzene polymer resin particles. Moderate packing pressures were found to decrease the HETP (height equivalent to a theoretical plate). This behaviour was ascribed to the increase in interstitial velocity within the bed during compression. This would enhance external-film mass transfer and improve intraparticle convective flow within resin particles, thereby, increasing the effective intraparticle-diffusion coefficient. Higher axial pressures were also found to increase HETP providing further evidence of an optimal packing pressure for column efficiency.

Part II investigates this problem and examines its potential implications for scale-up of the WGFE ion-exchange system. An existing mathematical model used to simulate protein adsorption-desorption in chromatographic systems is modified to account for compression effects. Compression-induced changes in packed-bed porosity and particle diameter for a laboratory (2 cm) and production-scale (20 cm) column are estimated from pressure-drop data using the new model for pressure-drop prediction developed in Part I. These are combined with model parameters from a previous experimental study for two major whey proteins, namely, lactoperoxidase and lactoferrin. Model simulations to replicate the behaviour of the ion-exchange system under the influence of compression are performed. The results are analysed to determine the impact of compression on WGFE ion-exchange system behaviour.

Part I: Pressure-Drop Prediction

CHAPTER 2

MODEL DEVELOPMENT

2.1 Objective - Part I

The principal goal of Part II in this thesis is to develop an accurate predictive model for pressure drop across compressible packed beds of chromatographic resin. The model will successfully account for the combined influence of resin compressibility and wall friction effects. Ultimately, it will allow prediction of packed-bed pressure drop in larger (diameter) columns that will be employed during scale-up of the WGFE ion-exchange system.

2.2 Preamble - Chapter 2

Pressure drop is a key constraint to the successful scale-up of the WGFE ion-exchange system. It restricts the combination of flowrates and bed heights that can be utilised. Pressure drop across a compressible packed-bed of Sepharose Big-Beads SP will display a functional dependence on column diameter. This is a result of wall friction effects. During scale-up, the packed-bed pressure drop will increase in larger (diameter) columns. The implications of such a change are potentially catastrophic. Some form of prediction is essential to ensure that a functional and successful production-scale design for the WGFE ion-exchange system. Unfortunately, existing models for pressure-drop prediction with compressible chromatographic resins are empirical. Genuine predictions can only be made over the experimental range for which they have been validated. Alternative models exist. Many provide a theoretical or mechanistic description of fluid flow through compressible media. True *a priori* prediction of pressure-drop behaviour is possible. However, these models do not account for wall friction effects.

2.3 Background Art - Compressible Chromatography Resins

While the impact of compression on the packed-bed pressure drop in chromatographic systems has been observed in a number of studies, a review of literature reveals only one

case where such effects have been explicitly studied. Mohammad *et al.* (1992) investigated the packed-bed pressure drop across several dextran-based compressible resins: Sephadex G-25 Course, Sephadex G-100 regular and Sephadex G-100 superfine. (These resins are commonly employed in size-exclusion chromatography.) Different column diameters (1.6, 2.0 & 5.0 cm), bed heights (5.0-33.0 cm) and superficial velocities (0-110 cm/min) were examined. Water was employed as the test fluid in all experiments.

Examples of experimental data collected by Mohammad *et al.* (1992) for Sephadex G-100 Regular as reproduced by the author are as follows. Variation in packed-bed pressure drop with superficial velocity, v_{sup}, at different (initial) bed heights, L_i, is shown in Figure 2.1. Similarly, the impact of column diameter, D, on packed-bed pressure drop is displayed in Figure 2.2.

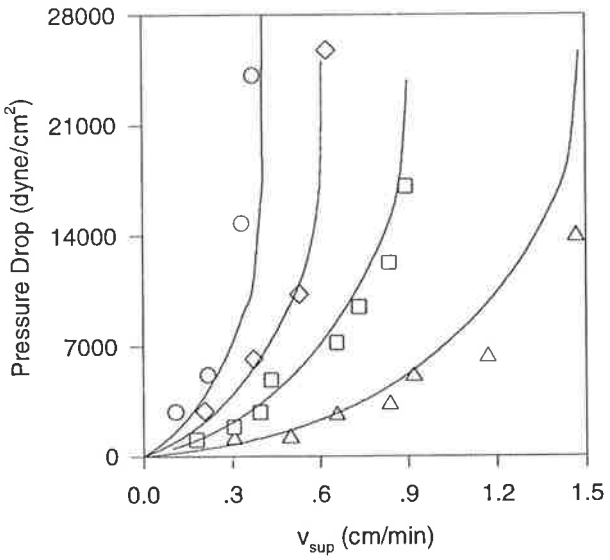

Figure 2.1: Pressure-drop data *vs.* model predictions for Sephadex G-100 Regular at varying lengths as reproduced from Mohammad *et al.* (1992): △ - L_i=5.0 cm; □ - L_i=12.9 cm; ◇ - L_i=21.0 cm; ○ - L_i=33.9 cm; model prediction - (——).

The pressure-drop behaviour of Sephadex G-100 Regular in Figure 2.1 is typical of compressible chromatography resins. Packed-bed pressure drop increases in a non-linear parabolic fashion with superficial velocity. This is a result of porosity changes and particle deformation caused by flow-induced compressive stresses acting within the bed. Non-linearity of the pressure-drop behaviour becomes more pronounced with bed height. In fact, for each bed height in Figure 2.1, a superficial velocity is observed which acts as an

asymptote for pressure drop. Pressure drop appears to rise sharply tending towards an infinite value. Mohammad *et al.* (1992) referred to this asymptote as the 'critical' velocity. Ladisch and Tsao (1978) observed similar effects in ion-exchange resins, although experimental measurements of pressure drop included pressure losses across the chromatographic column and its peripherals (*ie* distributor, frits, conduits *etc*). They postulated that the phenomena was due to a small region of resin particles at the bottom of the bed where flow-induced compressive stresses peak. At large flowrates, this region becomes highly compressed resulting in an extremely low bed porosity. Any further increase in compressive stress leads to change in bed porosity that is large relative to this small value. Even a minor change in flowrate induces a large increase in pressure drop.

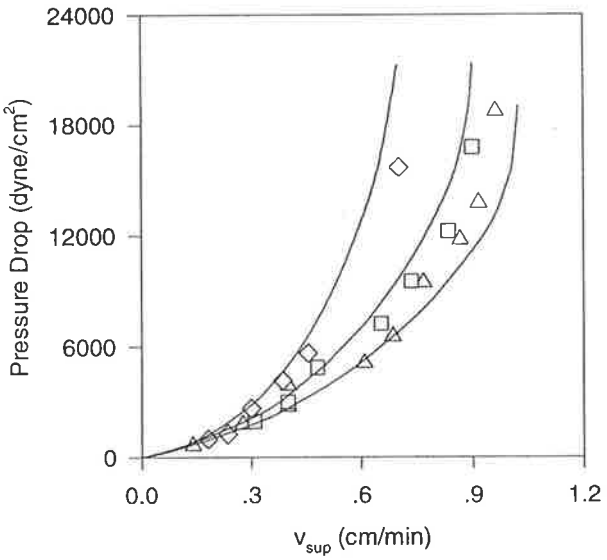

Figure 2.2: Pressure-drop data *vs.* model predictions for Sephadex G-100 Regular at different column diameters as reproduced from Mohammad *et al.* (1992): △ - D=1.6 cm, L_i=12.3 cm; □ - D=2.8 cm, L_i=12.8 cm; ◇ - D=5.0 cm, L_i=12.4 cm; model prediction - (——).

The influence of wall friction on packed-bed pressure-drop behaviour of chromatographic resins is clearly illustrated in Figure 2.2. Wall friction supports the packed bed as it is compressed. The effects are less significant in larger (diameter) columns, and thus, greater compression and higher pressure drops are observed.

An empirical model for correlation of experimental packed-bed pressure drop data for the compressible gel packings was developed by Mohammad *et al.* (1992):

$$\Delta P = \frac{\mu v_{sup} L}{k_o d_p^2} \Phi \exp\left(a v_{sup} L\right) \tag{2.1}$$

where k_o is the initial permeability constant; a is a measure of rigidity for the packing material (min/cm^3); v_{sup} the superficial velocity through the column (cm/min); L is (compressed) column length (cm); d_p is the resin particle diameter (before compression) (cm); μ is the fluid viscosity (g/(cm.s)); a is an empirical measure of packing material rigidity (min/cm^2); and

$$\Phi = 1 + \frac{1}{C_1\left(1 - \frac{v_{sup} L}{v_{sup,cri} L}\right)} \tag{2.2}$$

where C_1 is a empirical constant specific to the resin of interest; and $v_{sup,cri}$ the critical velocity which acts as the asymptote for pressure drop.

Equations 2.1 and 2.2 relate pressure drop to (superficial) velocity, (compressed) column length (*ie* bed height), permeability, column diameter, fluid viscosity and particle diameter. Column length changes with compression and Mohammad provides an additional empirical relationship for its estimation:

$$\frac{L - L_i}{L_i} = \frac{b_1 v_{sup} L}{b_2 + v_{sup} L} \tag{2.3}$$

where L_i is the initial packed-bed height in the column; and b_1 and b_2 are variable parameters.

Mohammad's empirical model accounts for both, the compressibility of the packed bed, and the functional dependence of pressure drop on column diameter. The parameters k_o, a, C_1 , $v_{sup,cri}$, b_1 and b_2 in the empirical model allow it be adapted to any compressible gel packing of interest, although, they must first be determined from experimental data describing the desired range of prediction. Of these, only k_o and C_1 are constant parameters for the

compressible gel packing being studied. b_1 and b_2 depend on column diameter, but are independent of packed bed height. $v_{sup,cri}$ and a vary with both column diameter and packed-bed height.

The parameters in the empirical model were determined by Mohammad for each compressible gel packing investigated in the study. A combination of linear and non-linear regression of the empirical model against experimental pressure-drop data was employed. b_1 and b_2 were determined for each column diameter studied. Arbitrary experimental functions were employed to describe the variation of $v_{sup,cri}$ and a with column diameter and packed-bed height. Model predictions compared with experimental data for Sephadex G-100 Regular as reproduced from model parameters given by Mohammad are shown in Figures 2.1 and 2.2. Excellent agreement can be observed. Similar results were obtained for other compressible gel packings.

Mohammad *et al.* (1992) employed the empirical model for pressure-drop prediction to develop a scaling procedure for the chromatographic separation of bovine serum albumin and nickel nitrate. Equations 2.1, 2.2 and 2.3 were combined with other empirical correlations describing the separation characteristics of the two compounds for each resin in smaller laboratory sized columns (1.0 & 1.6 cm). A scaling analysis was performed to determine the optimal particle size, bed height, superficial velocity and column diameter for the separation.

Due to the empirical nature of the model, however, the analysis was restricted to the column-diameter range and packed-bed heights tested during experiments. Extrapolation to larger-diameter columns (>5.0 cm) could not be performed. This restriction highlights the major deficiency of such an empirical-type model. Genuine predictions can only be made over the experimental range for which they have been validated. Extrapolation beyond this range cannot be performed with confidence and are likely to generate erroneous predictions. True *a priori* predictions are not possible.

Mohammad's empirical model could be employed to predict packed-bed pressure drop of Sepharose Big-Beads SP. To be confident of accurate predictions, however, experimental packed-bed pressure-drop data in production-scale columns would be required for the desired flow range, bed heights, fluid properties and column sizes that would be considered

during scale-up. The problem dimensionality is large and numerous tests would be required. The volume of Sepharose Big-Beads SP resin, and the number and type of production-scale columns, that would be required for such an extensive study would also involve considerable expense. This is a prohibitive financial penalty from a practical perspective.

Instead, it would be ideal if some form of prediction could be made from experimental data gathered at a smaller-scale (*eg* in the pilot-plant or at laboratory-scale) with extrapolation of results to the desired production-scale column. Clearly, extrapolation would need to be based on some physical model of pressure-drop behaviour in packed beds of compressible chromatographic resins with a predictive ability. This predictive ability would account for the combined influence of resin compressibility and wall friction effects. As we will discover, alternative models with such a predictive ability of pressure-drop behaviour in compressible media do exist. However, they do not account for wall friction effects.

2.4 Background Art - Other Compressible-Type Media

Packed beds of compressible chromatography resin are similar to compressible packed beds of granular media encountered in other industries. In particular, where filtration of particulates from a liquid stream is required. Pressure-drop behaviour across such compressible-type packed beds has been the subject of a vast number of articles. It is therefore not surprising that many have dealt with the limitations of experimental descriptions of pressure-drop behaviour. Attempts to develop a predictive empirical, semi-empirical or a fundamental or mechanistic model are numerous. Topical papers and reviews on this subject have been provided by Ruth (1946), Tiller and Huang (1961), Shirato *et al.* (1963), Foust *et al.* (1980), Willis *et al.* (1983), Perry and Green (1984), Willis *et al.*(1985), and Jönsson and Jönsson (1992).

While each of these could be reviewed in detail, it would serve no practical purpose in this thesis (and for the reader's continuing interest). Most modern-day predictive models of pressure-drop behaviour in such systems have a common origin: the volume-averaged continuum theory of multiphase processes. This theory was first developed nearly two decades ago and is based on the fundamental concepts of the conservation of mass and momentum. It provides a firm theoretical basis for examination of multiphase systems. For

analysis of flow through packed beds of particulate solids, a modified form known as the multiphase theory of filtration is widely employed. In this thesis, it will suit our purposes to use it as a basis of a new predictive model of pressure drop across compressible packed beds of chromatography resin. The multiphase theory of filtration will therefore be subsequently described with this aspiration in mind.

2.5 The Multiphase Theory of Filtration

An introduction to the multiphase theory of filtration is best served by a practical example of its application. Chase and Willis (1992) provide a description of how the multiphase theory of filtration can employed to analyse compressible cake filtration of compressible fibrous-cellulose particles. For the readers further interest, a more comprehensive definition of the volume-averaged continuum theory of multiphase processes from which the multiphase theory of filtration is derived is given by Hassanizadeh and Gray (1980). An excellent description of its historical development and alternative applications is provided by Willis *et al.* (1983).

A simple schematic of the cake-filtration process is illustrated in Figure 2.3. A liquid stream is applied to a filter medium (the septum) which is impermeable to the particulates it contains. The particulates are retained on the surface of the filter medium and accumulate forming a cake (packed bed). The cake is nominally divided into two phases. The solid phase is the volume of compressible cake delineated by the particle exterior boundaries and their interior. All remaining external volume in the cake is the fluid phase.

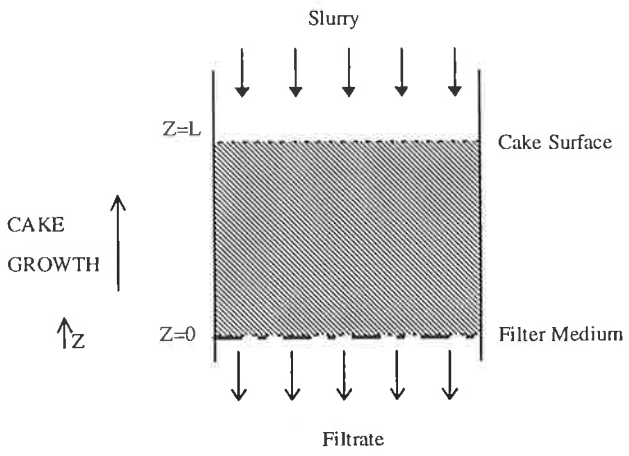

Figure 2.3: Compressible cake filtration.

The multiphase theory of filtration describes the rectilinear flow through the vertically oriented filter cake illustrated in Figure 2.3 by determining the mass and momentum balances for each phase:

$$\frac{\partial \varepsilon_f}{\partial t} + \frac{\partial\left(\varepsilon_f v_z^f\right)}{\partial Z} = 0 \tag{2.4}$$

$$\frac{\partial \varepsilon_s}{\partial t} + \frac{\partial\left(\varepsilon_s v_z^s\right)}{\partial Z} = 0 \tag{2.5}$$

$$\varepsilon_f \frac{\partial P}{\partial Z} + F_z^d = 0 \tag{2.6}$$

$$\varepsilon_s \frac{\partial P}{\partial Z} - F_z^d + \frac{\partial \tau_{zz}^s}{\partial Z} + \varepsilon_s(\rho^s - \rho^f)g = 0 \tag{2.7}$$

where Z is the axial coordinate in the cake; t is the temporal coordinate; ε_s is the solid-phase void fraction; τ_{zz}^s is the axial solid matrix stress acting to compress the cake; F_d^z is the drag force acting on cake particles and induced by fluid flow; ρ^s and ρ^f are the solid- and fluid-phase densities, respectively; and v_z^s and v_z^f are the solid- and fluid-phase velocities, respectively.

Equations 2.4 and 2.5 are the fluid-phase and solid-phase mass balances, respectively. Equations 2.6 and 2.7 represent the fluid-phase and solid-phase momentum balances, respectively.

The mass balance for the fluid phase, *eq.* 2.4, describes the accumulation that occurs during compression, and bulk convection as liquid passes down through the cake. In a similar fashion, accumulation and convection of the particles in the cake are described by the solid-phase mass balance, *eq.* 2.5. The fluid-phase momentum balance, *eq.* 2.6, accounts for the change in fluid pressure generated by drag between the moving fluid and cake particles. The solid-phase momentum balance, *eq.* 2.7, describes the drag-induced change in fluid pressure, the drag force, the net change in axial stress, and buoyant forces (due to the difference in phase densities) acting on particles in the bed.

Equations 2.4 to 2.7 provide a sound theoretical basis for analysing compressible cake filtration, but do not represent a determinate set of equations. A sequence of constitutive relations for both drag force and solid matrix stress are required. Chase and Willis (1992) present such a set based on several hypotheses. These hypotheses, while specifically related to the cake filtration, apply equally to compressible packed beds of chromatographic resin, except for one instance. This exception will be discussed subsequently. The sequence of constitutive relations presented by Chase and Willis are as follows. Drag force is described by

$$F_d^z = R^f (v_z^f - v_z^s) \tag{2.8}$$

The resistance function, R^f, depends on the fluid-phase volume fraction and specific-surface area of the particles. This is explicitly described by the Blake-Kozeny expression:

$$R^f = \frac{B\mu(a_s\varepsilon_s)^2}{\varepsilon_f} \tag{2.9}$$

where B is a constant empirical parameter for the system of interest. Specific particle-surface area, a_s, is related to solid-phase volume fraction by a power-law function:

$$a_s = a_s^e \left(\frac{\varepsilon_s}{\varepsilon_s^e} \right)^N \tag{2.10}$$

where N is an constant empirical parameter; and a_s^e and ε_s^e are the specific particle-surface area and solid-phase void fraction, respectively, evaluated at the equilibrium or unstressed condition at the top of the filter cake, and are both constant parameters.

Solid matrix axial stress in a deformable solid phase is related to the axial strain (deformation), e_{zz}^s, by Hookes Law:

$$\tau_{zz}^s = \sigma^s e_{zz}^s \tag{2.11}$$

The modulus, σ^s, in Hookes Law depends on the volume fraction according to the following empirical expression:

$$\sigma^s = \frac{\sigma^e\left[(\varepsilon_s^e / \varepsilon_s)^M - 1\right]}{M\left[(\varepsilon_s^e / \varepsilon_s) - 1\right]} \tag{2.12}$$

where σ^e is the unstressed value of the modulus; and M is a constant empirical parameter.

Finally, solid-phase volume is conserved during compression of the cake and strain is related to the solid-phase volume fraction by

$$e_{zz}^s = \left(\frac{\varepsilon_s^e}{\varepsilon_s} - 1\right) \tag{2.13}$$

The problem is further simplified as follows. The weight of the cake is regarded as inconsequential and can be omitted from the solid-phase momentum balance. Particles accumulating in the cake are stationary and their axial velocity is therefore also omitted (*ie* $v_z^s = 0$). Superficial velocity, v_{sup}, is substituted for fluid-phase velocity, v_z^f:

$$v_z^f = \frac{v_{sup}}{\varepsilon_f} \tag{2.14}$$

Equations 2.4 to 2.14 are now a determinate set of equations once material specific parameters B, N, M, σ^s, a_s^e and ε_s^e are known for the cake particles. Their solution provides the solid-state stress and pressure distribution as well as the variation in fluid-phase void fraction and specific-surface area of particles throughout the cake. For the purposes of illustration, fluid pressure in the compressible cake can be explicitly described by substitution of *eq.* 2.9 and the Blake-Kozeny expression, *eq.* 2.8, into the fluid-phase momentum balance, *eq.* 2.6, and rearranging:

$$\frac{\partial P}{\partial Z} = -\frac{B\mu(a_s\varepsilon_s)^2 v_z^{sup}}{\varepsilon_f^3} \tag{2.15}$$

Equation 2.15 is strikingly similar in form to the common empirical relationships that have been formulated for incompressible packed beds (*eg* see Carmen-Kozeny Equation (Foust *et al.*, 1980), or alternatively Leva's correlation (Perry & Green, 1985)). However, the functional dependence of drag-induced fluid-pressure variations on local bed properties in a compressible bed is now recognised.

Likewise, summing solid- and fluid-phase momentum balances, substituting *eq.* 2.9 and the Blake-Kozeny expression, and rearranging gives an explicit expression for the axial stress in the solid phase:

$$\frac{\partial \tau^{s}_{zz}}{\partial Z} = -\frac{\partial P}{\partial Z} = \frac{B\mu(a_s \varepsilon_s)^2 v_z^{sup}}{\varepsilon_f^3} \qquad (2.16)$$

Chase and Willis (1992) employed the analysis described above to investigate the compressible cake filtration of fibrous cellulose particles in water. Internal porosity and fluid-pressure values within a fibrous cellulose cake were measured during an experimental cake-filtration trial. Internal porosity was monitored by electro-conductive porosity probes (which indicate variations in electrical conductivity generated by porosity changes in the cake). Pressure taps provided internal measurements of fluid pressure, and thus, solid-phase axial stress in the cake (*ie* by integrating *eq.* 2.15). Pressure gradient was calculated from fluid-pressure measurements and employed to estimate drag-force values. Non-linear regression of model equations to a single set of experimental data was employed to determine material specific parameters in the model for fibrous cellulose particles. Predictions of cake-filtration behaviour were made. These were compared to experimental measurements of cake-porosity profiles and pressure drop under varying cake-filtration conditions. Excellent agreement was observed.

The advantage of the multiphase theory of filtration for analysis of compressible media is apparent in the example described above. It provides a fundamental or mechanistic description of the physical processes that occur in multiphase systems. Its generality and theoretical basis implies that is therefore applicable to a wide range of multiphase systems regardless of their size or alternative physical characteristics. This is a universal property

which is associative. It can be conferred upon any multiphase system for which it is used to describe. Chase and Willis (1992) employed this multiphase theory of filtration as a template to develop a physical model of compressive cake filtration, although, the model was adjunct to generalistic constitutive relations empirically validated for the system studied. As a result, its universal property is conferred upon the resultant compressive cake-filtration model. That is, it should be applicable to any cake-filtration system regardless of size and physical characteristics, except where the empirical properties of the constitutive relations so used are not compromised. True *a priori* prediction within these realms should be possible. This concept is illustrated in Chase and Willis's study. Predictions made by the compressible cake-filtration model were successfully validated against experimental data. This predictive ability is the very property we seek. In our case, for the prediction of packed-bed pressure drop across compressible packed beds of chromatographic resin.

2.6 Scope and Application

The multiphase theory of filtration can be employed to analyse fluid flow through compressible packed beds of chromatography resin in a similar manner to Chase and Willis's analysis of compressible cake filtration. However, a key decision must first be made on the scope of application. Is it necessary to describe the entire dynamic process of compression in a packed bed of chromatographic resin? This is an important question and it is addressed in the following discussion.

When fluid flow is initiated through a compressible packed bed it experiences a dynamic transformation. The pressure gradient in the packed bed induced by fluid flow creates the axial stress field within the bed that compresses it. However, compression alters the bed properties that determine the pressure gradient. An increase in pressure gradient within the bed is induced which leads to even greater compression of the packed bed and so on. A continual process of compression and increasing pressure drop occur as the axial stress field in the bed fluctuates as bed properties continue to vary. Ultimately, the axial stress field does stabilise and a steady state is achieved where the forces induced by the pressure gradient within the bed balance the opposing forces generated by the internal modulus of the packed bed (and wall friction). For the purposes of scale-up and design of production-scale systems, it is this steady state that we are concerned with. It represents the point of

greatest compression in, and highest pressure drop that will be experienced by, the bed during fluid flow. These will be the bounds that define the pressure constraint and limit fluid flow during scale-up. Although information on the dynamic variation in compression in pressure drop that lead to this steady state would be interesting, it is not necessary for this purpose. It will therefore be assumed that we are concerned only with developing a model to describe compression and pressure drop at this steady state after compression has taken place.

Unfortunately, before we proceed, this decision creates a practical question. Does this steady state when compression of a packed bed stabilises, itself, remain constant during its life cycle of operation? The answer may be no! Repeated application of fluid flow to a packed bed can induce particle reorganisation. This may be permanent and lead to further and irreversible compression of the packed bed. Bed compression at steady state may gradually increase, and with it, pressure drop. Ultimately, particle reorganisation will cease and particles in the bed will find a permanent and stable arrangement. A final steady state of compression, if it can be so called, where steady-state pressure drop will stabilise. This phenomena is widely acknowledged in particulate systems (Foust *et al.*, 1980), and has been observed in packed beds of chromatographic resin (Sarker & Guiochon, 1995). It must be considered. It represents the final state of compression and the worst-case scenario for system design. Therefore, at a practical level, model scope and application should describe a packed bed of chromatographic resin at this final steady state. While it has no further bearing on model development in this Chapter, this phenomena and its implications for model application will be considered further in Chapters 3 and 4.

2.7 A Model for Compressible Systems at Steady State

The multiphase theory of filtration is easily simplified to describe fluid flow through compressible packed beds of chromatography resin under steady-state conditions. The similarities and deviations with necessary modifications are summarised as follows.

The system is analogous to compressible cake filtration, except that fluid flow is at steady state with fixed solid-phase boundaries. Fluid- and solid-phase mass balances of the continuum theory are extraneous and can be ignored. Drag force and solid-state stress can be described by an identical set of constitutive relations. Equations 2.15 and 2.16 can be

employed to determine variation in pressure and stress if material specific properties of the chromatographic resin in the compressible packed bed are known.

However, the ability to relate strain to the solid-phase volume fraction, *eq.* 2.13, underpins Chase and Willis's analysis of compressible behaviour in cake filtration. It makes the assumption that volume changes in the cake only occur due to attrition of fluid from interparticle voids. Particle- or solid-phase volume in the cake remains constant. The boundary that delineates the fluid- and solid-phase fraction is not compromised. This may be true for fibrous cellulose particles, but unlikely in compressible chromatography resin particles. Their highly porous structure means that deformation ultimately alters their internal fluid-phase void fraction within the particles. A net transfer of fluid from these internal voids of the solid phase to the fluid phase in the packed bed is generated during compression. Solid-phase volume is not conserved. Another method to describe the porosity variation that occurs during compression of a packed bed of chromatography resin must be provided.

Furthermore, Chase and Willis assume axial stress acting in the bed is always equivalent to the change in fluid pressure. As we already know this does not entirely reflect reality. Even for compressible cake filtration, the increase in axial stress is likely to be balanced (in part) by support due to wall friction with the structure that contains it. This corrupts the integrity of the solid-phase momentum balance. To the authors knowledge, this limitation of the multiphase theory of filtration has never been acknowledged. One can only assume that the type and size of filtration support structures mean wall friction effects are irrelevant for the types of problems that have been studied. However, we know these wall friction effects are significant in chromatographic systems. Wall support has a significant influence on the compressive stresses acting in a bed.

In summary, the multiphase theory of filtration gives a theoretical basis for studying fluid flow and compression in packed beds of chromatography resin. Two momentum balances describe the solid and fluid phases. They can be used to estimate the fluid-pressure profile (*ie eq.* 2.15) and axial stress distribution (*ie eq.* 2.16) in the bed under steady state conditions during fluid flow. True *a priori* predictions of pressure-drop behaviour can be made, if two key limitations can be overcome. First, successfully describing the functional dependence of bed properties on axial stress where solid particle-phase volume is not

conserved. Secondly, the influence of wall friction effects on the solid-phase momentum balance.

2.8 Accounting for Wall Friction

While wall friction effects are not important in filtration, they are critical to the solution of another engineering problem. The design of hoppers and grain silos rely on the accurate prediction of internal stresses acting in the packed beds of pulverulent materials they contain (Nedderman, 1982). These internal stresses are generated by the weight of the pulverulent material. They determine the whether flow of pulverulent material in a packed bed can occur, and the structural strength required by the hopper or silo to contain it. Wall friction between the pulverulent material and silo or hopper walls plays an important role in both of these situations. Three major techniques have been developed to estimate the influence of wall stresses in silos and hoppers (Hancock & Nedderman, 1974): Coulomb's method of wedges; the method of differential slices; and the method of characteristics.

The following is intended as summary of each technique. An exhaustive description of the many terms and concepts that will be introduced are given in general texts for stress analysis and prediction, and specific texts for analysis and design of grain silos and hoppers. To elucidate upon them in greater detail as they arise would require an impractical body of text. This would disrupt the intended purpose of the discussion: to find a practical method of predicting wall effects for packed beds in chromatography columns. The discussion is therefore restricted to gaining a meaningful understanding of each technique so their relevant attributes can be assessed towards meeting this purpose. Unfamiliar terms and concepts will be met, accepted or explained on their merits to minimise any diversion.

2.8.1 Coulomb's Method of Wedges

The first important work on wall friction effects was the prediction of forces on retaining walls for pulverulent materials by Coulomb in 1776 (Nedderman, 1982). While the concept of stress was not fully understood at the time, the technique has since been widely adapted for prediction of stresses in packed beds of pulverulent materials in bunkers. This technique is known as Coulomb's method of wedges. Unfortunately, it cannot be applied to bunkers of circular cross-section (Nedderman, 1982) and is unsuitable for prediction of wall effects

of packed beds within cylindrical chromatography columns. It will not be considered any further.

2.8.2 The Method of Characteristics

The method of characteristics determines an exact solution for the stress field in the presence of wall effects for a packed bed of pulverulent material in a silo or hopper (Horne & Nedderman, 1975). A brief synopsis of the analysis is as follows. Consider an infinitesimal two-dimensional element of pulverulent material in a packed bed contained within a hopper or silo as illustrated in Figure 2.4. Note that, the two-dimensional element has been drawn in cartesian coordinates, and it is assumed that the physical shape of the hopper is of rectangular cross section rather than circular.

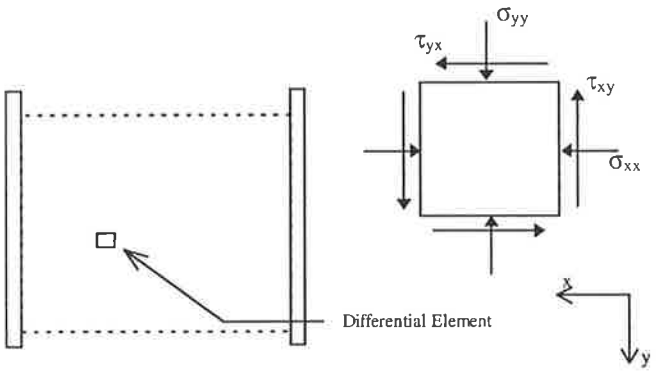

Figure 2.4: A two-dimensional differential element in a hopper.

The element exists in a state of stress. This is a result of the weight of the pulverulent material it contains, and its interaction with the pulverulent material that surrounds it. Normal stresses, σ_{xx} and σ_{yy}, respectively, and shear stresses, τ_{xy} and τ_{yx}, respectively, act on the opposite faces of the element in perpendicular planes x and y. The shear stresses, τ_{xy} and τ_{yx}, are equal and opposite:

$$\tau_{xy} = -\tau_{yx} \tag{2.17}$$

The stress state of the element is described by the equations of equilibrium (these are effectively momentum balances carried out on the differential element). Resolving horizontally and vertically in x and y planes these are, respectively,

$$\frac{\partial \sigma_{xx}}{\partial x} + \frac{\partial \tau_{xy}}{\partial y} = 0 \tag{2.18}$$

$$\frac{\partial \sigma_{yy}}{\partial y} + \frac{\partial \tau_{xy}}{\partial x} = \gamma \tag{2.19}$$

where γ is the weight density ρg of the pulverulent material.

Assuming the density of the pulverulent material is known, there are three unknowns in *eq.s* 2.18 and 2.19: σ_{xx}, τ_{xy}, and σ_{yy}. One degree of freedom exists which must be eliminated to determine the stress field in the hopper. Additional relationships are required. A number of assumptions are made regarding the behaviour of a pulverulent material in the silo or hopper. First, all material in a hopper or silo is an ideal Coulomb material, and therefore, must have a yield locus of

$$|\tau| = \kappa + \phi\sigma \tag{2.20}$$

where τ and σ are the shear and normal stress, respectively, that may be acting at any point on any arbitrary hypothetical plane within in the packed bed; ϕ is the coefficient of internal friction (for the pulverulent material); and κ is the cohesion (of the pulverulent material). The only exception to this rule is at the wall where the yield locus is assumed to have a modified form:

$$|\tau_w| = \kappa_w + \phi_w \sigma_w \tag{2.21}$$

where τ_w and σ_w are the (frictional) shear and normal stress, respectively, acting on pulverulent material at the hopper wall; ϕ_w is the coefficient of wall friction; and κ_w is the cohesion of the pulverulent material at the wall. Frequently, the analysis is concerned with cohesionless materials for which κ and κ_w are zero (Nedderman, 1982). These two terms will be omitted from further consideration.

Both the coefficient of internal friction and wall friction are typically specified as the internal angle of friction, φ, and the angle of wall friction, φ_w, respectively, of the pulverulent material. These quantities are related as follows:

$$\phi = \tan\varphi \tag{2.22}$$

$$\phi_w = \tan\varphi_w \tag{2.23}$$

Secondly, the pulverulent material in the packed bed is at incipient yield. At any point in the bed, the stress state is defined by the Mohr circle which intersects the yield locus of the pulverulent material, *eq.* 2.20. This is graphically illustrated in Figure 2.5. (Note: that in Figure 2.5, σ_{maj} and σ_{min} are the major and minor principal stresses, respectively.

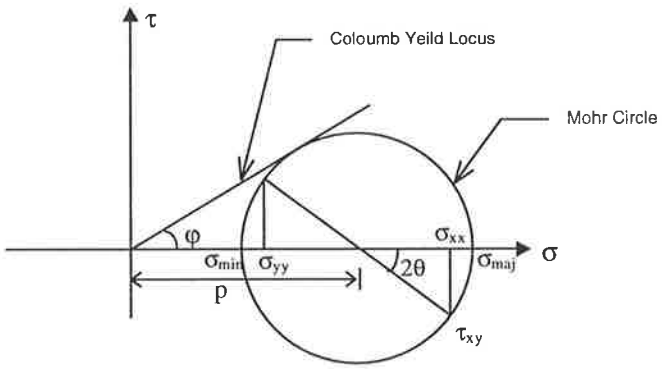

Figure 2.5: The Mohr Circle which defines the stress state of an ideal Coulomb material at incipient yield.

In Figure 2.5, p is the distance from the centre to the origin, and θ is the angle measured anticlockwise at the centre of the Mohr Circle from the x direction in the major principal stress direction. With some elementary mensuration it can be seen that:

$$\sigma_{xx} = p(1 + \sin\varphi\cos 2\theta) \tag{2.24}$$

$$\sigma_{yy} = p(1 - \sin\varphi\cos 2\theta) \tag{2.25}$$

$$\tau_{yx} = -\tau_{xy} = p\sin\varphi\sin 2\theta \tag{2.26}$$

Equations (2.24) to (2.26) provide the additional relationships required. Substituting into the equations of stress equilibrium gives the following pair of first-order partial differential equations:

$$(1+\sin\varphi\cos 2\theta)\frac{\partial p}{\partial x}-2p\sin\varphi\sin 2\theta\frac{\partial\theta}{\partial x} + \sin\varphi\sin 2\theta\frac{\partial p}{\partial y}y+2p\sin\varphi\cos 2\theta\frac{\partial\theta}{\partial y}=0 \tag{2.27}$$

$$(1-\sin\varphi\cos 2\theta)\frac{\partial p}{\partial y}+2p\sin\varphi\sin 2\theta\frac{\partial\theta}{\partial y} + \sin\varphi\sin 2\theta\frac{\partial p}{\partial x}y+2p\sin\varphi\cos 2\theta\frac{\partial\theta}{\partial x}=\gamma \tag{2.28}$$

Boundary conditions for the system apply at the hopper wall. These are specified by the yield locus of the pulverulent material at the wall, *eq.* 2.21 (but with $\kappa_w = 0$).

An analytical solution to *eq.s* 2.27 and 2.28 is normally unavailable, and therefore a numerical solution is employed. The partial differential equations form a hyperbolic set and due to this property the method of characteristics has been widely employed. The popularity of this numerical method in providing the solution has lent its name to the technique itself. The result yields an exact description of the stress field in a hopper in terms of p and θ which can be subsequently transformed into σ_{xx}, σ_{yy}, and τ_{xy}.

The partial differential equations describing the stress field above have been derived in cartesian coordinates for a hopper with rectangular cross-section. However, they can easily be formulated for any coordinate system. For example, cylindrical coordinates for a packed bed of a pulverulent material in a cylindrical hopper or silo (or chromatography column).

As stated, the method of characteristics accounts for the influence of wall (friction) effects acting in a packed bed in a hopper or silo, and provides an exact solution to the resulting stress field. An immediate analogy of the technique to the theory of multiphase theory of filtration can be made. Instead of the weight of the pulverulent material, it is the flow of fluid and fluid pressure variations that induce a similar stress field in a packed bed of chromatographic resin. However, wall effects create a variation in the stress state acting in the bed with both axial and lateral (or radial) position. The multiphase theory of filtration would need to recast as a two-dimensional problem.

2.8.3 The Method of Differential Slices

Most circular bunkers typical of modern storage silos and hoppers are designed by variants on the method of differential slices first proposed by Janssen in 1895 (Hancock & Nedderman, 1974). Janssen's original analysis provides an introduction to these techniques.

Consider a differential slice, dZ, of isotropic and homogenous pulverulent material in a packed bed contained within a cylindrical hopper as illustrated in Figure 2.6. The diameter, circumference and area of the hopper are D, c and a, respectively. The slice is subject to an axial stress, $\sigma_{zz,Z}$, acting upon it due to the weight of pulverulent material above it, and applies an axial stress, $\sigma_{zz,Z+dZ}$, to the packed bed beneath it. The slice also exerts a radial stress, σ_{rr}, on the wall of the hopper or silo that confines the packed bed, and which induces a (frictional) shear stress, τ_w, which supports it.

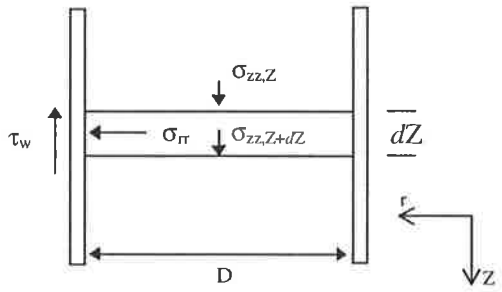

Figure 2.6: A differential slice of pulverulent material in a cylindrical hopper.

The forces acting on the slice in Figure 2.7 are its weight $\gamma a dZ$, where γ is the weight density ρg; the compressive force from above, $\sigma_{zz,Z}a$; the compressive force from below, $(\sigma_{zz,Z+dZ})a$; the wall forces, $\sigma_{rr}cdZ$; and the associated reaction, $\tau_w cdZ$ due to wall friction. All stresses acting in the system are functions of the Z coordinate only. A force balance in the vertical direction gives the net change in the downward force on the slice:

$$\frac{d\sigma_{zz}}{dZ} = \gamma - \frac{4}{D}\tau_w \qquad (2.29)$$

Again, a number of assumptions are made regarding the behaviour of a pulverulent material in an silo or hopper. First, the pulverulent material in the hopper is an ideal Coulomb material, cohesionless and at a state of incipient failure. (Identical assumptions to those

employed by the method of characteristics.) The frictional shear stress at the wall is therefore specified by the yield locus given in *eq.* 2.21 in Section 2.6.2 (but with $\kappa_w = 0$). This relates τ_w to the radial stress, σ_{rr}, acting at the wall. Substituting into the force balance gives

$$\frac{d\sigma_{zz}}{dZ} = \gamma - \frac{4}{D}\sigma_{rr}\tan\varphi_w \tag{2.30}$$

Note that, the coefficient of wall friction has now nominally been expressed in terms of the angle of wall friction, φ_w.

Secondly, σ_{zz} and σ_{rr} are equivalent to the principal stresses acting in the system. Referring to Figure 2.5 (in Section 2.6.2), and again considering some elementary mensuration, σ_{zz} and σ_{rr} are therefore related by the ratio

$$\frac{\sigma_{rr}}{\sigma_{zz}} = \frac{1-\sin\varphi}{1+\sin\varphi} \tag{2.31}$$

Substituting into *eq.* 2.30 gives

$$\frac{d\sigma_{zz}}{dZ} = \gamma - \frac{4}{D}\tan\varphi_w \frac{1-\sin\varphi}{1+\sin\varphi}\sigma_{zz} \tag{2.32}$$

Equation 2.32 is a simple first-order ordinary differential equation. It can be solved bed if material parameters γ, φ_w, and φ are known to give the axial stress field in the hopper. The axial stress field gives the radial stress field acting at the wall (refer *eq.* 2.31), and thus, the frictional (shear) stress field supporting the packed bed at the wall.

Variants of Janssen's original method of differential slices largely revolve around the modifications to the second assumption that the axial and radial stresses represent the principal stresses (see *eq.* 2.31) which many regard as unsatisfactory. Other studies have provided alternative analyses. Only one, presented by Walker and others (Walters, 1973;

Hancock & Nedderman, 1974), has been widely adopted as a practical alternative. It gives the ratio of σ_{zz} and σ_{rr} by

$$\frac{\sigma_{rr}}{\sigma_{zz}} = \frac{1 - \sin\varphi\cos(\omega - \varphi_w)}{1 + \sin\varphi\cos(\omega - \varphi_w)} \tag{2.33}$$

where

$$\sin\omega = \left(\sin\varphi_w / \sin\varphi\right) \tag{2.34}$$

In a similar manner to Janssen's original analysis, this ratio is substituted into *eq.* 2.30. The resultant ordinary differential equation is solved to predict the stress fields in the hopper or silo.

The method of differential slices based on Janssen's original analysis or Walker's modification is popular technique that today enjoys widespread use. However, with the availability an exact solution using the method of characteristics, one might question its usefulness. It ignores radial variation in axial and radial stress that occurs in a hopper. As a result, the solution it provides is only an estimate of the stress field.

There appear to be several reasons for its continuing utility. Besides simplicity and intuitive appeal, the most important is its accuracy. Many studies have compared its predicted stress field, both for Janssen's original analysis and Walker's modification, with that provided by the method of characteristics (Hancock & Nedderman, 1974). Results have indicated, that in most cases, the predicted stress field is nearly always in close agreement with the exact solution. Most deviations were less than 1 to 3 %, although occasionally up to 5%. This is a relatively acceptable disparity. Internal comparisons between Janssen's original analysis have also been performed (Hancock & Nedderman, 1974). Both provided similar results, except Janssen's analysis was more accurate at lower depths (< 10 m) of a packed bed, whereas Walker's modification seemed better at larger depths (> 10 m).

In a similar manner to the method of characteristics, an immediate analogy between the method of differential slices and the theory of multiphase theory of filtration can be made.

However, the stress field is now independent of radial position. The multiphase theory of filtration does not need to recast as a two dimensional problem. In fact, the influence of wall effects characterised by the frictional shear stress, τ_w, from the force balance in *eq.* 2.29 can be directly substituted into the solid-phase momentum balance, *eq.* 2.16. Using Janssen's original analysis (as packed beds of chromatographic resin are usually less than 10 m, and with no better reason in mind), a modified form of *eq.* 2.16 can be derived:

$$\frac{d\tau^{s}_{zz}}{dZ} = -\frac{B\mu(a_s\varepsilon_s)^2 v_z^{sup}}{\varepsilon_f^3} - \frac{4}{D}\tan\varphi_w \frac{1-\sin\varphi}{1+\sin\varphi}\tau^{s}_{zz} \qquad (2.35)$$

Note that, the axial stress field, σ_{zz}, in Janssen's original analysis has been replaced by the symbol, τ^{s}_{zz}, nominally employed to specify the axial stress field in the multi-phase theory of filtration. This equation provides an explicit expression for the axial stress in the solid-phase of compressible media which can account for wall friction effects. Our intended purpose has been achieved. Equation 2.35 along with e*q.* 2.15 will be tentatively used for preliminary attempts carried out to analyse and predict pressure drop in packed beds of compressible chromatography resin.

2.9 Porosity and Particle Deformation

It would be ideal if the same material-property constitutive relations described by Chase and Willis (1992) for compressible cake filtration could be employed to describe the functional dependence of porosity and particle deformation on axial stress for a chromatographic resin. However, this proposition is untenable. As mentioned, solid-phase volume is not conserved during compression of a chromatographic resin. Equation 2.13 cannot be used to describe the relationship between strain and solid-phase volume fraction. An alternative must be employed.

An additional constitutive relationship could be nominated to empirically describe the variation in strain with solid-phase fraction. For example,

$$e^{s}_{zz} = \left(\left[\frac{\varepsilon^{e}_{s}}{\varepsilon_{s}} \right]^{J} - 1 \right) \tag{2.36}$$

where J represents another material specific parameter that must be determined for the system of interest. However, this would add another degree of freedom and unnecessarily complicate the analysis. In this study, a much simpler approach is proposed. The fluid-phase momentum balance, *eq.* 2.15, is modified. The contribution to fluid-pressure variations in the compressible bed due to porosity and specific-surface area are combined with the constant, B, to form an arbitrary empirical expression, $\chi(\tau^{s}_{zz})$. The modified version of the fluid-phase momentum balance is

$$\frac{dP}{dZ} = -\mu v_{z}^{sup} \chi(\tau^{s}_{zz}) \tag{2.37}$$

In a similar manner, the solid-phase momentum balance is modified:

$$\frac{d\tau^{s}_{zz}}{dZ} = \mu v_{z}^{sup} \chi(\tau^{s}_{zz}) - \frac{4}{D} \tan \varphi_{w} \frac{1-\sin\varphi}{1+\sin\varphi} \tau^{s}_{zz} \tag{2.38}$$

$\chi(\tau^{s}_{zz})$ effectively expresses of all flow-induced bed-property variations in a compressible bed as an explicit function of the axial stress. The function may be of any description and will need to be experimentally determined for the chromatographic resin of interest in the desired range of applied axial stress. In a similar manner to determination of material specific parameters by Chase and Willis (1992), this can to be achieved by regression of model equations to experimental data. Accordingly, an initial estimate of $\chi(\tau^{s}_{zz})$ may be useful. Consider the following empirical correlation for pressure-drop prediction across incompressible packed beds developed by Leva $\chi(\tau^{s}_{zz})$.

$$\frac{\Delta P}{\Delta Z} = -\frac{200\mu\varepsilon_{s}^{2} v_{sup}}{d_{pv}^{2}\phi^{2}\varepsilon_{f}^{3}} \tag{2.39}$$

Comparison of *eq.* 2.39 to the fluid-phase momentum balance allows $\chi(\tau^s_{zz})$ to be nominally expressed in terms of the initial bed porosity, (volume-)mean particle diameter and (particle-)shape factor:

$$\chi(\tau^s_{zz}) = \frac{200\varepsilon_s^2}{d_{pv}^2 \phi^2 \varepsilon_f^3} \tag{2.40}$$

2.10 Variation in Bed Height

Consider a compressible packed bed of chromatographic resin. Given $\chi(\tau^s_{zz})$, φ_w, and φ, the model proposed in Section 2.9 is designed to predict its pressure drop by integrating *eq.s* 2.37 and 2.38 over its bed height, Z_c. However, Z_c is the height of the packed bed after compression. This value is unknown (unless determined experimentally). A facility for prediction of the compressed packed bed height must be built into the model to allow it to successfully fulfil its purpose. If solid-phase volume in the packed bed was conserved, Z_c could be easily determined from fluid-phase volume fraction:

$$Z_c = \int_0^{L_i} \left(\frac{\varepsilon_f\left(\tau^s_{zz}\right)}{\left(1-\varepsilon_s^e\right)} \right) dZ \tag{2.41}$$

where L_i is the initial bed height (prior to compression); and $\varepsilon_f(\tau^s_{zz})$ is the local porosity in the compressed packed bed. However, solid-phase volume is not constant. Furthermore, this requires an estimation of local porosity, which has been excluded as an explicit parameter in the proposed model.

For the purposes of this thesis, compressed bed height will be determined by

$$Z_c = \int_0^{L_i} f_c(\tau^s_{zz})\, dZ \tag{2.42}$$

where $f_c(\tau^s_{zz})$ is an empirical parameter describing local variation in bed height during compression. This dispenses with need to characterise variations in solid-phase volume or estimate local porosity.

2.11 Concluding Remarks

The existing art in pressure-drop prediction across compressible packed beds has been examined. There is only one instance of a predictive-type model that has been proposed. It is empirically based and its predictive ability is limited by experimental validation of the desired range of investigation. Other types of predictive models exist. They have their origins in filtration of particulate materials where packed-bed compressibility is a common phenomena. Many are based on the multiphase theory of filtration which provides a mechanistic description of the physical behaviour of fluid flow through packed beds of pulverulent material. These models allow true *a priori* predictions of pressure-drop behaviour once they have been validated for the system of interest, but do not account for wall friction effects. However, wall friction effects in fluid flow through packed bed is analogous to wall friction in packed beds of pulverulent materials in hoppers and silos. Methods for prediction of stress fields in cylindrical hoppers and silos allow wall friction effects to be quantitatively determined. This chapter has fused a common theoretical thread between the multiphase theory of filtration and the method of differential slices which predicts the stress field in hoppers. A new model for pressure-drop prediction in compressible packed beds of chromatographic resin has been proposed. The model is described by three equations, *eq.s* 2.37, 2.38 and 2.42. It accounts for both, the compressibility of a packed bed of chromatographic resin, and the influence of wall friction effects upon it in a cylindrical chromatographic column. It relies on four model parameters: φ_w, φ, $f_c(\tau^s_{zz})$ and $\chi(\tau^s_{zz})$. These describe the relevant physical properties of the chromatographic resin that allow the model to describe its behaviour within a packed bed during compression. The model parameters must be determined before the model predictions can be made.

CHAPTER 3

EXPERIMENTAL

3.1 Preamble

A new model for packed-bed pressure-drop prediction in compressible packed beds of chromatographic resin has been proposed. It has immediate utility for scale-up of the WGFE ion-exchange system. However, a number of model parameters that describe the inherent behaviour of the chromatographic resin in the WGFE ion-exchange system (Sepharose Big-Beads SP) must first be determined. These are its internal angle of friction, φ, angle of wall friction, φ_w, and two empirical parameters, $f_c(\tau^s_{zz})$ and $\chi(\tau^s_{zz})$. φ and φ_w can be determined by experiment. $f_c(\tau^s_{zz})$ describes the local variation in packed-bed height with applied axial stress during compression. It can also be determined by experiment. $\chi(\tau^s_{zz})$ describes the variation in packed-bed properties with applied axial stress during compression. It must be determined by regression of model equations against experimental pressure-drop data for a compressible packed bed. For this purpose, an initial estimate of $\chi(\tau^s_{zz})$, can be determined from initial bed porosity, ε_f, (volume-)mean particle diameter, d_{pv}, and (particle-)shape factor, ϕ, of the chromatographic resin.

This Chapter will briefly outline the apparatus, procedure and results of the experimental investigations used to determine each of these parameters for Sepharose Big-Beads SP, except $\chi(\tau^s_{zz})$. $\chi(\tau^s_{zz})$ will be determined subsequently in Chapter 4.

3.2 Initial Volume-Mean Particle Diameter

3.2.1 Introduction

The particle-size distribution of Sepharose Big-Beads SP resin particles is required for calculation of volume-mean particle diameter. There are a number of techniques available for measuring particle size. Sepharose Big-Beads SP is dispersed in a solvent, and

therefore, the measurement technique must be able to monitor particle size under 'wet conditions'. For the purpose of this investigation, a laser-ensemble light-scattering non-imaging optical system: Malvern System 2600 Particle Sizer (Malvern Instruments Ltd, Malvern, England), was employed. The following is a introductory description of the Malvern System 2600 Particle Sizer with specific reference to size measurement of particulate matter dispersed in a fluid. For further information, the reader should refer to Malvern Instruments Ltd System 2600 Instruction Manual (Malvern Instruments, 1991).

The conventional configuration of the Malvern System 2600 Particle Sizer for size analysis of particulate matter dispersed in a fluid is shown diagrammatically in Figure 3.1.

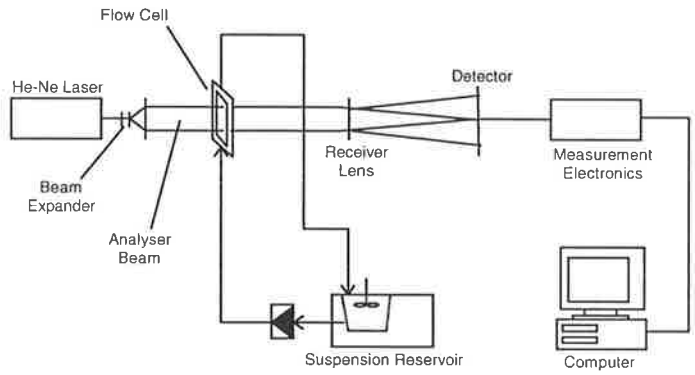

Figure 3.1: Malvern System 2600 Particle Sizer configuration for size measurement of particles dispersed in a fluid.

A low-power Helium-Neon laser and beam expander create a collimated and monochromatic beam of light. This is referred to as the analyser beam. Particulate matter dispersed in a fluid is presented to the analyser beam by a flow cell system. The flow cell system consists a fluid reservoir (volume ~ 1 L), with mixer, where particles are maintained in suspension; a pump to recirculate particle-bearing fluid to a flow cell; and a flow cell with glass windows. The glass windows in the flow cell are transparent to, and in-line with, the analyser beam. Particles in the fluid travelling through the flow cell intercept the analyser beam and scatter light creating a diffraction pattern. This pattern is focussed by a receiver lens onto a detector consisting of multiple concentric sectors as depicted in Figure 3.2. Each concentric sector represents a discrete sizeband. Light intensity incident on a concentric sector of the detector gives the relative volume of particles in that sizeband. It is instantaneously measured and converted to an electronic signal which is recorded by a

personal computer. The signal is interpreted by proprietary software, and the results of the particle size analysis presented as a volume particle-size distribution, $f_V(d_{pi})$, where d_{pi} is the mean particle size in a discrete sizeband. Note: all particles are regarded as spherical during analysis of the diffraction pattern generated by the Malvern System 2600 Particle Sizer pattern.

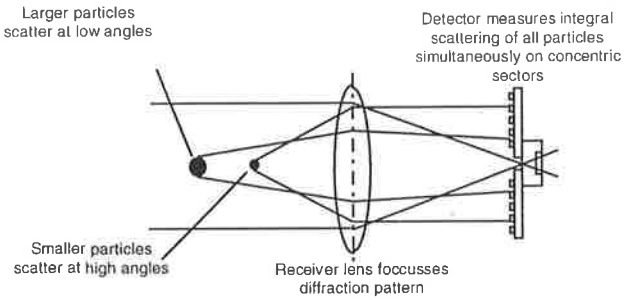

Figure 3.2: Light scattering and detection in the Malvern System 2600 Particle Sizer.

The volume-mean particle diameter, d_{pv}, can be determined from the volume particle-size distribution provided by the Malvern System 2600 Particle Sizer:

$$d_{pv} = \left[\frac{\sum f_V(d_{pi})}{\sum \left(f_V(d_{pi}) / d_{pi}^3 \right)} \right]^{1/3} \tag{3.1}$$

Likewise, other properties that may be useful in describing the particle-size distribution can also be determined. For example, the Sauter-mean particle diameter, d_{ps}:

$$d_{ps} = \frac{\sum f_V(d_{pi})}{\sum \left(f_V(d_{pi}) / d_{pi} \right)} \tag{3.2}$$

3.2.2 Experimental Apparatus and Procedure

Sepharose Big Beads-SP was supplied by Amrad Pharmacia Biotech (Sydney, Australia) as a 1 L pack of resin slurry (~95% by vol. of settled particles) dispersed in 20% (by wt.) ethanol in water. A 250 mL stock solution/slurry (20% by vol. of settled particles) of Sepharose Big-Beads SP dispersed in water - pH 7, was prepared as follows. 50 mL of

Sepharose Big-Beads SP slurry dispensed from the 1 L pack was batch-washed 10 times with softened, double filtered (to 5 μm), carbon pre-filtered, reverse-osmosis water in a standard 1 L glass beaker. Batch washing procedure involved addition of water, mixing, settling and decantation of excess water.

Stock solutions of varying solvents, likely to be encountered by the resin in the WGFE ion-exchange process, were prepared. These were 1 M sodium hydroxide (*ie* sanitisation and regeneration); 1 M sodium chloride - pH neutral (*ie* elution); water - pH 7 (*ie* frontal adsorption and resin wash); and 30 % (by wt.) ethanol in water (*ie* resin storage). An additional solvent dissimilar to aqueous environments encountered in the WGFE ion-exchange system was also prepared: water - pH 2. Standard laboratory-grade chemicals and softened, double filtered (to 5 μm), carbon pre-filtered, reverse-osmosis water were used to make up all solvent preparations. Concentrated hydrochloric acid (34% by wt.) and 5 M sodium hydroxide were employed for pH correction.

For each experiment, a solvent was selected and added to the reservoir of the flow-cell system of the Malvern System 2600 Particle Sizer. Flow-cell system pump was primed and solvent recirculated through the flow cell. A small volume (~10-15 mL) of Sepharose Big-Beads SP stock solution/slurry (shaken not stirred) was added to the reservoir to obtain a suitable particle concentration (typically around 0.5%) for analysis. Particle size was measured. Six separate particle-size analyses were performed in each solvent. Volume-mean particle diameter was determined for each case.

3.2.3 Results and Discussion

The result of a single particle-size analysis for Sepharose Big-Beads SP in water (pH 7), is illustrated in Figure 3.3. The volume particle size distribution is bi-modal. The majority of Sepharose Big Beads-SP resin particles (>98% by volume) are between 100 to 300 microns. However, a minor peak (<2% by volume) in the range 50 to 70 microns is present. Similar observations were apparent in all other instances. This data compares well with particle size ranges quoted by the resin manufacturer (Pharmacia Bioprocess Technology, 1995).

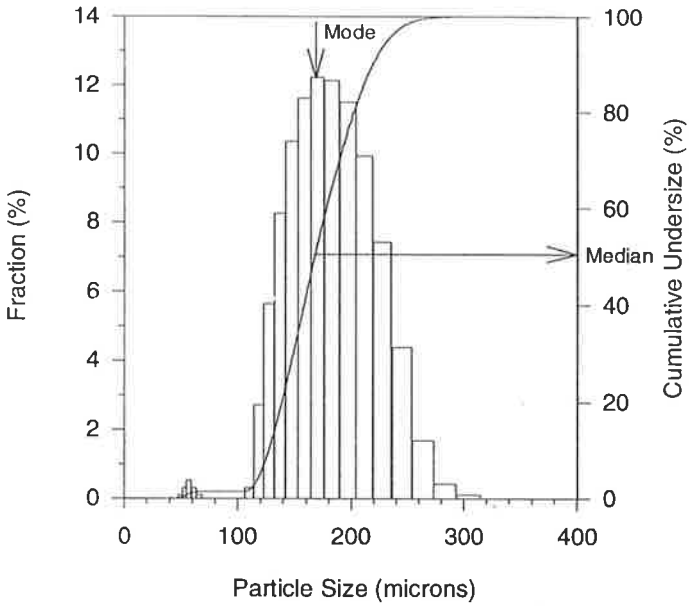

Figure 3.3: Volume particle-size distribution and cumulative undersize (——) for Sepharose Big-Beads SP dispersed in water - pH 7.

Mode and median for the volume-size distribution in Figure 3.3 are 170 and 167.7 μm, respectively. Volume-mean particle diameter is 150.4 μm. James (1994) measured the particle size of Sepharose Big-Beads SP in water and determined its median. Laser diffraction with a Malvern Mastersizer/E analyser was employed. A value of 200 μm was obtained. Unfortunately, details regarding solvent type, sample preparation, and analysis technique were not included in the study. This disparity cannot be explained.

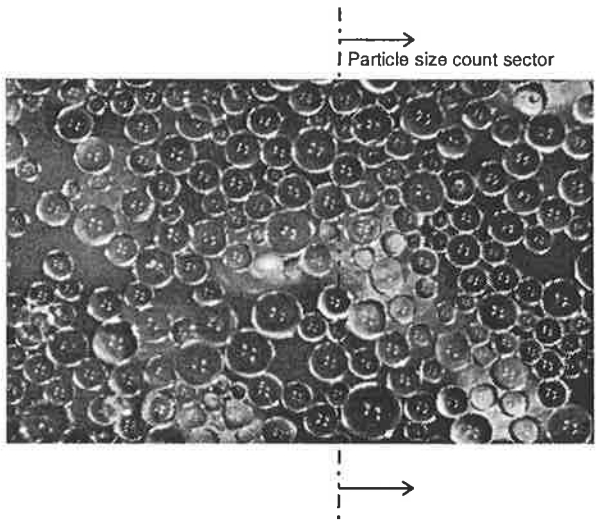

Figure 3.4: Microscopy image of Sepharose Big-Beads SP in water - pH 7, at 20× magnification.

The Malvern System 2600 Particle Sizer analyse in Figure 3.3 was confirmed by microscopy. A photograph of a microscopy image at 20× magnification is displayed in Figure 3.4. All resin particles are spherical in shape. A sector of the microscopy image was selected and a 'rough' particle size count (number *vs.* size) was conducted. Results are summarised in Table 3.1. A volume particle-size distribution determined from the particle size count is also presented. It corresponds closely to the volume particle-size distribution of Sepharose Big-Beads SP displayed in Figure 3.3. Volume-mean particle diameter determined from the particle-size distribution in Table 3.1 is 156 μm.

Table 3.1: Particle size count and volume particle-size distribution for Sepharose Big-Beads SP determined from Figure 3.4.

Size (microns)	Number (no.)	Volume (%)
0 - 33	0	0.0
33 - 66	2	1.7
66 - 132	58	10.8
132 - 198	38	30.6
198 - 264	15	40.9
264 - 330	2	11.7
330+	0	0.0
TOTAL	**115**	**100.0**

Mean and standard deviation for volume-mean particle diameter of Sepharose Big-Beads SP from particle-size analyses in each solvent are summarised in Table 3.2. Particle size can be considered invariant with solvent conditions, except in 30% (by wt.) ethanol where a minor decrease (less than 2%) is observed.

Table 3.2: Mean-volume particle diameter for Sepharose Big-Beads SP.

Solvent	$\mu_{d_{pv}}$ (microns)	$\sigma_{d_{pv}}$ (microns)
Water, pH= 7.0	150.15	0.35
Water, pH= 2.0	151.66	0.08
1 M NaOH	152.09	0.04
1 M NaCl	151.89	0.02
30% (by wt.) ethanol	148.81	1.02

This confirms information provided by the resin manufacturer that Sepharose Big-Beads SP is a 'relatively stable' chromatographic resin (Amrad Pharmacia Biotech, 1994). A cross-linked Sepharose material has a rigid structure, and unlike dextran gels, will not swell or shrink at high or low ionic strength, or in different solvents.

This has important implications for application of the proposed model to pressure-drop prediction in compressible packed beds of Sepharose Big-Beads SP. Model predictions during scale-up will depend on the validity of model parameters $f_c(\tau^s_{zz}), \chi(\tau^s_{zz})$, φ and φ_w over the desired range of prediction. This may include not only packed-bed height or flowrate, but different solvents. $\chi(\tau^s_{zz})$, itself, depends on the variation of bed properties with compression. These can be considered to be closely related to porosity, particle size and shape factor. If there is no significant variation in particle size, it is likely that other bed properties will remain relatively constant, regardless of solvent conditions. Likewise, $f_c(\tau^s_{zz})$, φ and φ_w may also remain unchanged. Model predictions based on model parameters in one solvent, for example, water, may be confidently employed for other solvents. Of course, the functional dependence of viscosity on solvent conditions would still need to be considered.

3.3 Pressure-Drop Data

3.3.1 Introduction

Before experimental apparatus and procedure are described, several issues that govern experimental design must be considered. First, column selection must ensure that angle of wall friction remains constant, regardless of column size or type.

Second, column selection should also ensure that angle of wall friction corresponds to angle of wall friction in the production-scale chromatographic column(s) that will be employed in the WGFE ion-exchange system. This will allow model predictions to be of direct utility. It is expected that the column(s) in the WGFE production-scale system will be selected from the Pharmacia collection of industrial-scale BioProcess™ Glass (BPG) columns. A Pharmacia BPG 300/500 column is currently employed in the pilot-plant process (refer Chapter 1, Section 1.5.2). BPG columns are available in various (column) diameters and

heights. Design and construction materials are identical, except for size variations in internal conduits and external fittings for fluid transmission (Amrad Pharmacia Biotech, 1996). In each column, the contact surface (with the packed bed) is formed by the internal face of a transparent boro-silicate glass cylinder.

Third, data collection should correspond with model scope and application dictated in Chapter 2. Pressure drop and height should be measured when packed-bed compression stabilises (*ie* at steady-state conditions). From a practical perspective, a period of time will be required during which bed compression is endured. Repeated application of fluid flow may also be necessary if particle reorganisation within the bed takes place.

3.3.2 Experimental Apparatus

The experimental system is illustrated in Figure 3.5. It consists of a tank to contain the test fluid; a pump for test-fluid transmission; a chromatographic column containing a packed bed of Sepharose Big-Beads SP; and pressure indicators located upstream and downstream of the column to monitor fluid pressure.

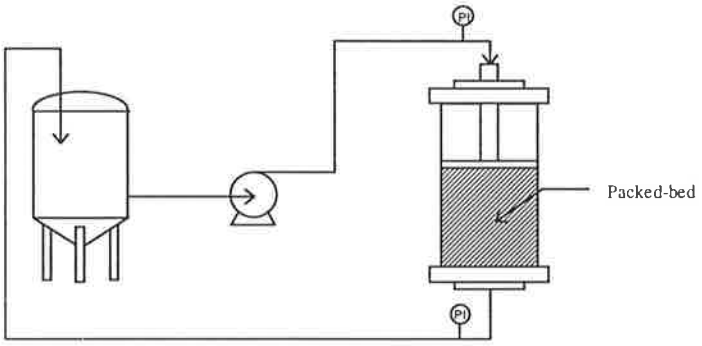

Figure 3.5: Experimental system employed to collect pressure-drop data.

Two variable-speed helical-screw pumps supplied by Mono-Pumps (Australia) Pty Ltd (Adelaide, Australia), model type: LF202 and LF502, with flowrate ranges of 0-2 L/s and 0-5 L/s, respectively, were used in all experiments.

Fluid temperature in the supply tank was maintained at a constant temperature of 20±2 ^{o}C. Manual temperature control was employed using external-forced convection with air

provided by a refrigerative air-conditioner located adjacent to the tank. Fluid temperature was monitored using a standard ethanol-filled thermometer.

Three bourdon-type pressure gauges (Budenberg, Sydney, Australia) with varying ranges were employed to indicate fluid pressure upstream and downstream of the column.

Three chromatographic columns, a Pharmacia XK 16/40, XK 50/60 and BPG 100/500, were used in experiments. Columns were kindly donated by the CRC for Tissue Growth and Repair. Each column is manufactured by Pharmacia (Uppsala, Sweden). Their internal diameters are 1.6, 5.0 and 10.0 cm, respectively. The contact surface (with the packed bed) in each column is formed by the internal face of a transparent boro-silicate glass cylinder. The boro-silicate glass cylinders in Pharmacia XK 16/40 and XK 50/60 possess a similar internal wall-surface finish to Pharmacia BPG columns (*ie* their angle of wall friction should be identical).

Two test fluids: water and 21 % ethanol (by wt.) in water, were used in all experiments. Test fluids were prepared from softened, double filtered (to 5 μm), carbon pre-filtered, reverse-osmosis water and industrial-grade azeotropic alcohol (CSR Distilleries Ltd, Yarraville, Australia). At 20°C, water and 21% (by wt.) ethanol in water have approximate viscosities of 0.99 and 2.15 cP, respectively (Weast, 1974).

3.3.3 Experimental Procedure

Experimental pressure-drop data for packed beds of Sepharose Big-Beads SP in the three columns were collected at different initial bed heights for a range of flowrates with each test fluid. Initial bed heights recorded before testing in the three columns with each test fluid are summarised in Table 3.3.

For each experiment (packed-bed height and flowrate), steady-state column pressure drop and packed-bed height under compression and relaxation were determined. A brief description of procedure employed during each experiments is as follows.

It should be noted the following discussion utilises the term load (as placed upon the packed bed). This should be regarded as synonymous with the act of bed compression as induced by fluid flow at a specified and constant flowrate.

Table 3.3: Initial height of packed beds in each column and test fluid during experiments to collect pressure-drop data.

Column	Test Fluid	Initial bed height (cm)
Pharmacia XK 16/40	Water	8.2, 13.2, 17.0, 22.8, 27.0
	21% (by wt.) ethanol	9.5, 15.7, 20.2
Pharmacia XK 50/60	Water	6.0, 10.3, 13.1, 16.7, 22.5, 28.1
	21% (by wt.) ethanol	8.6, 18.9, 25.6
Pharmacia BPG 100/500	Water	7.4, 10.9, 16.5, 22.0, 27.4
	21% (by wt.) ethanol	9.5, 16.1, 23.2

The test column was packed with Sepharose Big-Beads SP to a specified initial bed height (refer Table 3.3). Resin for testing in all experiments was from Pharmacia 1 L resin-slurry packs of Sepharose Big-Beads SP. Before column packing, resin was batch-washed in a 20 L bucket with water. Batch-washing protocol was identical to particle-size analysis experiments as described in Section 3.2.2.

Testing in each experiment was divided into two phases. First, particle re-organisation in the bed was induced by cyclical loading. Repeated periods of bed compression at a specified and constant flowrate were applied, and pressure drop and bed height under compression and relaxation monitored. A common cycle period and frequency protocol, optimised in preliminary tests, was used in all experiments. It consisted of up to twenty cycles with twenty minutes of compression followed by twenty minutes of relaxation. Complete particle re-organisation was established when pressure drop under compression (at 20 min.) stabilised.

Secondly, a continuous load at the specified flowrate was applied and pressure drop and bed height under compression monitored. When pressure drop stabilised at a constant value, the load on the bed was released and the bed allowed to expand. Bed expansion was complete when bed height stabilised. Continuous load application was repeated until a reproducible value of pressure drop was obtained. In many cases, a common period of

continuous load and relaxation were employed in all experiments. It consisted of 1 hour continuous load and 1 hour relaxation. In others tests, load and relaxation periods were extended until stabilisation of pressure drop was attained.

At the cessation of an experiment, the packed bed in the column was fluidised and allowed to gravity settle for testing at another flowrate.

The final value of column pressure drop in each experiment after continuous loading is the desired steady-state pressure drop across the column. However, it includes the extra-column pressure drop due to column, tubing, fittings and frits (*ie* excluding packed bed). Extra-column pressure drop as a function of flowrate was obtained for each column by measuring column pressure drop for each test fluid in the flowrate range investigated during packed-bed experiments. For each experiment, extra-column pressure drop was subtracted from column pressure drop to give packed-bed pressure drop.

3.3.4 Results and Discussion

An example of variation in bed height and packed-bed pressure drop across a compressible packed-bed of Sepharose Big-Beads SP, test column: Pharmacia XK 50/60, test fluid: water, initial bed height: 13.1 cm, with cyclical (first 20 cycles) and continuous loading (subsequent 5 cycles), during an experiment is presented in Figure 3.6. Trendlines are provided for the purpose of illustration. Particles in the bed attain a stable arrangement after fifteen cycles during which packed-bed pressure drop increases by 36% from 113 kPa to 154 kPa. Application of a continuous load (after 20 cycles) leads gives a steady-state value for packed-bed pressure drop of 162 kPa. Bed height at relaxation and load conditions during cyclical loading decrease from 13.15 to 12.7 cm, and 12.00 to 11.55 cm, respectively. Continuous loading induces an additional decrease in bed height during compression of 0.05 cm. Similar behaviour was observed in all experiments. Clearly, particle re-organisation plays an important role in pressure drop behaviour of compressible packed beds of Sepharose Big-Beads SP.

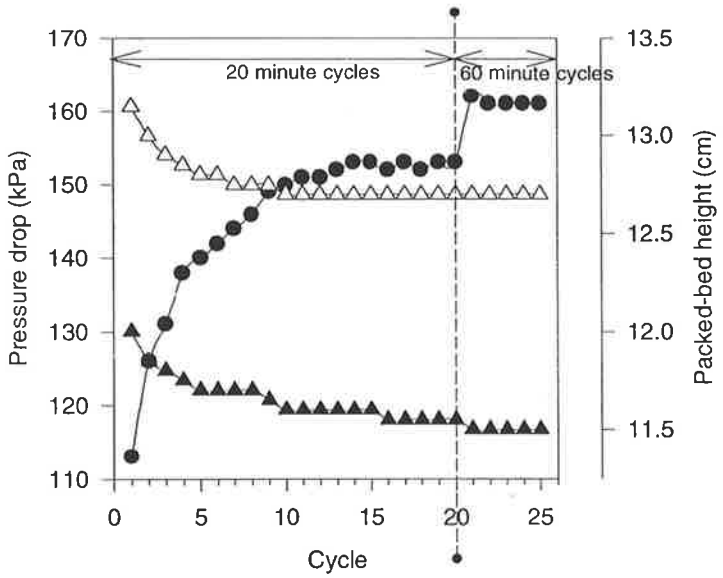

Figure 3.6: Variation in bed height and pressure drop during cyclical and continuous loading: pressure drop - (—●—); bed height at 'load' condition - (—▲—); and bed height at 'relaxation' condition - (—△—).

An example of variation in steady-state pressure drop and bed height (at relaxation and under load conditions) with flowrate for a packed bed of Sepharose Big-Beads SP, initial height: 16.70 cm, test column: Pharmacia XK 50/60, test fluid: water, is shown in Figure 3.7. Again, trendlines are provided for the purpose of illustration.

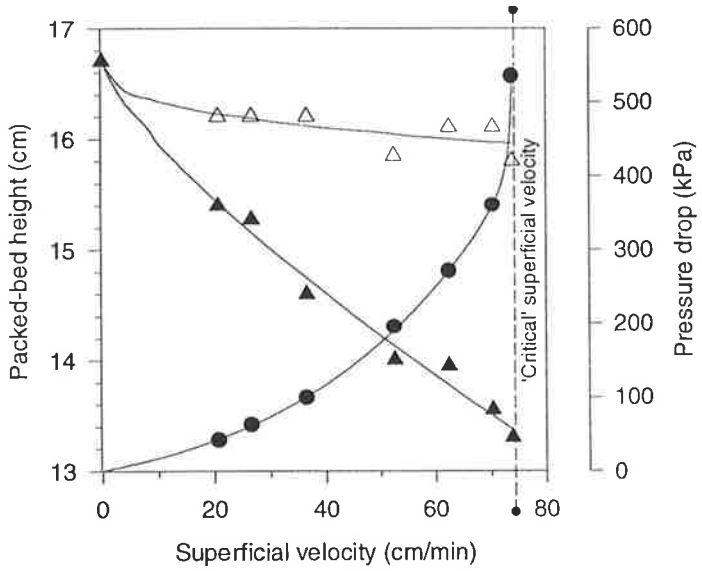

Figure 3.7: Variation in steady-state pressure drop (●) and bed height, at relaxation (△) and compression (▲), with flowrate plus trendlines (——).

Steady-state pressure-drop behaviour in Figure 3.7 is typical of a compressible-type packed bed as described in Chapter 2 (refer Section 2.3). Pressure drop increases in a non-linear parabolic fashion with flowrate. A 'critical' superficial velocity is observed at 74.5 cm/min. Variation in steady-state bed height during compression confirms compression effects are responsible.

Figure 3.8 shows packed-bed pressure-drop behaviour (with trendlines) for Pharmacia XK 16/40, XK 50/60 and BPG 100/500 test columns at similar initial bed heights. Water was the test fluid and the initial bed height in each column was 22.80, 22.50 and 22.00 cm, respectively. The functional dependence of packed-bed pressure drop on column diameter can be observed. 'Critical' velocity is a clear indicator of variation in pressure-drop behaviour with column diameter. It decreases from approximately 90 to 56, and then, to 48 cm/min, as test-column diameter increases from 1.6 cm to 5.0 cm, and then, to 10 cm, respectively.

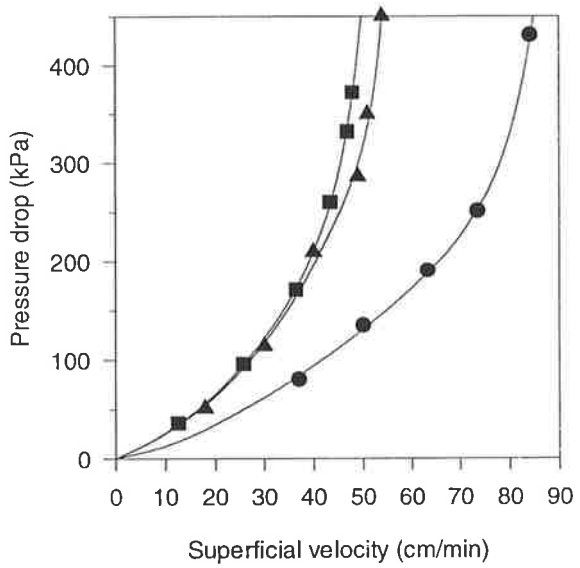

Figure 3.8: Packed-bed pressure-drop behaviour as a function of test-column diameter: Pharmacia XK 16/40 - (●) ; Pharmacia XK 50/60 - (▲); Pharmacia BPG 100/500 - (■); and trendlines - (——).

Figure 3.9 shows packed-bed pressure-drop behaviour (with trendlines) at various initial bed heights with 21% (by wt.) ethanol as the test fluid. The test column was the Pharmacia XK 50/60, and initial bed heights were 8.6, 18.9 and 25.6 cm.

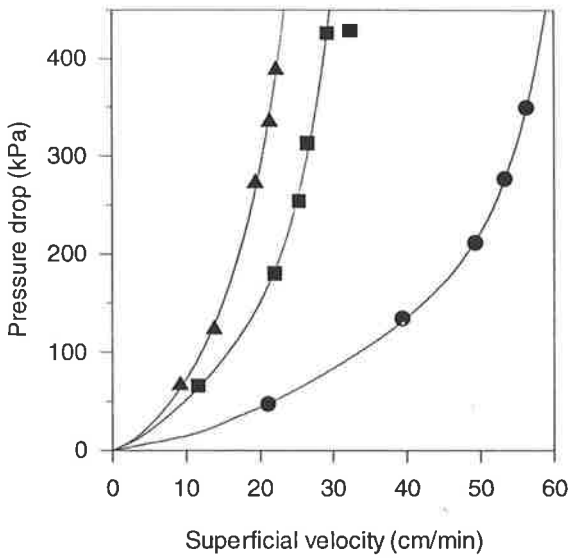

Figure 3.9: Packed-bed pressure-drop behaviour for the Pharmacia XK 50/60 as a function of initial packed-bed height with 21% (by wt.) ethanol: L_i=8.6 cm - (●); L_i=18.9 cm - (■); L_i=25.6 cm - (▲); and trendlines - (——).

3.4 Internal Angle of Friction

3.4.1 Introduction

Chapter 2 introduced the internal angle of friction as a property of particulate matter, such as grain or barley in silos or hoppers, for example, which describes its resistance to failure by shear. However, it is a universal parameter and can be employed for this purpose in any particulate system. The particulate material in hoppers and silos are dry, and in this respect, can be considered dissimilar to packed bed of chromatographic resin dispersed in a solvent. The phenomena of shear failure in chromatographic systems has greater similarities to problems encountered in soil mechanics where particulate material is often subject to 'wet conditions'. Shear tests in soils have been specifically designed to elicit the internal angle of friction for soil samples dispersed in a solvent. These tests may be divided into three categories: the direct shear test, the tri-axial compression test and the torsion test. The facility for each test was available to the author. For the purposes of this investigation, the tri-axial compression shear test was employed. The author is not an authority in this field, and discrimination in favour of the tri-axial compression test was based on a recommendation by a colleague (Kaggwa, 1993) with specialist expertise. For the readers

further interest, an excellent review, and comparison, of shear tests, in soil mechanics is provided by Craig (1981).

The following is a brief description of the tri-axial compression shear test. It is a standard procedure for measurement of the internal angle of friction for soils and other pulverulent materials. Additional information and detailed descriptions of the test procedure and apparatus can be found in Craig (1981) or Akroyd (1957). Furthermore, while apparatus and procedure for the tri-axial compression shear test has largely been standardised for measurement of internal angle of friction in pulverulent materials, it should be noted that this description specifically refers to apparatus and procedure employed by the author.

An elementary diagram of experimental apparatus typically employed in a tri-axial compression shear test is illustrated in Figure 3.10. Actual tri-axial testing apparatus (Wykeham Farrance Eng. Ltd, Slough, England) used in this thesis is shown in the photograph presented in Figure 3.11. It was kindly made available by the Department of Civil & Environmental Engineering, University of Adelaide.

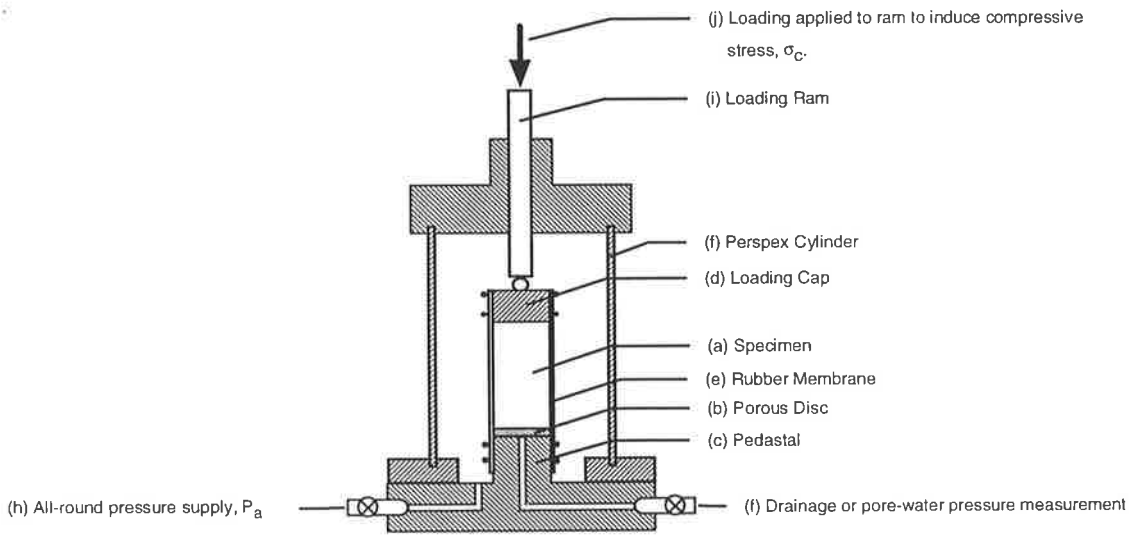

Figure 3.10: The tri-axial test apparatus.

Test procedure with reference to Figure 3.10 is as follows. A cylindrical specimen (a) of particulate material dispersed in the desired solvent is encapsulated in a rubber membrane (e) between two sintered discs (b) and placed on central pedestal (c) within a perspex cell (g). A loading cap (d) is placed on top of the specimen. O-rings placed around the pedestal

and loading cap ensure that the cylindrical specimen is sealed within the membrane. A small negative pressure is induced through the porous disc and drainage conduit (f) in the pedestal to drain excess solvent and stabilise the specimen.

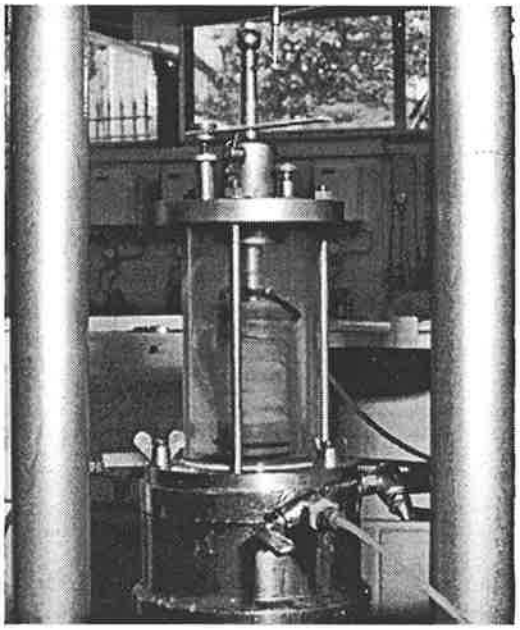

Figure 3.11: The tri-axial compression shear test apparatus with specimen of Sepharose Big-Beads SP in its pre-test state.

A loading ram is placed nominally placed on the loading cap (i). Specimen height and diameter are measured to provide the initial specimen volume and cross-sectional area. The specimen is ready for testing.

The perspex cell is sealed, filled with water (via external conduit (h)) and pressurised to create a constant pressure, P_a. This pressure acts on the external surface of the specimen. Consolidation takes place as P_a forces fluid out of the sample (through the porous disc and pedestal conduit (f)). Variation in the specimen volume is equal to fluid displaced.

A compressive axial stress, σ_c, is progressively applied to the specimen via the loading ram (j) under constant strain. Increase in σ_c and loading ram deflection, δ_a, are monitored by stress and strain dial, respectively (not shown in Figure 3.10), attached to the loading ram. Change in specimen volume is monitored to determine variation in its cross-sectional area.

Specimen compression generates a state of stress. This is defined by a radial and axial stress, σ_{rr} and σ_{zz}, respectively, acting on the sample. The radial stress is equivalent to P_a. The axial stress is equivalent to the sum of P_a and σ_c. Ultimately, the specimen reaches the point of incipient yield for the particulate material, and shear failure occurs. A graphical depiction of a specimen at failure is shown in Figure 3.12. Failure occurs in an arbitrary plane when σ_f and τ_f exceed the yield locus of the pulverulent material.

Failure of a specimen during a tri-axial compression test is detected by monitoring the behaviour of σ_c with axial strain in the sample as measured by δ_a. Under constant strain conditions, σ_c increases with δ_a as the specimen is compressed. When failure occurs, σ_c will ideally stabilise at a constant value as the specimen shears in the failure plane. Failure can also be identified visually in the specimen as physical distortion in the failure plane takes place.

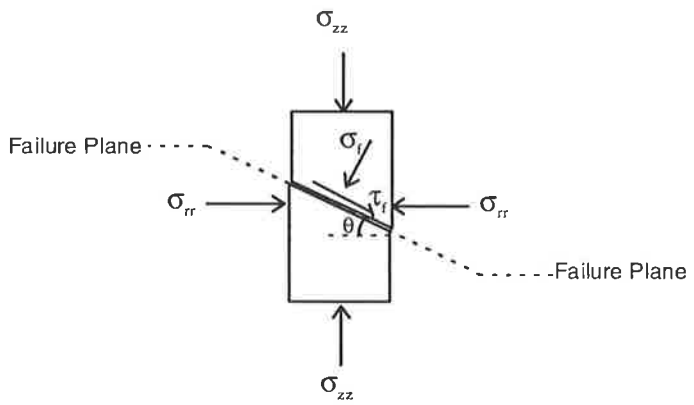

Figure 3.12: Graphical depiction of a specimen at failure during a tri-axial compression test.

The stress state at failure of a specimen in a tri-axial test represents its point of incipient yield. In fact, the axial and radial stress, σ_{zz} and σ_{rr}, acting on the specimen in the tri-axial compression shear test are its major and minor principal stresses, respectively, when failure occurs. Therefore

$$\sigma_{rr} = P_a = \sigma_{min}$$

and

$$\sigma_{zz} = \sigma_{rr} + \sigma_c = \sigma_{maj}$$

σ_{maj} and σ_{min} define the Mohr circle of the pulverulent material at incipient yield. As discussed in Chapter 2, the yield locus of the pulverulent material intersects this Mohr circle as a tangent. (Refer Figure 2.5, Chapter 2, which graphically depicts the failure of a pulverulent (ideal Coulomb) material at incipient yield.) Therefore, a number of tri-axial compression shear tests carried out at various σ_{rr} (*ie* P_a), and measuring σ_c at failure (*ie* to determine σ_{zz}), will define a sequence of Mohr Circles at incipient yield. The yield locus (refer *eq.* 2.20, Chapter 2) is the tangent to these Mohr circles. The internal angle of friction can be determined.

A direct relationship between effective minor and major principal stresses at failure and internal angle of friction can be determined by algebraic manipulation of *eq.* 2.31 in Chapter 2:

$$\left(\sigma_{maj} - \sigma_{min}\right) = \sin\varphi\left(\sigma_{maj} + \sigma_{min}\right) \tag{3.3}$$

Equation 3.3 is known as the Mohr-Coulomb failure criterion. (Note: the pulverulent material is assumed to be cohesionless *ie* κ=0). Instead of drawing Mohr circles and graphically plotting the yield locus, linear regression of *eq.* 3.3 against shear-test experimental data can be employed to determine internal angle of friction.

3.4.2 Experimental Apparatus and Procedure

In a similar manner to the procedure described in Section 3.2.2, a 700 mL stock solution/slurry of Sepharose Big-Beads SP was prepared from a Pharmacia 1 L standard pack of Sepharose Big-Beads SP. However, resin in the stock solution was dispersed in distilled water, rather than water - pH 7. Furthermore, the particle concentration in slurry was approximately 80% (by vol. settled particles).

Distilled water, instead of water - pH 7, was used due to access restrictions to tri-axial shear compression testing equipment. Shear-testing equipment in the Department of Civil &

Environmental Engineering, The University of Adelaide, is commonly used for soil analysis. Distilled water is employed to replicate 'wet conditions'. Other solvents cannot be used in order to prevent equipment contamination and maintenance problems. This was a key constraint on tri-axial compression shear tests conducted in this thesis. Internal angle of friction could only be measured for resin dispersed in water. No other solvents could be tested.

Specimens were prepared from the stock solution/slurry of Sepharose Big-Beads SP. Tri-axial shear compression tests were performed. (After each tri-axial compression shear test, specimens were recovered, re-suspended in distilled water, and employed for subsequent tests.) Varying all-round pressures (P_a) up to 500 kPa were examined. Applied axial compression stress (σ_c) at failure was measured.

3.4.3 Results and Discussion

A photograph of a specimen of Sepharose Big-Beads SP in its pre-test state prior to a tri-axial compression test is illustrated in Figure 3.11. A photograph of the same specimen at failure is shown Figure 3.13. Distortion of the specimen, and the distinct shear plane, that develops at failure can be clearly observed.

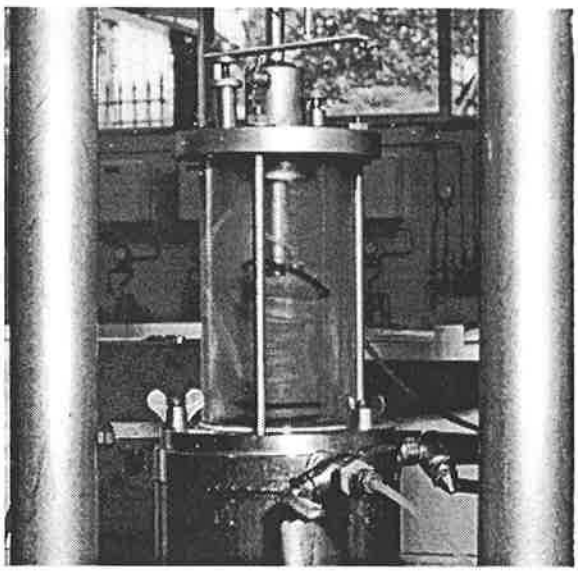

Figure 3.13. Specimen of Sepharose Big-Beads SP (as illustrated in Figure 3.11) at failure.

Figure 3.14 displays the variation in axial compressive stress, σ_c, with axial strain, as measured by loading ram deflection, δ_a, for a Sepharose Big-Beads SP specimen in water at a radial pressure, σ_{rr}, of 428 kPa. A parabolic increase in σ_c is observed with δ_a. Failure is observed when σ_c peaks. This occurs suddenly, afterwhich σ_c begins to decline. This behaviour was apparent in all tri-axial compression tests conducted with Sepharose Big-Beads SP. While σ_c should ideally stabilise at a constant value during shear failure, its sudden decline appeared to be a result of specimen distortion in the failure plane. Specimen distortion would compromise conditions of constant strain during compression after failure. It appears this type of specimen distortion during failure is unique to Sepharose Big-Beads SP, perhaps, an artefact of its compressibility. Chromatographic resins are highly compressible compared to sands and clays - the common subject of shear tests in soil mechanics.

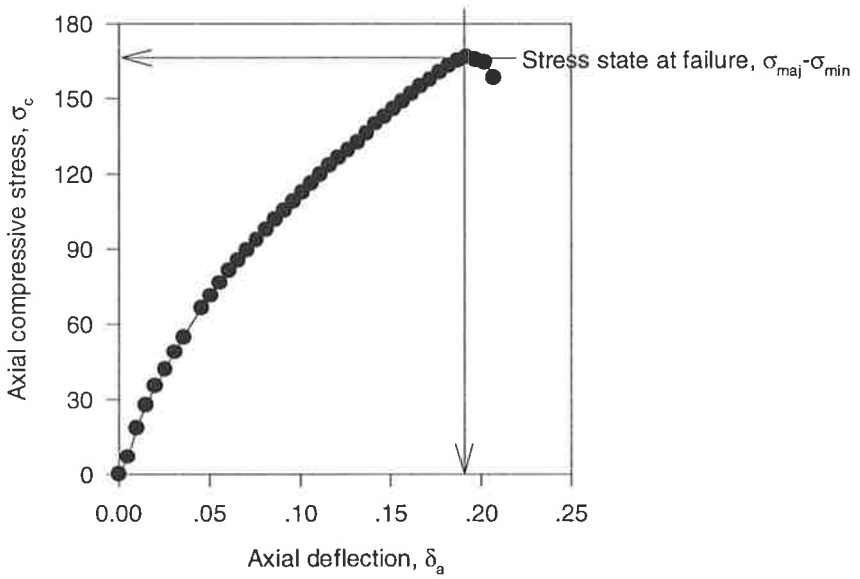

Figure 3.14: Variation of axial compressive stress (—●—) during a tri-axial compression shear test, σ_{rr}=428 kPa.

Figure 3.15 presents several Mohr circles determined from tri-axial compression shear tests.

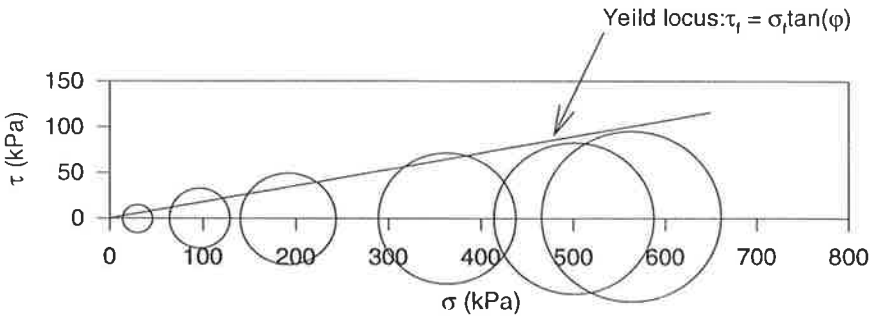

Figure 3.15: Various Mohr circles determined at incipient failure of Sepharose Big-Beads SP *vs.* yield locus (——) for an internal angle of friction of 10.3°.

Experimental data expressed as individual Mohr-Coulomb failure criterion (refer *eq.* 3.3) stress points are shown in Figure 3.16. Least-squares linear regression indicates that the internal angle of friction for Sepharose Big Beads-SP is 10.3°. The yield locus determined from this value is displayed in Figure 3.15.

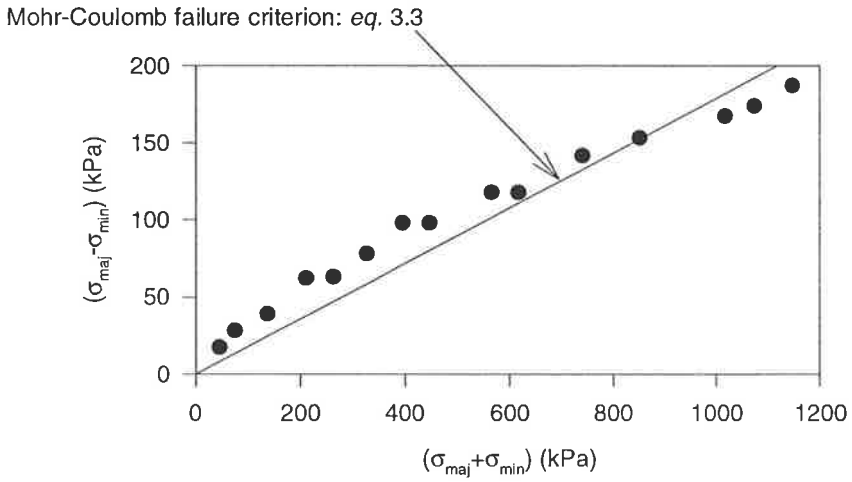

Figure 3.16: Experimental Mohr-Coulomb failure criterion stress points (●) for Sepharose Big-Beads SP *vs.* Mohr-Coulomb failure criterion (——) at an internal angle of friction of 10.3°.

A degree of non-linearity can be observed in experimental Mohr-Coulomb failure criterion stress points displayed in Figure 3.16. This non-linearity is also apparent in Figure 3.15 where the yield locus is compared to Mohr circles plotted from experimental tri-axial compression shear test data. A decrease in angle of failure (plane), θ, and decline in shear strength, τ, can be observed as the effective principal stresses at failure increase. This could be an experimental artefact. More likely, it is an indication that Sepharose Big-Beads SP is

not an 'ideal Coulomb material'. For example, it may contain cohesive properties. Alternatively, its compressibility may compromise pulverulent material homogeneity. Compressibility would result in particle deformation during a shear test. Orientation, particle shape and contact surface area would vary. This would alter shear conditions in a pulverulent material during a tri-axial compression shear test, and its shear strength at failure.

Figure 3.17 compares experimental data against σ_{maj} predicted from *eq.* 2.31. Equation 2.31 will be used to estimate the ratio of principal stresses in the proposed model for pressure-drop prediction developed in Chapter 2. At an internal angle of 10.3°, prediction errors display a strong functional dependence on σ_{min}. Prediction error is 50% at σ_{min} less than 50 kPa, but diminishes rapidly to less than 15% at σ_{min} greater than 150 kPa. Between a σ_{min} of 200 kPa and 500 kPa, prediction error is less than ± 5%.

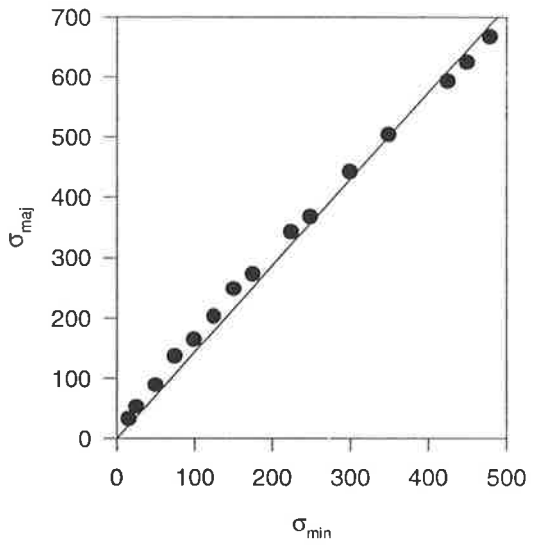

Figure 3.17: Prediction of major principal stress with *eq.* 2.31 at an internal angle of friction of 10.3° (——) *vs.* experimental data (●).

3.5 Angle of Wall Friction

3.5.1 Introduction

Determination of the angle of wall friction can be treated in a similar manner to internal angle of friction. It was also introduced in Chapter 2 as a property of dry particulate

matter, but instead, describes its resistance to failure by shear at an impermeable surface. Likewise, suitable techniques for determination of wall friction for chromatographic resin dispersed in a solvent are required. However, there is no direct test for angle of wall friction in soils. Some creativity was required. A direct-shear test, commonly employed to determine internal angle of friction, was modified.

The following is a brief description of the direct-shear test, with modifications employed in this investigation. The reader will note that apparatus and procedure are identical to measurement of the internal angle of friction in soils and other pulverulent materials, except for the insertion of a shear plate in the metal shear box to provide the desired shear surface. For additional information and detailed descriptions of the direct-shear test procedure and apparatus please refer to Craig (1981) or Akroyd (1957).

A photograph of the actual direct-shear testing apparatus (Rheostatic Co. Ltd, Slough, England) employed in this thesis is shown in Figure 3.18. It was kindly made available by the Department of Civil & Environmental Engineering, University of Adelaide. The key component in the direct-shear test apparatus is a metal shear box contained within a rectangular receptacle.

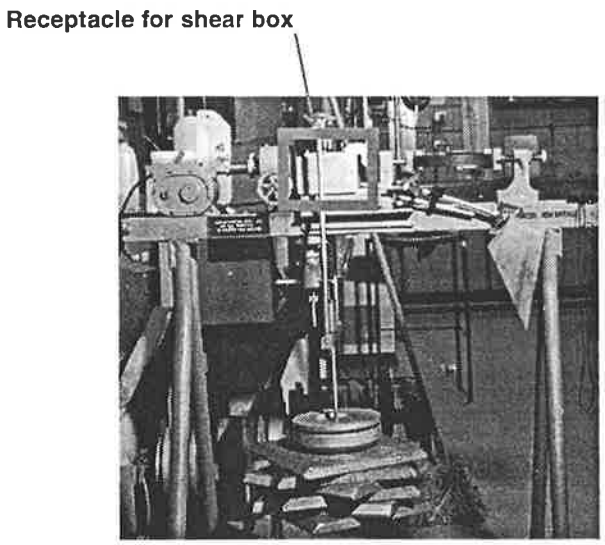

Figure 3.18: Direct-shear test apparatus employed for determination of angle of wall friction.

An elementary diagram of the metal shear box is illustrated in Figure 3.19.

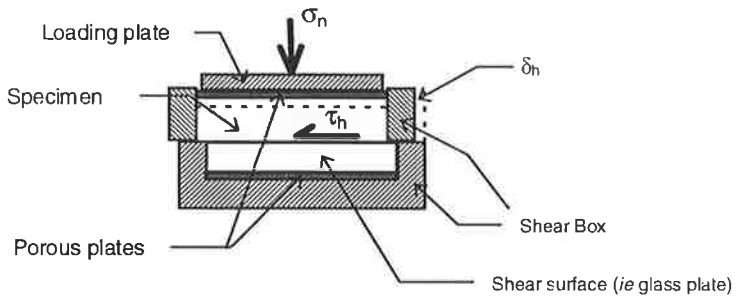

Figure 3.19: The metal shear box of the direct-shear test apparatus.

With reference to Figure 3.19, a specimen of pulverulent material is suspended in the desired fluid and confined to a metal shear box of square cross-section and split horizontally at mid-height. (The box is physically divided into two halves.) A shear plate containing the desired shear surface is placed in the bottom half of the metal box. The shear plate is designed to create a shear surface flush with the box's mid-height horizontal plane. This will become the axis of shear during the test. The specimen to be tested is placed in the upper half of the shear box. Porous plates below the shear plate and above the specimen sample allow free drainage of fluid. The entire metal shear box containing the specimen is immersed in test fluid contained within a rectangular receptacle (refer Figure 3.18).

A loading plate on the specimen in the shear box creates a vertical stress, σ_n. A shear stress, τ_h, is progressively applied by effectively moving the two halves of the box relative to each other (in the horizontal axis) under conditions of constant strain. Increase in τ_h is measured together with the relative shear displacement, δ_h. (The change in thickness of the specimen is also measured.)

As the test progresses, the increase in τ_h, which acts on the specimen in contact with the shear surface, will eventually induce failure, namely, the specimen begins to move across the shear surface. τ_h then stabilises at a constant value as the specimen shears in the failure plane at the shear surface.

If a number of such tests are carried out at varying σ_n, and τ_h measured at failure, a sequence of stress points for shear failure of the pulverulent material can be defined. These represent the yield locus (refer *eq.* 2.21) of the pulverulent material against the shear surface being tested. The angle of wall friction can be determined.

3.5.2 *Experimental Apparatus and Procedure*

Random samples of boro-silicate glass were purchased. Square inserts for the metal shear box were cut. Surface characteristics of individual inserts were inspected, and compared to internal surface finish of boro-silicate glass in test columns employed for collection of experimental pressure-drop data (refer Section 3.3). A compatible rectangular insert was selected and placed in the metal-shear box for testing. A photograph of the metal shear box with square-glass insert is illustrated in Figure 3.20.

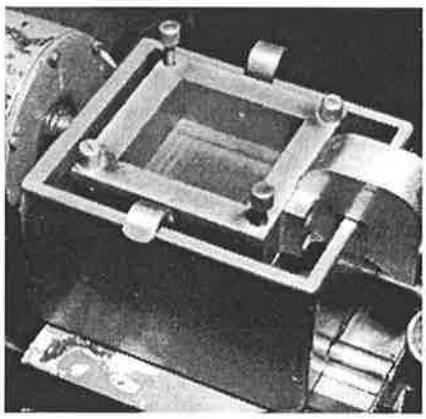

Figure 3.20: Metal shear box in modified direct-shear test with glass insert.

The stock solution/slurry of Sepharose Big-Beads SP employed for tri-axial compression shear tests in Section 3.4 was used for all direct shear tests. Access restrictions for direct-shear testing equipment were identical to tri-axial shear compression tests. Direct shear tests were restricted to Sepharose Big-Beads SP dispersed in distilled water. No other solvents were tested.

Resin specimens in the metal shear box were prepared. A metal shear box containing Sepharose Big-Beads SP ready for testing is illustrated in Figure 3.21. Direct-Shear tests were conducted. (Specimens were recovered after testing, re-suspended in distilled water, and employed for subsequent tests.) Varying normal loads (σ_n) up to 350 kPa were examined. Shear stress (τ_h) at specimen failure was measured.

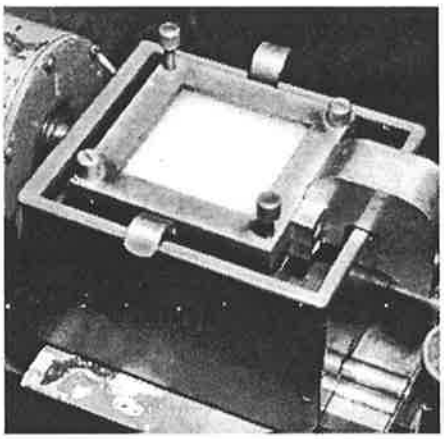

Figure 3.21: Metal shear box in modified direct-shear test with Sepharose Big-Beads SP specimen prepared for testing.

3.5.3 Results and Discussion

Figure 3.22 shows the variation in shear stress, τ_h, with relative shear displacement, δ_h, for a modified direct-shear test with Sepharose Big-Beads SP against boro-silicate glass at a vertical stress, σ_n, of 168 kPa. A parabolic increase in τ_h is observed with δ_h. Shear failure occurs when τ_h stabilises at a constant value. This behaviour was observed in all modified direct-shear tests with Sepharose Big-Beads SP.

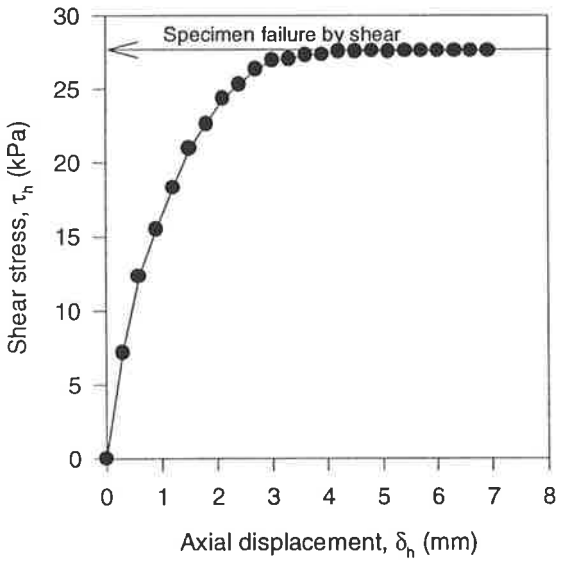

Figure 3.22: Variation of axial compressive stress (—●—) during a modified direct-shear test.

Experimental data expressed as stress points at shear failure are shown in Figure 3.23. Least-squares linear regression with *eq.* 2.21 (note that, the pulverulent material is assumed to be cohesionless with κ_w=0) indicates that the angle of wall friction for Sepharose Big-Beads SP dispersed in water, and in contact with boro-silicate glass, is 8.0°.

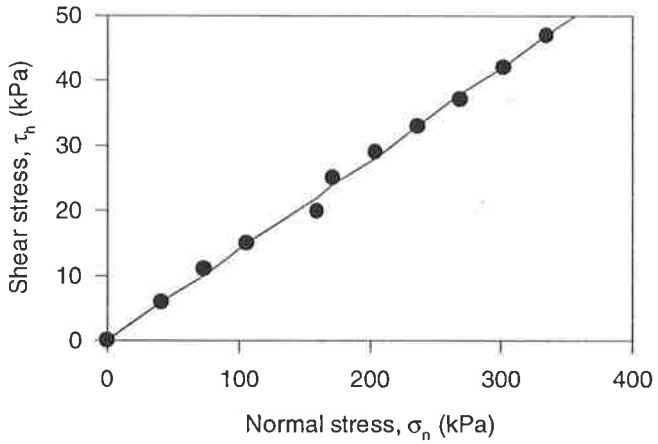

Figure 3.23: Variation in shear stress with applied normal stress (●) *vs.* yield locus (——) at angle of wall friction of 8.0° for modified direct-shear tests with Sepharose Big-Beads SP.

3.6 Initial Shape Factor

Visual observation of Sepharose Big-Beads SP by microscopy in Section 3.2 has shown that all resin particles are spherical, regardless of size. Their shape factor is therefore unity.

3.7 Initial Porosity

3.7.1 Introduction

The void fraction between resin particles in packed bed, ε_f, can be found with relative certainty. Standard protocol in protein chromatography (James, 1994) involves elution of a tracer, which is excluded from the intraparticle voids of a resin particle, from a packed bed to measure its interparticle void volume, V_v. Comparison of void volume to bed volume, V_b, gives interparticle porosity:

$$\varepsilon = \frac{V_v}{V_b} \qquad (3.4)$$

3.7.2 Experimental

Tracer-elution experiments were conducted with an automated FPLC system (Pharmacia, Uppsala, Sweden). A small volume of tracer (200 µL) was applied to a Pharmacia XK 16/40 column containing 10 mL Sepharose Big-Beads SP equilibrated with a 50 mM sodium citrate buffer at pH 6.5. Sodium citrate buffer was prepared from standard laboratory-grade chemicals and Milli-Q water.

The molecular-weight exclusion limit of Sepharose Big Beads SP is 4,000 kDa (Pharmacia Bioprocess Technology, 1995) or approximately 0.3-0.4 µm. To ensure complete exclusion, the tracer was prepared from a 1.1 µm calibrated polystyrene latex microsphere standard (Epics Division of Coulter Corp., Hialeah, Florida) dispersed in 50 mM sodium citrate buffer at pH 6.5 at an arbitrary concentration. Elution was isocratic at 0.5 mL/min with the equilibration buffer described above. Tracer elution was detected by UV absorbance at 280 nm. Multiple (five) experiments were performed. Porosity in each experiment was determined by comparison of elution volume to bed volume (refer *eq.* 3.4).

3.7.3 Results and Discussion

Mean and standard deviation determined for porosity were 0.38 and 0.02 µm, respectively. This compares well with the value of 0.35 determined for Sepharose Fast-Flow S (Skidmore *et al.*, 1990) using very high molecular weight dextran. Sepharose Fast-Flow S is identical to Sepharose Big-Beads SP, except for ion-exchange functional group and particle size. Void fractions in a packed bed of well packed spherical particles are fairly constant regardless of particle size (James, 1994).

3.8 Variation in Local Bed Height, $f_c(\tau^s_{zz})$

3.8.1 Introduction

One key issue will govern experimental design for determination of $f_c(\tau^s_{zz})$. The proposed model is defined by its scope and application. Model predictions are limited to steady-state conditions. Variation in local bed height, $f_c(\tau^s_{zz})$, must correspond with this restriction.

3.8.2 Experimental Apparatus

The experimental system is illustrated in Figure 3.24. It consists of a gas cylinder with regulator containing pressurised air; a pressure indicator; a pneumatic piston; a cylindrical chamber with internal compression plate, and containing a packed bed of chromatographic resin; a strain gauge to measure compression plate deflection; and a bucket filled with solvent;

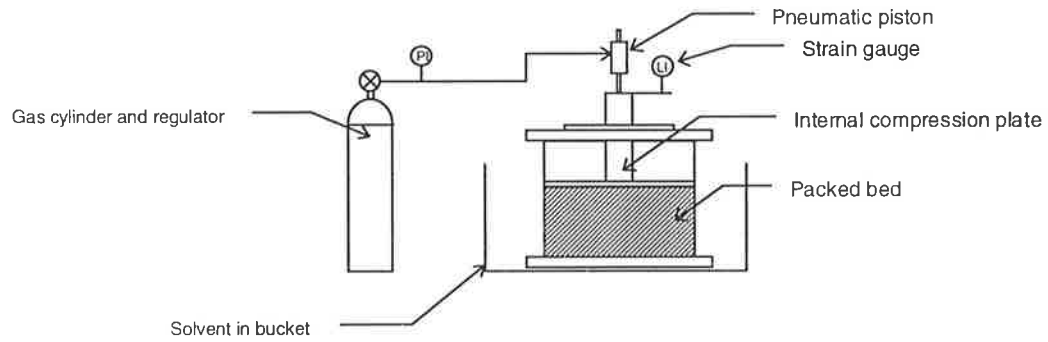

Figure 3.24: Experimental system employed to collect variation in local bed-height data.

The gas cylinder and regulator was supplied by BOC (Adelaide, Australia). The pressure indicator was a bourdon-type pressure gauge (Budenburg, Sydney, Australia).

The cylindrical compression chamber was discovered in a Department of Chemical Engineering, University of Adelaide, workshop. Its origin is unknown. As illustrated in Figure 3.24, it consisted of a cylinder chamber, internal diameter - 10 cm, with an internal compression plate. Construction materials appeared to be brass, and rapidly corroded under

aggressive conditions. For this reason, compression experiments to determine $f_c(\tau^s_{zz})$ were restricted to water. Other solvents were not tested

The face of the internal compression plate (in contact with the packed bed) was perforated. This allowed free drainage of solvent contained in the packed bed during compression. A shaft attached to the compression plate through a circular orifice at the top of the compression chamber allowed transmission of an external force to the packed bed via the pneumatic piston. (Like the compression chamber, the pneumatic piston, itself, was also inadvertently discovered in a Department of Chemical Engineering workshop. Its origin and specifications are unknown.) Compression plate deflection during compression was measured by a strain gauge attached to the shaft adjacent the pneumatic piston.

For the purposes of testing, the cavity in the chamber between the base and piston face plate was packed with Sepharose Big-Beads SP dispersed in solvent. Immersion of the compression chamber within a bucket containing solvent was employed to ensure that resin was maintained under 'wet conditions' at all times during testing.

3.8.3 Experimental Procedure

Sepharose Big-Beads SP, dispersed in distilled water, and employed in tri-axial compression shear tests (refer Section 3.4), were used for all experiments.

For each experiment, resin samples were placed in the compression chamber, and allowed to gravity settle to the container bottom thereby forming packed beds of specified height (approximately 3 cm). This initial packed-bed height was selected to maximise the container diameter-bed height ratio in an attempt to exclude wall-friction effects. Its value was carefully measured and recorded prior to testing.

Compression testing was divided into two phases. First, particle re-organisation in the bed was induced by cyclical loading. Repeated periods of bed compression using the pneumatic piston at a constant pre-determined pressure were applied to the packed bed. Bed height under compression and relaxation were monitored. A common cycle period and frequency protocol, optimised in preliminary tests, was used in all experiments. It consisted of up to twenty cycles with five minutes of compression followed by five minutes of relaxation.

Complete particle re-organisation was established when bed height under compression stabilised.

Second, a continuous load at the specified pressure was applied and bed height under compression monitored. When bed height stabilised at a constant value, the load on the bed in the compression chamber was released and the bed allowed to expand. Bed expansion was complete when bed height stabilised. Continuous load application was repeated until a reproducible value of bed height was obtained. This ensured that steady-state conditions were achieved. In many cases, a common period of continuous load and relaxation (*ie* bed expansion) was used. It consisted of thirty minutes continuous load and thirty minutes relaxation. Occasionally, load and relaxation periods were extended until stabilisation of bed height was attained.

After each experiment, packed beds in the compression chamber were re-dispersed (by mixing) and allowed to gravity settle for further testing.

Compression tests, as described above, were performed under various external loads (up to 450 kPa applied axial stress, τ_{zz}^{s}).

3.8.4 Results and Discussion

$f_c(\tau_{zz}^{s})$ is the fraction of original bed height remaining after compression of a packed bed. However, before the results of the compression tests are presented, a careful distinction must be made whether bed height at compression should be compared to initial bed height prior to compression, or bed height after bed expansion at steady-state conditions. The variation in bed height necessary to determine compressed packed-bed height in a chromatographic column is the fraction of initial bed height remaining after compression. This is $f_c(\tau_{zz}^{s})$ as defined in Chapter 2. However, one could say that the variation in bed height that actually contributes to particle deformation is the fraction of bed height at relaxation. For the purpose of illustration, let us refer to this variation in bed height as $f_d(\tau_{zz}^{s})$.

The results of the compression experiments are summarised in Figure 3.25. Experimental values for $f_c(\tau^s_{zz})$ are displayed as a function of applied axial stress, τ^s_{zz} applied to the packed bed via the compression plate. Also shown is bed height during relaxation (*ie* bed expansion) at steady-state conditions expressed as a fraction of initial bed height (before compression and particle reorganisation). $f_d(\tau^s_{zz})$ is the difference between this fraction of initial bed height (at relaxation) and $f_c(\tau^s_{zz})$.

$f_c(\tau^s_{zz})$ under compression at 400 kPa is nearly 0.7. This is a change in bed height of 30%. Consider an initial (interparticle) porosity of 0.35. If solid-phase volume was constant during compression, this would equate to a change in fluid-phase volume of 85% with a final porosity of 0.05. One can say that this is an unlikely scenario. Changes in solid-phase volume during deformation would inevitably contribute to bed height variations. However, it reflects the level of compression that a packed bed of Sepharose Big-Beads SP may experience in a chromatographic column during fluid flow. In particular, the large change in porosity at the bottom of a packed bed where compressive stresses could peak at these levels.

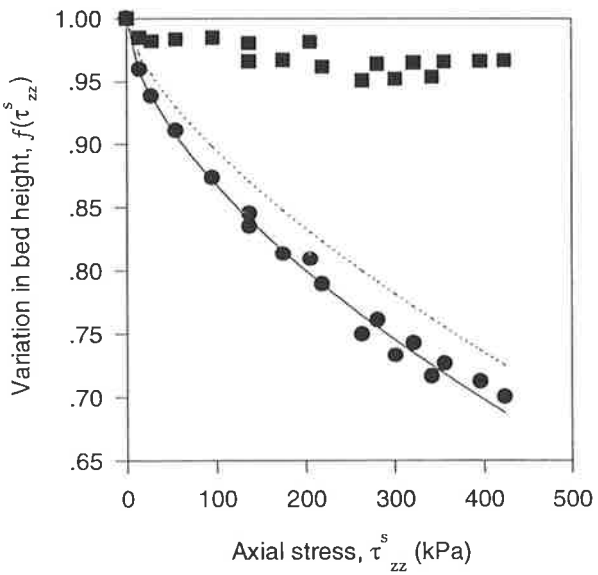

Figure 3.25: Experimental fraction of initial bed height at compression (●) and relaxation (■) for Sepharose Big-Beads SP dispersed in water compared with *eq.s* 3.5 (——) and 3.6 (·····) for $f_c(\tau^s_{zz})$ and $f_d(\tau^s_{zz})$, respectively.

Particle reorganisation contributes to nearly 7% to the 30% of the fractional change in height during compression at 400 kPa. Again, it is clear that particle re-organisation plays an important role in compression of packed beds containing Sepharose Big-Beads SP.

$f_c(\tau^s_{zz})$ was correlated with applied stress using a simple empirical relationship:

$$f_c(\tau^s_{zz}) = 1 - 0.00864\ \tau^{s\ 0.593}_{zz} \tag{3.5}$$

Likewise, $f_d(\tau^s_{zz})$ was also correlated to applied stress:

$$f_d(\tau^s_{zz}) = 1 - 0.00492\ \tau^{s\ 0.665}_{zz} \tag{3.6}$$

Equations 3.5 and 3.6 are compared with experimental data in Figure 3.25.

3.9 Concluding Remarks

Model parameters and experimental data for application of the proposed model to packed bed pressure-drop prediction of Sepharose Big-Beads SP in the WGFE ion-exchange system were experimentally measured. This includes pressure-drop data, internal angle of friction, angle of wall friction (boro-silicate glass), initial volume-mean particle diameter, initial shape factor, initial porosity and the empirical parameter $f_c(\tau^s_{zz})$.

Initial volume-mean particle diameter was determined by a laser-ensemble light-scattering non-imaging optical technique in various solvents. Results indicate that particle size of Sepharose Big-Beads SP is largely invariant with solvent conditions with a volume-mean particle diameter of approximately 148 to 152 μm.

Steady-state pressure-drop data were collected in various columns of different diameter with test fluids of varying viscosity. Each column was constructed of boro-silicate glass to replicate the internal surface characteristics in the Pharmacia BPG range of industrial-scale chromatographic columns. These will be employed in the production-scale WGFE ion-

exchange system. Pressure-drop data will be used to determine $\chi(\tau^s_{zz})$ and validate model predictions.

Internal angle of friction of Sepharose Big-Beads SP dispersed in water was determined by tri-axial shear compression test. Its value was 10.3°. Compression effects during shear failure in Sepharose Big-Beads SP may influence this value. Unfortunately, the internal angle of friction of Sepharose Big-Beads SP dispersed in other solvents could not be investigated. However, particle-size measurements imply that it may remain relatively constant, regardless of solvent conditions.

Angle of wall friction of Sepharose Big-Beads SP dispersed in water against boro-silicate glass was determined by a modified direct-shear test. Its value equalled 8.0°. Again, angle of wall friction of Sepharose Big-Beads SP dispersed in other solvents could not be investigated. However, as described above, it is likely to remain constant in different solvents.

All resin particles in Sepharose Big-Beads SP are spherical. Their initial shape factor is unity.

Interparticle void-volume measurements of packed beds of Sepharose Big-Beads SP were employed to determine initial porosity. Its value was 0.38. This compared well with published values.

Variation in packed-bed height with axial stress for Sepharose Big-Beads SP in water was investigated. An empirical relationship, *eq.* 3.5, for the model parameter $f_c(\tau^s_{zz})$ was presented. Additionally, the variation in bed height which contributes to particle deformation, $f_d(\tau^s_{zz})$, was also measured and correlated to a simple empirical function, *eq.* 3.6.

CHAPTER 4

VALIDATION & PREDICTION

4.1 Preamble

Model parameters φ, φ_w and $f_c(\tau^s_{zz})$ have been determined. These parameters are specific to Sepharose Big-Beads SP and the WGFE ion-exchange system. $\chi(\tau^s_{zz})$ can now be calculated. This will be achieved by regression of model predictions against experimental pressure-drop data. Initial values for ε_f, d_{pv}, and ϕ, allow a preliminary estimate of $\chi(\tau^s_{zz})$ to be made.

With $\chi(\tau^s_{zz})$ known, true *a priori* prediction of compressible packed-bed pressure-drop behaviour of Sepharose Big-Beads SP will be possible. This will allow validation of the model to assess its utility for pressure-drop prediction during scale-up of the WGFE ion-exchange system.

4.2 Determination of $\chi(\tau^s_{zz})$

$\chi(\tau^s_{zz})$ is an arbitrary approximation function. It describes the functional dependence of pressure gradient in a compressed packed bed on key bed properties (refer *eq.* 2.40). It must be determined by regression of the proposed model against experimental pressure-drop data using the experimental values for model parameters presented in Chapter 3.

Figure 4.1 presents experimental pressure-drop and compressed bed-height data collected in the Pharmacia BPG 100/500 test column at various initial bed heights, L_i, with water as the test fluid. A data set at a superficial velocity of 45.2 cm/min was selected. Values for pressure drop and compressed bed height at this superficial velocity are shown in Figure 4.1. Trendlines were used to interpolate between experimental data points. This data set will be used to determine $\chi(\tau^s_{zz})$.

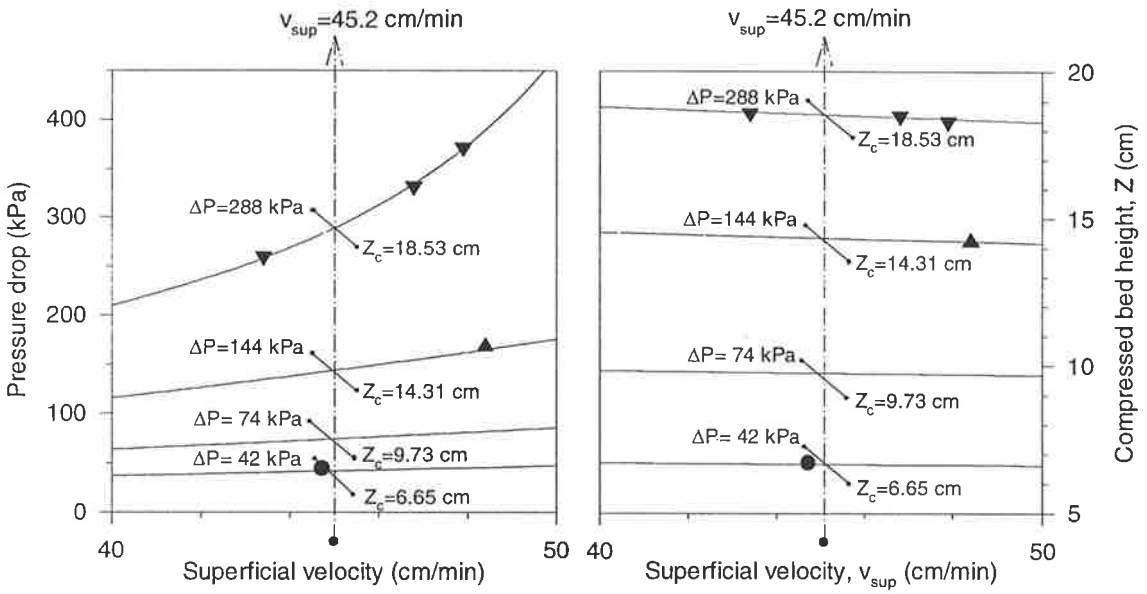

Figure 4.1: Experimental pressure-drop, ΔP, and compressed bed-height, Z_c, data selected for determination of $\chi(\tau^s_{zz})$: L_i=22.0 cm - (▼); L_i=16.5 cm - (▲); L_i=10.9 cm - (■) -; L_i=7.4 cm - (●); and trendlines (——).

It is important to note that experimental pressure-drop data in Figure 4.1 were recorded at the compressed bed height, Z_c. Model predictions (*ie* the solution to *eq.s* 2.37 and 2.38) are at the compressed bed height, and will correspond directly to experimental values. It is not necessary to solve *eq.* 2.42 simultaneously.

A purpose-built Microsoft Excel v5.0 (Microsoft Corporation, USA) Workbook was created for all numerical calculations. Various approximation functions were selected and used to solve *eq.s* 2.37 and 2.38. A 4th-order Runge-Kutta algorithm with manual step-size control (Kreyszig, 1988) was employed to integrate model equations. Approximation function initial values were set to 6.23×10^{10}, the approximate result of *eq.* 2.40 using experimental values for initial volume-mean particle diameter, initial shape factor and initial porosity determined in Chapter 3. Experimental values of φ_w and φ of 8.0 and 10.3°, respectively, were used to describe angle of wall friction and internal angle of wall friction. A value of 1.002 cP was used to describe the viscosity of water at 20°C. The model solution for packed-bed pressure drop at 45.2 cm/min was compared to experimental pressure-drop data at compressed bed heights given in Figure 4.1. A least squares non-linear regression using Microsoft Excel's Solver facility was employed to decide which

approximation function for $\chi(\tau^s_{zz})$ would provide the best fit to experimental pressure-drop data. The following approximation function was selected:

$$\log\left[\chi(\tau^s_{zz})\right] = 3.277\text{x}10^{-9}(\tau^s_{zz})^3 - 1.588\text{x}10^{-5}(\tau^s_{zz})^2 + 7.924\text{x}10^{-3}\tau^s_{zz} + 10.7684 \quad (4.1)$$

Model predictions of packed-bed pressure drop with *eq.* 4.1 *vs.* experimental data employed for regression (refer Figure 4.1) are shown in Figure 4.2.

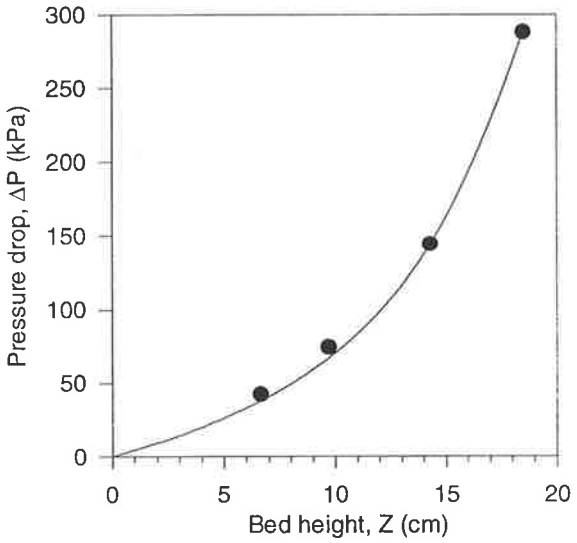

Figure 4.2: Model prediction of packed-bed pressure drop (——) using *eq.* 4.1 to represent $\chi(\tau^s_{zz})$ *vs.* experimental data (●) used for regression.

Equation 4.1 is graphically depicted in Figure 4.3 to illustrate its variation with τ^s_{zz}. The model prediction for τ^s_{zz} at a bed height of 18.53 cm, the maximum bed height in the experimental data set used for regression, was 238 kPa. This represents the prediction limit of *eq.* 4.1.

The porosity of a packed-bed of Sepharose Big-Beads SP at different stages of compression can be estimated from $\chi(\tau^s_{zz})$ using *eq.* 2.40 and experimental values for initial volume-mean particle diameter and initial shape factor. The results are also shown in Figure 4.3. They indicate an initial bed porosity of approximately 0.38. This value compares favourably with the initial porosity determined by experiment. (Perhaps, an expected result given it

was used to determine the initial value of $\chi(\tau^s_{zz})$ during regression in the first place.) At an axial stress of 238 kPa, Figure 4.3 indicates that bed porosity may decrease to a value of approximately 0.2. This is nearly a 50% reduction in void space available for fluid flow.

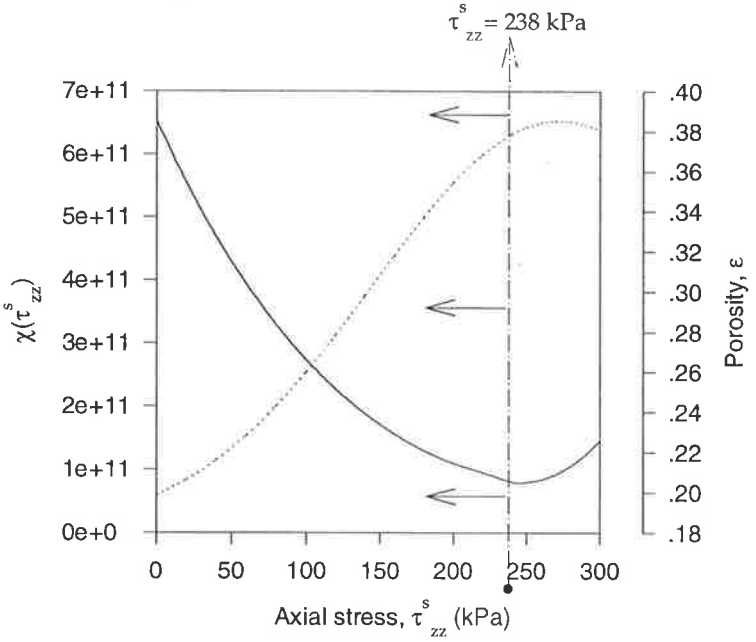

Figure 4.3: Variation in $\chi(\tau^s_{zz})$ (·····) and bed porosity (——) with axial stress as predicted by *eq.* 4.1 and estimated from *eq.* 2.40, respectively.

4.3 Model Validation

$\chi(\tau^s_{zz})$ has been determined. Model predictions are now possible. However, unlike model predictions in Section 4.2, the compressed bed height is unknown. Equation 2.42 is required. While it could be solved simultaneously with *eq.s* 2.37 and 2.38, these two equations can be recast by regarding 'initial' bed height (prior to compression and excluding particle reorganisation) and 'compressed' bed height as two separate spatial domains, L and Z, respectively. Each domain is related by *eq.* 2.42. Differentiating *eq.* 2.42 with respect to L gives

$$\frac{dZ}{dL} = f_c(\tau^s_{zz}) \tag{4.2}$$

Substituting *eq.* 4.2 into *eq.s* 2.37 and 2.38 gives

$$\frac{dP}{dL} = -\mu v_z^{sup} \chi(\tau_{zz}^s) f_c(\tau_{zz}^s) \tag{4.3}$$

and

$$\frac{d\tau_{zz}^s}{dL} = \left(\mu v_z^{sup} \chi(\tau_{zz}^s) - \frac{4}{D} \tan\varphi_w \frac{1-\sin\varphi}{1+\sin\varphi} \tau_{zz}^s \right) f_c(\tau_{zz}^s) \tag{4.4}$$

respectively.

Equations 4.3 and 4.4 express the variation in fluid pressure and axial stress with initial bed height. Model predictions can be made by integration of *eq.s* 4.3 and 4.2 without simultaneously solving *eq.* 2.42. Of course, the integration domain is now initial bed height, L_i, instead of the compressed bed height, Z_c. Furthermore, once the axial stress field in the bed is determined, 'compressed' bed height can then be directly determined from *eq.* 2.42.

In addition, it may also be useful to determine the 'expanded' bed height (*ie* during relaxation and after particle reorganisation), Z_e. This can be determined as follows:

$$Z_e = \int_0^{L_i} \left[f_c(\tau_{zz}^s) - f_d(\tau_{zz}^s) \right] dL \tag{4.5}$$

where $f_d(\tau_{zz}^s)$ is the fractional change in height that contributes to particle deformation as defined in Section 3.7.3, Chapter 3.

A purpose-built MathCad PLUS v5.0 (MathSoft Inc., USA) file was created for all numerical calculations. Symbolic formulas were employed to encode, and integrate, *eq.s* 4.2 and 4.3. Equation 4.1 was used to describe $\chi(\tau_{zz}^s)$. Experimental values of 8.0 and 10.3°, respectively, were used for angle of wall friction and internal angle of wall friction. A value of 1.002 and 2.15 cP was used to describe the viscosity, at 20°C, of water and 21% (by wt.) ethanol, respectively. (These were the test solutions used to collect experimental

pressure-drop data in Chapter 3.) $f_c(\tau^s_{zz})$ and $f_d(\tau^s_{zz})$ were described by empirical formulas *eq.s* 3.5 and 3.6, respectively. The MathCad file was also encoded to calculate 'compressed' and 'expanded' bed height using *eq.s* 2.42 and 4.5, respectively, once the axial stress field of a packed bed was known.

Model predictions for experimental data presented in Figure 3.7 - Chapter 3, are shown in Figure 4.4. Figure 3.7 illustrated the experimental pressure-drop and bed-height behaviour in the Pharmacia XK 50/60 test column at an initial bed height of 16.7 cm. Water was the test fluid. Figure 4.4 is identical to Figure 3.7, except trendlines have been omitted, and experimental data are overlayed by model predictions for pressure drop and 'expanded' and 'compressed' bed height. Furthermore, the reader should note that model predictions in Figure 4.4 were restricted by the prediction limit of *eq.* 4.1 ($\tau^s_{zz} < 238$ kPa) which was encountered at a superficial velocity of 61 cm/min.

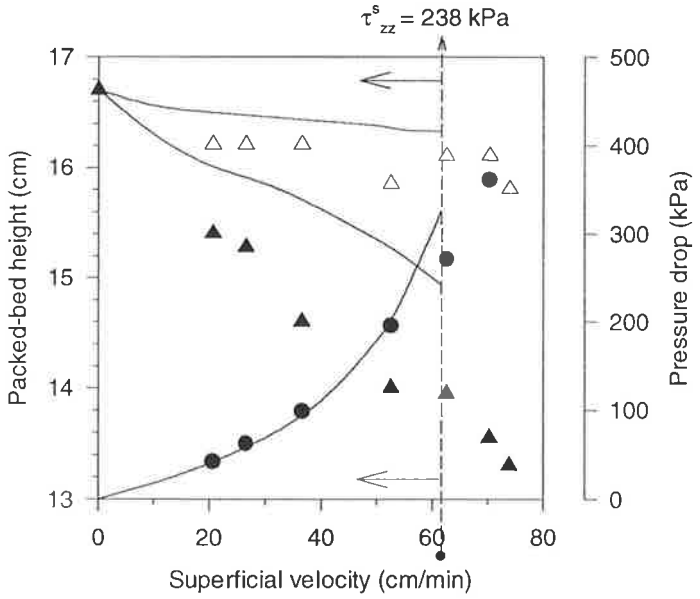

Figure 4.4: Model predictions (——) *vs.* experimental pressure-drop and bed-height data presented in Figure 3.7 - Chapter 3: pressure drop - (●); 'expanded' bed height - (△); and 'compressed' bed height - (▲).

Model predictions for pressure drop in Figure 4.4 correlate closely with experimental data, although deviations become apparent at higher (>55 cm/min) superficial velocities. However, model predictions (*eq.s* 2.42 and 4.5) of 'expanded' and 'compressed' bed height compare poorly with their experimental counterparts. Experimental variation in steady-

state bed height at relaxation and during compression grossly exceed prediction, by almost 1 cm in some cases.

Another example of model predictions *vs.* experimental data for pressure drop and bed height of a compressible packed bed of Sepharose Big-Beads SP is shown in Figure 4.5. Experimental pressure-drop and bed-height data were collected in the Pharmacia XK 16/40 test column at an initial bed height of 20.2 cm with 21% (by wt.) ethanol as the test fluid. Like Figure 4.4, model predictions for pressure-drop data correspond closely with experimental data, while model prediction of 'expanded' and 'compressed' bed height correlate poorly with their experimental counterparts.

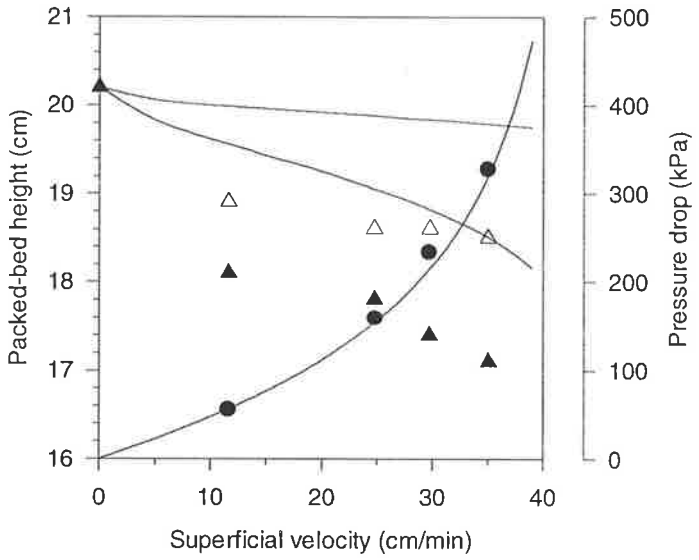

Figure 4.5: Model predictions (——) *vs.* experimental pressure-drop and bed-height data, Pharmacia XK 16/40, 21% (by wt.) ethanol, L_i=20.2 : pressure drop - (●); 'expanded' bed height - (△); and 'compressed' bed height - (▲).

Model predictions for experimental data presented in Figure 3.8 - Chapter 3, are shown in Figure 4.6. Figure 3.8 illustrated the experimental pressure-drop behaviour of the three test columns at similar bed heights. Water was the test fluid and the initial bed heights were 22.8, 22.5 and 22.0 cm, respectively. Again, the reader will note that Figure 4.6 is identical to Figure 3.8, except trendlines have been omitted, and experimental data are overlayed by model predictions for pressure drop

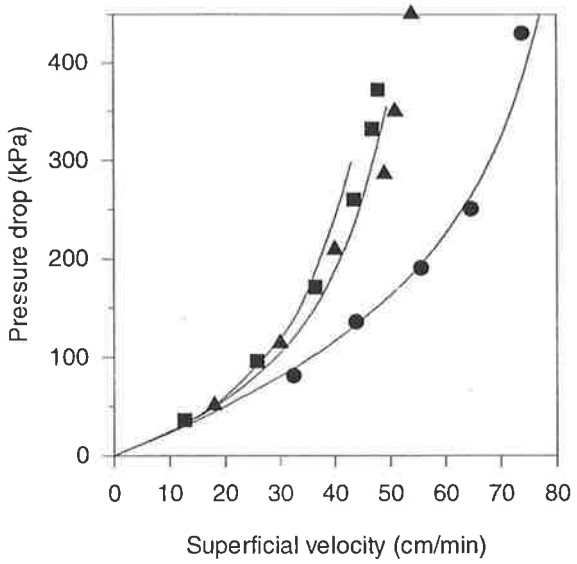

Figure 4.6: Model predictions (——) *vs.* experimental pressure-drop data presented in Figure 3.8 - Chapter 3: D=1.6 cm, L_i=22.8 cm - (●); D=5.0 cm, L_i=22.5 cm - (▲); and D=10.0 cm, L_i=22.0 cm - (■).

Model predictions in Figure 4.6 correspond exceptionally well with experimental data. Furthermore, they show that the model can successfully account for wall friction effects by accurately adapting its predictions for column size.

The results presented in Figures 4.4, 4.5 and 4.6 indicate that while the proposed model can quantitatively predict pressure drop in a compressed packed bed, its prediction of bed height variation is erroneous. This is confirmed by parity plots shown in Figures 4.7, 4.8 and 4.9. Figure 4.7 compares model predictions of pressure drop *vs.* experimental data for all experimental pressure-drop data collected in Chapter 3, with the exception of data where model predictions exceed the prediction limit of *eq.* 4.1. Presentation of results in the parity plot is divided into separate data sets for each test column. Similarly, Figures 4.8 and 4.9 compare model prediction of 'compressed' and 'expanded' bed height, respectively, with all experimental (bed-height) data.

A significant variation between model predictions and experimental pressure-drop data in Figure 4.7 can be observed, although the majority of deviations are less than ±20%. This can be considered an acceptable level of disparity, but its magnitude gives a misleading perception of the model's propensity to simulate pressure-drop behaviour. Consider Figure 4.5, the model appears to accurately describe variation in pressure drop with superficial

velocity in each test column. However, closer examination reveals that deviations between prediction and experiment in some cases are nearly 20%. For example model prediction *vs.* experiment for the Pharmacia XK 50/60 column at a superficial velocity of 48.6 cm/min are 334 and 286 kPa, respectively. This reflects the sensitivity of the model to compression effects, in particular as superficial velocity approaches the 'critical' velocity. A small variation in superficial velocity can induce a significant change in packed bed pressure drop.

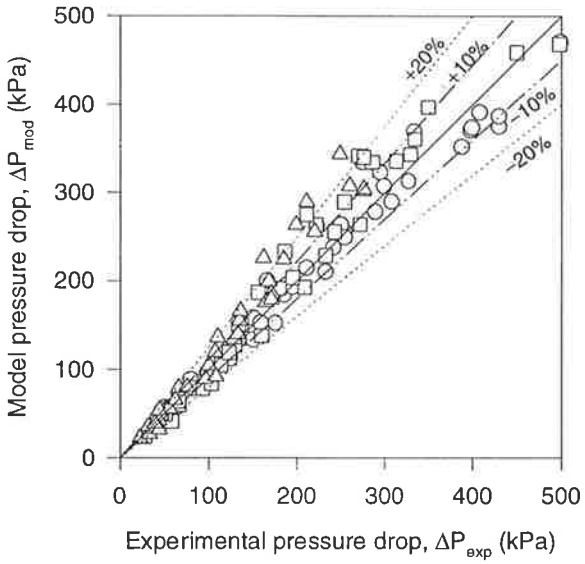

Figure 4.7: Parity plot of model predictions, ΔP_{mod}, *vs.* experimental pressure drop, ΔP_{exp}, for all experimental data collected in Chapter 3: D=1.6 cm - (○); D=5.0 cm - (□); and D=10.0 cm - (△).

Despite this, Figures 4.4, 4.5 and 4.6 show that model does possess an excellent predictive capability. It can predict the onset of compression effects quite accurately. For example, compare the superficial velocity at which model predictions for pressure drop in the Pharmacia XK 50/60 column in Figure 4.4 are equal to the experimental value of 286 kPa. It is 46.4 cm/min, only a 4.5% deviation from 48.6 cm/min. One could say that deviations between model predictions and experimental pressure-drop data in Figure 4.7 appear worse than they actually are.

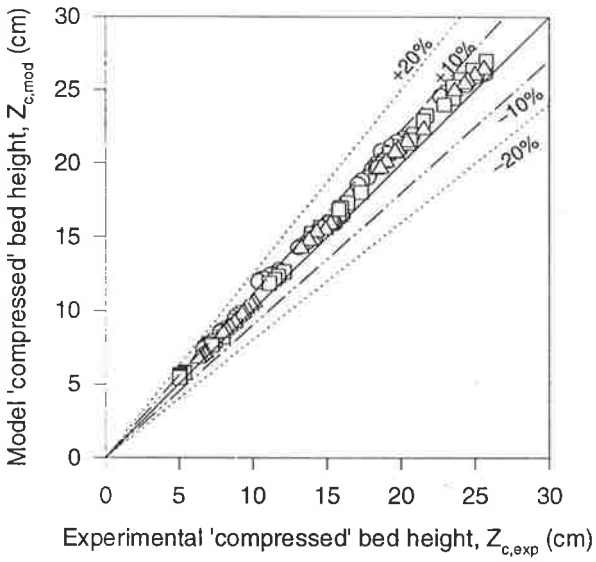

Figure 4.8: Parity plot of model predictions, $Z_{c,mod}$, *vs.* experimental 'compressed' bed height, $Z_{c,exp}$, for all experimental data collected in Chapter 3: D=1.6 cm - (○); D=5.0 cm - (□); and D=10.0 cm - (△).

Figure 4.7 displays no obvious bias in favour of test column size. Further confirmation that the proposed model can successfully account for wall friction effects.

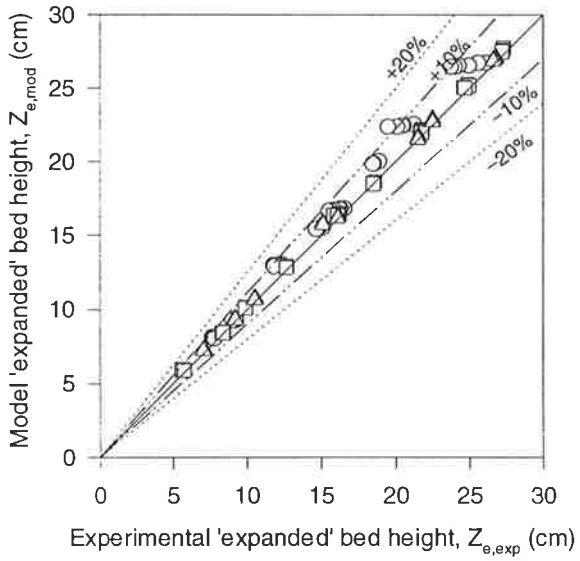

Figure 4.9: Parity plot of model predictions, $Z_{e,mod}$, *vs.* experimental 'expanded' bed height, $Z_{e,exp}$, for all experimental data collected in Chapter 3: D=1.6 cm - (○); D=5.0 cm - (□); and D=10.0 cm - (△).

However, model predictions in Figure 4.7 do display a positive bias. While random variation in model predictions is observed, most model predictions are greater than experimental data. This appears to reflect the incapacity of the model to accurately predict variation in bed height. Figure 4.8 reveals that all model predictions of 'compressed' bed height were greater than their experimental counterparts. Given that 'compressed' bed height is the integration domain for the model, this has a critical impact on prediction, even though the variations are less than 10%. For example, Figure 4.10 illustrates the sensitivity of model predictions to bed height. It presents model predictions of pressure drop across a hypothetical packed bed at a 'compressed' bed height of 25 cm in a 5 cm internal diameter column with water at 20°C. The reader should note that compressed bed height was fixed for all model predictions. Figure 4.10 also shows the percentage deviation in model prediction for the same system, but with a ±10% variation in compressed bed height (*ie* 22.5 or 27.5 cm instead of 25 cm).

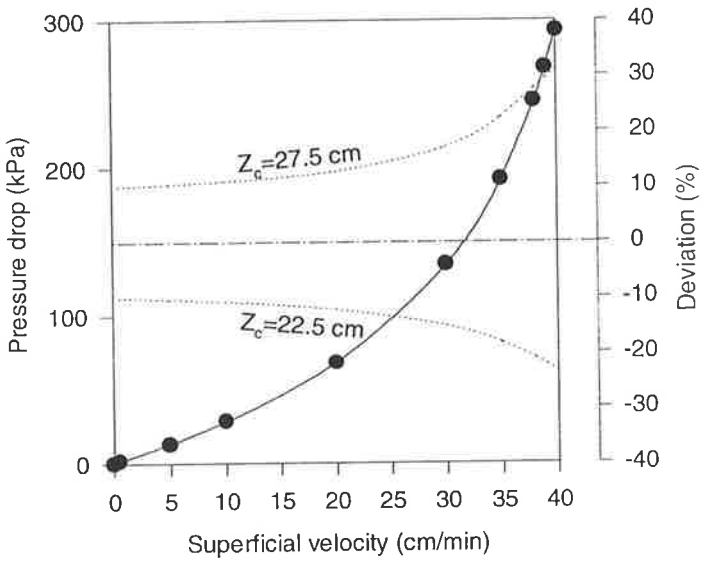

Figure 4.10: Sensitivity of model predictions (—●—) for pressure drop across a 25 cm packed bed to variation in bed height: model-prediction deviation at ±10% Z_c - (·····).

As one would expect, percentage deviation for model predictions in Figure 4.10 is identical to (percentage) bed-height variation at low superficial velocity. However, as compression effects in the bed are induced at higher superficial velocity, percentage deviation gradually increases. An exponential increase in percentage deviation is observed as the superficial velocity approaches the system's 'critical' velocity. Evidently, over-estimation of bed

height by the model can be considered the key contributor to positive bias displayed in Figure 4.7. In particular, when the increase in predicted bed height expands the integration domain at the base of the packed bed where compression effects are greatest.

The incapacity of the model to accurately predict bed height is open to debate. For example, it could be the direct result of experimental error in measurement of $f_c(\tau^s_{zz})$ and $f_d(\tau^s_{zz})$. However, consider Figures 4.4 and 4.5. While the model grossly overestimates 'compressed' and 'expanded' bed height, predictions appear to imitate experimental variations in bed height. Predicted bed-height variations would almost map experimental data if a lower initial bed height had been employed for the integration domain. This appears to indicate that the experimental value for initial bed height is erroneous. But this is unlikely. Bed height was carefully recorded during collection of experimental pressure-drop data.

There is an alternative explanation. Consider, for example, the Pharmacia XK 16/40 and XK 50/60 test columns. Chromatographic resin is added to each column with an equivalent (resin) mass to (column) area ratio. The resin gravity settles to create a packed bed. The initial bed heights in each column are equal? The answer is no *per se*. Initial bed height in each column depends on the packing density of particles. This is a function of the compressive stress field acting on, and within, the bed. In the absence of fluid flow, this is created by the combination of fluid and particle weight, and ironically, wall friction effects. Wall friction effects mitigate the influence of fluid and particle weight by supporting the packed bed. Initial packing density of a packed bed of pulverulent material in a vessel depends on its size. This has been observed experimentally (Foust *et al.*, 1980), although not explicitly for a chromatographic system where resin is contained within a cylindrical column. Therefore, initial packing density is lower in small columns and higher in large columns. The initial bed height in the Pharmacia XK 16/40, for our example above, should be higher than the Pharmacia XK 50/60.

$f_c(\tau^s_{zz})$ and $f_d(\tau^s_{zz})$ were measured using a packed bed in an experimental system without wall friction effects. The initial packing density of the bed was determined solely by fluid and particle weight. It would be higher than for a packed bed in a chromatographic column where wall friction effects mitigate compressive forces. Variation in bed height for $f_c(\tau^s_{zz})$

and $f_d(\tau^s_{zz})$ was measured relative to this initial packing density. They therefore underestimate the level of compression that takes place in a chromatographic column. This is the source of prediction error for bed height in the model. In fact, one would expect that the magnitude of prediction error should be a function of column diameter. Prediction should become more accurate in larger columns as disparity between initial packing density used for measurement of $f_c(\tau^s_{zz})$ and $f_d(\tau^s_{zz})$, and the packed bed in a chromatographic column, decrease. Average prediction error for 'compressed' bed height in Figure 4.6 for each test column was determined. It was 6.5, 6.0 and 4.9% for the Pharmacia XK 16/40, XK 50/60 and BPG 100/500, respectively. The incapacity of the model to predict bed height is an inherent limitation in its current form.

However, this does not account for the considerable random variation between model prediction and experiment observed in Figure 4.7. There are a number of explanations. It may be a result of using Janssen's analysis, instead of the method of characteristics, to account for wall friction effects. As discussed in Chapter 2, Janssen's analysis ignores the radial variation in axial and radial stress that occurs in the cylindrical vessel. It only provides an estimate of the stress field. This is an extremely accurate estimate in hoppers and silos where prediction error is usually less than 3% when compared to the exact solution generated by the method of characteristics. Unfortunately, the accuracy of Janssen's analysis is unquantified for prediction of wall friction effects in a chromatographic system.

Alternatively, it may correspond to experimental error encountered during collection of pressure-drop data. In particular, variation in test fluid viscosity. The control limit for test-fluid temperature in the experimental system employed for pressure-drop measurement was ±2°C. Fluid viscosity is very sensitive to temperature. A ±2°C temperature variation for water leads to a variation of +5.1 and -4.7%, respectively. Model predictions allow us to quantify the impact fluid viscosity variation may have had on experimental pressure-drop data. Figure 4.11 illustrates the sensitivity of model predictions to viscosity. Model predictions are presented for pressure drop across a hypothetical packed bed at an initial bed height of 25 cm in a 7.0 cm internal diameter column with water at 20°C. Percentage deviation in model prediction for the same system, but with a ±5% variation in fluid viscosity (*ie* 1.05 or 0.95 cP instead of 1.0 cP) are also displayed.

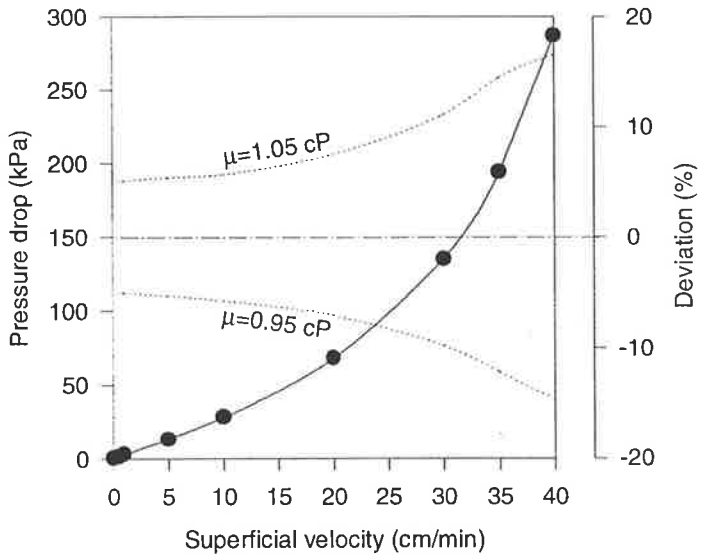

Figure 4.11: Sensitivity of model predictions for pressure drop at μ=1 cP (—●—) to fluid viscosity: model-prediction deviation at ±10% μ - (·····).

Figure 4.11 indicates that a small fluctuation in viscosity can generate a large variation in measured experimental pressure drop across a packed bed. While this is inconvenient for accurate validation of model predictions, of greater concern is its impact on $\chi(\tau^s_{zz})$. This parameter was determined by regression of model predictions against an arbitrary set of experimental pressure-drop data. Any uncertainty in experimental pressure-drop data would generate an error in $\chi(\tau^s_{zz})$, and therefore, model prediction.

Another possible contributor to the random variation observed in Figure 4.7 may have been the sensitivity of model parameters φ_w, φ, $f_c(\tau^s_{zz})$ and $\chi(\tau^s_{zz})$ to solvent conditions. This is examined in Figure 4.12. It replicates Figure 4.7, except results in the parity plot are divided into separate data sets for each test fluid, instead of by test column. No bias in favour of either test fluid is observed.

In summary, it can be said that Figures 4.4, 4.5, 4.6 and 4.7 provide strong evidence that the proposed model can accurately predict steady-state pressure-drop behaviour in compressible packed beds of Sepharose Big-Beads SP in various size columns. This is despite significant deviation in prediction of bed height during compression. While this leads to a positive bias in most cases, it does not appear to seriously compromise the

predictive capability of the model. It does, however, represent an inherent limitation in the model. Figure 4.12 shows that model predictions were also independent of solvent type. Given that particle size measurements in Chapter 3 were invariant with solvent conditions, this indicates that the model parameters measured for Sepharose Big-Beads SP in water could be employed for pressure-drop prediction with other solvents. A key uncertainty during validation of model predictions was the integrity of experimental pressure-drop data. Variation in fluid temperature of test fluid during collection may have been responsible for random variation observed in Figure 4.7. More importantly, it also may have introduced error in determination $\chi(\tau^{s}_{zz})$, and therefore, model prediction.

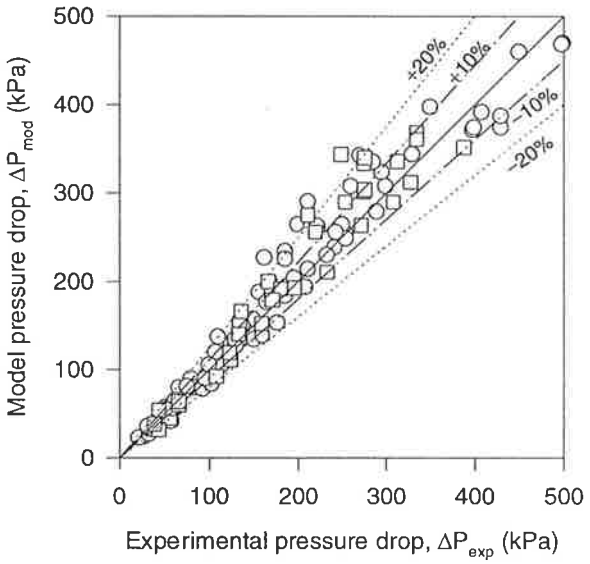

Figure 4.12: Parity plot of model predictions *vs.* experimental pressure drop for all experimental data collected in Chapter 3 by test fluid: water -(○): and 21% (by wt.) ethanol - (□).

4.4 Model Prediction and Scale-Up

$\chi(\tau^{s}_{zz})$ has been determined. Model predictions have been validated against experimental data. It is now possible to make true *a priori* predictions of packed-bed pressure-drop behaviour during scale-up of the WGFE ion-exchange system. This section uses the model to make a predictions of packed-bed pressure drop of Sepharose Big-Beads SP for the WGFE ion-exchange system. Special focus is placed on considering the variation in pressure-drop behaviour that may occur during scale-up. The reader should note that all

model predictions in this Section were generated by the purpose-built MathCad PLUS v5.0 file described in Section 4.3.

Of particular interest, is the influence of column diameter on pressure drop during scale-up. Figure 4.13 shows the variation in model prediction of pressure drop for a 20 cm (initial height) packed bed of Sepharose Big-Beads SP with column diameter at five different superficial velocities: 25, 35, 40, 45 and 50 cm/min.

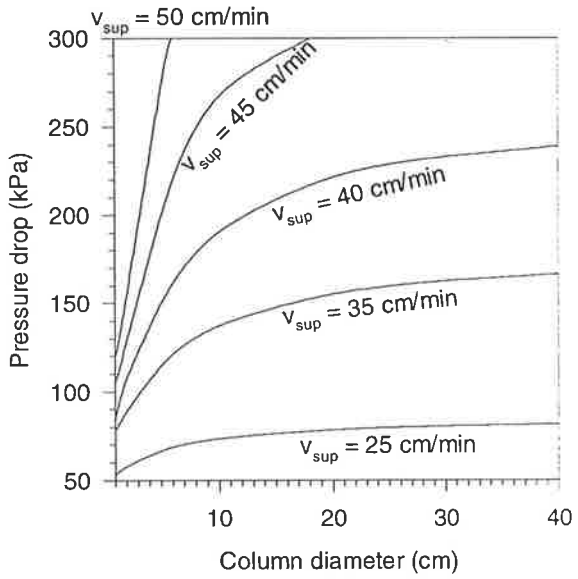

Figure 4.13: Functional dependence of model prediction for pressure drop (——) on column diameter at varying superficial velocities, v_{sup}.

Figure 4.13 illustrates the functional dependence of pressure drop across compressible packed beds of Sepharose Big-Beads SP on column diameter. Even at 25 cm/min when compression effects only just begin to manifest themselves, wall friction effects play an important role in supporting the packed bed. For example, an increase in column diameter from 2 cm to 20 cm leads to a 35% increase in pressure drop. Wall support assumes an even greater role as superficial velocity increases. Consider the variation in pressure drop with column diameter at a superficial velocity of 50 cm/min. In a 2 cm diameter column, packed-bed pressure drop is only 120 kPa. However, at a column diameter of 6 cm, it is more than double, and exceeds 300 kPa.

These results demonstrate that careful consideration must be given to the impact of column diameter on packed-bed pressure drop. It is not safe to assume that it will remain constant during scale-up of the WGFE ion-exchange system.

Besides pressure drop, the model also actually allows us to examine how wall friction actually effects the applied axial stress field, τ^s_{zz}, in the packed bed. For example, model predictions of variation in τ^s_{zz} with bed height in a 2 and 20 cm internal diameter column for the packed-bed system of Figure 4.13 are presented in Figure 4.14. The superficial velocity used to generate model predictions was 35 cm/min. In addition, model predictions were used to generate the axial stress field that would be present in the absence of wall friction (*ie* D = ∞). These are shown in Figure 4.14 for comparison.

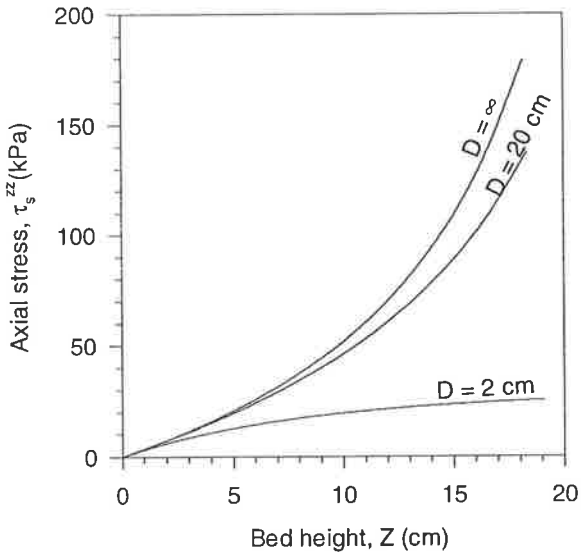

Figure 4.14: Impact of wall friction effects on axial stress, τ^s_{zz}.

The effect of wall friction on τ^s_{zz} can be clearly observed in Figure 4.14. Consider the model prediction for the larger column. While applied stress begins to increase linearly with height at the top of the bed, deeper into the packed-bed τ^s_{zz} increases exponentially as it responds to bed compression. Comparison with model predictions where wall friction effects were excluded indicate that wall friction in the larger column is not significant and does not markedly influence τ^s_{zz}. In the smaller column, however, variation in τ^s_{zz} is quite different. It initially increases with bed height, but at a much lower rate than in the larger column. Wall friction effects are significant. They support the packed bed and mitigate

compressive forces. Further into the bed, the applied stress ceases to rise and tends toward an asymptotic value. At this point, wall friction begins to balance the compressive forces being generated in the bed.

This behaviour is similar to that observed in packed beds of pulverulent materials in different-sized grain silos and hoppers. However, for grain silos, the increase in applied stress is induced by the weight of pulverulent material (Hancock & Nedderman, 1974), rather than the pressure gradient due to fluid flow through a packed bed.

Figure 4.14 also allows us to investigate how compression might alter the bed properties, in particular porosity, in a packed bed during scale-up. For example, compare model predictions of the τ_{zz}^{s} at the base of the bed in each column. They are 25 and 137 kPa for the 2 and 20 cm column, respectively. Figure 4.3 can be used to estimate the bed porosity which may correspond to these values of τ_{zz}^{s}. It gives values of approximately 0.35 and 0.24, respectively. This is quite a difference. It indicates that the 20 cm internal diameter column will experience a 37% decrease in porosity from top to bottom of the packed bed. This is a significant change in the packed-bed interparticle void space and nearly five times the variation (8%) in the 2 cm internal diameter column.

During scale-up of the WGFE system, we will not only be concerned with the pressure drop at the desired column size, but also its variation with bed height and superficial velocity. In particular, the bed height and superficial velocity where pressure drop may exceed the pressure constraint for the production-scale system, whether this be the pressure rating of the column or the head a feed pump can provide. For example, consider model predictions of packed-bed pressure drop for Sepharose Big-Beads SP in a Pharmacia BPG 100/500 chromatographic column with water (at 20°C). They are presented in Figure 4.15 as a contour plot of pressure drop *vs.* superficial velocity and bed height. Each contour allows us to identify the possible combinations of superficial velocity and bed heights that may be employed for a desired packed-bed pressure drop.

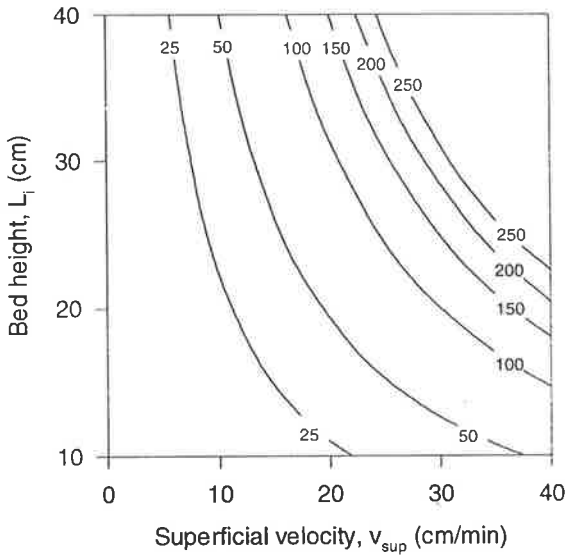

Figure 4.15: Contour plot of predicted packed-bed pressure drop for Sepharose Big-Beads SP in a Pharmacia BPG 100/500 column.

However, the pressure constraint applies to the pressure drop across the entire chromatographic system, not just the packed bed. This includes the external pressure losses before and after the column, as well as column pressure losses in the column, but excluding the packed bed. Pressure losses before and after the column are the result of fluid transmission through external piping and fittings. The pressure losses inside the column include pipe fittings, internal conduits for fluid transmission and the distributor plate. For the readers interest, a schematic diagram of the Pharmacia BPG 100/500, copied from technical information provided by the manufacturer (Pharmacia Bioprocess Technology, 1996b), is provided in Figure A1.1 - Appendix 1. It depicts the passage of fluid though various fittings and internal conduits in the column. An accompanying table, Table A1.1 provides an inventory of parts.

The schematic diagram and parts list in Appendix 1 provide a typical example of the Pharmacia range of BPG production-scale columns. While different column sizes are available, their design and construction are largely identical, except for size variations in internal conduits and pipe fittings used for fluid transmission (Amrad Pharmacia Biotech, 1996).

The column pressure losses across a Pharmacia BPG 100/500 column, excluding the packed bed, have already been determined. They were measured for the experimental system used

to collect pressure-drop data in Chapter 3. These pressure losses for water and 21% (by wt.) ethanol are shown in Figure 4.16.

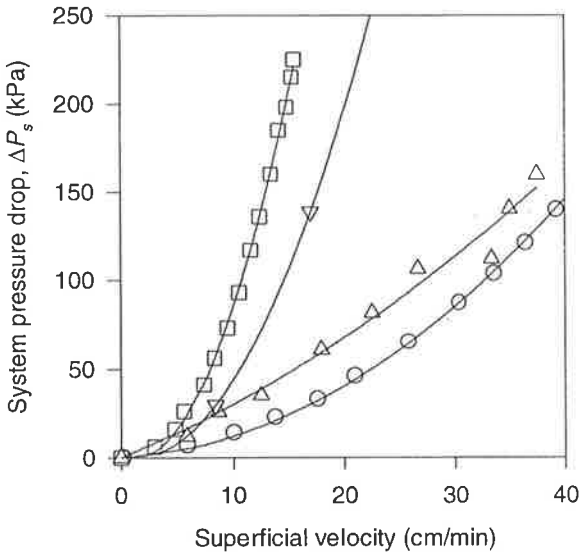

Figure 4.16: Column pressure losses in Pharmacia BPG columns for various fluids: BPG 100/500, water at 20°C - (○); BPG 100/500, 21% (by wt. ethanol) at 20°C - (□); BPG 300/500, water at 25°C - (△); BPG 300/500, microfiltered whey at 25°C -(▽); with trendlines (——).

The column pressure losses in the Pharmacia BPG 100/500 column for water and 21% (by wt.) ethanol are vastly different. This reflects their different viscosity. There also appears to be no direct correlation between pressure loss and each fluid's physical properties. This is unfortunate. We cannot exploit this information to determine the column pressure losses for the Pharmacia BPG 100/500 column with a fluid of different viscosity.

It is important to note that the pressure-loss data in Figure 4.16 are for the Pharmacia BPG 100/500 column alone. It does not include pressure losses as a result of fluid transmission to, and from, the column. Despite this, we will use it to give an indication of the impact of external and column pressure losses may have the pressure-drop behaviour of our system. For example, pressure-loss data for water in Figure 4.16 can be added to model predictions of packed-bed pressure drop in Figure 4.15. Figure 4.17 presents the result as a contour plot of pressure drop *vs.* superficial velocity and bed height. The addition of column pressure losses plays an important role in determining the position of each contour.

Contour movement is greatest at low bed height and high superficial velocity where column pressure losses are greatest.

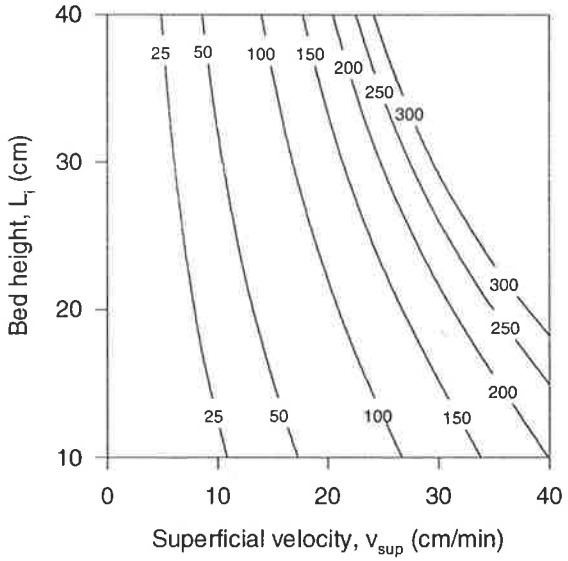

Figure 4.17: Contour plot of predicted system pressure drop for Sepharose Big-Beads SP in a BPG 100/500 column.

Figure 4.17 indicates that column pressure losses would be an important consideration in the design of a chromatographic system which uses a Pharmacia BPG 100/500 column. In some cases, they even exceed the packed-bed pressure drop.

The prediction of pressure drop in the Pharmacia BPG 100/500 have served the useful purpose of illustration. However, it is not the column size that will be employed in a production-scale ion-exchange system to manufacture WGFE. The pilot-plant currently employs two Pharmacia BPG 300/500 columns. One would expect that an even larger column would be required. It has been suggested that the Pharmacia BPG 450/500 column will be selected (Regester, 1996). A similar analysis can be performed. Model prediction of packed-bed pressure drop can be combined with column pressure losses to determine variation in pressure drop with bed height and superficial velocity. Furthermore, if we know the pressure constraint that will apply to the production-scale system, we will then be able to identify the possible design scenarios that will be available during scale-up.

However, a key decision must first be made. There are a variety of fluids that are employed in the WGFE ion-exchange system. Each has a different viscosity. Which one, or all,

should be examined? The operation of the pilot-plant currently employs two separate flowrate regimes during a cycle. A superficial velocity of 14.2 cm/min is employed for load, wash and elution steps during product separation. The fluids employed in sequence are microfiltered whey, deionised water, 0.4 M NaCl and 1.0 M NaCl. Resin regeneration step is then conducted at 3.2 cm/min. The fluids employed in sequence are deionised water, 1M NaOH and deionised water. Based on literature values (Weast, 1974), the viscosity at 20°C of each fluid employed in the WGFE ion-exchange cycle is shown in Table 4.1.

Table 4.1: Viscosity at 20°C of various fluids employed in the WGFE ion-exchange system.

Fluid	Viscosity (cP)
Microfiltered Whey	1.25*
Deionised water	1.00
0.4 M NaCl	1.04
1.0 M NaCl	1.10
1.0 M NaOH	1.25

* Estimate value based on 7.5% (by wt.) lactose in water.

The viscosity of microfiltered whey in Table 4.1 is an estimate value based on the literature value for 7.5% (by wt.) lactose in water (Weast, 1974). Raw whey is a dilute solution of 5-7% dry matter. Its major constituents include lipids (3-4%), lactose (4-5%), and whey proteins (0.5-1.0%). A reported value for the viscosity of whey is 1.3 cP (Carrére *et al.*, 1994). However, microfiltration effectively di-lipidises the whey. A better estimate of viscosity can be made based on its lactose concentration. In this case, a value slightly higher than normal: 7.5%, was arbitrarily selected to account for the presence of protein.

For the purpose of this analysis, we will concern ourselves only with product separation because of its chronological dominance of the WGFE ion-exchange cycle. Resin regeneration will not be considered. Furthermore, let us assume that the pilot-plant flow regime during product separation (*ie* constant superficial velocity during load, wash and elution) will be retained at production-scale, although the superficial velocity and bed height may be altered. Viscosity becomes the critical determinant of pressure-drop behaviour. Microfiltered whey has the highest viscosity, and therefore, will set the limiting conditions for flowrate. Comparison of its variation in pressure drop against the system pressure

constraint will determine the possible combinations of bed height and superficial velocity that can be employed during scale-up.

However, while model predictions of the packed-bed pressure-drop behaviour for microfiltered whey can be easily generated, specific information for column pressure losses in the Pharmacia BPG 450/500 column are unavailable. These could be measured by experiment, but this was not possible as a result of financial constraints. Some estimate must be made. This would ideally be based on external pressure-loss data for the Pharmacia BPG 450/300 column with another fluid of similar viscosity. No information of this type is recorded in the literature. An alternative must be considered. It could be estimated by comparison with column losses in another Pharmacia BPG column. Information from the pilot-plant provides two pressure-drop data points during the load step in a Pharmacia BPG 300/500 column at an initial bed height of 21 cm (CSIRO, 1995). These are 0.6 bar and 2.0 bar at a superficial velocity of 8.5 an 17.0 cm/min, respectively. However, this data includes both packed-bed pressure drop and column pressure losses. Column pressure losses can be isolated by subtracting packed-bed pressure drop. Model predictions were employed to predict pressure-drop behaviour for a 21 cm (initial height) packed bed of Sepharose Big-Beads SP with microfiltered whey at 20°C. Values were used to extract column pressure-loss data from each data point. The results with a trendline are shown in Figure 4.16.

Pharmacia also provides pressure-loss data for Sepharose Big-Beads SP in a Pharmacia BPG 300/500 column with water at 25°C (Pharmacia Bioprocess Technology, 1995). This has been reproduced by the author in Figure 4.18. Again, this includes packed-bed pressure drop and column pressure losses. Model predictions were employed to predict pressure drop behaviour for a 20 cm (initial height) packed bed of Sepharose Big-Beads SP with water at 25°C. Values were used to extract column pressure-loss data from Figure 4.18. The results with a trendline are shown in Figure 4.16.

It is interesting to note that pressure losses for the Pharmacia BPG 300/500 column with water are much higher that the Pharmacia BPG 100/500 column, even though the viscosity of water is 10% lower at 25°C. This appears to be a result of size variation in internal conduits and pipe fittings for fluid transmission within each column. For example, the Pharmacia BPG 100/500 column accepts a 6 mm feed tube (refer Figure A1.1 - Appendix

1), while the Pharmacia BPG 300/500 column takes a 10 mm feed tube (Pharmacia Bioprocess Technology, 1996b). The size of internal conduits in each column apparently reflect this disparity, although exact dimensions were not provided by the manufacturer (despite a number of polite requests by the author). It is obvious that the 2.7-fold increase in conduit and fitting cross-sectional flow area does not compensate for the 9-fold increase in flowrate one would expect with the increase in column diameter. Evidently, the BPG 300/500 column has been poorly designed for scale-up from a Pharmacia BPG 100/500 column. Likewise, the Pharmacia BPG 450/500 column is designed to accept a feed tube of 10 mm (Amrad Pharmacia Biotech, 1996), identical to the Pharmacia BPG 300/500 column. Furthermore, the size of internal conduits and fittings in both columns are apparently similar. Clearly, the Pharmacia BPG 450/500 column has also been designed poorly to cater for the 1.8 fold increase in flowrate one would expect during scale-up from a Pharmacia BPG 300/500 column.

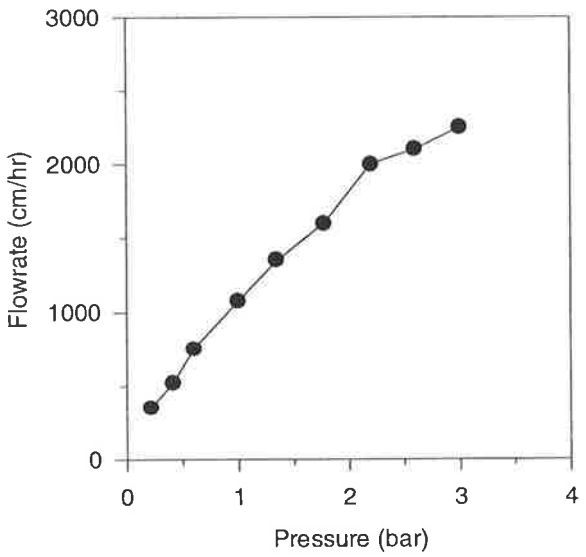

Figure 4.18: Column pressure-loss data (—●—) for Sepharose Big-Beads SP in a Pharmacia BPG 300/500 column with water at 25°C (Pharmacia Bioprocess Technology, 1995).

Therefore, while comparative information for microfiltered whey in the Pharmacia BPG 300/500 column is available, it is highly unlikely they will be correspond to external pressure losses in the Pharmacia BPG 450/500 column. In fact, pressure losses in the Pharmacia BPG 450/500 column are likely to be much higher. Despite this, we will use pressure-loss

data for microfiltered whey in the BPG 300/500 column to replicate column pressure losses in the Pharmacia BPG 450/500 column for the purpose of illustration.

Model predictions of packed-bed pressure drop of microfiltered whey for Sepharose Big-Beads SP at various superficial velocities and bed heights were performed. Column pressure-loss data for microfiltered whey in the Pharmacia BPG 300/500 column presented in Figure 4.16 was combined with model predictions. (The trendline in Figure 4.16 was used to interpolate between data points.) Figure 4.19 presents the result as a contour plot of pressure drop *vs.* superficial velocity and bed height.

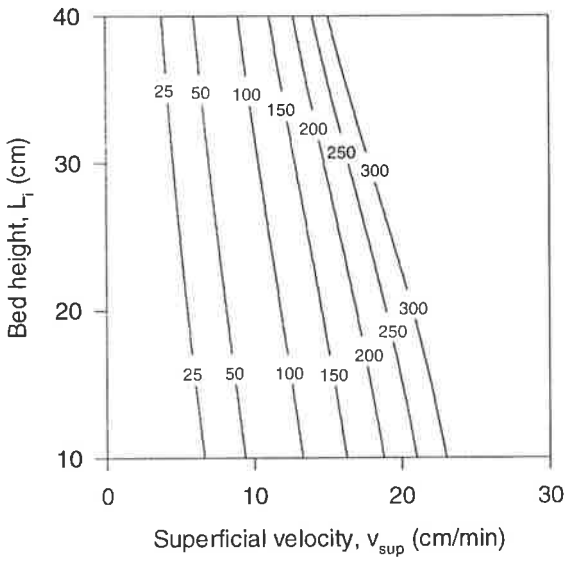

Figure 4.19: Contour plot of WGFE ion-exchange system pressure drop in a Pharmacia BPG 450/500 production-scale column.

The pressure constraint in the WGFE ion-exchange system after scale-up will be the pressure rating of the Pharmacia BPG 450/500 column assuming a positive-displacement pump is retained for fluid transmission. This rating is specified by the manufacturer as 3 bar (Amrad Pharmacia Biotech, 1996). It corresponds to the 300 kPa contour in Figure 4.19. The area beneath this contour can be considered as the feasible region for design. It contains the set of superficial velocities and bed heights which will not compromise the pressure constraint during scale-up.

However, it is important to observe that the contours in Figure 4.19 are almost vertical. This is symptomatic of the dominant contribution to system pressure drop of column

pressure losses. Figure 4.16 reveals column pressure losses were often more than 60% of the system pressure drop, and in some cases, greater than 90%. Column pressure losses appear to govern system pressure drop in the WGFE ion-exchange system during scale-up, instead of packed-bed pressure drop. This is of great concern. The Pharmacia BPG 300/500 column was used replicate column pressure losses in the Pharmacia BPG 450/500 column. There is no doubt that column pressure losses in the Pharmacia BPG 450/500 column will probably be much higher. Consider the proposed operating conditions during the load step in the ion-exchange system. The pressure drop at a bed height of 21 cm and superficial velocity of 14.5 cm/min is 150 kPa. An increase in column pressure loss would leave only a small margin of error before the pressure constraint would be compromised. Pressure losses in the Pharmacia BPG 450/500 column during the load step need to be measured before scale-up of the WGFE ion-exchange system to eliminate this uncertainty.

4.5 Concluding Remarks

The final parameter, $\chi(\tau_{zz}^{s})$, for Sepharose Big-Beads SP in the proposed model was determined by regression of model predictions against experimental pressure drop data. It is described by *eq.* 4.1. The prediction limit of *eq.* 4.1 for $\chi(\tau_{zz}^{s})$ was $\tau_{zz}^{s} < 238$ kPa.

Model predictions using $\chi(\tau_{zz}^{s})$ were compared against experimental pressure-drop and bed-height data. The model was able to successfully adapt predictions of steady-state pressure-drop behaviour for compressibility of the packed bed and the influence of wall friction effects. It can predict the impact of column diameter on packed-bed pressure drop during scale-up. This was despite significant deviation in model prediction of bed height during compression. Anecdotal evidence was also found that model predictions for Sepharose Big-Beads SP were independent of solvent type. This indicates that the model parameters measured for Sepharose Big-Beads SP in water may be employed for pressure-drop prediction with other solvents.

The model was used to predict the packed-bed pressure-drop behaviour of Sepharose Big-Beads SP during scale-up. The impact of column diameter was examined. The results demonstrate packed-bed pressure drop can increase markedly with column diameter. It is not safe to assume that it will remain constant during scale-up of the WGFE ion-exchange

system. Model predictions were combined with data describing column pressure losses in various Pharmacia BPG columns. Column pressure losses play an important role in determining the overall system pressure drop of the WGFE ion-exchange system during scale-up. Packed-bed pressure drop cannot be considered alone. An attempt to estimate the variation in system pressure drop with bed height during the load step with microfiltered whey for the proposed production-scale column: the Pharmacia BPG 450/500 column, was made. A key assumption was the use of column pressure-loss data experimentally measured for the Pharmacia BPG 300/500 column. Column pressure losses were found to dominate system pressure drop in the WGFE ion-exchange system. Given that column pressure losses in the BPG 450/500 column are likely to be higher than the BPG 300/500 column, scale-up at the proposed pilot-plant operating conditions may compromise the pressure constraint in the system. Column pressure losses in the BPG 450/500 must be measured before scale-up to eliminate this uncertainty.

Part II: Compression Effects

CHAPTER 5

A MATHEMATICAL MODEL

5.1 Objective - Part Ii

The aim of Part II in this thesis is to investigate the impact of compression effects on the performance of the WGFE ion-exchange system during scale-up.

5.2 Preamble - Part II

Part I of this thesis has indicated that increased compression of the packed bed in the WGFE ion-exchange system will occur during scale-up. This gives rise to important issue that must be considered. Would this increased compression be significant enough to alter the performance of the system? A number of studies have experimentally observed that compression can influence chromatographic efficiency (Freitag *et al.*, 1994; Sarker & Guiochon, 1995), although there are only two cases where such effects have been explicitly investigated. Both examined compression in HPLC systems (Freitag *et al.*; 1994). Compression was also artificially induced, in contrast to the WGFE ion-exchange system where compression is an artefact of the increase in column diameter. Their results have no direct relevance to this study, except that they show that compression may alter the performance of a chromatographic system.

The conventional studies described above attempted to measure compression effects on system behaviour experimentally. An experimental investigation was unfeasible in this study. An alternative approach was considered: to simulate the impact of compression effects on the WGFE ion-exchange system during scale-up with a mathematical model.

There are a number of drawbacks to this approach. A suitable model which can describe protein adsorption-desorption in a chromatographic system must be developed. The model must also be capable of describing the effect of packed-bed compression. The parameters in the model need to be estimated for the WGFE ion-exchange system. The model must then

actually be used to simulate its behaviour. This is a significant challenge. The model will inevitably consist of mathematical equations. These will need to be solved to provide the solution. A suitable numerical technique may need to be developed. It is also ideal if model prediction can be validated against experimental data which describes the real-life behaviour of the chromatographic system.

While each of these problems will be considered, the goal of this Chapter is to formulate and implement a suitable model to describe protein adsorption-desorption in a chromatographic system, and which can be successfully adapted for compression effects.

5.3 Background Art - Mathematical Models

Chromatography is a universal technique. It is employed in a wide variety of industries for separation of chemical or biochemical compounds. Common examples, besides biotechnology, include water treatment, petrochemicals and food technology. Simulation of chromatographic systems with mathematical models has been popular topic in the literature. There are numerous types of mathematical models with different complexities. An excellent review is given by Ruthven (1984). He classified models into three different categories: equilibrium theory, plate models and rate models.

Each type of model uses some form of mass balance equation as the basis to describe transmission of species through, and their adsorption-desorption in, the packed bed. The distinguishing characteristic of each category is the level of simplifying assumptions they make about transmission and adsorption-desorption mechanisms (Yu & Wang, 1989). Local equilibrium models assume the mobile and stationary phase are equilibrium. They neglect hydrodynamic dispersion, external-film mass transfer and intraparticle diffusion. Stage models divide the column up into many stages. Each stage is assumed to be independent and completely mixed. Rate-equation models solve the dynamics of mass balance equations for the combined effects of convection, dispersion, external-film mass transfer, intraparticle diffusion and adsorption-desorption. They minimise simplifying assumptions used to describe the system, and provide a complete description of species transmission and adsorption-desorption in a packed bed.

Each model type has at some time have found application to protein separation in biotechnology. Various instances can be found throughout the literature. However, rate models dominate contemporary simulation practice in chromatographic systems. There is a consensus that equilibrium theory and plate models are inappropriate for preparative and large-scale chromatographic systems (Gu, 1995). They are incapable of accurately describing external-film mass transfer and intraparticle-diffusion effects under mass-transfer limiting conditions. This phenomena is common in large-scale chromatographic systems. James (1994) has confirmed that mass-transfer limiting conditions will be encountered in the WGFE ion-exchange system. This is an important consideration. Possible effects that compression may have on transmission of species, and adsorption-desorption, in a packed bed were hypothetically examined in Section 1.5.6 - Chapter 1. Variations in external-film mass transfer and intraparticle diffusion were identified as two key concerns. Equilibrium theory and plate models will not be suitable for modelling compression effects. A rate model must be employed.

5.4 Rate Models

The are numerous types of rate model. Most conform, or are based, on a comprehensive set of mathematical equations referred to as the general non-linear multicomponent rate-equation model. This generic version has been widely presented in the literature (Gu *et al.*, 1990; Gu *et al.*, 1991; Bernhinger *et al.*, 1991; Whitley *et al.*, 1993), and successfully validated for simulation of a number of experimental chromatographic systems (Whitley *et al.*, 1993). The following is a brief description.

Consider a packed bed in a chromatographic column. It is assumed to consist of uniform homogeneous porous particles. Fluid that enters the bed travels through the interstices between the particles. The species present in the fluid are subject to axial dispersion; mass transfer to, and from, resin particles through an external film in the bulk phase; intraparticle diffusion in the particle phase; and adsorption and desorption on the particle stationary phase. The species concentration in the bulk phase are independent of radial position. Exclusion effects are not important. All processes occurring in the bed are isothermal. Species concentration at any point in the packed bed can be described by mass balances formulated, and non-dimensionalised, for bulk, particle and particle-stationary phases. These are as follows. (Please note: the reader should refer to the nomenclature for symbol

definitions. These have been omitted from the following discussion to aid clarity of presentation.)

The dimensionless governing equation for the concentration of each component in the bulk phase, c_{bi}, is (Gu *et al.*, 1990):

$$-\frac{1}{Pe_{Li}}\frac{\partial^2 c_{bi}}{\partial z^2} + \frac{\partial c_{bi}}{\partial z} + \frac{\partial c_{bi}}{\partial \tau} + \xi_i (c_{bi} - c_{pi,r=1}) = 0 \qquad (5.1a)$$

The dimensionless concentration profile in the particle phase, c_{pi}, is given by (Gu *et al.*, 1990):

$$\frac{\partial}{\partial \tau}\left[(1-\varepsilon_p)c_{pi}^s + \varepsilon_p c_{pi}\right] - \eta_i \left[\frac{1}{r^2}\frac{\partial}{\partial r}\left(r^2 \frac{\partial c_{pi}}{\partial r}\right)\right] = 0 \qquad (5.2a)$$

The dimensionless governing equation for the particle stationary-phase concentration, c_{pi}^s, using second order kinetics to describe adsorption and desorption is (Gu *et al.*, 1995):

$$\frac{\partial c_{pi}^s}{\partial \tau} = Da_i^a\, c_{pi}\left(c_i^\infty - \sum_{j=1}^{N_s}\frac{C_{oj}}{C_{oi}}\theta_{ij}c_{pj}^s\right) - Da_i^d\, c_{pi}^s \qquad (5.3a)$$

If Damköhler numbers, Da_i^a and Da_i^d, are sufficiently high (>1000), *eq.* 5.3b is commonly simplified to its equilibrium-rate equivalent, the multicomponent Langmuir isotherm (Gu, 1995):

$$c_{pi}^s = \frac{a_i\, c_{pi}}{1 + \sum_{j=1}^{N_s}(b_j C_{oj})\, c_{pj}} \qquad (5.4)$$

where $b_i C_{oi} = \dfrac{Da_i^a}{Da_i^d}$ and $a_i = b_i C_i^\infty$.

The reader should note that this simplification does involve a critical assumption. Namely, that extraneous terms, due to uneven maximum adsorption capacities in the multicomponent Langmuir isotherm, generated from the algebraic manipulation of *eq.* 5.3a can be ignored.

The boundary and initial conditions which apply to *eq.s* 5.1a, 5.2a, and 5.3a are:

$$\text{I.C.} \quad t = 0, \quad c_{bi} = c_{bi}(0,z),\ c_{pi} = c_{pi}(0,r,z)$$

$$\text{B.C.} \quad z = 0, \quad \frac{\partial c_{bi}}{\partial z} = Pe_{Li}\left(c_{bi} - \frac{C_{fi}(\tau)}{C_{oi}}\right)$$

$$z = 1, \quad \frac{\partial c_{bi}}{\partial z} = 0$$

$$r = 0, \quad \frac{\partial c_{pi}}{\partial r} = 0$$

$$r = 1, \quad \frac{\partial c_{pi}}{\partial r} = Bi_i\,(c_{bi} - c_{pi,r=1}) \qquad (5.5)$$

5.5 Accounting for Compression Effects

The general non-linear multicomponent rate-equation chromatography model assumes that the porosity, particle diameter and intraparticle porosity are constant throughout the packed bed. In a compressed bed, these will vary with axial position. The general non-linear multicomponent rate-equation chromatography model must be modified to account for compression effects. This is easily achieved. Modified analogues of *eq.s* 5.1a, 5.2a and 5.3a are, respectively:

$$-\frac{\partial\left(\frac{1}{Pe_{Li}}\frac{\partial c_{bi}}{\partial z}\right)}{\partial z} + \frac{\partial c_{bi}}{\partial z} + \frac{v_o L}{L_o v}\frac{\partial c_{bi}}{\partial \tau} + \xi_i\,(c_{bi} - c_{pi,r=1}) = 0 \qquad (5.1b)$$

$$\frac{v_o}{L_o}\frac{L}{v}\frac{\partial}{\partial \tau}\left[(1-\varepsilon_p)c^s_{pi} + \varepsilon_p c_{pi}\right] - \eta_i\left[\frac{1}{r^2}\frac{\partial}{\partial r}\left(r^2\frac{\partial c_{pi}}{\partial r}\right)\right] = 0 \qquad (5.2b)$$

$$\frac{v_o}{L_o}\frac{L}{v}\frac{\partial c^s_{pi}}{\partial \tau} = Da^a_i\, c_{pi}\left(c^\infty_i - \sum_{j=1}^{N_s}\frac{C_{oj}}{C_{oi}}\theta_{ij}c^s_{pj}\right) - Da^d_i\, c^s_{pi} \qquad (5.3b)$$

Equations 5.1b, 5.2b and 5.3b will be referred to as the adapted model. It is important to note that the adapted model is designed for steady-state conditions during compression. Variation in porosity, particle diameter and intraparticle porosity are assumed to be invariant with time.

The modifications in the adapted model from *eq.s* 5.1a, 5.2a and 5.3a are self-evident. They recognise the functional dependence of porosity, particle diameter and intraparticle porosity on axial position. Dimensionless time has also been redefined to account for the variation of interstitial velocity in the packed bed:

$$\tau = t/(L_o/v_o)$$

This maintains the chronological integrity of *eq.s* 5.1b, 5.2b and 5.3b in the compressed packed bed.

The boundary and initial conditions that apply to the adapted model are identical to those for *eq.s* 5.1a, 5.2a and 5.3a.

5.6 Key Model Parameters

The modified version of the general non-linear multicomponent rate-equation model is characterised by a number of key dimensionless groups. These are the Peclet number, Biot number, ξ_i, η_i, and the adsorption and desorption Damköhler numbers, Da_i^a and Da_i^d, respectively, for each component, i, in the system.

Before the model can be employed to simulate a chromatographic system, each dimensionless group must be specified or determined from various model parameters. These can be divided into two categories: system parameters and individual component physical and chemical parameters. System model parameters include bed height, L, porosity, ε, resin particle diameter, d_p, and superficial velocity, v_{sup}. Component model parameters include the dispersion coefficient, D_{bi}, intraparticle diffusivity, D_{pi}, intraparticle voidage (to which proteins have access), ε_{pi}, multicomponent adsorption-desorption kinetic

or equilibria data (to estimate Damköhler numbers and maximum adsorption capacity, c_i^{∞}) and external-film mass transfer coefficient, k_i.

5.7 Solving Model Equations - Numerical Strategy

To calculate effluent history and concentration profiles, the model equations in the general non-linear multicomponent rate equation model must be solved. These consist of two coupled partial differential equations (*eq.s* 5.1b & 5.2b) and an ordinary differential equation (*eq.* 5.3b). Normally, an analytical solution is unavailable and a numerical solution must be provided (Gu *et al.*, 1990).

A variety of numerical techniques have been employed to solve the general non-linear multicomponent rate-equation model (Gu *et al.*, 1990). The following summarises the numerical strategy that was used in this study. It is largely based on the numerical strategy presented by Gu *et al.* (1990), although its implementation was carried out entirely by the author. There are, however, some variations made by the author and these are included.

The partial differential equations, *eq.s* 5.1b and 5.2b, were transformed to a system of ordinary differential equations (ODEs) using the finite-element method and orthogonal collocation, respectively (Gu *et al.*, 1990).

To describe the bulk-phase concentration profiles on each finite element, second-order Lagrangian interpolation polynomials (Zienkiewicz & Morgan, 1983) were used. The Galerkian method (Zienkiewicz & Morgan, 1983) was employed to choose function weightings for integration. Ten-point Gauss-Legendre quadratures (Stroud & Secrest, 1966) provided the basis for integrations. Variation in Peclet number, Biot number, η_i, ξ_i and interstitial velocity due to variation in model parameters in each element were incorporated into bulk-phase ODEs during the transformation process.

For orthogonal collocation, the same symmetric polynomials described by Finlayson (1972) were employed. Collocation points, the roots of these polynomials, were deduced from Tables listed in Stroud & Secrest (1966). Equation 5.3b, already an ODE, did not require transformation and was directly incorporated into the bulk and particle-phase ODE system.

To deduce concentration values at the particle surface, the boundary condition, *eq.* 5.5, was transformed using the method of orthogonal collocation to an algebraic expression (Gu *et al.*, 1990). This was then manipulated to explicitly give particle-surface concentration as a function of bulk and particle-phase concentrations.

This procedure generates a N_s $(2N_c + 1)$ $(2N_e + 1)$ ODE system where N_s, N_e and N_c are the number of species, bulk-phase finite elements and internal particle-phase collocation points, respectively. Integration of the ODE system provides the moving concentration profiles in the packed bed and its effluent history. For this purpose, an implicit backward-difference formula (BDF) variable-step variable-order (VSVO) algorithm (Lambert, 1991) was employed.

The solution strategy described above was encoded in C* for the CM-5 Connection Machine (Thinking Machines Corporation, Cambridge, Massachusetts, USA) at the South Australian Centre for Parallel Computing (SACPC), University of Adelaide, Australia. The SACPC CM-5 is a 32-node connection machine with the equivalent of 1 Gigabyte distributed memory.

5.8 Numerical Strategy - Validation

To validate the numerical algorithm and executable code, model simulations were compared against similar numerical simulations published in the literature. Figure 5.1 depicts one such example. It presents model predictions for a single-component frontal adsorption based on a set of hypothetical model parameters which are summarised in Table 5.1.

The model predictions in Figure 5.1 provide an exact match to an identical numerical simulation presented by Gu (1995). A photocopy of an excerpt from Gu's study containing the table (Table 3.1, refer parameter values for Figure 3.8) outlining model parameters for, and the figure (Figure 3.8) displaying the results of, this simulation is included in Appendix 2 for comparison.

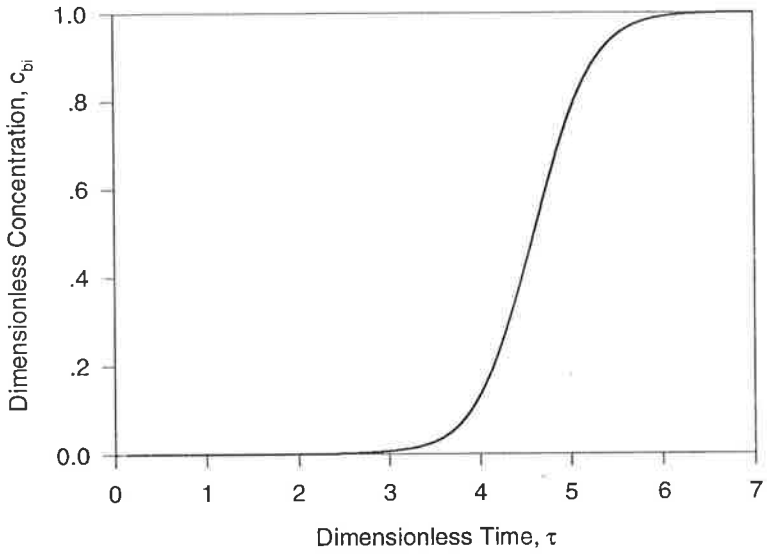

Figure 5.1: Model simulation (——) of a single-component frontal adsorption for hypothetical model parameters presented in Table 5.1.

Table 5.1: Hypothetical model parameters used for the numerical solution of the non-linear multicomponent rate-equation model presented in Figure 5.1.

Model Parameter	Value
N_s (Species)	1
N_e (Finite Elements)	4
N_c (Collocation Points)	2
Pe_{Li}	50
Bi_i	10
η_i	2
a_i	8
bxC_{oi}	7x0.2
ε_b	0.4
ε_p	0.4

5.9 Simulating Compression Effects - A Hypothetical Study

To investigate the propensity of the model to simulate compression effects, numerical simulations where carried out for three hypothetical packed bed systems. These were single-component frontal adsorption; binary-component frontal adsorption; and binary-component gradient elution with modulator.

The following outlines the general approach to simulation and details relevant empirical relationships and correlations that were employed to determine various model parameters for each system. All remaining model parameters were specified at simulation time. These were estimated from some applied guesswork to replicate the value of dimensionless groups used by Gu *et al.* (1990) in a previous simulation study.

To imitate compression in each system, a linear variation of porosity with bed length was used:

$$\varepsilon(Z) = \varepsilon_i \left(1 - 0.5\left(\frac{Z}{Z_c}\right)\right) \tag{5.6}$$

For the purposes of the study, the initial porosity at the top of the bed, ε_i, was assumed to be 0.4. It was also assumed that solid-phase volume in the bed remained constant during compression. Effects of compression on particle diameter and intraparticle diffusion were ignored. Furthermore, *eq.* 5.6 could therefore be used to directly calculate the compressed bed height for the integration domain:

$$L_i(1-\varepsilon_i) = \int_0^{Z_c} (1-\varepsilon(Z))\, dZ \tag{5.7}$$

The Peclet Number was directly calculated from a correlation presented by Chung and Wen (1965):

$$Pe_{Li} = \frac{L}{2\varepsilon R}\left(0.2 + 0.011\, Re^{0.48}\right) \tag{5.8}$$

The external-film mass transfer coefficient was determined from the correlation of Kataoka *et al.* (1973):

$$\frac{k_i}{v} = 1.85\, m^{1/3}\, Re^{-2/3}\, Sc^{-2/3} \tag{5.9}$$

Damköhler numbers were determined by comparison to multicomponent Langmuir equilibrium isotherm parameters specified for each hypothetical system, and arbitrarily set to values greater than 1000.

For frontal adsorption and isocratic elution, multicomponent equilibrium isotherm parameters a_i and b_i remain constant. However, for gradient elution, b_i varies with modulator concentration. Melander *et al.* (1989) proposed a generic relationship to describe the variation of b_i with modulator concentration:

$$\log b_i = \alpha_i - \beta_i \log C_m + \gamma_i C_m \qquad (5.10)$$

where C_m is the modulator concentration.

Equation 5.10 was employed to determine the variation in b_i with modulator concentration during simulation of the binary-component gradient elution with modulator. The following equation was employed to simulate variation in dimensionless modulator concentration, c_m:

$$c_m = \left[0.001 + 0.114\left(\tau - \tau_{imp}\right)\right] / C_{om} \qquad (5.11)$$

where C_{om} was an arbitrary modulator concentration - set to 0.2 M - to non-dimensionalise its concentration; and τ_{imp} (set equal to 0.2) was the impulse time for the feed containing the two components to be separated.

Model simulations for each system are presented in Figures 5.2, 5.3 and 5.4, respectively. Model parameters, including number of finite elements and collocation points, are summarised in Table 5.2.

Figure 5.2 depicts the breakthrough curve for a compressed bed during frontal adsorption in the single-component system. The breakthrough curve without compression (*ie* L_i = 0.4 with ε constant at 0.4) is also included for comparison.

Table 5.2: Model parameters for simulation of compression effects in three hypothetical compressed packed-bed systems.

System	Single-component frontal adsorption		Binary-component frontal adsorption		Binary component elution with modulator		
N_s (Species)	1		2		2		
N_e (Finite Elements)	30		20		12		
N_c (Collocation Points)	1		1		2		
L_i /Z_c (m/m)	0.4/0.3483		0.4/0.3483		0.4/0.3483		
ε_p	0.5		0.5		0.5		
R_p (microns)	1500		1500		1500		
Component	1	2	1	2	1	2	Modulator
D_f ($x10^9$ m^2/s)	7.2	-	7.2	7.2	7.2	7.2	720
D_p ($x10^9$ m^2/s)	1.55	-	1.55	1.55	1.55	1.55	150
a_i	2	-	2	15	2	15	-
$b \times C_{oi}$ ($M^{-1} \times M$)	4 × 0.1	-	4 × 0.1	4 x 0.1	- × 0.1	- × 0.2	-
α_i, β_i, γ_i	-	-	-	-	-3, 3, 3.2	-3, 3.5, 3.2	-

While compression of the bed induces premature breakthrough in Figure 5.2, its shape or profile appears to closely correlate the breakthrough curve without bed compression.

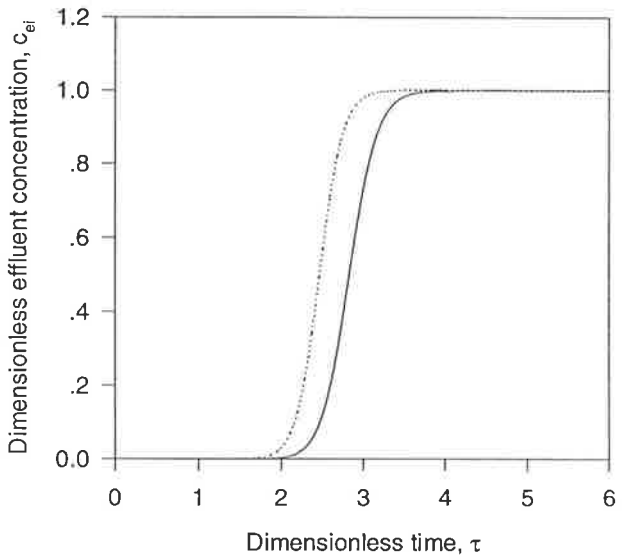

Figure 5.2: Breakthrough curves of a compressed (·····) and uncompressed bed (——) for single-component frontal adsorption in a hypothetical packed bed system.

Figure 5.3 shows the breakthrough curve for model simulation of a compressed packed bed during frontal adsorption in the binary-component system. Again, the breakthrough curve

in the absence of compression is included for comparison. In a similar manner to Figure 5.2, bed compression induces premature breakthrough, but curve profiles still closely imitate the breakthrough curves in the absence of compression.

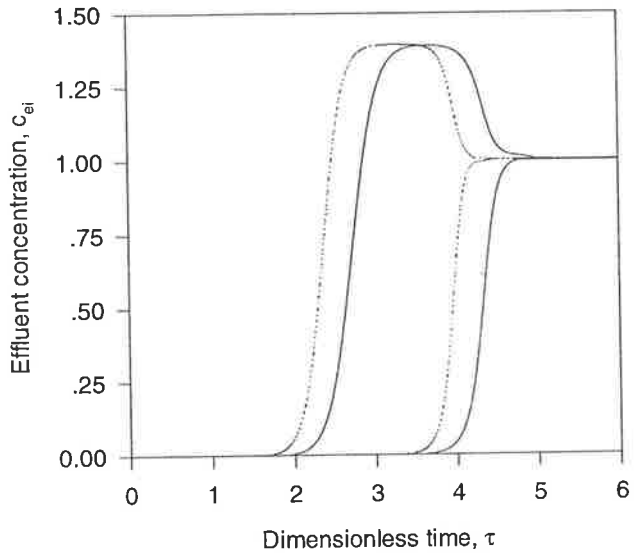

Figure 5.3: Breakthrough curves of a compressed (·····) and uncompressed bed (——) for binary-component frontal adsorption in a hypothetical packed bed system.

The breakthrough curves for a compressed packed bed system during gradient elution in a binary component system with modulator are displayed in Figure 5.4. The breakthrough curves in the absence of compression are also shown. Once more, bed compression induces premature breakthrough. This appears to result in an attenuation of, and decrease in the difference in retention time between, elution peaks. However, while curve profiles are again similar to that without bed compression, increased skew in the peaks is observed.

Figures 5.2, 5.3 and 5.4 all indicate that compression can influence system behaviour in packed bed. However, this has been a simplistic analysis. Model parameters were selected to replicate the values of dimensionless groups in another numerical study. This study was largely hypothetical. It has no realistic bearing on the large-scale chromatographic systems that may be encountered in biotechnology, or specifically, to the WGFE ion-exchange system.

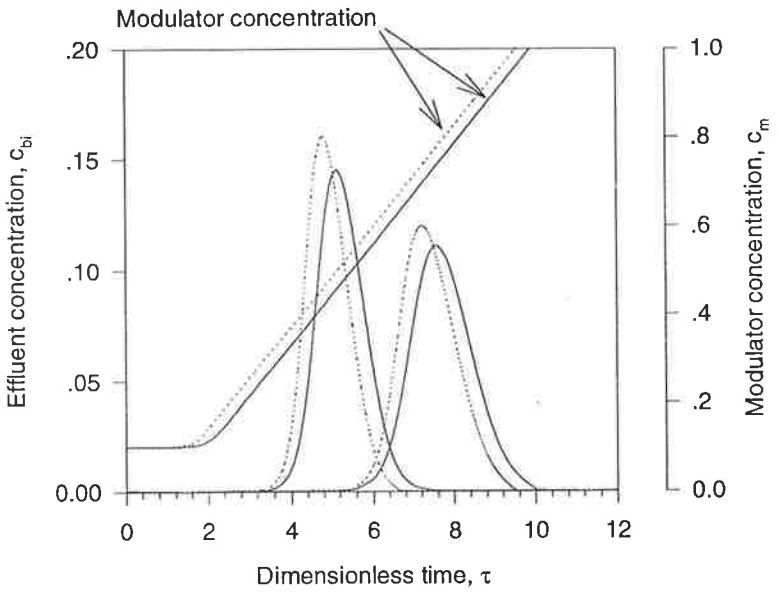

Figure 5.4: Breakthrough curves of a compressed (·····) and uncompressed (——) bed for binary-component gradient elution with modulator in a hypothetical packed bed system.

Some observations, however, may be indicative of the impact that compression could have on the WGFE ion-exchange system during scale-up. For example, the premature breakthrough was symptomatic of the decrease in fluid-phase volume experienced by a packed bed during compression. For the three hypothetical systems, this decrease was 33%. A similar decrease in species retention time, as they travel through the interstices in the bed, could be expected.

Besides this, it was difficult to discern the influence of other compression-induced effects. For example, dispersion and external-film mass transfer. Both display a functional dependence of interstitial velocity. In our hypothetical example, there was an increase in interstitial velocity of 28% from top to bottom of the compressed packed bed. One may have expected to observe some other variation.

However, this is not surprising if we closely examine the Biot and Peclet number in each system. These dimensionless groups give a relative indication of the magnitude of external-film mass transfer compared to intraparticle diffusion, and bulk-phase convection to axial dispersion, respectively. Their values in the compressed bed for the model simulations

conducted above were between 100 to 250 and 30 to 60. It has been shown that when the Biot number exceeds 20, intraparticle diffusion rather than external-film mass transfer controls the inter-phase mass transfer that takes place in a packed bed (James, 1994). Therefore, even if an increase in external-film mass transfer was present, it would be unlikely to have any great influence. Likewise, the Peclet number indicates that dispersion effects were very small compared to convection.

Clearly, the value of these dimensionless groups may be specific to the hypothetical systems analysed in this study. It would be difficult to generalise these results to other systems where this may not be the case.

5.10 Concluding Remarks

A model has been formulated to describe the impact of compression effects on system performance of the WGFE ion-exchange system. It is a modified version of the non-linear multicomponent rate-equation model and described by *eq.s* 5.1b, 5.2b and 5.3b. Key model parameters have been identified. A numerical solution has been developed and validated against a simulation from an independent study. A preliminary investigation to simulate compression effects in a hypothetical system was conducted. The results indicate that compression effects can have a significant influence on the behaviour of a chromatographic system. Unfortunately, the investigation was inconclusive. It was unclear whether the model parameters selected for each hypothetical system truly mirrored real-world systems, in particular, the high values of Peclet (~100-250) and (~30-60) Biot numbers. Intraparticle mass transfer was diffusion limited and convection dominated axial dispersion. This would have minimised the influence of compression-induced variations in dispersion and external-film mass transfer on system behaviour. The study could not be generalised to other systems where this may not be the case.

CHAPTER 6

MODEL PARAMETERS & VALIDATION

6.1 Preamble

A modified version of the non-linear multicomponent rate-equation model has been developed to describe compression in a chromatographic system. It will be used to simulate the behaviour of the WGFE ion-exchange system during scale-up. However, the model requires a knowledge of a number of model parameters. These describe the system properties and the physical and chemical properties of species present in the chromatographic system. System model parameters include bed height, L, porosity, ε, resin particle diameter, d_p, and superficial velocity, v_{sup}. Species model parameters include the dispersion coefficient, D_{bi}, intraparticle diffusivity, D_{pi}, intraparticle voidage (to which proteins have access), ε_{pi}, multicomponent adsorption-desorption kinetic or equilibria data (to estimate Damköhler numbers and maximum adsorption capacity, c_i^{∞}) and external-film mass transfer coefficient, k_i.

This chapter will present the methodology to determine the system and species model parameters for simulation of the WGFE ion-exchange system. These will be used to validate the model by comparing model-generated predictions for the WGFE ion-exchange system behaviour against experimental data. However, the reader should note that this chapter does not immediately consider compression effects and their impact on model parameters. All model simulations will be conducted for packed beds with constant porosity, particle diameter and intraparticle porosity. The problem of compression effects will be discussed subsequently in Chapter 7.

6.2 Selecting Indicator Compounds

The microfiltered whey applied during the load step, and the products generated during elution consist of a number of biological compounds. Analysis of the two fractions generated during elution at 0.4 and 1.0 M NaCl indicate that the first consists predominantly

of lactoperoxidase. Also present are a range of immunoglobulins, lactoglobulins and the growth factors which provide the WGFE with its biological activity (Francis *et al.*, 1995). The second fraction consists mainly of lactoferrin.

It would be ideal if we could investigate the behaviour of all biological compounds that participate in the WGFE ion-exchange system. Model parameters necessary for each compound would be determined. Counting α- and β- lactoglobulin, lactoperoxidase, lactoferrin and IgA, IgG, IgM, IgD and IgE makes at least nine such constituents at a glance. Of the growth factors, there are probably between ten to twenty different types. For example, epidermal growth factor, insulin-like growth factor I, insulin-like growth factor II and transforming growth factor-β are known to be present.

It is clearly not practical to simulate the behaviour of every compound present in microfiltered whey, in particular, from a numerical point of view. It is also not necessary. A similar study by James (1994) also attempted to use a general multicomponent rate-equation model to simulate the behaviour of adsorption and desorption of whey on Sepharose Big-Beads SP. It was unsuccessful. The reason for this, and the results of James's study will be discussed later in this chapter. However, James restricted the participating species during the study to lactoperoxidase and lactoferrin. This assumption provided an excellent simplification of problem. While other compounds are present, lactoperoxidase and lactoferrin quantitatively dominate the adsorption-desorption behaviour in the WGFE ion-exchange system. In fact, a lactoperoxidase enzyme assay is used in the pilot-plant of the WGFE system to identify breakthrough during frontal adsorption. It is also used to monitor elution of the WGFE product and predict product yield.

A similar approach will be employed in this study. Lactoperoxidase and lactoferrin will be used as indicator compounds to examine the impact of compression effects on the performance of the WGFE ion-exchange system. An added benefit of tackling the problem in this manner is that a number of model parameters required in the general non-linear multicomponent rate-equation chromatography model for each protein have already been experimentally determined by James (1994). These include the intraparticle-diffusion coefficient, and the multicomponent Langmuir and single-component extended Langmuir-Freundlich equilibrium isotherm parameters.

6.3 System Model Parameters

Except for ε and d_p, all other system model parameters, namely, v_{sup} and L, were arbitrarily specified by the author at simulation time.

6.3.1 Bed Porosity

The porosity in a packed bed of Sepharose Big-Beads SP has already been experimentally measured in Chapter 3. A value for porosity between 0.36 to 0.4 was obtained. A value for porosity was also determined from $\chi(\tau^{s}_{zz})$ in Chapter 4. Its value was 0.38. A study by Skidmore *et al.* (1990) calculated the porosity in a similar 6% cross-linked agarose resin: Sepharose Fast-Flow S, as 0.35. This value was used by James (1994) to simulate the behaviour of lactoperoxidase and lactoferrin in Sepharose Big-Beads SP.

A value of 0.356 was nominally used for porosity during model simulations in this Chapter.

6.3.2 Particle Diameter

The particle diameter for Sepharose Big-Beads SP has already been experimentally measured in Chapter 3. Particle-size analyses were performed and the volume-mean particle diameter of resin particles was determined for various solvent conditions. An average value of 151 μm for volume-mean particle diameter was used in Chapter 4 to generate an initial estimate of $\chi(\tau^{s}_{zz})$. However, the mean particle dimension most appropriate in systems where external-film mass transfer is important is the Sauter-mean particle diameter (Foust *et al.*, 1980). This is the case for adsorption and desorption processes in packed beds (Foust *et al.*, 1980). Sauter-mean particle diameter was determined from particle-size analyses of Sepharose Big-Beads SP in Chapter 3. An average value of approximately 167 μm was selected for model simulations in this chapter.

6.4 Species Model Parameters

There are three separate species that will be present during simulation of the WGFE ion-exchange system. The two indicator compounds: lactoperoxidase and lactoferrin, and salt. This section outlines the species model parameters for each of these compounds.

6.4.1 Intraparticle-Diffusion Coefficient

James (1994) has determined the intraparticle-diffusion coefficient for lactoperoxidase and lactoferrin during adsorption and desorption under a number of experimental conditions. A sequence of batch adsorption experiments in 50 mM sodium citrate buffer at 20°C for different pH values and varying salt concentration was employed. For the purposes of this study, it will be assumed that the pH of microfiltered whey, deionised water and eluents employed in the commercial-scale WGFE ion-exchange system are all approximately 6.5. Adsorption intraparticle-diffusion coefficients for each protein at this pH are shown in Table 6.1. These will be used to describe intraparticle diffusion during frontal adsorption and wash cycles in the WGFE ion-exchange system.

Table 6.1: Intraparticle diffusivity parameters for lactoperoxidase and lactoferrin during adsorption at 0 M sodium chloride and desorption in 0.4 and 1.0 M sodium chloride (James, 1994).

	$D_{pi} \times 10^{11}$ (m^2/s)		
	0 M NaCl	0.4 M NaCl	1.0 M NaCl
Lactoferrin	0.6	6.5	6.5
Lactoperoxidase	1.5	6.5	6.5

Desorption intraparticle-diffusion coefficients for each protein in the presence of 0.4 and 1.0 M sodium chloride are also presented in Table 6.1. These will be used to describe intraparticle diffusion during the 0.4 and 1.0 M step elutions, respectively.

James (1994) also provides a value of 3.8×10^{-10} m^2/s for the intraparticle diffusivity of salt. This value will be employed for simulation during all steps of the WGFE ion-exchange cycle.

6.4.2 Intraparticle Voidage

Intraparticle voidage is the fraction of solid-phase volume in a resin particle which a protein can access. This value is different to the actual internal voidage of a chromatographic resin, which for a 6% cross-linked agarose resin like Sepharose Big-Beads SP, is 0.94.

There are no published experimental values of intraparticle-voidage values for lactoperoxidase and lactoferrin in Sepharose Big-Beads SP. James (1994) in his study used a value of 0.5 extrapolated from previous data by Chase (1990). This value will be employed for this study. For simplicity, it will also be employed to represent the intraparticle voidage of salt.

6.4.3 Damköhler Numbers and Adsorption Capacity

Damköhler numbers, Da_i^a and Da_i^d, and adsorption capacity, C_i^∞ for lactoperoxidase and lactoferrin were determined from equilibria data presented by James (1994).

Multicomponent Langmuir equilibrium parameters for lactoperoxidase and lactoferrin are summarised in Table 6.2. They were experimentally determined using batch adsorption experiments under progressively increasing concentrations of 1:1 solutions of each protein.

Table 6.2: Multicomponent Langmuir and single-component extended Langmuir-Freundlich equilibrium parameters.

	Single-component extended Langmuir-Freundlich equilibrium parameters				
	C_i^∞ (moles/m^3)	b_{pi} ($M^{-\eta_p}$)	η_p	b_{si} ($M^{-\eta_s}$)	η_s
Lactoperoxidase	1.577×10^{-3}	6.6×10^{4}	1.0	6.6×10^{2}	0.38
Lactoferrin	1.8722×10^{-3}	2.1×10^{5}	1.0	3.1×10^{2}	0.33
	Multicomponent Langmuir equilibrium parameters				
	C_i^∞ (moles/m^3)	b (M)			
Lactoperoxidase	1.577×10^{-3}	4.0×10^{5}			
Lactoferrin	1.8722×10^{-3}	1.0×10^{7}			

Multicomponent Langmuir isotherms determined from parameters in Table 6.3 compared to experimental multicomponent equilibria data (James, 1994) are shown in Figure 6.1.

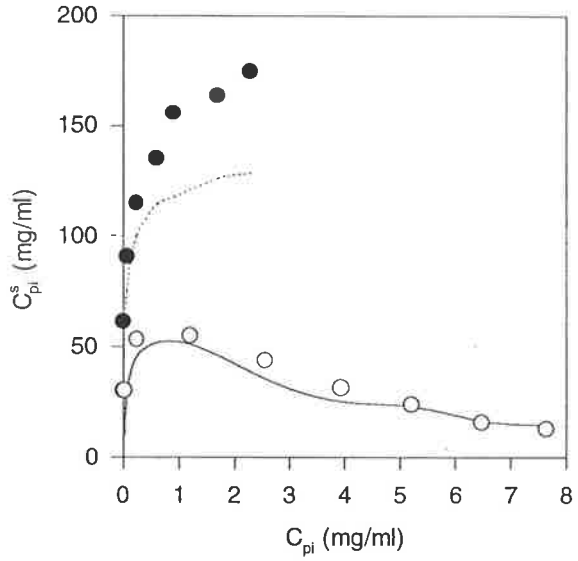

Figure 6.1: Multicomponent equilibria data (James, 1994) for lactoperoxidase (○) and lactoferrin (●) with multicomponent Langmuir isotherms for lactoperoxidase (——) and lactoferrin (·····).

Damköhler numbers and adsorption capacity can be determined for each protein from the multicomponent Langmuir isotherm, *eq.* 5.4, by comparing it to *eq.* 5.3b at equilibrium conditions. b_i only provides the ratio of Da_i^a to Da_i^d, and values for Damköhler numbers were arbitrarily selected to ensure they exceeded 1000.

Damköhler numbers and adsorption capacity determined from multicomponent Langmuir isotherm will be employed to describe adsorption-desorption equilibria for frontal adsorption and wash steps.

The single-component extended Langmuir-Freundlich equilibrium parameters for each protein are also included in Table 6.2. Again, James (1994) determined isotherm parameters by batch adsorption experiments in 50 mM citrate buffer at pH 6.5 using sets of progressively increasing concentrations of each protein in the presence of varying salt concentration. Single-component extended Langmuir-Freundlich isotherms determined from these parameters compared to experimental single-component equilibria (James, 1994) at 0 and 0.4 M for lactoperoxidase, and 0 and 0.6 M for lactoferrin, are shown in Figure 6.2.

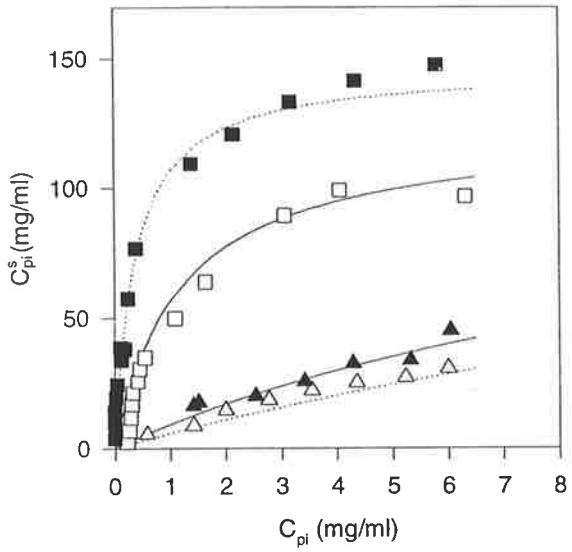

Figure 6.2: Single-component equilibria data (James, 1994) for lactoperoxidase, 0 M (□) and 0.2 M (△) NaCl, and lactoferrin, 0 M (■) and 0.6 M (▲) NaCl, with single-component extended Langmuir-Freundlich isotherms for lactoperoxidase (——) and lactoferrin (·····).

Damköhler numbers and adsorption capacity can be determined from the single-component extended Langmuir-Freundlich isotherm by considering its multicomponent version:

$$c^s_{pi} = \frac{a^*_i \, c_{pi}^{\,1/\eta_{pi}} \left(C_{oi}^{(1/\eta_{pi})-1} \right)}{1 + \sum_{j=1}^{N_s} \left(b^*_j \, C_{oj}^{\,1/\eta_{pi}} \right) c_{pj}^{\,1/\eta_{pi}}} \qquad (6.1)$$

where $a^*_i = b^*_i \; C^\infty_i$ and $b^*_i = \frac{b_{pi}}{1 + b_s \, C_s^{\,1/\eta_{si}}}$.

From Table 6.2, η_{pi} for lactoperoxidase and lactoferrin equal to 1. Equation 6.1 effectively reduces to the multicomponent Langmuir isotherm with b_i equivalent to b^*_i. Single-component b_{pi}, b_s and η_s and salt concentration, C_s, can be used to determine b_i, and therefore, Damköhler numbers. (Again, values were arbitrarily selected to ensure they exceeded 1000.) Similarly, adsorption capacity can also be determined from a^*_i.

Damköhler numbers and adsorption capacity determined from the single-component extended Langmuir-Freundlich isotherm will be employed to describe adsorption-desorption equilibria for frontal adsorption, wash and elution steps during the WGFE ion-exchange cycle.

To simulate the behaviour of salt, it was assumed that the number of sodium ions adsorbed or displaced on the ion-exchange resin during protein adsorption-desorption was small compared to the protein. It was therefore also assumed that these ions did not adsorb or interact with the ion-exchange surface. (Their adsorption or release was implied empirically by the multicomponent Langmuir and single-component extended Langmuir-Freundlich isotherms (James, 1994)). Damköhler numbers and adsorption capacity for salt will be set to a value of zero for all model simulations.

The reader should note that maximum adsorption capacities for each protein in Table 6.2 are based on a total settled-particle volume basis. The maximum adsorption capacity in the adapted model is defined on a total stationary-phase volume basis. Adsorption capacity was converted from total settled-particle volume to total stationary-phase volume basis using the values already given for intraparticle voidage and interparticle porosity. The results are summarised in Table 6.3.

Table 6.3: Maximum (experimental) adsorption capacities for lactoperoxidase and lactoferrin on a total stationary-phase basis (TSPB).

	C_i^{∞} (moles/m^3)
Lactoferrin	8.86×10^{-3}
Lactoperoxidase	10.52×10^{-3}

6.4.4 Dispersion Coefficient

Dispersion coefficients for lactoperoxidase and lactoferrin are not available in the literature. Instead, Peclet number for each protein was estimated from the empirical correlation by Chung and Wen (1965). This has already been presented in Chapter 5 (*eq.* 5.8). This correlation was also used to determine the salt Peclet number.

6.4.5 External-Film Mass Transfer Coefficient

External-film mass transfer coefficients for lactoperoxidase and lactoferrin have not been published. For the purpose of this study, these were estimated from a correlation (*eq.* 5.9) by Kataoka *et al.* (1973). Similarly, the correlation of Kataoka *et al.* (1973) was also used to determine the external-film mass transfer coefficient of salt.

In order to estimate the Schmidt number in *eq.* 5.9, the bulk-phase diffusivities, D_f, of each protein and salt were required. For lactoperoxidase and lactoferrin the bulk-phase diffusivity was estimated from the following semi-empirical equation (Polson, 1950):

$$D_f = 9.4 \times 10^{-11} \frac{T}{\mu (MW)^{1/3}} \qquad (6.2)$$

Using a molecular weight, MW, of 78,000 (James, 1994), both proteins have a diffusivity of 6.5×10^{-11} m^2/s in water (at 20°C).

James (1994) provides a value for the bulk-phase diffusivity of sodium ions. It equals 1.33×10^{-9} m^2/s.

6.5 Model Validation

6.5.1 Experimental Data

To validate the model and its parameters, simulation results were compared with experimental data measured by James (1994). The data provide a number of experimental binary-component frontal adsorption and step-elution breakthrough curves for lactoperoxidase and lactoferrin on Sepharose Big-Beads SP at a pH of 6.5. It was collected using a 1 cm internal diameter laboratory column. The packed-bed height was 1.3 cm. Purified lactoperoxidase and lactoferrin were used. Feed solutions consisted of 50 mM citrate buffer at a pH of 6.5 plus protein. The concentration of each protein in feed solutions applied to the column was 0.1 mg/ml. Column temperature was maintained at 20°C. Two different feed flowrates, 1.3 and 4.3 ml/min, were investigated.

Figure 6.3 shows the experimental data collected for frontal adsorption of lactoperoxidase and lactoferrin at a feed flowrate of 1.3 ml/min (a superficial velocity through the column of 1.66 cm/min) and at a pH of 6.5.

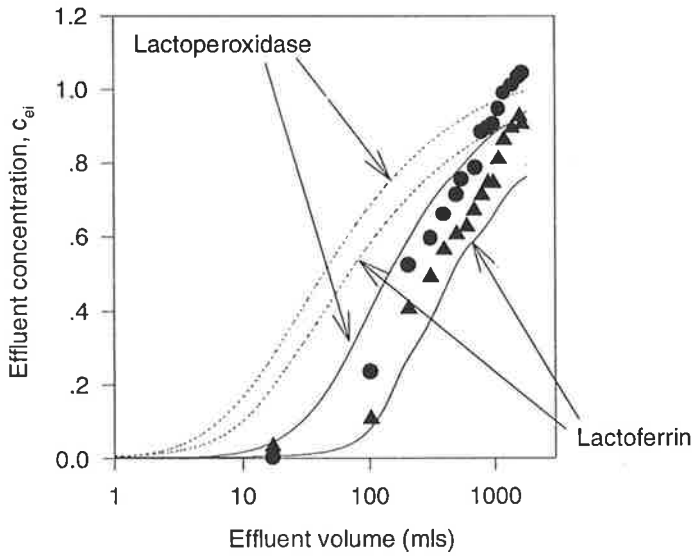

Figure 6.3: Experimental binary-component frontal-adsorption data (James, 1994) for lactoperoxidase (●) and lactoferrin (▲) *vs.* model predictions using single-component extended Langmuir-Freundlich isotherms (·····) and multicomponent Langmuir isotherms (——).

Figure 6.4 shows experimental data collected for the step-elutions at 0.4 and 1.0 M NaCl with an eluent flowrate of 1.3 ml/min and pH of 6.5. Prior to step-elution, the column was loaded with 250 ml of feed solution (as described above) and washed with two column volumes of 50 mM citrate buffer at a pH of 6.5. The two step-elutions were then performed. The first with 13 ml of 0.4 M salt in 50 mM citrate buffer. The second with 11 ml of 1.0 M salt in 50 mM citrate buffer.

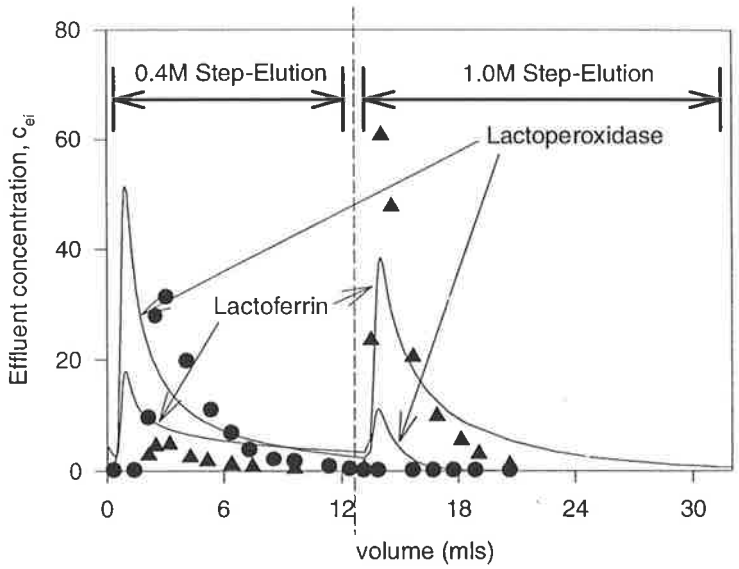

Figure 6.4: Experimental binary-component step-elution data (James, 1994) for lactoperoxidase (●) and lactoferrin (▲) *vs.* model predictions using single-component extended Langmuir-Freundlich isotherms (——).

6.5.2 Optimal Numerical Parameters

The optimal numerical parameters for solution of the general non-linear multicomponent rate-equation chromatography model with the experimental system were selected. Single-component frontal-adsorption simulations with lactoferrin were performed. Different combinations of bulk-phase finite elements and particle-phase collocation points were evaluated. Model parameters were specified at experimental frontal-adsorption conditions. The feed concentration of lactoferrin was 0.1 mg/ml. Water (at 20°C) was used to estimate physical properties of the feed solution. Multicomponent Langmuir isotherm parameters for lactoferrin were used to replicate single-component lactoferrin adsorption equilibria. Compression effects were not considered and porosity in the packed bed fixed at a value of 0.356. Table 6.3 summarises the model parameters and finite-element and collocation-point combinations employed in each simulation. Figure 6.5 displays the frontal adsorption breakthrough curves for all simulations.

Table 6.4: Important model parameters and values of key dimensionless groups employed for selection of optimal numerical parameters.

Numerical Parameters			System		Component	
Refer Figure 6.5	**N_e**	**N_c**	**v**	4.66 cm/min	**C_f**	1.282×10^{-6} M
1(a)	10	2	**L**	0.013 m	**C_o**	1.282×10^{-6} M
1(b)	10	3	**ε**	0.356	**Pe**	44.3
1(c)	10	5	**ε_p**	0.5	**Bi**	412.3
1(d)	10	8	**R_p**	83.5 μm	**η**	0.007
1(e)	10	11	**Re**	0.046	**ξ**	16.1
1(f)	10	13			**Da[a]**	12820
1(g)	20	13			**Da[d]**	1000

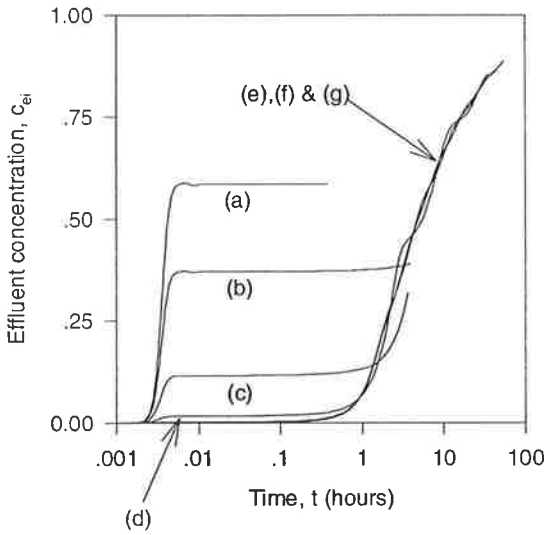

Figure 6.5: Model predictions (——) using different combinations of numerical parameters: (a)-N_e=10, N_c=2; (b)-N_e=10, N_c=3; (c)-N_e=10, N_c=5; (d)-N_e=10, N_c=8; (e)-N_e=10, N_c=11; (f)-N_e=10, N_c=13; (g)-N_e=20, N_c=13.

Ten finite elements were required to describe bulk-phase concentration profiles. However, a large number of collocation points (≥ 11) are necessary to accurately approximate particle and stationary-phase concentration profiles. This unusually high compared to reported values used in the literature, where no more than 5 collocation points are normally employed, but reflects the high affinity of lactoferrin for Sepharose Big-Beads SP. Its high adsorption capacity (almost three orders of magnitude greater than the feed concentration) and large b_i mean that when lactoferrin enters a resin particle from the bulk phase it is almost instantaneously adsorbed. This rapid adsorption continues until the highest stationary-phase concentration that can be attained on the internal resin surface is nearly

reached. While this takes place, lactoferrin effectively does not travel beyond this point into the interior of the particle. A steep concentration gradient defining a boundary between resin with adsorbed protein and resin free of protein is created. As protein adsorbing on the resin finally approaches its maximum adsorption capacity, this boundary proceeds into the interior of the particle like a wave until resin particle-adsorption capacity is exhausted.

This behaviour is graphically illustrated in Figure 6.6 which displays the chronological development of numerical particle- and stationary-phase concentration profiles during a frontal-adsorption simulation with ten finite elements and thirteen collocation points. The resin particle from which concentration profiles were captured was located at the top (Z = 0 cm) of the bed.

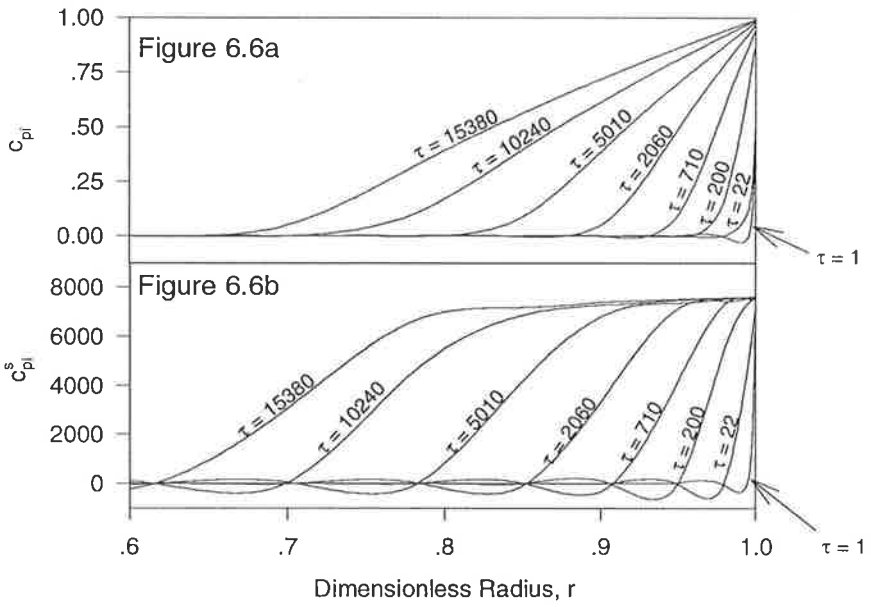

Figure 6.6: Model predictions (Z=0 cm) of particle- (Figure 6.6a) and stationary-phase (Figure 6.6b) concentration profiles, respectively (N_e=10 and N_c=13).

There are no published reports that indicate that these types of steep internal particle-and stationary-phase concentration profiles are present during protein adsorption in chromatography. This is perhaps a reflection of the rudimentary hypothetical and experimental systems employed in previous studies where mathematical models have been used to simulate chromatographic processes. The model compounds or species have been typically low in molecular weight (< 1,000) with simplistic structures, and thus, unlikely to induce strong adsorption characteristics. These are quite opposite, however, to the

complex high molecular weight bio-molecules that are encountered in real-life bio-pharmaceutical chromatographic processes. In these systems, the strong and irreversible adsorption observed in Figure 6.6 will probably be common. The selection of an appropriate number of collocation points will be essential if simulation with a general non-linear multicomponent rate-equation model is being considered.

An important observation about the adsorption behaviour of lactoferrin on Sepharose Big-Beads SP can be made by comparing Figures 6.5 and 6.6. While the effluent concentration at the end of the simulation (τ ~ 15,000) in Figure 6.5 exceeds 0.85, corresponding stationary-phase particle concentration profiles in Figure 6.6 indicate that only 60 to 70 % of the available resin-particle adsorption capacity has been utilised. Further examination reveals that at breakthrough this value was less than 5%. Clearly, particle-adsorption capacity utilisation for either case would have been less for resin particles deeper in the bed. This is not ideal. Breakthrough, which is normally the termination step in any frontal adsorption process, should be accompanied by high levels of particle-adsorption capacity utilisation in the bed.

This observation reflects the inter-phase mass-transfer dynamics in the single-component frontal adsorption system. Consider a lactoferrin molecule in the bulk-phase adjacent to a resin particle. For adsorption to occur, three separate processes must occur. First, it must travel across the external film which surrounds the particle to its surface. Second, it must diffuse through the particles internal pores into its interior to an available ion-exchange group. Third, adsorption on the functional group must occur. The relative rates of these processes are markedly different. Protein adsorption, the third process, is always much faster than external-film mass transfer or intraparticle diffusion. Additionally, the Biot number is 412. As mentioned in Chapter 5, when the Biot number (*ie* ratio of convection to intraparticle diffusion) exceeds 20, intraparticle diffusion, rather than external-film mass transfer, will control inter-phase mass transfer. Intraparticle diffusion limits the lactoferrin uptake from the bulk-phase, and therefore, the total protein adsorption rate in resin particle within the packed bed during frontal adsorption.

This explains the extended and shallow breakthrough curve observed in Figure 6.5. Developing particle-phase concentration profiles in Figure 6.6, which determine the rate of intraparticle diffusion, lead to a rapid decrease in inter-phase mass transfer, and therefore,

lactoferrin uptake by resin particles. This induces early breakthrough. The decline in inter-phase mass transfer continues as particle-phase concentration profiles mature. Subsequent curve development proceeds slowly as lactoferrin uptake continues to diminish and the remaining particle-adsorption capacity is gradually utilised.

6.5.3 Model Validation - Frontal Adsorption

Two simulations to validate model parameters against frontal-adsorption experimental data were conducted. The first employed single-component extended Langmuir-Freundlich isotherm parameters for each protein to characterise their binary-adsorption behaviour on Sepharose Big-Beads SP. The second used multicomponent Langmuir isotherm parameters. For each simulation, model parameters were determined for the experimental conditions described, except the physical properties of the feed solution, for which water at 20°C was used. Compression effects were also excluded with porosity in the packed bed fixed at 0.356. Ten finite elements and thirteen collocation points were used. Table 6.4 summarises important model parameters and values of key dimensionless groups for each simulation.

Table 6.5: Important model parameters and values of key dimensionless groups employed for the binary-component frontal-adsorption simulation with lactoperoxidase and lactoferrin.

System		Component		
v	4.66 cm/min		**Lactoferrin**	**Lactoperoxidase**
L	0.013 m	C_f	1.282×10^{-6} M	1.282×10^{-6} M
ε	0.356	C_o	1.282×10^{-6} M	1.282×10^{-6} M
ε_p	0.5	**Pe**	44.3	44.3
R_p	83.5 μm	**Bi**	412.3	164.9
Re	0.046	η	0.007	0.018
		ξ	16.1	16.1
		$Da^{a,1}$	1000	1000
		$Da^{d,1}$	3714	11820
		$Da^{a,2}$	12820	1000
		$Da^{d,2}$	1000	1950

1 Damköhler numbers based on single-component extended Langmuir-Freundlich equilibrium isotherms for each protein.

2 Damköhler numbers based on multicomponent Langmuir equilibrium isotherms for each protein.

Predicted frontal-adsorption breakthrough curves are compared with experimental data in Figure 6.3. Whilst the multicomponent Langmuir isotherm parameters provide a reasonable fit to experimental frontal adsorption data, the single-component extended Langmuir-Freundlich isotherm parameters do not. Single component extended Langmuir-Freundlich isotherms predict much earlier breakthrough. Premature development of effluent concentration profiles for each protein also indicate a much lower predicted packed-bed adsorption capacity. Predictions using multicomponent Langmuir isotherms provide superior agreement. Breakthrough points for each protein occur at almost the same point, and development of effluent concentration profiles closely follow experimental frontal-adsorption curves.

From these observations, it could be concluded that single-component adsorption isotherm parameters inadequately describe multicomponent equilibria. However, to explain the difference in model predictions between multicomponent Langmuir and single-component extended Langmuir-Freundlich parameters, the experimental multicomponent and single-component equilibria data upon which they were based (Figures 6.1 and 6.2) need to be re-examined. It can be clearly observed that multicomponent and single-component equilibria data are not consistent. Significant discrepancies exist between measured stationary-phase concentrations at low particle-phase concentrations (less than 1.0 mg/ml). Multicomponent equilibria display much stronger adsorption of both proteins than single-component equilibria. Intuitively, it would be expected that competing adsorption in a multicomponent system would lead to weaker adsorption and lower stationary-phase concentrations of participating proteins. James (1994) recognised this in his study and devoted significant discussion to its possible causes.

He proposed that the inconsistency was principally the result of different measurement techniques for protein concentration in equilibrated protein solutions. For multicomponent data, protein concentration was determined by high-performance liquid chromatography (HPLC). Protein concentration in single-component equilibrated protein solutions was measured directly by absorbance at 280 nm. James (1994) suggested non-binding, denatured or contaminating proteins may have been present with lactoperoxidase or lactoferrin in experimental equilibrated protein solutions. For direct absorbance measurement, this would contribute to the measured absorbance and suggest higher

concentrations of lactoperoxidase or lactoferrin than actually present. HPLC excludes these mitigating proteins. Consequently, experimentally measured protein concentrations for single-component adsorption equilibria were overestimated. Whether this is a plausible explanation is unknown. James (1994) suggested a number of other possible explanations for the inconsistencies between single- and multi-component equilibria data. They included protein-protein interactions and non-competitive adsorption.

James (1994) also performed simulations to validate model parameters against experimental frontal adsorption data using a general multicomponent rate-equation chromatography model. The model was similar to that described in this study, however, *eq.* 5.3b was not employed to describe protein adsorption-desorption. Adsorption-desorption equilibria were calculated directly from empirical multicomponent Langmuir isotherms. Furthermore, orthogonal collocation on finite elements instead of the Galerkian method was used to approximate bulk-phase concentration profiles.

Unfortunately, model predictions in James's study could not be reconciled with experimental data. Model predictions for both proteins were almost always characterised by instantaneous breakthrough from the packed bed. Subsequent development of concentration profiles provided poor agreement with experimental data. The discrepancy between model predictions and experimental data was attributed by James to the presence of convective flow through resin particles. Convective flow would increase the effective intraparticle-diffusion coefficient of proteins in the resin particle. According to the boundary condition, *eq.* 5.5 in Chapter 5, which describes the surface-particle flux, this would enhance net mass transfer between bulk and particle phases delaying the onset of premature breakthrough. Increased values of intraparticle-diffusion coefficient were employed in an attempt to reconcile model predictions to experimental data, but with little success.

However, James only used two internal collocation points to describe particle-phase concentration profiles in his study. As already demonstrated, this is inadequate to accurately approximate the steep particle concentration profiles occurring in resin particles for this system. Model predictions of particle-phase concentration profiles with low numbers of collocation points underestimate the particle-surface flux. This decreases the predicted net mass transfer between the bulk and particle phases and leads to the premature

breakthrough observed by James (1994). In fact, the breakthrough curve for the single-component frontal-adsorption simulation displayed in Figure 6.5 with two collocation points displays a remarkable similarity to model predictions presented by James (1994).

The discrepancies between single- and multi-component equilibria data may have corrupted adsorption and desorption intraparticle-diffusion coefficients determined by James (1994). Values for these parameters were calculated from dynamic batch adsorption-desorption experiments. Protein-free Sepharose Big-Beads SP resin was immersed in single-component protein solutions and the change in protein concentration measured. Results were compared to the numerical solution of a macropore-surface and micropore-diffusion model describing external-film mass transfer, intraparticle diffusion and protein adsorption-desorption. Intraparticle-diffusion coefficients were estimated by fitting the model solution to experimental results. To characterise protein adsorption-desorption in the model, single-component extended Langmuir-Freundlich isotherms were employed. Clearly, any flaw in the model description of adsorption equilibria would affect values selected for intraparticle-diffusion coefficients. Furthermore, numerical solution of the model employed the method of orthogonal collocation to approximate particle-phase concentration profiles. In his study, James (1994) does not reveal the number of collocation points used. If a similar number of collocation points as employed in general multicomponent rate-equation chromatography model simulations (described above) were used, an incorrect numerical solution may have been obtained.

However, James (1994) validated single-component adsorption and desorption intraparticle-diffusion coefficients by performing batch binary adsorption-desorption experiments. These were compared to model predictions of binary-adsorption behaviour using single-component adsorption and desorption intraparticle-diffusion coefficients. Multicomponent Langmuir isotherm parameters were employed to describe binary-adsorption equilibria. Single-component extended Langmuir-Freundlich isotherm parameters were used to describe binary-desorption equilibria for model predictions of batch desorption experiments. In most cases, model predictions gave good agreement with experimental data.

Regardless, it is obvious that multicomponent Langmuir isotherms provide a superior description of experimental frontal-adsorption data. However, this description is also imperfect. Model predictions indicate the lactoferrin effluent concentration profile develops

much later than observed experimentally. Multicomponent isotherm parameters over-estimate the adsorption capacity of lactoferrin, although this may have been due to errors in intraparticle-diffusion coefficients as discussed above. Multicomponent Langmuir isotherm parameters also appear to be unable to accurately describe binary-adsorption equilibria for lactoferrin and lactoperoxidase. The multicomponent equilibria data estimated by James (1994) were based on a single experimental data set. This set was determined from increasing concentrations of 1:1 protein solutions. Multicomponent Langmuir isotherm parameters estimated from this data set may not accurately describe adsorption equilibria at disproportionate protein concentrations which occur during frontal adsorption in the packed bed. Furthermore, a low protein concentration of 0.1 mg/ml was used in the feed solution to obtain experimental frontal adsorption data. This represents the concentration range where the highest initial slopes of protein adsorption exist. Clearly, experimental data will exhibit the highest sensitivity to experimental error in this region. Multicomponent Langmuir isotherms will also display the greatest sensitivity to isotherm parameters selected to replicate experimental data.

The discrepancies in single- and multi-component isotherm model predictions of experimental frontal-adsorption data emphasise an important point. Accurate information describing adsorption equilibria are necessary to ensure successful reconciliation of the model and its parameters with reality.

It is also interesting to note the Biot number of lactoperoxidase in Table 6.4. It is 165. In a similar manner to lactoferrin, lactoperoxidase uptake during frontal adsorption in the experimental WGFE ion-exchange system is controlled by intraparticle diffusion. Despite being a binary-component system, both proteins display the early breakthrough and extended breakthrough curve development which was observed in the single-component lactoferrin simulations of Section 6.5.

The frontal-adsorption behaviour in the binary-component system display a common phenomena referred to as roll-up. The exit concentration of lactoperoxidase, which emerges in the effluent from the packed bed before lactoferrin, rises to a value which exceeds its feed concentration. This is the result of a displacement effect. The phenomena was well explained by James (1994). Initially, a concentration front of weaker binding (but faster intraparticle diffusion) lactoperoxidase, proceeds into the packed bed more quickly

than the concentration front of stronger binding (but slower intraparticle diffusion) lactoferrin. However, as the lactoferrin concentration front catches up, it displaces the adsorbed lactoperoxidase. This 'free' lactoperoxidase is pushed down in front of the lactoferrin concentration front as it continues to proceed into the bed. As more lactoperoxidase is pushed down the column, its local concentration rises, exceeding its feed value.

6.5.4 Model Validation - Step Elution

A simulation to validate model predictions to experimental step-elution data was conducted. Without multicomponent isotherms to describe binary-desorption equilibria (during elution), single-component extended Langmuir-Freundlich isotherm parameters for each protein were employed. However, multicomponent Langmuir isotherm parameters were retained to describe adsorption equilibria during frontal adsorption and wash steps. Feed concentration profiles and duration of feed, wash and elution steps used to obtain experimental step-elution data were replicated. Model parameters for each step were determined from experimental conditions described. Physical properties of all feed solutions were estimated from water at 20^{o}C. Compression effects were excluded with porosity in the packed bed set to a constant value of 0.356. Ten finite elements and eleven collocation points were used. Important component model parameters and values of key dimensionless groups during each elution step for the simulation are summarised in Table 6.5. (Model parameters during frontal adsorption and wash steps were identical to frontal-adsorption model parameters displayed in Table 6.4.)

Figure 6.4 compares model predictions of step-elution concentration profiles for each protein with experimental data. Surprisingly, it indicates that single-component extended Langmuir-Freundlich isotherm parameters provide an excellent description of binary-desorption equilibria. The position of the major elution peak for lactoferrin during the 1.0 M step-elution corresponds exactly with experimental data, although, predicted peak height is lower. However, the model now predicts the presence of a small minor lactoperoxidase peak co-eluting with major lactoferrin elution peak at 1.0 M. During the 0.4 M step-elution, the model predicts earlier breakthrough and peak development for the major lactoperoxidase and minor lactoferrin peaks. The major lactoperoxidase and minor

lactoferrin peaks are also larger in peak height and area than their experimental counterparts.

Table 6.6: Important model parameters and values of key dimensionless groups employed for binary-component step-elution simulations with lactoperoxidase and lactoferrin.

Component Model Parameters		
	Lactoferrin	**Lactoperoxidase**
C_f	0 M	0M
C_o	1.282×10^{-6} M	1.282×10^{-6} M
Pe	44.3	44.3
Bi	38.1	38.1
η	0.078	0.078
ξ	16.1	16.1
Da^a, 0.4M[1]	1000	1000
Da^d, 0.4M[1]	75400	7.11×10^5
Da^a, 1.0M[1]	1000	1000
Da^d, 1.0M[1]	1.16×10^6	7.8×10^6

[1] Damköhler numbers for each protein at 0.4 and 1.0 M salt concentration. These values are not constant during model simulations, but vary with salt concentration in the packed bed.

The discrepancies between model predictions and experimental step-elution data are almost certainly due to inaccuracies of single-component extended Langmuir-Freundlich isotherm parameters in describing desorption equilibria. Single-component isotherms parameters employed with multicomponent isotherms do not always accurately describe multicomponent equilibria. This is especially true if they are flawed as suspected. Furthermore, Figure 6.2 indicates that single-component extended Langmuir-Freundlich isotherms do not exactly describe experimental single-component adsorption equilibria, in particular for lactoferrin. In addition, experimental adsorption equilibria for lactoperoxidase were investigated up to salt concentrations of 0.2 M and 0.6 M for lactoperoxidase and lactoferrin, respectively. Single-component extended Langmuir-Freundlich isotherms were not validated for salt concentrations employed in step-elution experiments.

However, the early appearance of major lactoperoxidase and minor lactoferrin elution peaks is more likely the result of the experimental step-elution protocol employed by James (1994). In James's experimental arrangement, a small dead-volume would have existed

prior to the column. This would have delayed the arrival of feed to the column. Such a small dead-volume may have been around 1-2 ml, thereby, delaying the step-change in salt concentration and emergence of major lactoperoxidase and minor lactoferrin peaks. The dead-volume would not have delayed the emergence of the major lactoferrin peak. The experimental step-change protocol would have initiated the second step-change 13 ml after the first. Only the first step-change in the sequence would be affected. Taking this possible dead-volume into account, the model is able to predict the exact positions of elution peaks for each protein.

Model simulations were performed by James (1994) to validate experimental data. Unfortunately, the results, performed with original single-component extended Langmuir-Freundlich isotherm parameters to describe desorption equilibria, were not presented making direct comparisons impossible. Apparently, model predictions provided poor agreement with experimental step-elution peaks. Again, only two collocation points were employed to approximate particle-concentration profiles. To overcome this poor agreement, James (1994) performed additional simulations employing modified values of b_{pi} for single-component extended Langmuir-Freundlich isotherms. Modified values were estimated by fitting model predictions to experimental step-elution data. At best, only a reasonable agreement between model predictions and experimental data was observed.

Therefore, model simulations indicate that the general non-linear multicomponent rate-equation model can quantitatively replicate experimental frontal adsorption and step-elution data. However, two apparently inconsistent sets of model parameters to describe multicomponent adsorption-desorption equilibria must be used. Multicomponent Langmuir isotherm parameters provide the best description of binary-adsorption equilibria during frontal adsorption. Single-component extended Langmuir-Freundlich parameters provide an accurate description of binary-desorption equilibria during step-elution.

Intraparticle-diffusion limitations also appear to influence the behaviour of the WGFE ion-exchange system during elution. The Biot numbers for each lactoperoxidase and lactoferrin during elution are identical for each protein at a value of 38.1. This is still greater than the threshold value of 20. Gu (1995) examined the impact of intraparticle diffusion in multicomponent elution systems. The results illustrate that Biot number has a profound influence on elution peak shape, which are normally bell-shaped or Gaussian. High values

of Biot number, greater than 20, were responsible for skew and tailing in elution peaks, although the effect was also a function of the dimensionless number η. Similar effects can be observed in Figure 6.4, and reflect the incapacity of intraparticle diffusion to keep pace with protein desorption during elution.

6.6 Concluding Remarks

The model parameters necessary to simulate the behaviour of the WGFE ion-exchange system using two proteins: lactoperoxidase and lactoferrin, without compression effects have been presented. These were used to validate the model and its parameters by comparing simulated behaviour of a laboratory-scale system during frontal adsorption and step-elution with experimental data. Quantitative agreement between model and experimental data indicate that the model could be successfully used to predict the impact of compression effects during scale-up. However, the selection of numerical parameters and accurate adsorption equilibria will be critical steps in ensuring successful reconciliation of model predictions with real-life behaviour of the WGFE ion-exchange system. In particular, a high number of orthogonal collocation points are required to accurately describe concentration profiles that are generated within resin particles during adsorption. Furthermore, two apparently inconsistent sets of model parameters to describe multicomponent adsorption-desorption equilibria must be used.

A further key observation was made during this chapter. Examination of the Biot number and internal particle-phase concentration profiles during model simulations reveal that inter-phase mass transfer in the WGFE ion-exchange system is controlled by intraparticle diffusion. This plays an important role in system behaviour during frontal adsorption and elution. For frontal adsorption, they lead to early breakthrough and extended breakthrough curve development. Early breakthrough is accompanied by low utilisation of resin-particle adsorption capacity within the packed bed. For elution, intraparticle-diffusion limitations skew elution peaks and lead to peak tailing.

CHAPTER 7

COMPRESSION EFFECTS

7.1 Preamble

A model has been developed to predict the impact of compression on WGFE ion-exchange system behaviour during scale-up. It is a modified version of the non-linear multicomponent rate-equation chromatography model. The modifications allow the model to account for the variation in bed properties: porosity and particle diameter, with axial position in a compressed packed bed. The goal of this section is to make some estimate of the variation in bed properties which may take place during scale-up of the WGFE ion-exchange system. This can then be combined with, or used to alter if necessary, the model parameters presented in Chapter 6. Prediction of its impact on system behaviour by simulation with the modified non-linear multicomponent rate equation chromatography model will then be possible.

7.2 Background Art - Porosity Variation in Compressed Beds

The key parameter used by the modified non-linear multicomponent rate-equation chromatography model to describe compression in a compressed packed bed is porosity. Porosity and the role it plays in fluid flow through porous media or packed-beds of granular media has been the subject of an extensive literature. Topical papers and reviews have been provided by Ruth (1946), Tiller & Huang (1961), Shirato *et al.* (1963), Foust *et al.* (1980), Willis *et al.* (1983), Perry & Green (1984), Willis *et al.*(1985), and Jönsson & Jönsson (1992). Pressure drop in filtration or separation processes has been the primary subject. The development of many predictive pressure-drop relationships, theories or correlations have relied on estimation of bed or media porosity.

Incompressible media display a linear (fluid-)pressure distribution through a packed-bed during fluid flow (Willis & Tosun, 1980). Porosity remains constant throughout the bed. Where fluid adsorption does not occur, porosity can be determined by displacement. If fluid

adsorption (or inclusion) by the media does occurs, tracer experiments must be used. A tracer that is not adsorbed (or excluded) by the media is chosen. The residence time of a tracer dispersed in a carrier fluid to travel through the bed is measured. Void volume is determined and compared to bed volume to estimate the porosity.

For compressible media, however, it is well known that fluid flow results in compression (Ruth, 1946). The porosity in the bed does not remain constant and depends on the compressive stress acting in the bed (Chase & Willis, 1992). A parabolic pressure distribution through the bed is often observed (Willis & Tosun, 1980). Tracer experiments can be used to determine bed porosity, but only an average value of bed porosity can be obtained.

Variation of bed porosity with stress acting in a compressible bed has been measured by a Compression-Permeability Cell (CPC) (Ruth, 1946; Tiller & Huang, 1961; Shirato *et al.*, 1963). The CPC, a piston-cylinder device, exposes a differential element of compressible media to differing axial stresses. Axial displacement of the piston as the element compresses allows bed porosity to be determined. (The initial bed porosity of the media must first be known). Measurement of the stress distribution in the packed bed then allows the porosity profile to be calculated. Typically, the stress distribution is determined from experimental measurements of the internal (fluid-)pressure distribution in the packed bed (Shirato *et al.*, 1963; Tiller & Huang, 1961). The stress acting at any point is equivalent to the pressure drop across that section. However, for compressible media where fluid adsorption occurs, compression can release previously adsorbed fluid. Fluid is effectively squeezed out of internal voidage contained within the media itself. This fluid contributes to volume changes during media deformation. Porosity measurements determined from axial displacement of the piston may be erroneous. Other criticisms of experimental CPC porosity data have been made. Side-wall friction in CPC test cells are known to significantly affect results (Willis *et al.*, 1985). Wall friction balances (in part) the compressive stresses acting in the bed. The compressive stress is no longer equal to the pressure drop determined from the experimental (fluid-)pressure distribution through the bed.

Alternatively, porosity can be indirectly determined by constitutive relationships that effectively relate pressure drop to porosity and particle deformation (Jönsson & Jönsson,

1992; Chase & Willis, 1992). These are used to construct porosity profiles from experimentally measured pressure distributions or pressure drop across a packed bed. Unfortunately, present techniques do not account for wall friction effects. Porosity profiles cannot be extrapolated to other systems.

Recently, direct measurement of porosity by electroconductivity (Chase *et al.*, 1990; Chase & Willis, 1992) has been employed. Electroconductivity probes are placed in a packed bed at varying bed heights. Conductivity measurements are calibrated to known values of bed porosity. Porosity profiles are measured during fluid flow through the bed. Accuracy is typically ±0.05 of measured porosity. Again, if wall friction effects are significant, porosity profiles cannot be extrapolated to other systems.

In summary, existing techniques for determination of porosity in compressed packed beds are unsuitable for chromatographic systems. Experimental techniques, for example, the CPC cell cannot accurately measure porosity when solid-phase volume is compromised. Electroconductivity probes, on the other hand, do not allow extrapolation when wall friction effects are significant. Porosity measurement would necessary for the system of interest. This is possible, but it would be difficult and expensive to acquire and modify a BPG 300/500 column, for example, for this purpose. This could not be considered in this study due to financial constraints. The alternative are in-direct techniques that use constitutive relationships to effectively relate pressure drop to porosity and particle deformation. However, existing models are inadequate. They fail to account for the functional dependence of compression and pressure drop on column size.

7.3 Methodology

Fortunately, the author has developed in Part I of this thesis a model for pressure drop which can account for the influence of wall friction effects. An in-direct technique for re-construction of porosity profiles in a compressed packed bed of chromatographic resin is proposed *per se*.

The model is described by *eq.s* 4.3 and 4.4. These equations predict the variation in fluid pressure and solid-phase axial stress, respectively, based on four model parameters: φ_w, φ,

$f_c(\tau^s_{zz})$ and $\chi(\tau^s_{zz})$. The model parameter $\chi(\tau^s_{zz})$ is an empirical function which accounts for bed compression effects on pressure gradient. It has been experimentally determined for the WGFE ion-exchange system and is described by *eq.* 4.1.

For the purpose of illustration, $\chi(\tau^s_{zz})$ was nominally related to porosity, ε, resin volume-mean particle diameter, d_{pv}, and resin particle shape factor, ϕ, in a compressed packed-bed in Chapter 2 by *eq.* 2.40:

$$\chi(\tau^s_{zz}) = \frac{200\,(1-\varepsilon)^2}{d_{pv}{}^2 \phi^2\, \varepsilon^3} \tag{2.40}$$

This relationship was used to provide an initial estimate of $\chi(\tau^s_{zz})$ in Chapter 4. However, it could also be extended to determine the variation in porosity, volume-mean particle diameter and shape factor in a compressed bed whose stress distribution had already been calculated. The stress distribution would give $\chi(\tau^s_{zz})$ at any point in the bed. This, in turn, would give bed porosity, volume-mean particle diameter and shape factor if the relationship between these variables, or with stress, was known. With such a method, the change in volume-mean particle diameter and shape factor would effectively characterise particle deformation during compression.

However, it was indicated in Chapter 6 that the mean particle dimension which should ideally be used for describing particle size in the modified general non-linear multicomponent rate-equation chromatography model is Sauter-mean particle diameter. Equation 2.4 was derived by comparison of *eq.* 2.37 to an empirical correlation for pressure-drop across incompressible packed-beds by Leva. An alternative correlation to Leva's based on the Sauter-mean particle diameter, d_{pS}, is the Carmen-Kozeny equation (Foust *et al.*, 1980):

$$\frac{\Delta P}{L} = \frac{180\,(1-\varepsilon)^2 \mu v_{sup}}{\varepsilon^3\, d^2_{pS}} \tag{7.1}$$

Comparison of *eq.* 2.37 to *eq.* 6.1 gives

$$\chi(\tau_{zz}^{s}) = \frac{180\,(1-\varepsilon)^2}{d_{pS}^{\,2}\;\varepsilon^3} \tag{7.2}$$

This expression relates $\chi(\tau_{zz}^{s})$ to bed porosity and Sauter-mean particle diameter. With no shape factor involved in *eq.* 7.2, changes in Sauter-mean particle diameter now characterise particle deformation.

There is one degree of freedom in *eq.* 7.2. Therefore, to determine bed porosity and Sauter-mean particle diameter through the compressed packed bed, an additional relationship between these variables, or with stress, must be found. This relationship can be estimated by considering how resin particles deform in a packed bed. Briefly, consider the particles in a packed bed prior to compression to be spherical with diameter, d_{pi}, and volume

$$V_{pi} = \frac{\pi}{6} d_{pi}^{3} \tag{7.3}$$

During compression, assume that the shape of the particle becomes ellipsoid. The ellipsoid particles have a semi-vertical axis, b and semi-horizontal axes, a. Their volume is

$$V_{pc} = \frac{4}{3}\pi a^2 b \tag{7.4}$$

If the semi-horizontal axis, a, of the compressed particle remains constant (equivalent to $d_{pi}/2$), then particle deformation during compression is restricted to axial strain in the vertical semi-axis, b. Vertical semi-axis strain can therefore be determined from

$$b = \frac{d_{pi}}{2} f_d(\tau_{zz}^{s}) \tag{7.5}$$

where $f_d(\tau_{zz}^{s})$ is the fractional change in height experienced by resin particles during deformation as defined in Chapter 3.

The surface area of the compressed particle, A_{pc}, is (Perry & Green, 1984)

$$A_{pc} = 2\pi a^2 + \frac{\pi b^2}{e} \ln\left(\frac{1+\omega}{1-\omega}\right) \tag{7.6}$$

where ω is the eccentricity of the ellipsoid resin particle.

The Sauter-mean diameter of the compressed particles is the diameter of a sphere with the same ratio of area to volume:

$$d_{pS} = \frac{6V_{pc}}{A_{pc}} \tag{7.7}$$

Equations 7.3 to 7.7 define the relationship between porosity and Sauter-mean particle diameter. The degree of freedom in *eq.* 7.2 has been eliminated. All that is required is a value for initial Sauter mean particle diameter in order to initialise *eq.* 7.5.

Being able to determine the deformation of the particles in the bed also allows us to estimate the variation in particle internal voidage, ε_p, that takes place. This can be determined by the change in particle volume during compression:

$$\varepsilon_p = 1-(1-\varepsilon_{pi})\left(\frac{V_{pi}}{V_{pc}}\right) \tag{7.8}$$

where ε_{pi} is the initial internal particle voidage before compression.

7.4 Initial Sauter-Mean Particle Diameter and Internal Voidage

As mentioned in Chapter 6, particle-size analyses for Sepharose Big-Beads SP have already been conducted in Chapter 3. An average value for initial Sauter-mean particle diameter was determined. Its value was 167 μm. Similarly, the initial internal voidage of a 6% cross-linked agarose resin is known. It value equals 0.94.

7.5 Prediction of Porosity and Particle-Deformation Profiles

To simulate compression effects during scale-up in the WGFE ion-exchange system in this thesis, two column sizes were arbitrarily selected. A 2 cm internal-diameter to represent a laboratory-scale column, and a 20 cm internal-diameter column as a typical production-scale column. Equations 4.3 and 4.4 were employed the predict the variation in solid-phase stress field in each column with water at 20°C for a 20 cm (initial-height) packed bed at a superficial velocity of 35 cm/min. Model predictions were generated by the purpose-built MathCad PLUS v5.0 file described in Section 4.3 - Chapter 4. Equation 4.1 was employed to describe $\chi(\tau^{s}_{zz})$. Experimental values of 8.0 and 10.3°, respectively, were used for angle of wall friction and internal angle of wall friction. A value of 1.002 cP was used to describe the viscosity, at 20°C, of water.

For the readers interest, the superficial velocity of 35 cm/min was selected as the model predicts that significant compression in the 20 cm internal diameter column will commence at this point.

The results of model predictions described above have already presented in Chapter 4 of this thesis. Variation of τ^{s}_{zz} with bed height for the 2 and 20 cm internal-diameter column were shown in Figure 4.14. The pressure drop across the packed bed predicted by the model in each columns was 89 kPa and 154 kPa, respectively. Model prediction of compressed packed-bed height was 19.1 cm and 18.4 cm, respectively.

Equations 7.2 to 7.8 were employed to estimate the variation in porosity, Sauter-mean particle diameter and internal particle voidage with bed height from the solid-phase stress field presented for each column in Figure 4.14. A Microsoft Excel v5.0 Workbook was created for all numerical calculations. Porosity cannot be explicitly determined from *eq.* 7.2, and therefore, a trial and error solution using a modified Newton technique was employed. The initial Sauter-mean particle diameter and internal particle voidage used to initialise *eq.s* 7.5 and 7.8 were 167 μm and 0.94, respectively.

The resultant porosity profile and variation in Sauter-mean diameter determined for the packed bed in each column is shown in Figures 7.1 and 7.2, respectively. Variation in internal particle voidage calculated for each column is illustrated in Figure 7.3.

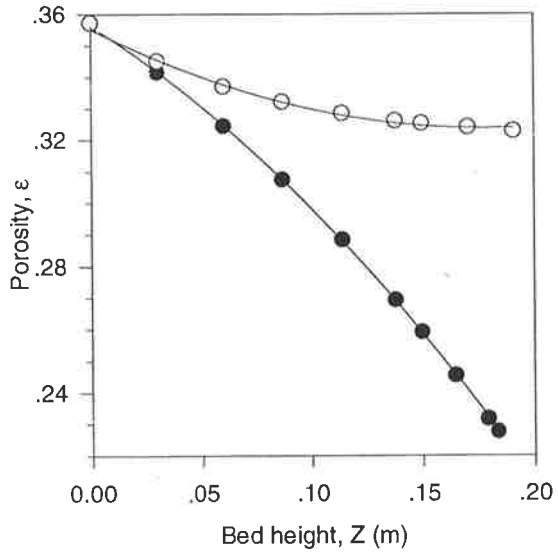

Figure 7.1: Predicted variation in porosity with bed height in the laboratory- (○) and production-scale (●) column *vs.* correlation by empirical function (——).

Figure 7.2 indicates a 36% decrease in bed porosity from top to bottom of the packed bed in the 20 cm internal-diameter column will take place. This is a significant change in the packed-bed interparticle void space and is nearly four times the predicted value (9%) for the 2 cm internal-diameter column.

The initial porosity determined from $\chi(\tau^{s}_{zz})$ using the Carmen-Kozeny equation is 0.356. This is marginally lower the initial bed porosity of 0.38 experimentally determined in Chapter 3, but compares well to the value of 0.35 presented by Skidmore (1990) for Sepharose Fast-Flow S. However, it is different to the value of 0.38 in Chapter 4 where Leva's correlation was used in place of the Carmen-Kozeny equation to estimate $\chi(\tau^{s}_{zz})$ by regression to experimental pressure-drop data. This emphasises the variance in pressure-gradient prediction of different empirical relationships. Different empirical correlations for pressure gradient would obviously provide different porosity profiles.

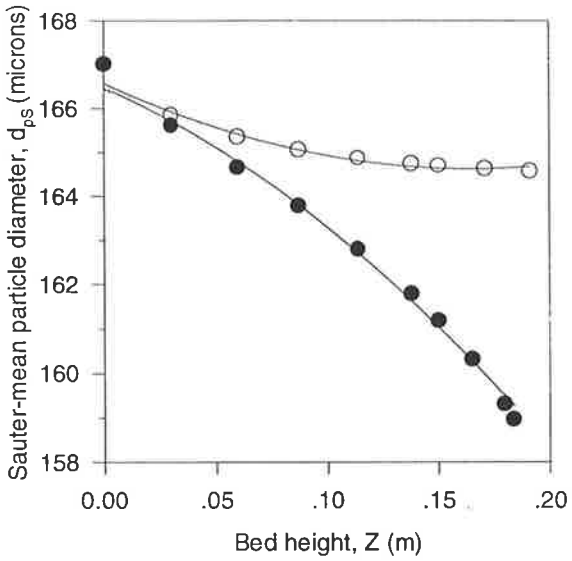

Figure 7.2: Predicted variation in Sauter-mean particle diameter with bed height in the laboratory- (○) and production-scale (●) column *vs.* correlation by empirical function (——).

Predicted change (from top to bottom) in Sauter-mean particle diameter for each column are approximately 2 and 5%, respectively. These seem moderate, but when compared against *eq.* 7.1 even a small variation of this type can produce a 4 and 11 % increase, respectively, in the pressure gradient. Evidently, deformation of particles appears to significantly influence the applied stress distribution within the packed bed during fluid flow.

Bed porosity and Sauter-mean particle diameter in Figures 7.1 and 7.2 were correlated to bed height for each column using simple interpolation functions. The results were as follows. For the 2 cm internal-diameter column:

$$\varepsilon(Z) = 0.3552 - 0.3531\ Z + 0.9921\ Z^2 \qquad (7.9)$$

$$d_{pS}(Z) = 1.666\times10^{-4} - 2.346\times10^{-5}\ Z + 7.099\times10^{-5}\ Z^2 \qquad (7.10)$$

For the 20 cm internal-diameter column:

$$\varepsilon(Z) = 0.3562 - 0.4423\ Z - 1.38\ Z^2 \qquad (7.11)$$

$$d_{pS}(Z) = 1.665\times10^{-4} - 2.261\times10^{-5}\ Z - 9.064\times10^{-5}\ Z^2 \qquad (7.12)$$

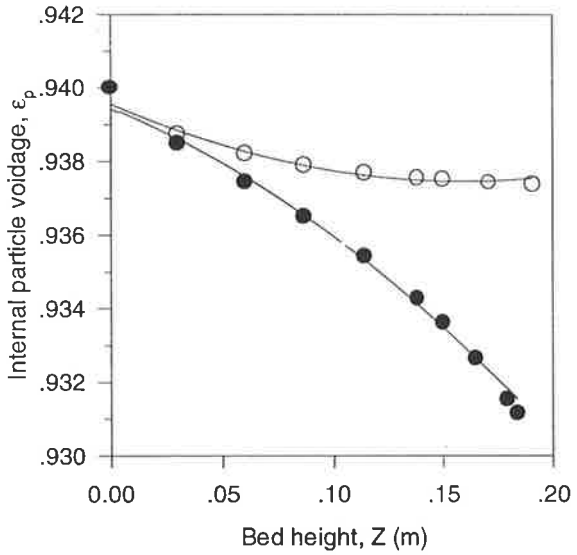

Figure 7.3: Predicted variation in internal particle voidage with bed height in the laboratory- (○) and production-scale (●) column *vs.* correlation by empirical function (——).

Internal particle voidage in Figure 7.3 was also correlated with bed height for the 2 cm and 20 cm internal-diameter columns, respectively:

$$\varepsilon_p(Z) = 0.9396 - 0.0264\,Z + 0.0828\,Z^2 \qquad (7.13)$$

$$\varepsilon_p(Z) = 0.9394 - 0.0250\,Z - 0.09812\,Z^2 \qquad (7.14)$$

The accuracy of predicted porosity, intraparticle porosity and Sauter-mean particle diameter profiles can be examined. The total particle stationary phase-volume (TPSV) and total particle volume (TPV) of the compressed bed in each column can be compared to that prior to compression. TPSV is determined from bed porosity and intraparticle voidage:

$$TPSV = A_{col} \int_0^{Z_c} (1 - \varepsilon)(1 - \varepsilon_p)\, dZ \qquad (7.15)$$

where A_{col} is the column cross-sectional area.

TPV is determined directly from bed porosity:

$$TPV = A_{col} \int_0^{Z_c} (1 - \varepsilon)\, dZ \qquad (7.16)$$

TPSV in each column after compression compared with that prior to compression are summarised in Table 7.1. TPSV after compression were determined from both actual and correlated values for bed porosity and internal particle voidage (*eq.s* 7.9, 7.10, 7.11 & 7.12) are presented for comparison.

Table 7.1: Total particle stationary-phase volume (TPSV) and total particle volume (TPV) for compressed beds in laboratory- and production-scale columns compared to that prior to compression.

	Production (L)	Laboratory (mL)
$TPSV_{compressed,\ actual}$	0.259	2.48
$TPSV_{compressed,\ regressed}$	0.259	2.48
$TPSV_{no\ compression}$	0.242	2.42
$TPV_{compressed,\ regressed}$	4.045	40.01
$TPV_{no\ compression}$	4.040	40.40

Table 7.1 indicates that no variation is observed between TPSV estimated from actual and correlated values for porosity and internal particle voidage. Comparison of TPSV before and after compression indicate that it has increased with the compression predicted in each column. This is obviously incorrect. TPSV should remain constant, regardless of compression. This is probably symptomatic of the inherent model-prediction error for bed height. It may also indicate that assumptions made regarding particle deformation during calculation of porosity are imperfect. Certainly, the restriction on strain in the semi-horizontal axis of the particle during deformation may not be correct. It could also indicate inaccuracies in pressure-gradient prediction by the Carmen-Kozeny equation for chromatographic resins.

The TPV after compression, using correlated values of bed porosity for each column, compared with TPV prior to compression are also presented in Table 7.1. Surprisingly, compression has increased TPV in the 20 cm diameter column and decreased it in the 2 cm

diameter column. Clearly, compression should reduce TPV. Again, this indicates the presence of an error in the in-direct prediction technique employed in this Chapter to determine the variation in porosity in Sauter-mean particle diameter.

7.6 Compression Effects on Model Parameters

Variation in porosity, Sauter-mean particle diameter, and internal particle voidage will obviously alter the values of model parameters presented in Chapter 6. These will need to be adapted for simulation of compression effects during scale-up of the WGFE ion-exchange system.

For porosity and Sauter-mean particle diameter, *eq.s* 7.9 to 7.14 can be directly used with the modified non-linear multicomponent rate equation chromatography model to replicate compression effects.

For model parameters k_i, v_i and Pe, the model solution strategy outlined in Chapter 5 is designed to automatically determine the deviation for each parameter with compression during a simulation. Interstitial velocity is directly calculated from v_{sup} and $\varepsilon(Z)$. k_i and Pe are determined from v_{sup} and $\varepsilon(Z)$ via empirical correlations presented in Chapter 6.

However, the impact of compression effects on remaining model parameters, for example, D_p, ε_p, and adsorption-desorption equilibria, is unclear. Figure 7.3 indicates that resin particles in the 20 cm internal diameter column will experience a 1% decrease in intraparticle voidage, compared to 0.2% in the 2 cm column. This is only a minor variation, but correspond to 7 % decrease in fluid-phase volume within resin particles at the bottom of the bed during scale-up. Clearly, a variation of this magnitude could have an deleterious impact on internal mass transfer and adsorption-desorption within resin particles. While there is an absence of specific reports in the literature on the impact of compression effects on resin particles, there have been some studies performed on variation in intraparticle void fraction and restricted diffusion in polymer gels. One in particular (Boyer and Hsu, 1992), examined intraparticle void fraction and restricted diffusion in Sepharose CL-6B. This resin is a 6% cross-linked agarose resin and similar to Sepharose Big-Beads SP, except for functional group and particle size. An empirical model developed by Ogston *et al.* (1973)

was considered. It describes the describe the functional dependence of intraparticle diffusion on fiber radius of the gel (r_f) and Stokes radius (r_s) of a protein:

$$\frac{D_p}{D_f} = \exp\left[-B(r_s + r_f)c_f^{0.5}\right] \tag{7.16}$$

Equation 7.16 was used to examine the restricted diffusion of a number of proteins in Sepharose CL-6B. Intraparticle diffusivity was found to vary significantly with molecular weight. For example, the ratio of intraparticle to bulk diffusivity for myoglobulin and albumin were 0.343 and 0.155. The molecular weight of each protein is 16,890 and 67,000, respectively.

Lactoperoxidase and lactoferrin already suffer from significant restricted diffusion in Sepharose Big-Beads SP. Equation 7.16 indicates that any variation in pore size within resin particles is likely, in some way, to effect intraparticle diffusivity. One would expect that even a minor decrease of 7% in fluid-phase volume would be enough to alter the size of, or even close off, pores within a resin particle, and thereby, restrict protein movement.

The study by Boyer and Hsu (1992) also examined the variation in intraparticle-void fraction with molecular weight of protein. It showed that the intraparticle voidage for each protein varied significantly with its molecular weight. For example, the void fraction for myoglobin, albumin and immunoglobulin-G in Sepharose CL-6B was 0.734, 0.55 and 0.457, respectively. (The molecular weight immunoglobulin G is 161,000). The intraparticle voidage of lactoperoxidase and lactoferrin in Sepharose Big-Beads SP has been estimated at 0.5. All of these are much lower than the particle internal voidage for a 6% cross-linked resin of 0.94. Evidently, these proteins are restricted from internal voidage because of their relative size compared with the internal pores in a resin particle. It therefore follows then that any change in pore size would alter a proteins intraparticle voidage. This of course would also probably change the surface area available for adsorption, and thus, the adsorption capacity.

These results of Boyer and Hsu (1992) serve the useful purpose of illustration. Particle compression is likely to affect D_p, ε_p, and adsorption-desorption equilibria. They,

unfortunately, cannot be used to help us to quantify the impact of compression on these model parameters for lactoperoxidase and lactoferrin with Sepharose Big-Beads SP. Additional theoretical or experimental information is required. This was not possible in this study. Instead, intraparticle diffusion, intraparticle porosity and adsorption-desorption equilibria will be assumed to be constant at values specified in Chapter 6 for simulation of compression effects in this thesis.

The variations in TPSV discovered in Section 7.5 with prediction of bed porosity will compromise the mass balance on the particle stationary-phase of the modified non-linear multicomponent rate-equation chromatography model. This is clearly unsatisfactory. The total adsorption capacity predicted for the 2 and 20 cm diameter columns during model simulation will be erroneous.

To rectify this problem, maximum adsorption capacities of the resin in the compressed bed were altered. The modified values will account for the change in TPSV available for adsorption. An intraparticle voidage of 0.5 was used for internal particle voidage in *eq.* 7.15. A new value of adsorption capacity was selected to ensure total packed-bed adsorption capacity was maintained during compression in each column. Modified values for lactoperoxidase and lactoferrin adsorption capacities based on correlated bed and intraparticle porosity in each column are presented in Table 7.2. These values will be used for compressed-bed simulations.

Table 7.2: Modified (TSPB) maximum adsorption capacities of lactoperoxidase and lactoferrin for compressed-bed simulations.

	C_i^{∞} (moles/m^3)	
	Laboratory-Scale	**Production-Scale**
Lactoferrin	8.85×10^{-3}	8.95×10^{-3}
Lactoperoxidase	10.50×10^{-3}	10.62×10^{-3}

7.7 Concluding Remarks

Existing techniques for porosity measurement have been reviewed. They are unsuitable for measuring the variation in bed properties of a compressed packed bed during scale-up of the WGFE ion-exchange system. Instead, an in-direct technique based on the new model

developed in Part I of this thesis for pressure-drop prediction was employed. $\chi(\tau^{s}_{zz})$ was nominally related to porosity, ε, and Sauter-mean particle diameter, d_{pS}, by comparing model equation, *eq.* 2.37, to the Carmen-Kozeny equation. The result was *eq.* 6.1. A number of assumptions were made about the deformation of resin particles in a packed bed to eliminate the degree of freedom in *eq.* 6.1. The variation in porosity, Sauter-mean particle diameter and internal particle voidage were determined for a packed bed in two columns of internal diameters 2 cm and 20 cm. The packed-bed height was 20 cm, the test fluid: water at 20°C, and the superficial velocity: 35 cm/min. The results were correlated with bed height using simple interpolation functions. This will allow them to be used for simulation with the modified version of the non-linear multicomponent rate-equation model.

The impact on compression on model parameters presented for the WGFE ion-exchange system in Chapter 6 was examined. Variation in ε, d_{pS}, k_i, v_i and Pe will be automatically incorporated into the model for compressed-bed simulations. Variation in D_p, ε_p, and adsorption-desorption equilibria could not be predicted with certainty. They will be regarded as constant, regardless of compression, for the purpose of this study.

The variation in total stationary-phase volume during compression, based on predicted porosity and intraparticle porosity profiles, was examined. The results indicate that predictions may compromise the mass balance for the modified non-linear multicomponent rate-equation model. This problem was overcome by modifying the maximum adsorption capacity of each protein for the 2 and 20 cm internal-diameter columns.

CHAPTER 8

SIMULATION & PREDICTION

8.1 Preamble

A model has been developed to predict the impact of compression on the system behaviour of a chromatographic system. Its model parameters have been determined for simulation of two proteins: lactoperoxidase and lactoferrin, with Sepharose Big-Beads SP. These were presented in Chapter 6. A model system for investigation of compression effects during scale-up of the WGFE ion-exchange system has been selected. It consists of two columns of different internal diameters: 2 and 20 cm, a packed-bed height of 20 cm in each column, with the packed beds subject to compression at a superficial velocity of 35 cm/min with water at 20°C. The variation in bed properties for each column, and their impact on model parameters, have been estimated in Chapter 7. Model simulations will now be conducted to investigate compression effects on WGFE ion-exchange system behaviour during scale-up.

8.2 Evaluation of Optimal Numerical Parameters

Prior to the compressed-bed simulations, the optimal numerical parameters for solution of the modified general non-linear multicomponent rate-equation chromatography model must be selected. Single-component frontal-adsorption simulations with lactoferrin were conducted. Different combinations of bulk-phase finite elements and particle-phase collocation points were evaluated. Model simulations were designed to imitate proposed compressed-bed simulations, but with compression effects excluded. Single-component adsorption equilibria were described by multicomponent Langmuir isotherm parameters. The superficial velocity was 35 cm/min. Bed height was 20 cm. Feed concentration was 0.1 mg/ml. Water was used to estimate physical properties of the feed. Feed temperature was assumed constant at 20°C. Compression effects were ignored and porosity and Sauter-mean particle diameter in the packed bed were fixed at values of 0.356 and 167 μm, respectively. Table 8.1 summarises the important model parameters, finite-element and

collocation-point combinations, and values of key dimensionless numbers employed in each simulation.

Table 8.1: Compressed-bed simulations: important model parameters and values of key dimensionless groups employed for selection of optimal numerical parameters.

Numerical Parameters			System		Component	
Refer Figure 8.1	N_e	N_c	v	98 cm/min	C_f	1.282×10^{-6} M
(a)	10	3	L	0.2 m	C_o	1.282×10^{-6} M
(b)	10	5	ε	0.356	Pe	709
(c)	10	8	ε_p	0.5	Bi	1139
(d)	10	11	R_p	83.5 μm	η	0.005
(e)	10	13	Re	0.97	ξ	32.5
(f)	20	13			Da^a	12820
					Da^d	1000

Convergence could not be achieved during preliminary attempts to identify the optimal numerical parameters for the single-component frontal-adsorption simulation. Propagating instabilities in the numerical solution were a common observation. These inevitably corrupted the moving concentration profiles in the packed bed and its effluent history beyond recognition.

Careful examination revealed that this was symptomatic of sub-optimal numbers of finite elements. It was concluded that in excess of 100 finite elements would be required to accurately describe bulk-phase concentration profiles during the single-component frontal-adsorption simulation. Perhaps, an expected result when we consider the height of the packed bed. Ten elements were required for a bed height of 1.3 cm during model simulations to validate model parameters in Chapter 6. Therefore, if number of elements is proportional to bed height, then at least one hundred and fifty might be expected at 20 cm. (With eleven internal collocation points this would generate a 13,864 ODE system). Such a large number of finite elements would create a system of ODEs that exceeded the capacity of the SACPC CM-5 for subsequent compressed-bed binary-component frontal-adsorption and step-elution simulations. Investigation of compression effects during scale-up of the WGFE ion-exchange system would not be possible.

However, a closer inspection revealed that these instabilities appeared to be a direct result of the feed concentration profile employed during simulation. The model introduces a species in the feed to the column as a step increase in concentration. To describe this mathematically, a Heaviside-type step function is employed:

$$C_{fi}(\tau - \tau_{step}) = \begin{cases} C_{fi,\tau<\tau_{step}} & \tau < \tau_{step} \\ C_{fi,\tau\geq\tau_{step}} & \tau \geq \tau_{step} \end{cases} \qquad (8.1)$$

During a simulation, such a step increase will generally retain its form as it initially proceeds into the bed. In doing so, it creates an extremely steep concentration gradient at the top of the bed. Large numbers of finite elements must normally be used to numerically describe its concentration profile. However, dispersion and inter-phase mass transfer eventually cause this gradient to subside. The high concentration gradients experienced during the step change dissipate and successively lower numbers of finite elements may be employed. In most cases, the period of time that the step increase maintains its original profile is small. The error created by initially using a low number of finite elements is minor, and does not compromise the final numerical solution.

However, in the single-component frontal-adsorption system the step increase in feed concentration acts like a shock wave. It enters the 20 cm bed at an interstitial velocity of 98 cm/min. High Peclet (~709) and Biot (~1139) numbers mean that convection and external-film mass transfer dominate dispersion and intraparticle diffusion, respectively. Dispersion effects are small. Inter-phase transfer is intraparticle-diffusion limited. The original profile for the step increase in concentration does not subside. Concentration gradients at the top of the bed remain inordinately high for an extended period of time. The error created by initially using a low number of finite elements does not dissipate, and this creates an unstable numerical solution. A higher number of elements must be maintained throughout the simulation to accurately describe the concentration profile.

A number of variations in the numerical solution strategy were proposed to provide a practical resolution to this problem. First, increasing the number of finite elements or mesh resolution at the entrance of the bed allows the numerical solution to adequately describe

steep concentration gradients induced by a step increase in concentration. This would require a re-formulation of the numerical solution strategy employed in this study.

Second, by adopting gradient-directed moving finite-element method (Yu & Wang, 1989) for solution of the dimensionless bulk-phase governing equation, the finite element mesh is refined where high concentration gradients occur. A greater number of elements are used where necessary to approximate concentration profiles. Mesh refinement is not stationary and is designed to follow movement of concentration gradients. The total number of finite elements required is reduced. A minimal number of elements to describe local concentration profiles is necessary. Similarly, applying a gradient-directed moving finite-element method requires re-formulation of the numerical solution strategy employed in this study.

Third, altering the feed concentration profiles causes a gradual introduction of the feed to the bed. This reduces the shock-wave effect experienced during step changes. Feed concentration profiles are selected to minimise instantaneous and high gradients at the packed-bed entrance. In fact, a gradual introduction of the feed to a packed bed actually replicates real-life behaviour. Feed concentration profiles are often dispersed in conduits, distributors and frits during their journey to the packed bed. True step changes in feed concentration rarely occur. Altering the feed concentration profiles ensures no modification to the current numerical solution strategy.

For the sake of simplicity, the third option was selected. Single-component simulations in Table 8.1 were repeated. Feed concentration profiles of each component were modified. A Sigmoid-type function was employed:

$$C_{fi}(\tau-\tau_{step})=\begin{cases} C_{fi,\tau<\tau_{step}} & \tau<\tau_{step} \\ C_{fi,\tau<\tau_{step}}+\left(\dfrac{1.041}{\left(1+\exp\left[\dfrac{-(\tau-(1.054+\tau_{step}))}{0.384}\right]\right)}-0.020\right)\left(C_{fi,\tau\geq\tau_{step}}-C_{fi,\tau<\tau_{step}}\right) & \tau_{step}\leq\tau<(\tau_{step}+3) \\ C_{fi,\tau\geq\tau_{step}} & \tau\geq(\tau_{step}+3) \end{cases} \tag{8.2}$$

Three dimensionless time units are now be required for full development of feed concentration profiles.

Figure 8.1 shows predictions of frontal-adsorption curves for all model simulations with modified feed concentration profiles described by *eq.* 8.2. Ten finite elements are adequate to describe bulk-phase concentration profiles. At least eleven internal collocation points are necessary to describe particle-phase concentration profiles. During development of the curve profile, the numerical solution oscillates about the exact solution. This is a function of the number of collocation points. Increasing their number reduces oscillatory behaviour and improves convergence.

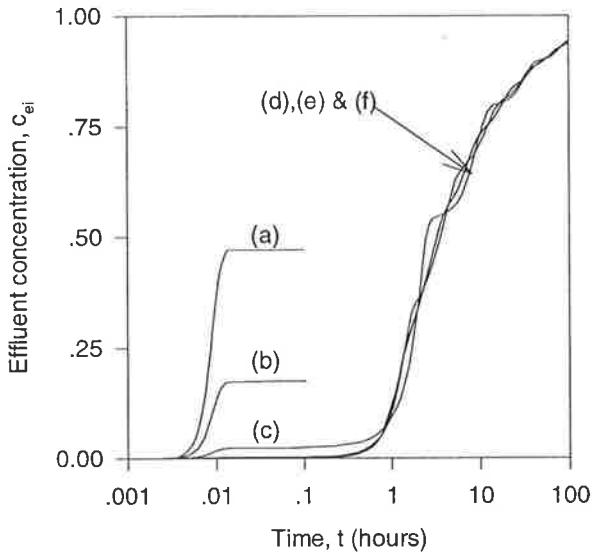

Figure 8.1: Single-component frontal-adsorption model predictions (——) using different combinations of numerical parameters: (a)-N_e=10, N_c=3; (b)-N_e=10, N_c=5; (c)-N_e=10, N_c=8; (d)-N_e=10, N_c=11; (e)-N_e=10, N_c=13; (f)-N_e=20, N_c=13.

8.3 Compression Effects during Frontal Adsorption

The optimal numerical parameters have been identified. At least 10 finite elements and 11 collocation points will be required as long as *eq.* 8.2 is used to describe feed concentration profiles. Model simulations to investigate the impact of compression effects are now possible.

Two binary-component frontal-adsorption simulations with lactoperoxidase and lactoferrin were performed. Compression effects on system behaviour during frontal adsorption in the 2 and 20 cm internal-diameter columns were examined. For each simulation, superficial velocity and bed height were 35 cm/min and 20 cm, respectively. Compression effects in

each column were described by porosity and Sauter-mean particle diameters profiles described in Chapter 7. Binary-component adsorption equilibria of each protein were described by multicomponent Langmuir isotherm parameters with the modified maximum adsorption capacities shown in Table 7.2. The feed concentration was 0.1 mg/ml. Feed concentration profiles were described by *eq.* 8.2. Physical properties of the feed solution were estimated from water at 20°C. Ten finite elements and eleven collocation points were used. Important model parameters and values of key dimensionless numbers for each simulation are summarised in Table 8.2.

Table 8.2: Important component and system model parameters and values of key dimensionless groups employed for compressed-bed frontal-adsorption simulations.

System		Component		
v	98[1], 108.7[2], 154.2[3] cm/min		**Lactoferrin**	**Lactoperoxidase**
L_i	0.2 m	**C_f**	1.282×10^{-6} M	1.282×10^{-6} M
L	0.1911[4], 0.1839[5] m	**C_o**	1.282×10^{-6} M	1.282×10^{-6} M
ε	0.356[1], 0.322[2], 0.227[3]	**Pe**	710[1], 793[2], 1167[3]	710[1], 793[2], 1167[3]
ε_p	0.5	**Bi**	1140[1], 1192[2], 1423[3]	456[1], 477[2], 569[3]
d_p	167[1], 165[2], 159[3] μm	**η**	0.005[1], 0.005[2], 0.004[3]	0.013[1], 0.012[2], 0.009[3]
Re	0.974[1], 0.963[2], 0.928[3]	**ξ**	32.5[1], 36.7[2], 53.7[3]	32.5[1], 36.7[2], 53.7[3]
		Da^a	12820	1000
		Da^d	1000	1950

1 Compression excluded or at top of compressed packed beds in laboratory- and production-scale columns.

2 At bottom of packed bed (maximum compression) in the laboratory-scale column.

3 At bottom of packed bed (maximum compression) in the production-scale column.

4 Laboratory-scale column.

5 Production-scale column.

In addition, a third binary-component frontal-adsorption simulation was performed. Model parameters were identical, however, compression effects were excluded. Porosity and Sauter-mean particle diameter in the packed bed were fixed at values of 0.356 and 167 μm, respectively.

Figure 8.2 illustrates the frontal-adsorption breakthrough curves for all compressed-bed frontal-adsorption simulations. The frontal-adsorption simulation without compression effects is also shown for comparison.

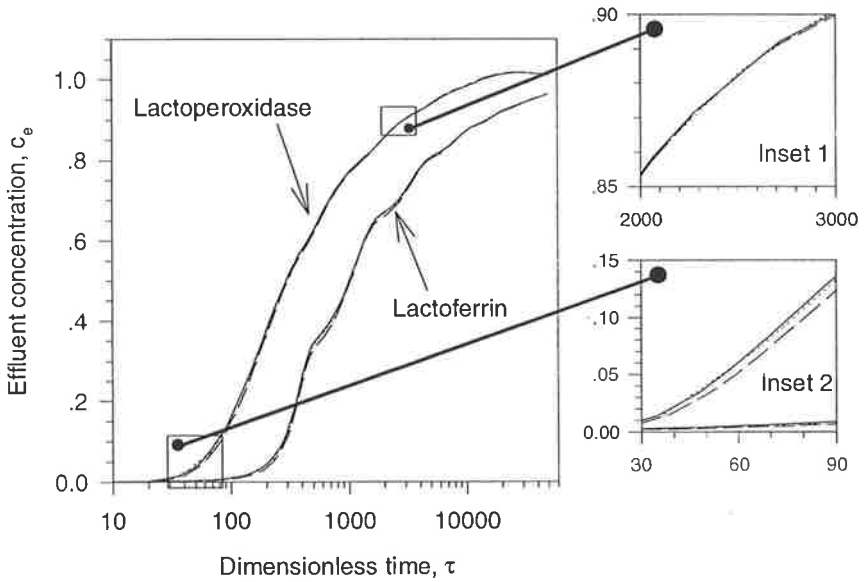

Figure 8.2: Compressed-bed simulations: frontal-adsorption model predictions with compression effects excluded (——) and for compressed packed beds in the laboratory- (·····) and production-scale (— —) column.

While numerical bulk-phase effluent concentration profiles in Figure 8.2 display some oscillatory behaviour, Figure 8.1 demonstrates that they still provide a true description of system behaviour. This oscillatory behaviour is a function of the number collocation points. Unfortunately, attempts to conduct further simulations with a higher number of collocation points to improve convergence generated a system of ODEs that would have exceeded the capacity of the SACPC CM-5 for subsequent step-elution simulations.

Despite this problem, breakthrough curves in Figure 8.2 are almost identical. Increased compression experienced in the laboratory and production-scale columns does not significantly affect system behaviour. However, small variations in curve profiles do exist. Compression effects appear to delay breakthrough and subsequent curve development. The extent of these variations is obscured by adoption of a logarithmic scale for dimensionless time. A linear scale (see Inset 1 - Figure 8.2) provides a true indication. The greatest delay in curve development occurs immediately after breakthrough. At dimensionless time equal to 90, the delay between laboratory- and production-scale column is almost 10 (dimensionless time units). This initial lag does not markedly increase in magnitude as the

breakthrough curve develops (see Inset 2 - Figure 8.2) and becomes increasingly trivial as frontal adsorption proceeds.

While the impact of compression on this system appears to be minor, it provides a fascinating example of the elaborate influence compression effects can have on chromatographic behaviour. Three competing mechanisms exist. The reduction in void volume which can induce premature breakthrough and accelerate subsequent curve development. Increased external-film mass transfer which enhances inter-phase mass transfer between bulk and particle phases within the bed. This can delay breakthrough and subsequent curve development. And finally, axial dispersion which can initially induce premature breakthrough and accelerate curve development, but may then subsequently delay further curve development. Which mechanism dominates depends on the relative importance of either external-film mass transfer and dispersion as a function of the two key dimensionless groups, the Biot and Peclet number, which govern the behaviour of the system.

The appearance of delays in breakthrough and subsequent curve development in Figure 8.2 indicates that the dominant mechanism in this system is compression-induced increases in external-film mass transfer. This is surprising given the high Biot number of each protein. As mentioned in Chapter 6, it has been shown that when the Biot number exceeds 20, intraparticle diffusion rather than external-film mass transfer controls inter-phase mass transfer (James, 1994). Even if increases in external-film mass transfer exist, it should have little or no influence on inter-phase mass transfer. Given the high Peclet number (which should suppress compression-induced variations in axial dispersion), the reduction in void volume within the bed should govern system behaviour. Premature breakthrough and accelerated curve development should be observed, rather than delayed breakthrough. This was the case during compressed-bed simulations for the hypothetical system presented in Chapter 5.

To explain this contradiction, we must re-examine the assertion that at high Biot numbers, intraparticle diffusion rather than external-film mass transfer controls inter-phase mass transfer. For example, during the initial phase of frontal adsorption, steep particle-phase concentration gradients are normally generated at the surface of particles within the bed. Surface-particle flux is likely to be controlled by external-film mass transfer, rather than

intraparticle diffusion. Obviously, compression effects can enhance inter-phase mass transfer during this initial period and generate delays in breakthrough and subsequent development of effluent concentration profiles. Eventually, intraparticle-diffusion limitations emerge as internal particle-phase concentration profiles gradually develop within the particles. Inter-phase mass transfer becomes independent of compression. Further increases in the magnitude of delays in effluent concentration profiles generated by compression are suppressed or even eliminated. Clearly, the impact of this compression-induced behaviour on effluent concentration profiles depends on the period overwhich inter-phase mass transfer is influenced by external-film mass transfer.

Particle-phase concentration profiles in Figure 6.6 of Chapter 6 indicate that the WGFE ion-exchange system does experience a prolonged period during which steep particle-phase concentration gradients are generated at the surface of particles within the bed. It appears that an initial period of enhanced inter-phase mass transfer induced by compression does create a delay in breakthrough and subsequent curve development as observed in Figure 8.2. Furthermore, even as intraparticle-diffusion limitations emerge throughout the bed, these delays in curve development still remain significant enough to overcome the influence of premature breakthrough and accelerated curve development generated by bed compression.

The full development of each frontal adsorption curve in Figure 8.2 takes place over a wide time frame. For example, breakthrough of lactoperoxidase occurs at $\tau \approx 20$ (dimensionless time units). Effluent concentration exceeds feed concentration at 15,000 (dimensionless time units). Figure 8.3 maps the chronological development of the numerical bulk-phase concentration profiles for lactoperoxidase captured during the frontal-adsorption simulation with compression effects excluded. Profile development does not propagate through the bed as an observable concentration front, rather it emanates slowly down from the top of the bed like a subsiding wave.

The slow development of the frontal adsorption-curve after breakthrough in Figure 8.3 reflects the high adsorption capacity within the bed. Strong protein adsorption within particles appears able to maintain a strong driving force for inter-phase mass transfer over an extended period, despite intraparticle-diffusion limitations. The numerical bulk-phase concentration profiles in Figure 8.3 illustrate that profile development is characterised by

shallow concentration gradients at the exit of the packed bed. This may explain why delays induced by increased external-film mass transfer are able to suppress the influence of premature breakthrough. As void volume (and retention time of the bed) is reduced, variations in effluent concentration are induced as proteins prematurely leave the bed. This increase (or decrease) in concentration depends on the concentration gradient that exists at the bottom of the bed. Shallow concentration gradients would conceal or minimise any observable variations in effluent concentration.

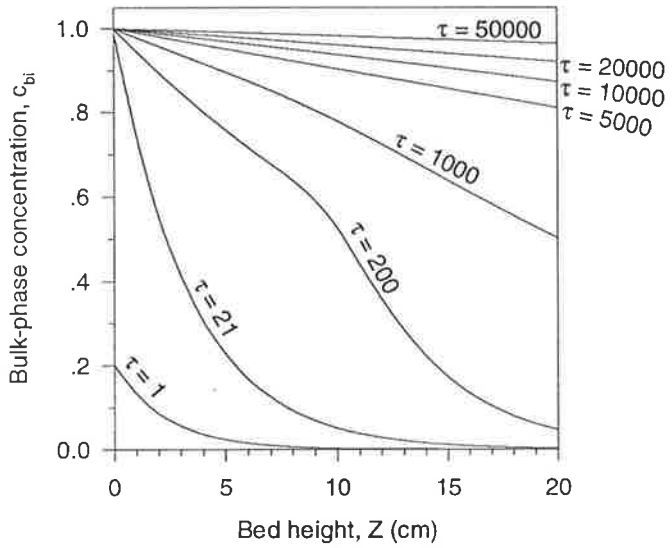

Figure 8.3: Chronological development of bulk-phase concentration profiles for lactoperoxidase in a packed bed during a binary-component frontal-adsorption simulation (compression effects excluded).

Further frontal adsorption simulations were conducted. Original model simulations were replicated, however, initial resin particle diameter was halved (to 83.5 μm). Similarity was maintained by reducing superficial velocity by a factor of four (to 9.25 cm/min). Consequently, pressure-drop and porosity profiles (*eq.s* 7.9 and 7.11) for each column were identical to those described above. Sauter-mean particle-diameter variations in each column were recalculated. Sauter-mean particle diameter correlated to bed height for laboratory- and production-scale columns, respectively, were

$$d_{pS}(Z) = (1.666\text{x}10^{-4} - 2.346\text{x}10^{-5}\,Z + 7.099\text{x}10^{-5}\,Z^2)/2 \qquad (8.3)$$

$$d_{pS}(Z) = (1.665\text{x}10^{-4} - 2.261\text{x}10^{-5}\,Z - 9.064\text{x}10^{-5}\,Z^2)/2 \qquad (8.4)$$

Remaining model parameters were unchanged. Table 8.3 summarises the variation in important model parameters and values of key dimensionless numbers for each simulation. Decreasing particle diameter and superficial velocity increase Peclet number and decrease Biot number in the packed-bed.

Table 8.3: Modified values of important system and component model parameters and key dimensionless groups for modified (resin particle size halved) frontal-adsorption simulations.

System		Component		
v	26.0[1] ,28.7[2], 40.8[3] cm/min		**Lactoferrin**	**Lactoperoxidase**
d_p	83.5[1], 82.6[2], 79.6[3] mm	**Pe**	1373[1], 1536[2],2261[3]	1373[1], 1536[2],2261[3]
Re	0.129[1], 0.127[2], 0.123[3]	**Bi**	580[1], 607[2], 725[3]	232[1], 243[2], 288[3]
		η	0.080[1], 0.074[2], 0.056[3]	0.199[1], 0.184[2], 0.139[3]
		ξ	250[1], 283[2], 414[3]	250[1], 283[2], 414[3]

1 Compression excluded or at top of compressed packed beds in laboratory- and production-scale columns.

2 At bottom of packed bed (maximum compression) in the laboratory-scale column.

3 At bottom of packed bed (maximum compression) in the production-scale column.

Figure 8.4 shows frontal adsorption curves for all simulations. Again, premature breakthrough is not observed. Increasing compression appears to delay emerging breakthrough curves (see Inset 1 - Figure 8.4). Once more, it appears that initial compression-induced increases in inter-phase mass transfer delay breakthrough. However, subsequent curve development does show signs of accelerated curve development (see Inset 2 - Figure 8.4). Curve profiles of both proteins emerge earlier from the production-scale column compared to their laboratory-scale counterparts. The maximum concentration observed during 'roll-up' of lactoperoxidase is higher.

Variations in curve profiles are obscured by the logarithmic scale for dimensionless time. Linear scales in figure insets give a true indication. Delays in emerging breakthrough curves are almost 100 dimensionless time units (see Inset 1 - Figure 8.4). This could be regarded as significant, but is trivial compared to the time at which breakthrough occurs. During the latter stages, breakthrough curves in the production-scale column emerge up to 150

dimensionless time unit (see Inset 2 - Figure 8.4) earlier than their laboratory-scale counterparts.

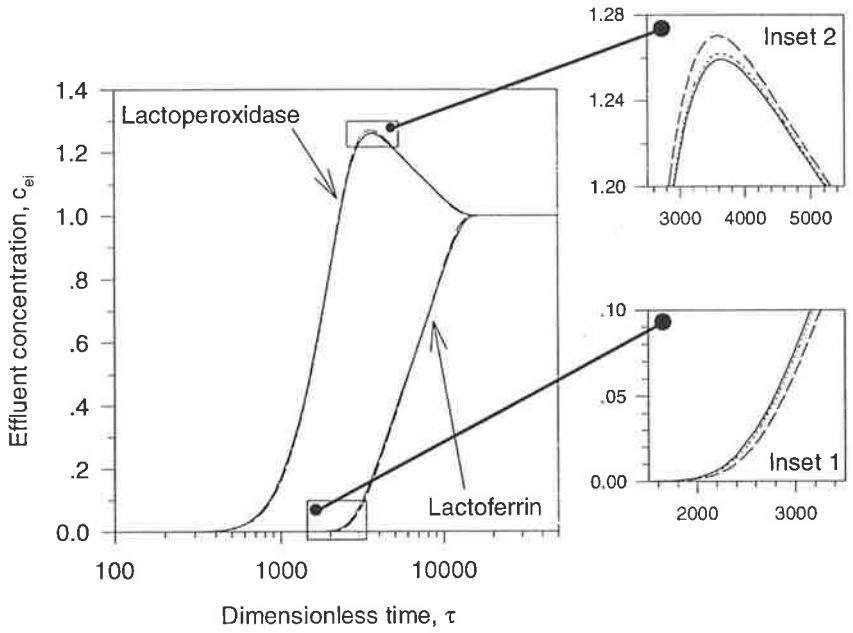

Figure 8.4: Modified (resin particle size halved) frontal-adsorption model predictions with compression effects excluded (——) and for compressed packed beds in the laboratory- (·····) and production-scale (— —) column.

The initial delays in emerging breakthrough curves exceed those in original model simulations shown in Figure 8.2. With a lower Biot number, compression-induced changes in external-film mass transfer appear to have a greater influence on effluent curve profiles. However, subsequent behaviour is dominated by accelerated curve development. This reflects the rapid development of the frontal adsorption curve. Higher bulk-phase concentration gradients are present at the bottom of the packed bed. These steep concentration gradients would induce higher effluent protein concentration as premature exit from the bed occurs.

Interestingly, Figure 8.4 indicates a greater feed volume can be applied to the packed bed before breakthrough occurs. Almost fifteen times more than in original model simulations. This means higher adsorption of feed proteins per cycle can be achieved during frontal adsorption. The early breakthrough that occurs in Figure 8.3 is delayed. Evidently, the smaller resin particle or lower superficial velocity alleviate the undesirable affects of intraparticle-diffusion limitations in the WGFE ion-exchange system. Unfortunately,

reducing superficial velocity leads to a four-fold increase in loading time per unit feed volume. In the same period of time, four column volumes at 35 cm/min can be applied to the packed bed compared to one column volume at 9.25 cm/min. Although, this is clearly offset by the feed volume increases that can be obtained.

In summary, two competing mechanisms act to influence compression-induced variations in system behaviour during frontal adsorption for this system. Delays are caused by compression-induced changes in external-film mass transfer. These occur while intraparticle-diffusion limitations do not apply to inter-phase mass transfer. The reduction in void volume causes premature breakthrough and accelerated development of effluent concentration profiles. Its extent depends on transient variations in bulk-phase concentration profiles at the exit to a packed bed. The presence and magnitude of either mechanism is a function of system characteristics. These studies do not allow examination of this relationship. A more fundamental study is required. Most importantly, however, compression does not markedly effect system behaviour during frontal adsorption. In fact, increased inter-phase mass transfer appears to enhance adsorption and delay breakthrough.

However, it is important to note that compression effects on intraparticle diffusion and adsorption capacity were not considered. Their impact on the WGFE ion-exchange system during frontal adsorption remain unquantified.

8.4 Compression Effects during Step-Elution

The original (*ie* particle diameter 167 μm) binary-component frontal-adsorption simulations in Section 8.2 were repeated. Loading was terminated after 295 dimensionless time units and a wash step performed. The duration of the wash step was 10 dimensionless time units. Two step elutions were applied. The first, with 0.4 M salt solution, for a period of 25 dimensionless time units. The second, with 1.0 M salt, continued until effluent protein concentration was negligible. During frontal adsorption, model parameters described above were retained. Model parameters for frontal adsorption were applied to the wash step. Binary-component step-elution adsorption equilibria were described by single-component extended Langmuir-Freundlich isotherm parameters. The sodium citrate buffer concentration in feed and wash solutions was 50 mM. Physical properties of the feed, wash

and eluent solutions were assumed to be identical to those of water at 20°C . Important model parameters and values of key dimensionless numbers during elution steps for each simulation are summarised in Table 8.4. During all simulations, step increases and decreases in feed concentration profiles were described by the Sigmoid-type function in *eq.* 8.2.

Table 8.4: Important component model parameters and values of key dimensionless groups employed for step-elution simulations in laboratory- and production-scale columns.

	Component	
	Lactoferrin	**Lactoperoxidase**
C_f	0 M	0 M
C_o	0 M	0 M
Pe	710[1], 793[2],1167[3]	710[1], 793[2],1167[3]
Bi	105[1], 110[2], 131[3]	105[1], 110[2], 131[3]
η	0.057[1], 0.053[2], 0.040[3]	0.057[1], 0.053[2], 0.040[3]
ξ	32.5[1], 36.7[2], 53.7[3]	32.5[1], 36.7[2], 53.7[3]
Da^a, 0.4M[4]	1000	1000
Da^d, 0.4M[4]	75400	7.11×10^5
Da^a, 1.0M[4]	1000	1000
Da^d, 1.0M[4]	1.16×10^6	7.8×10^6

1 Compression excluded or at top of compressed packed beds in laboratory- and production-scale columns.

2 At bottom of packed bed (maximum compression) in the laboratory-scale column.

3 At bottom of packed bed (maximum compression) in the production-scale column.

4 Damköhler numbers for each protein at 0.4 and 1.0 M salt concentration. These values are not constant during model simulations, but vary with salt concentration in the column.

Figure 8.5 illustrates the step-elution breakthrough curves for all simulations. As for frontal adsorption, breakthrough curves during each step-elution appear to be almost identical. Only small variations in curve profiles can be observed. These are highlighted in figure insets (see Insets 1 & 2 - Figure 8.5). Premature breakthrough and accelerated curve development dominate effluent concentration profiles. Higher concentrations are observed as curve profiles peak. This behaviour is not surprising given the high concentration gradients that would be generated at the exit to the packed bed during elution. However, Biot numbers are much lower than during frontal adsorption. Even though they still exceed

20, one might expect compression-induced changes in external-film mass transfer would have a greater influence given the large moving bulk-phase concentration variations experienced in resin particles within the packed bed. This may also be the case. Of the two mechanisms, premature breakthrough appears to eclipse any compression-induced delays that exist.

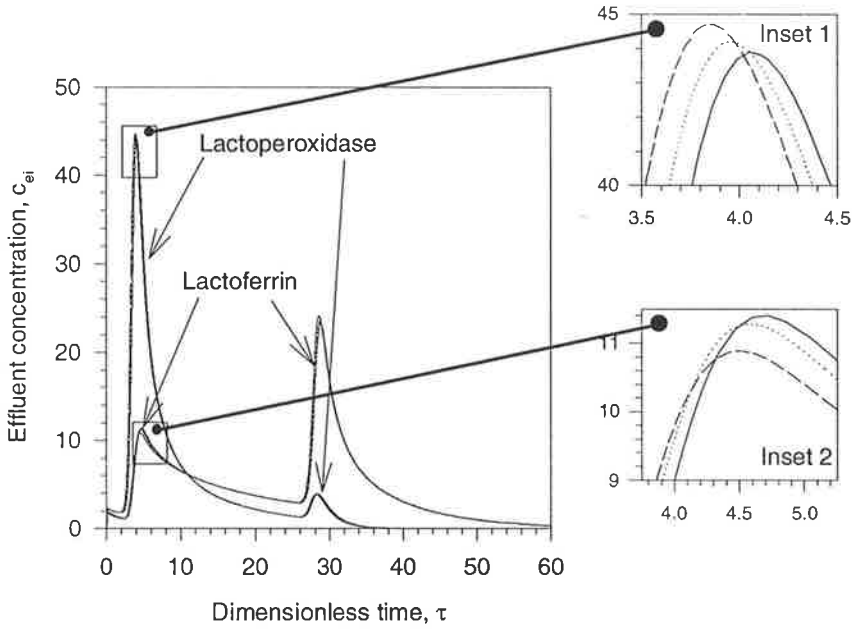

Figure 8.5: Compressed-bed simulations: step-elution model predictions with compression effects excluded (——) and for compressed packed beds in the laboratory- (·····) and production-scale (— —) column.

However, the minor lactoferrin peak (0.4 M salt step-elution) does display contrary behaviour (see Inset 2 - Figure 8.5). Although increasing compression induces premature development of effluent curve profiles, peak concentrations decrease. In this case, compression-induced changes in inter-phase mass appear to dominate the influence of premature breakthrough and accelerated curve development

Modified (*ie* resin particle diameter halved to 83.5 μm) model simulations performed during binary-component frontal-adsorption studies in Section 8.3 were repeated. Compression effects on step-elution were examined. The sequence and duration of feed, wash and step-elution stages were identical to original model simulations described above. Modified values of important model parameters and key dimensionless numbers for these simulations are summarised in Table 8.5.

Table 8.5: Compressed-bed simulations: modified values of component model parameters and key dimensionless groups used in modified (resin particle halved) step-elution simulations.

	Component	
	Lactoferrin	**Lactoperoxidase**
Pe	1373[1], 1536[2],2261[3]	1373[1], 1536[2],2261[3]
Bi	54[1], 56[2], 67[3]	54[1], 56[2], 67[3]
η	0.861[1], 0.798[2], 0.606[3]	0.861[1], 0.798[2], 0.606[3]
ξ	250[1], 283[2], 414[3]	250[1], 283[2], 414[3]

1 Compression excluded or at top of compressed packed beds in laboratory- and production-scale columns.

2 At bottom of packed bed (maximum compression) in the laboratory-scale column.

3 At bottom of packed bed (maximum compression) in the production-scale column.

Breakthrough curves for all simulations are illustrated in Figure 8.6. While premature breakthrough is clearly observed in all elution peaks, no signs of compression-induced delays are apparent even though the Biot number is lower. Premature breakthrough is the dominant mechanism influencing compression-induced changes in effluent curve profiles. Once more, the variations observed in Figure 8.6 (refer Insets 1 & 2) are trivial when compared to the size and magnitude of effluent curve profiles. Smaller particles do not markedly increase compression effects during elution.

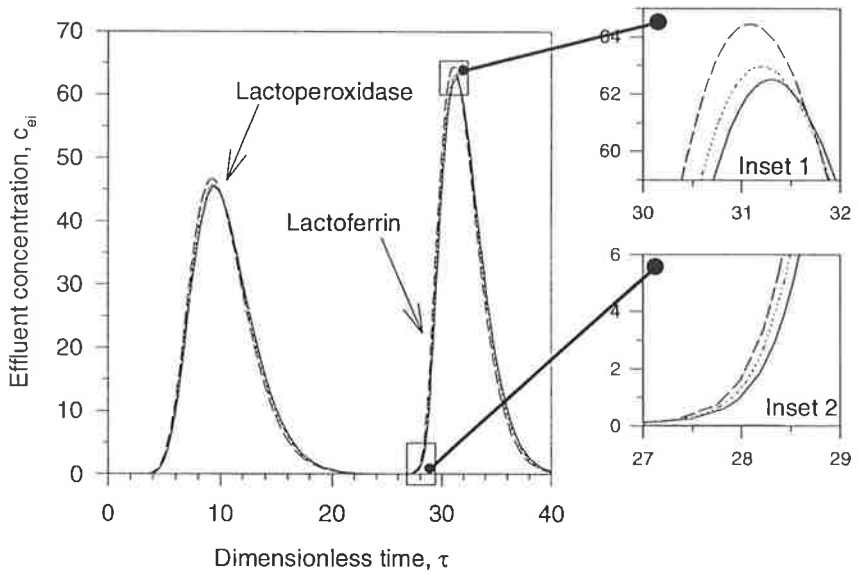

Figure 8.6: Modified (resin particle diameter halved) step-elution model predictions with compression effects excluded (——) and for compressed packed beds in the laboratory- (·····) and production-scale (— —) column.

Interestingly, the asymmetric elution peaks in Figure 8.6 are much larger in area compared to the skewed profiles observed in Figure 8.5. Higher amounts of protein are eluted from the packed bed containing smaller resin particles. This confirms observations of greater protein uptake during frontal adsorption in Figure 8.4. The asymmetric elution peaks in Figure 8.6 also eliminate protein carry-over from the 0.4 M to 1.0 M step. Furthermore, minor lactoferrin and lactoperoxidase peaks co-eluting with major lactoperoxidase and lactoferrin peaks, respectively, have disappeared. Step-elutions are now able to clearly separate each component. Only lactoperoxidase is eluted during the 0.4 M salt step elution and lactoferrin at 1.0 M. Lactoferrin contamination in the WGFE product is removed without the need for further processing. These outcomes would be clearly desirable for the WGFE ion-exchange system. Whether they are a function of lower superficial velocity or smaller particle diameter, or both, cannot be identified. Such observations warrant further investigation and confirm observations in Section 8.3. Perhaps, a smaller resin particle diameter or lower superficial velocity may be more appropriate for the WGFE ion-exchange system.

8.5 Concluding Remarks

Compression effects on the scale-up of a commercial ion-exchange process to manufacture WGFE have been investigated using a modified non-linear multicomponent rate-equation chromatography model. System behaviour during frontal adsorption and step-elution was simulated by using model parameters for two major whey proteins, namely lactoperoxidase and lactoferrin. The impact of compression on system behaviour in two packed beds of varying compression in 2 and 20 cm internal-diameter columns was compared. Variation in porosity and Sauter-mean particle diameter for each column were determined from in-direct technique based on the new model for pressure-drop prediction developed in Part I of this thesis.

For both frontal adsorption and step elution, system behaviour was largely independent of compression. Increasing compression generated only small and trivial variations in effluent concentration profiles. Two competing mechanisms appeared to influence these variations. Bed compression decreased void volume producing premature breakthrough and accelerated development of effluent concentration profiles. Compression-induced changes

in external-film mass transfer caused delays. Decreasing particle diameter and superficial velocity did not markedly alter the influence of compression effects. However, compression effects on intraparticle diffusion, intraparticle voidage and adsorption capacity were not considered. Their contribution to observed behaviour described above is unquantified. In their absence, however, it can be concluded that the impact of increased compression does not need to be considered during scale-up of the WGFE ion-exchange system.

The results of this study cannot be easily generalised. A more fundamental study of compression effects is required.

While the aim of this chapter was to investigate compression effects, another important observation was made. Namely, the impact of resin particle size and superficial velocity on system behaviour. Decreasing both particle diameter and superficial velocity had a profound effect on WGFE ion-exchange system behaviour. During frontal adsorption, it delayed breakthrough increasing the volume of whey that could be sustained by the packed bed during each cycle. For elution, it eliminated tailing and skew from elution peaks. It also isolated each protein in their respective step-elution peaks, and eliminated protein carry-over. These variations can all be regarded as beneficial for performance of the WGFE ion-exchange system. Unfortunately, this claim must be considered speculative. A further and more extensive investigation into the impact of resin particle size and superficial velocity on WGFE ion-exchange system behaviour is required.

Part III: Optimisation

CHAPTER 9

SCALE-UP & OPTIMISATION

9.1 Objective - Part III

The aim of Part III in this thesis is to investigate the optimal design for scale-up of the WGFE ion-exchange system.

9.2 Preamble - Part III

Part II of this thesis introduced a modified general non-linear multicomponent rate-equation model. It was used to simulate the behaviour of the WGFE ion-exchange system and investigate the impact of compression effects. While model predictions of system behaviour were not perfect, the model can also serve as a useful tool to help optimise the scale-up of the WGFE ion-exchange system. The impact of important design parameters on its performance can be examined by simulation.

In this Chapter, the overall process economics of the WGFE ion-exchange system during scale-up will be examined. The general non-linear multicomponent rate-equation chromatography model will be employed to simulate the behaviour of the WGFE ion-exchange system. Various combinations of two selected design parameters: frontal-adsorption superficial velocity and packed-bed height, will be trialed to assess their impact on different performance indicators. A system of cost-capacity equations to describe the process economics of the WGFE ion-exchange system will be established and correlated to system behaviour. The sensitivity of a dimensionless operating cost to frontal-adsorption superficial velocity and packed-bed height will be investigated. A set of design parameters which optimise the cost of a proposed commercial-scale WGFE ion-exchange system are discovered.

9.3 Background Art - Optimisation of Chromatography

Chromatographic scale-up is a common topic in the literature. However, very few published reports explicitly refer to optimisation of cost. Instead, they refer to optimisation of some type of performance indicator. For example, Gallant et al. (1995) considered the 'optimisation' of step-gradient separations of proteins α-chymotrypsinomogen, cytochrome-C and lysozyme. The study used production rate, PR, as a performance indicator:

$$PR_i = \frac{C_i V_f Y_i}{t_{cyc} V_{col}} \tag{9.1}$$

where C_i was the mobile-phase concentration of an individual protein; V_f its the feed volume; Y_i its cyclic yield; t_{cyc} is the cycle time of the chromatographic step; and V_{col} was the empty column volume. The production rate in *eq.* 9.1 essentially refers to the quantity of protein generated per unit time per unit resin volume. A combination of mathematical model simulation and experiment were used in the study to vary the step-elution concentration, and its time period, to maximise PR. Gallant *et al.* (1995) proposed that to maximising PR would also minimise the resin volume required by the chromatographic system during scale-up, and therefore, its cost.

In contrast, a study by Wankat & Moo (1988) on scaling rules for protein separation during isocratic elution identified resolution, R_N, as its objective function:

$$R_N = \frac{R_{new}}{R_{old}} = \frac{\left(L_{new}/L_{old}\right)\left(D_{new}/D_{old}\right)^{2n}}{\left(d_{p,new}/d_{p,old}\right)^{n+1}\left(Q_{new}/Q_{old}\right)^{n}} \tag{9.2}$$

where L was the packed bed height; D was the column diameter, d_p was the resin particle diameter; Q was flowrate; and n an empirical exponent. The aim of the study was not to maximise or minimise *eq.* 9.2, but rather ensure R_N remained equal to one during scale-up. The flowrate, particle diameter and column diameter in a chromatographic system could all

be safely increased, without compromising the efficacy of the desired separation. A corresponding reduction in cost of the chromatographic system was expected.

These two examples can be referred to as heuristic techniques. They each consist of an objective function (*ie eq.s* 9.1 and 9.2), and a set of simplified rules designed to allow a particular state of the objective function to be realised (*ie* maximised, minimised *etc*). A common feature of each technique was a loose correlation between either, the objective function, or simplified rules, with cost.

These examples also reflect the wider approach to process scale-up in biotechnology. Instead of cost, the biochemical engineer most often sets out to optimise, or maximise, the yield and purity of a desired product. This is indicative of the high added value of many commercial biological-derived products which far outstrip their cost of manufacture. The greatest profit is directly proportional to the purity and quantity of product that is generated. Additionally, the biochemical engineer also considers the opportunity cost involved with development and scale-up of a process. From the time a new product is discovered, and a patent application is submitted, it is essential to complete process development and gain regulatory approval as quickly as possible (Petrides *et al.*, 1989). Shortening the time to market is critical to take advantage of a products monopoly during its patent protection period and to maximise financial return. In the majority of cases, the challenge is to scale-up an existing laboratory technique in the most accurate, reliable, cost-effective and expeditious manner (Middelberg, 1992).

Heuristic techniques play an important role in helping the biochemical engineer achieve this goal (Middelberg, 1995). A simplified set of rules allow the scale of a laboratory process to be successfully increased with reasonable certainty to meet a desirable performance criteria or some other goal defined by its objective function. In many cases, the objective function, or the design parameters of the process which are varied to achieve it, have some association with cost.

Besides the two presented in this Section, there are many other examples of heuristic techniques that have been developed for chromatographic scale-up. The reader can find some enjoyable reading in articles by Janson and Hedman (1987), Kang and Ryu (1991), Mohammad *et al.* (1992), Felinger and Guiochon (1994) and Jennings *et al.* (1995),. In

most cases, the objective function or goal is described by various terms that relate to some measure of performance. Resolution, recovery, throughput and productivity are common examples. The design parameters which are varied to achieve the goal include column size, flowrate, packed-bed height, protein or modulator concentration. However, because there are so many different chromatographic techniques and applications, the goals and design parameters employed in different heuristic techniques vary widely. The terms used to describe them are also often quite indeterminate, except in the context for which they are applied. It is difficult to generalise.

However, one particular heuristic approach does stand out. It appears to be widely used in biotechnology for chromatographic scale-up. It is unusual in that it does not employ an explicit objective function or goal. Instead, the approach to scale-up is governed only by general rules. These depend on whether the separation is step or gradient elution. For gradient-elution, the rules are generally:

MAINTAIN:

- Bed height
- Linear flow
- Sample concentration
- Gradient volume: media volume

INCREASE:

- Sample load
- Volumetric flowrate
- Column diameter

For step-elution, the rules become:

INCREASE:

- Sample load
- Linear flow and therefore volumetric flowrate (with pressure drop as the constraint)
- Column diameter
- Sample concentration
- Particle diameter (to increase flowrate)

DECREASE:

- Bed height (if pressure drop remains a problem)

The different rules for gradient and step elution reflect their distinct modes of separation. Resolution and bandwidth are important in gradient elution and can only be effectively maintained by keeping sample concentration, packed-bed height, particle diameter and linear flowrate constant. A chromatographic system which employs step-elution does not suffer from this constraint. The rate at which the elution of a desired product takes place rarely influences the separation performed in a subsequent step-elution.

While there is no explicit objective function in this heuristic technique, some implicit goals can be recognised. For gradient-elution, the goal is to scale-up the chromatographic system without compromising the integrity of the separation. The goal for step-elution is to scale-up the chromatographic system to maximise its productivity. Productivity is similar to the production rate defined by Gallant *et al.* (1995) in *eq.* 9.1. It represents the product yield per unit time per unit volume resin.

These goals also reflect the relative position of step- and gradient-elution techniques in the purification scheme for a process. Step-elution is conventionally employed upstream for separation. The target stream is large in volume with a low product concentration. The aim is to recover the desired product as quickly as possible. The scale of the chromatographic systems is relatively large and maximising productivity will minimise resin volume, and therefore, cost. Gradient elutions are used downstream for purification, rather than separation. The aim is to eliminate impurities from the desired product for its final formulation. The target stream is small in volume and high in product concentration. The chromatographic system is smaller in scale. Maintaining product yield and purity during scale-up is more important than achieving a reduction in processing cost.

There is no exact origin for this heuristic technique, rather it seems to be a historical artefact of chromatographic scale-up practice in the biotechnology industry. In fact, Pharmacia, the industry's leading manufacturer of chromatographic resin, actively promotes this type of heuristic approach to its customers (Pharmacia LKB Technology, 1991). In using Pharmacia resins, the CRC for Tissue Growth and Repair relied on the advice of Pharmacia in its efforts to scale-up of the WGFE ion-exchange step. This was briefly discussed in Chapter 1.

In conclusion, there is no published generic technique or procedure for optimisation of cost during scale-up of a chromatographic system. There are heuristic techniques, but these are largely designed to expeditiously scale-up existing laboratory techniques. Many are based on an objective function or scale-up goal which describes performance or separation efficiency. Simplistic rules are used to vary design parameters to satisfy the objective function or scale-up goal. To optimise cost during the scale-up of the WGFE ion-exchange system, an alternative must be considered.

9.4 Study Methodology

The conventional chemical engineering approach to optimising the cost during scale-up is to develop a comprehensive design for the proposed process. This design is correlated to an appropriate objective function which describes its cost. Alternative design scenarios are then considered, and the sensitivity of the objective function to various design parameters is investigated. The optimal design which minimises cost is selected.

Similarly, this study will attempt to develop a comprehensive design for the WGFE ion-exchange system in a proposed commercial facility. The commercial facility will be located in dairy factory which generates cheese whey. Its design capacity will be 200 kL of whey per week. It will operate continuously 24 hours a day for 351 days each year.

The design will be based on the simplified schematic of the WGFE ion-exchange system in the commercial facility displayed in Figure 9.1. The WGFE ion-exchange system is considered separate to other processes in the commercial facility. Only the equipment in the commercial facility in the immediate vicinity is included. The ion-exchange system receives microfiltered whey from the microfiltration process in the proposed commercial facility. It is stored in a tank and then loaded onto a series of ion-exchange columns. The frontal adsorption step is terminated at breakthrough. Column effluent during the load step is discharged to an external factory waste stream. A wash step is performed with deionised water from the tank farm. Column effluent is discharged to the factory waste stream. The wash step is concluded and the first step elution initiated. Pre-prepared 0.4 M sodium chloride at a pH of 6.5 from the tank farm is applied to each column. Column effluent is collected and stored in a tank. It is subsequently ultrafiltered and then sent for further processing in another part of the commercial facility. The second step-elution is

commenced with 1.0 M NaCl. A second wash step is performed with deionised water. The sanitisation step is performed with 1.0 M NaOH. This is followed by another wash step. Column effluent in each of these subsequent steps is discharged to the factory waste stream. The WGFE ion-exchange cycle is complete. The entire sequence may be repeated. A single integrated pump and control system controls the entire chromatographic process. It operates pumps and actuates valves throughout the system.

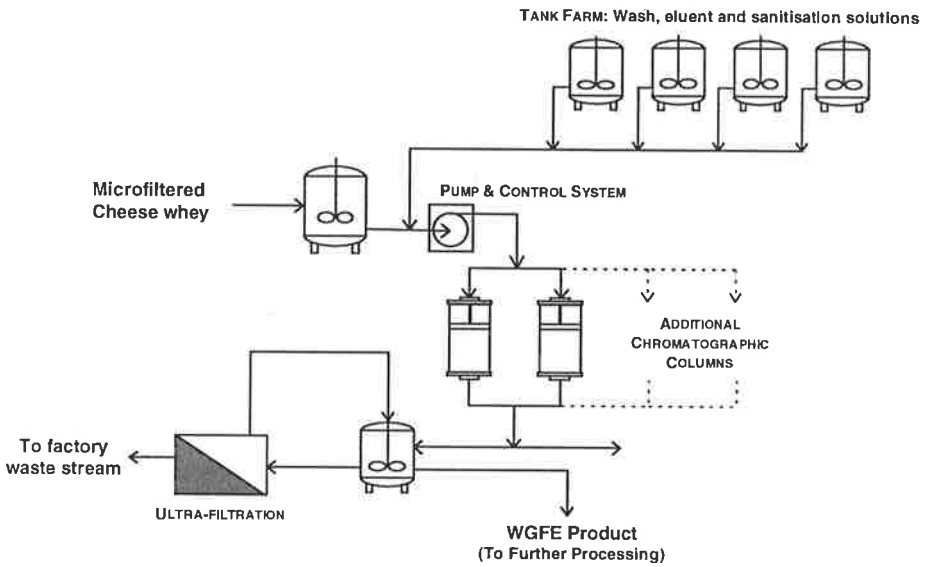

Figure 9.1: A simplified schematic of the WGFE ion-exchange system and associated equipment in the proposed production-scale facility.

9.5 Scale-up studies - Key design variables

A comprehensive design for a commercial-scale facility is to be developed. This will be used to examine the cost of the facility and investigate its sensitivity to various design parameters. This will allow an optimal design to be identified.

There are numerous design variables in the WGFE ion-exchange system which could be used during scale-up to optimise cost. For example, the superficial velocity in each step, the packed-bed height, the concentration of salt in the eluent or the pH of the microfiltered whey. Even the resin particle size could be considered. It is clearly not possible to examine every possible permutation. Instead, it is desirable to select those design parameters which will have the greatest influence on the current performance of the system and its overall cost. Whilst performing an optimisation, the variations which are considered must also be

practical. They must be easily incorporated into the current design and operation of the WGFE ion-exchange system without compromising the integrity of the existing separation and quality of the WGFE product.

For the purpose of this study, two design variables will be investigated. These are superficial velocity during the frontal-adsorption step in the WGFE ion-exchange cycle and packed-bed height in the column. The frontal-adsorption step chronologically dominates the WGFE ion-exchange cycle. For example, the load step in the pilot-plant takes 3.2 hours, while primary wash, 0.4 M and 1.0 M step elution, secondary wash and sanitisation and final wash steps take 25, 11, 6.5, 8 and 25 min, respectively. The volume of microfiltered whey applied to the column during frontal adsorption also determines the quantity of WGFE product recovered in each cycle. The impact of superficial velocity on breakthrough, the termination point during frontal adsorption, has already been observed in Part II. Likewise, the packed-bed height will set the total adsorption capacity which is available during frontal adsorption It will also control the total WGFE product that can be adsorbed prior to breakthrough.

While superficial velocity and packed-bed height have a minor influence on other steps, it is likely that performance and cost of the WGFE ion-exchange system will be significantly affected by a variation in each of these parameters during frontal adsorption. Furthermore, a variation in each parameter is unlikely to alter the WGFE product characteristics if all other design and operational parameters in the WGFE ion-exchange system remain relatively constant.

9.6 Scale-up studies - System Design

The general non-linear multicomponent rate-equation chromatography model used in Part II of this thesis can be employed to investigate the impact of superficial velocity and packed-bed height on the frontal-adsorption step in the WGFE ion-exchange system. A key assumption will be employed to make this possible. Namely, lactoperoxidase and lactoferrin can be used to quantitatively represent two separate fractions in the microfiltered whey. Lactoperoxidase will represent that fraction which is the WGFE product. It presence in column effluent during frontal adsorption at breakthrough is the termination point for this step. Similarly, the recovery of lactoperoxidase in the first step elution is directly

proportional to the active components of the WGFE product that provide its growth promoting capability.

The remaining fraction is lactoferrin which will represent itself. It competes with lactoperoxidase during frontal adsorption to determine the behaviour of the WGFE ion-exchange system during this step. In a similar manner, it also interacts with lactoperoxidase during the first step elution.

Model simulations were performed to investigate the impact of superficial velocity (2-20 cm/min) and packed bed height (10-30 cm) on the frontal adsorption step in the WGFE ion-exchange system. The pH of the microfiltered whey was assumed equal to 6.5. All model parameters are identical to those presented in Chapter 6 and to those employed for model-validation studies in the same chapter. Protein concentration of lactoperoxidase and lactoferrin in the whey feed were assumed to be 0.1 mg/ml. This is slightly higher than the concentration values in raw whey, but reflects the concentrating effect of the microfiltration step. Multicomponent Langmuir isotherm parameters were used to replicate binary-component adsorption equilibria. Compression effects were not considered and porosity and Sauter-mean particle diameter in the packed bed were fixed at values of 0.356 and 167 μm, respectively. Different finite-element and collocation-point combinations were employed in each simulation depending on the packed-bed height and superficial velocity. These were specified prior to simulation by using single component model simulations with lactoferrin to determine optimal numerical parameters. At least 11 collocation points were employed in each simulation to describe internal particle-phase concentration profiles. To minimise finite elements, the Sigmoid-type function of *eq.* 8.2 was used to imitate the feed concentration profile of each protein. Typical numbers of finite elements employed for simulation ranged from 9 at a bed height of 10 cm and superficial velocity of 2 cm/min, to 16 at a bed height of 10 cm and superficial velocity of 20 cm/min.

Figure 9.2 displays the frontal-adsorption breakthrough curve of lactoperoxidase for three separate simulations. It illustrates the variation in dimensionless effluent concentration with dimensionless time in the WGFE ion-exchange system for different combinations of bed height and superficial velocity. These combinations are 15 cm and 5 cm/min, 30 cm and 5 cm/min, and 30 cm and 20 cm/min for bed height and superficial velocity, respectively.

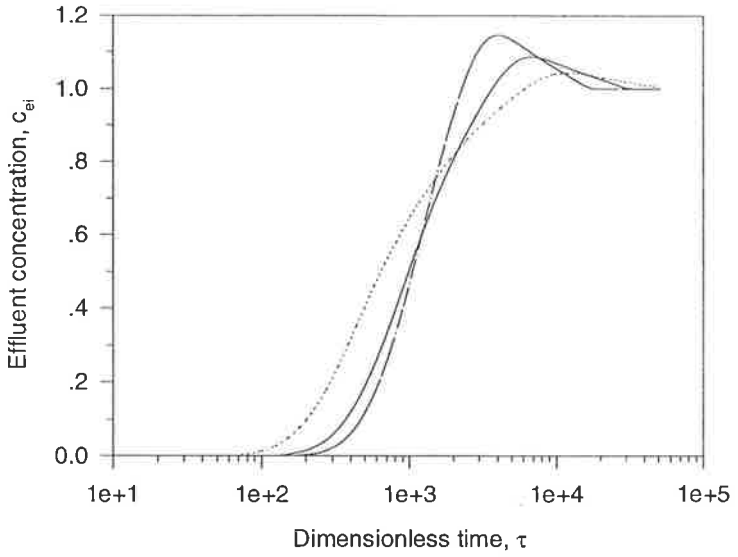

Figure 9.2: Frontal-adsorption breakthrough curve for lactoperoxidase in the WGFE ion-exchange system at different combinations of bed height and superficial velocity: L_i=15 cm, v_{sup}=5 cm/min - (——); L_i=30 cm, v_{sup}=5 cm/min - (— · —); L_i=30 cm, v_{sup}=20 cm/min - (·····).

The breakthrough curves in Figure 9.2 yields important information about the behaviour of the WGFE ion-exchange system during scale-up. For example, the breakthrough point in Figure 9.2 (*ie* when protein is detected in the column effluent) represents the termination point in the frontal-adsorption step when the microfiltered whey in the column feed is replaced by deionised water for the wash step. Its value gives an indication of the relative volume of whey that can be sustained by the ion-exchange system each cycle. The volume of whey is proportional to the quantity of WGFE product which is ultimately recovered. Present measurements in the pilot plant indicate that at least 40g of WGFE product will be generated from every ton or kilolitre of microfiltered whey which is processed.

In this respect, the impact of bed height and superficial velocity on breakthrough can be clearly observed. Quite simply, an increase in superficial velocity will decrease the whey volume that can be applied per cycle and therefore the cyclic WGFE product yield, while an increase in bed height will increase whey volume and cyclic WGFE product yield. These observations are confirmed in Figure 9.3. It presents a contour plot which summarises the variation in dimensionless time at breakthrough with superficial velocity and bed height. The breakthrough point for each simulation was selected as 0.5% of lactoperoxidase feed concentration in column effluent. This was considered the lower limit of detection for the

lactoperoxidase enzyme assay currently employed to monitor breakthrough in the pilot plant.

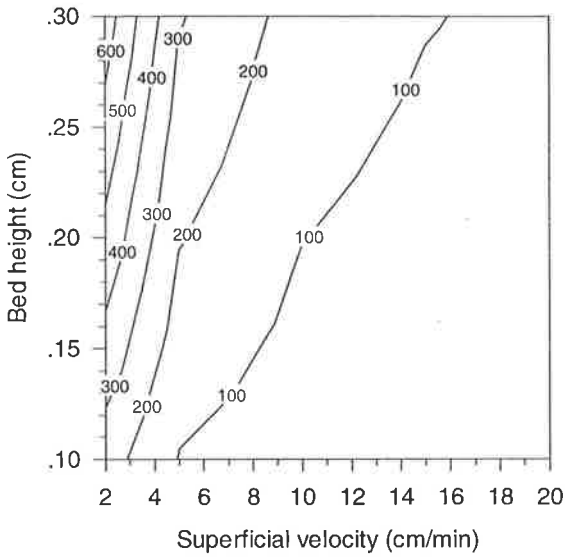

Figure 9.3: Contour plot of dimensionless time at breakthrough during frontal-adsorption model simulations.

Figure 9.3 demonstrates that it is not safe to assume that the quantity of WGFE product recovered per cycle will not remain constant as superficial velocity increases. In fact, a higher superficial velocity will significantly diminish the cyclic WGFE product yield as measured by whey volume. For example, at a bed height of 20 cm, an increase in superficial velocity from 2 cm/min to 20 cm/min leads to 22-fold decrease in whey volume based on dimensionless time values. Similar behaviour is observed at other bed heights. This reflects the undesirable impact of intraparticle-diffusion limitations which are present in the WGFE ion-exchange system. Intraparticle diffusion controls the total protein adsorption rate in the ion-exchange system during the frontal-adsorption step, and remains relatively constant, despite any variation in superficial velocity.

The data in Figure 9.3 can be used to make a quantitative estimate of the variation in cycle time with frontal-adsorption superficial velocity and packed-bed height. This requires a number of assumptions regarding the operation and performance of remaining steps in the WGFE ion-exchange cycle. First, their superficial velocity remains identical to current operating conditions in the pilot-plant. Second, time periods for wash, elution and sanitisation steps monitored under pilot-plant operating conditions (L_i = 21 cm and v_{sup} =

8.5 cm/min) remain constant regardless of the superficial velocity in the frontal-adsorption step. Third, these time periods can be adapted proportionally to account for bed height. For example, if the proposed bed height for the ion-exchange step was 10.5 cm, time periods for wash, elution and sanitisation steps would be halved before being added to the model prediction for breakthrough time during frontal adsorption.

Dimensionless breakthrough time data in Figure 9.3 were converted to real time. These values were added to the time periods for primary wash, 0.4 and 1.0 M step elutions, secondary wash and sanitisation steps, and adapted for bed height, to determine cycle time. The results are presented in the contour plot displayed in Figure 9.4.

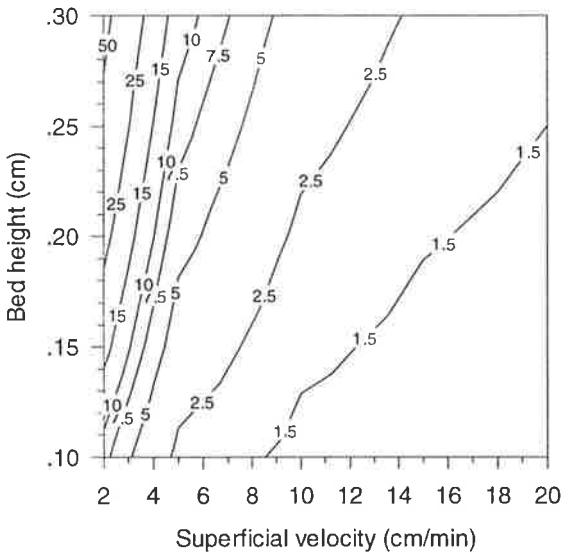

Figure 9.4: Contour plot of cycle time as a function of superficial velocity and packed-bed height.

Figure 9.4 illustrates the benefit of increasing superficial velocity during frontal adsorption. It decreases the cycle time in the WGFE ion-exchange system and allows more cycles to be performed in a unit period of time.

The cycle time and dimensionless time at breakthrough for the frontal adsorption step can be employed to determine the productivity, Ψ, of the WGFE ion-exchange system:

$$\Psi = \frac{t_{bk}\, Q_f\, Y_p}{V_b}\,\omega_c = \frac{\tau_{bk}}{\varepsilon}\, Y_p\, \frac{24 \text{ hours}}{t_{cyc}} \qquad (9.3)$$

where t_{bk} is the (real) time at breakthrough during frontal adsorption; Q_f is the volumetric flowrate of whey; V_b is the volume of chromatographic resin in the packed bed; Y_p is the WGFE product yield per litre of whey; ω_c is the number of cycles (per day); τ_{bk} is the dimensionless time at breakthrough during frontal adsorption; and t_{cyc} is the (real) cycle time in hours.

Data presented in Figures 9.3 and 9.4 for τ_{bk} and t_{cyc}, respectively were combined with a value of 40 mg per litre of whey for Y_p. The productivity of the WGFE ion-exchange system as a function of superficial velocity and packed bed height is presented as a contour plot in Figure 9.5.

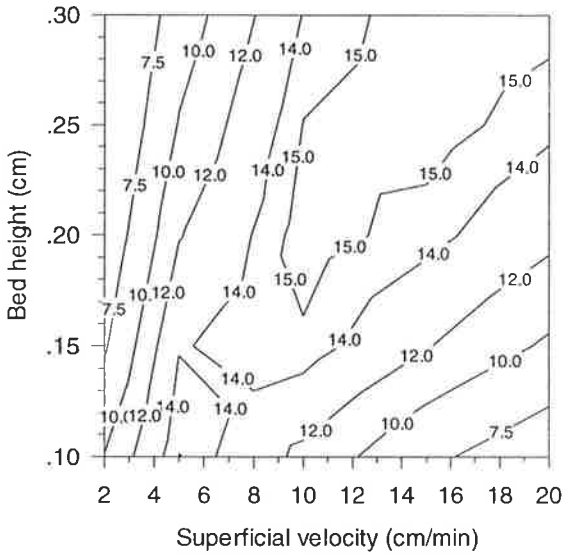

Figure 9.5: Contour plot of productivity, Ψ, as a function of frontal-adsorption superficial velocity and packed-bed height.

At any packed-bed height, Figure 9.5 indicates that the productivity of the WGFE ion-exchange system will initially rise with an increase in superficial velocity. However, it eventually reaches a limit, an optimal superficial velocity, beyond which it begins to decline. This optimal superficial velocity rises from 5 cm/min at a bed height of 10 cm to nearly 20 cm/min at 30 cm. There are a multiple number of scenarios for the superficial velocity in

the frontal-adsorption step and packed-bed height that will maximise productivity of the WGFE ion-exchange system.

The current operating conditions at a superficial velocity of 8.5 cm/min and packed bed height of 21 cm correspond to a value outside this optimal region. The merit of an increase in superficial velocity to 14 cm/min, which is being presently proposed for the WGFE ion-exchange system, can be considered. This will improve productivity, although, productivity will begin to decline with an increase in superficial velocity beyond this value. This quantitatively corresponds with real-life experimental observations in the pilot-plant described in Chapter 1.

The behaviour of productivity in Figure 9.5 illustrates the dramatic decline with superficial velocity of whey volume that can sustained during the frontal adsorption step. An increase in superficial velocity improves the cycle frequency, but at the expense of WGFE product yield per cycle. At the optimal superficial velocity, the reduction in cyclic WGFE yield begins to outweigh the benefits gained from any further increase in cycle frequency.

This has important implications for scale-up of other similar step-elution chromatographic systems where intraparticle-diffusion limitations may be important. Many will employ the heuristic technique described in Section 9.3 for scale-up where arbitrary increases in linear flowrate are encouraged in order to improve productivity. This is designed to minimise resin volume required by the chromatographic system, and therefore, its cost. However, Figure 9.5 shows that this strategy is fraught with danger. An increase in flowrate will not always necessarily improve productivity. Clearly, productivity needs to be carefully monitored during scale-up of step-elution chromatographic systems if a variation in packed-bed height or superficial velocity is being considered.

From the cycle time and system productivity, critical design parameters for sizing individual process equipment in the WGFE ion-exchange system for the proposed commercial-scale facility can be evaluated. This includes total resin volume, total column surface area, and cyclic and annual volume requirements for wash, eluent and sanitisation solutions. The results are not presented here for the purpose of brevity, but will be subsequently employed to establish a foundation for examining the overall process economics of the WGFE ion-exchange system during scale-up.

9.7 An Appropriate Objective function for Cost

To optimise the scale-up of the WGFE ion-exchange system, an appropriate objective function for cost must be selected. This must be correlated to system behaviour and design of the WGFE ion-exchange system in the proposed commercial facility. A typical objective for a grass-roots facility might be to minimise the total annual operating cost, ϕ_{Γ}^{*} (Middelberg, 1996):

$$\phi_{\Gamma}^{*} = \frac{\phi_{dfc} + \phi_{con} + \phi_{wt} + \phi_{other}}{\phi_{ch}} \tag{9.4}$$

where ϕ_{dfc} is the amortised annual cost for direct-fixed-capital (DFC) dependent items including maintenance, depreciation, insurance and local taxes; ϕ_{con} is the annual cost of consumables including chromatography media; ϕ_{wt} is the annual charge for waste treatment; ϕ_{other} is the annual charge for other items such as labour, utilities and research and development; and ϕ_{ch} is some characteristic cost.

Equation 9.4 is designed to investigate the total annual operating cost of an entire process. This study is restricted to the ion-exchange system in the WGFE production process. For the purpose of the analysis, the annual charges for waste treatment and other items will be excluded. Waste from the commercial facility will be absorbed by treatment facilities already present in the dairy factory. Annual charges for labour, utilities and research and development will either, be insensitive to variations in system size during scale-up, or assimilated by existing operations in the dairy factory.

9.8 Evaluating Component Costs

For *eq.* 9.4 to be of utility, estimates for the remaining individual component costs, ϕ_{dfc} and ϕ_{con}, for the WGFE ion-exchange system must be determined. As a first approximation, the DFC-dependent cost can related to the total equipment purchased cost, ϕ_{ep}, of individual equipment items using a simple factor, ζ (Middelberg, 1996):

$$\phi_{dfc} = \zeta \phi_{ep} \,. \tag{9.5}$$

Individual equipment items that can be considered part of any proposed commercial-scale WGFE ion-exchange system are shown in the simplified schematic of Figure 9.1. They include the pump and control system, ϕ_{pcs}; chromatographic columns, ϕ_{col}; six tanks for mixing and storage of process, buffer, eluent or sanitisation solutions, $\phi_{t,i}$; and an ultrafiltration unit for subsequent processing of the WGFE product generated during the 0.4 M step-elution, ϕ_{uf}. Hence,

$$\phi^{*}_{dfc} = \frac{\phi_{dfc}}{\phi_{ch}} = \frac{\zeta(\phi_{col} + \phi_{pcs} + \sum_{i=1}^{6} \phi_{t,i} + \phi_{uf})}{\phi_{ch}} \tag{9.6}$$

A value for the simple factor, ζ, in *eq.* 9.6 that is commonly used for this type of process is 1.45 (Middelberg, 1996). This value was also employed for this study.

Each of the individual costs in *eq.* 9.6 must now be correlated to a design parameters which describe the scale-up of the WGFE ion-exchange system.

9.8.1 Chromatographic columns

The individual component costs of chromatographic columns are directly proportional to number of columns, N_c:

$$\phi_{col} = N_c \gamma_c \tag{9.7}$$

where γ_c is the unit cost of an individual column. The number of columns can be determined from the system productivity (g WGFE/(h.L)), packed-bed height (m) and the cross-sectional area of the chromatographic column, A_c, in m^2, which will be employed in the production-scale facility:

$$N_c = \frac{V_w Y_p}{\Psi L A_c} \frac{1\ m^3}{24\ hours \times 7\ days \times 1000L} \tag{9.8}$$

where V_w is the total volume of whey to be processed by the facility per week in L. This value is of course 4,000 L per week based on the design capacity of the system. Equation 9.8 will yield a real value for column number. For costing purposes, these were rounded up to the nearest integer value.

The chromatographic column employed during scale-up has already been identified in Part I of this thesis. It will be a Pharmacia BPG 450/500 column. Its cross sectional area, A_c, is 0.159 m^2. Its unit cost, γ_c, is $AUD 48,675 (Amrad Pharmacia Biotech, 1996).

9.8.2 Pump & Control System

The pump and control system for a chromatographic process normally involves a single integrated unit which is purpose designed. It therefore represents a singular unit cost, γ_{pcs}:

$$\phi_{pcs} = \gamma_{pcs} \tag{9.9}$$

A Pharmacia (Uppsala, Sweden) UNICORN Multipurpose Control System was selected for the pump and control system. It can automatically handle a variety of flowrates and number of columns that may be required by the production-scale facility. Its cost, γ_{pcs}, was estimated from a ball-park figure provided by Amrad Pharmacia Biotech (1996) as $AUD 250,000.

9.8.3 Tanks

Mixing and storage tanks were sized at cyclic feed and product volumes and cyclic volume requirements for wash, buffer and sanitisation solutions determined in Section 9.4, but with an additional 20% redundant capacity. Individual tank costs ($\phi_{t,i}$) were determined from a cost-capacity equation (Middelberg, 1996) based on tank volume:

$$\phi_{t,i} = 10^{\alpha_i} V_{ti}^{\beta_i} \tag{9.10}$$

where V_{ti} is the tank volume; and α_i and β_i are cost parameters specific to each type of tank. For the purpose of this study, α_i and β_i were assumed to be identical for each tank at values of, 4.17 and 0.54, respectively. These are similar to values used by Middelberg (1996).

9.8.4 Ultrafiltration Unit

The cost of the ultrafiltration unit, ϕ_{uf}, was estimated from a cost-capacity equation based on membrane area (Middelberg, 1996):

$$\phi_u = 10^{\alpha_u} A^{\beta_u} \tag{9.11}$$

Assuming a linear relationship between membrane area, A, and flux, J, gives

$$A = \frac{v_o - v_{prod}}{J} \tag{9.12}$$

where v_o and v_{prod} are the volumetric flowrates of retentate and permeate, respectively. Typically v_o is much greater than v_{prod}, and v_{prod} can be ignored in *eq.* 9.12.

v_o was selected to meet anticipated cyclic product volumes and constrained within arbitrary cycle time limitations. Values provided by Middelberg (1996) of 3.21, 0.88 and 15 L/h.m^2 were used for parameters α_u, β_u and J, respectively.

9.9 Principal Consumable Costs

The principal costs for consumables in the ion-exchange step include recurrent expenditure on the chromatographic resin, ϕ_r, the deionised water wash solutions, ϕ_w, eluent solutions, ϕ_{e1} and ϕ_{e2} (for 0.4M and 1.0 M sodium chloride solutions, respectively), the sanitisation solution, ϕ_s, and replacement membranes for ultrafiltration unit, ϕ_m. Therefore,

$$\phi^{*}_{con} = \frac{\phi_{con}}{\phi_{ch}} = \frac{(\phi_r + \phi_w + \phi_{e1} + \phi_{e2} + \phi_s + \phi_m)}{\phi_{ch}} \tag{9.13}$$

9.9.1 Chromatographic Resin

The recurrent expenditure on chromatographic media, ϕ_r, is directly proportional to the annual consumption of resin, $\dot{V}_{res}$:

$$\phi_{res} = \dot{V}_{res}\,\gamma_{res} \tag{9.14}$$

where γ_{res} is the unit cost of Sepharose Big-Beads SP. Resin annual consumption was determined from ion-exchange system resin volume, V_r, and daily cycle frequency, ω_c, based on a media life expectancy for Sepharose Big-Beads SP of at least 1000 cycles:

$$\dot{V}_{res} = V_r \frac{\omega_c \times 351}{1000} \tag{9.15}$$

A value of $AUD 641 for γ_{res} was provided by Amrad Pharmacia Biotech (1996).

9.9.2 Wash, Eluent, & Sanitisation Costs

Wash, ϕ_w, eluent, ϕ_{e1} and ϕ_{e2}, and sanitisation solution, ϕ_s, costs were determined from the concentration of their chemical constituents, including acid and base for pH correction, and their total annual volume requirements determined in Section 9.4. The cost of water to make-up solutions was assumed to be negligible. The cost of deionised water wash solutions was therefore zero. Costs of chemical additives were provided by Ajax Chemicals (Adelaide, Australia). Appropriate modifications were made to account for the influence of scale. Final values of unit costs used for wash, eluent and sanitisation solutions are summarised in Table 9.1.

Table 9.1: Unit costs for wash, eluent and sanitisation solutions.

Solution	Unit Cost ($AUD/L)
1.0 M NaOH	0.14
0.4 M NaCl	0.15
1.0 M NaCl	0.21

9.9.3 Ultrafiltration Membranes

Membrane replacement costs, ϕ_m, were based on membrane area, expected membrane life, L, and an estimated membrane cost, γ_u, for a typical ultrafiltration unit employed in this type of process:

$$\phi_m = \frac{A}{L}\gamma_u \qquad (9.16)$$

Values provided by Middelberg (1996) of 100 and $AUD 250 were employed for L and γ_u, respectively.

9.10 The Characteristic Cost

To complete dimensionless annual cost calculations, a characteristic cost to non-dimensionalise annualised operating cost must be selected. This cost must be constant and independent of scale variations in the WGFE ion-exchange system with frontal-adsorption superficial velocity and packed-bed height during scale-up. For the purpose of this study, the equipment cost for the pump and control system, ϕ_{pcs}, was selected as the characteristic cost.

9.11 Costing - Results and Discussion

The non-dimensional variation in DFC costs, *eq.* 9.6, with frontal-adsorption superficial velocity and packed-bed height was determined for the WGFE ion-exchange system in the proposed commercial-scale facility. It is illustrated in the contour plot presented in Figure 9.6.

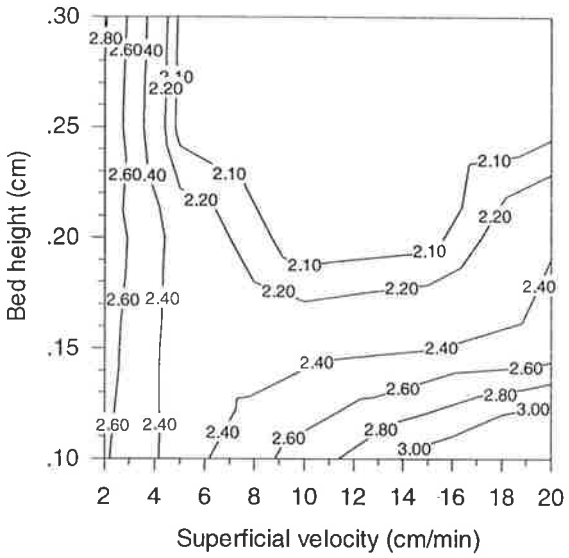

Figure 9.6: Contour plot of non-dimensionalised direct-fixed-capital costs, ϕ^*_{dfc}, as a function of frontal-adsorption superficial velocity and packed-bed height.

The annualised DFC costs for the WGFE ion-exchange system lie within a narrow band of $AUD 500,000 to 750,000. The minimum values correspond with values of maximum productivity displayed in Figure 9.5, and this reflects the dominant contribution to DFC costs of resin volume and number of columns.

The dimensionless variation in consumable costs, *eq.* 9.13, with frontal-adsorption superficial velocity and packed-bed height is illustrated in the contour plot displayed in Figure 9.7.

Figure 9.7 indicates that the consumable costs will vary widely depending on frontal-adsorption superficial velocity and packed-bed height. The consumable costs are dominated by chemical costs for eluent and sanitisation solutions. Regardless of variation in superficial velocity and packed-bed height, the volume of eluent and sanitisation solutions required each cycle will remain relatively constant. The consumable costs therefore display a direct correlation with cycle frequency. They rise with either an increase in superficial velocity or a decrease in packed-bed height.

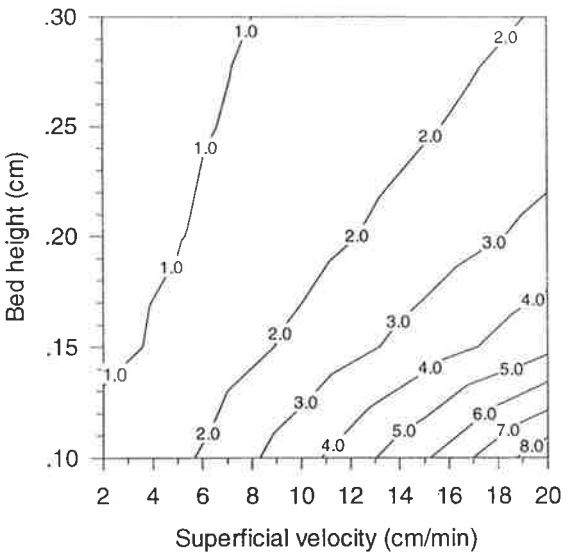

Figure 9.7: Contour plot of non-dimensionalised consumable costs, ϕ^*_{con}, as a function of frontal-adsorption superficial velocity and packed-bed height.

The non-dimensional costs for DFC and consumables are combined in Figure 9.8. It presents a contour plot of annualised dimensionless cost for the WGFE ion-exchange system in the proposed commercial scale-facility.

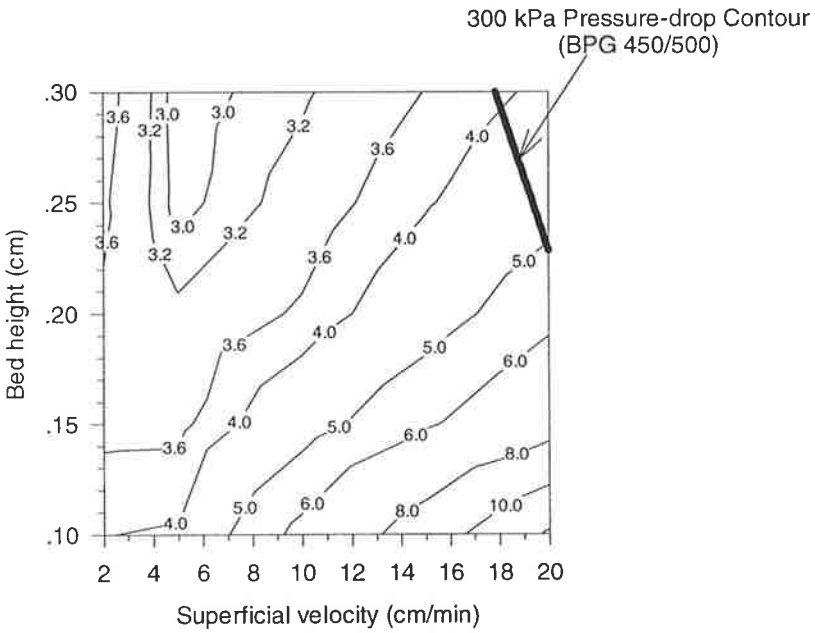

Figure 9.8: Contour plot of dimensionless costs, ϕ^*, as a function of frontal-adsorption superficial velocity and packed-bed height with predicted 300 kPa pressure-drop contour for the Pharmacia BPG 450/500 column.

Figure 9.8 reveals that an optimal region for cost during scale-up of the WGFE ion-exchange system does exist. The region is bounded between a superficial velocity of 4 to 6 cm/min at bed heights of 25 to 30 cm and greater. The optimal region does not correspond to region which maximises productivity in Figure 9.5. This is an important observation. While the heuristic technique currently employed to scale-up the WGFE ion-exchange system aims to maximise productivity and minimise the cost of resin and columns, it does not take into account the cost of consumables items. These dominate the annualised non-dimensionless cost contours in Figure 9.8.

Furthermore, Figure 9.8 indicates that the current operating conditions in the pilot-plant are sub-optimal. Moving the packed bed height and superficial velocity to the optimal region in Figure 9.8, for example, 27 cm and 5 cm/min, respectively, would cut dimensionless annual operating cost by 15 to 20%. While an increase the superficial velocity to 14 cm/min, as presently proposed, will increase dimensionless annual operating cost by 25 to 30%.

9.12 The Pressure Constraint

Section 9.11 has indicated that a reduction in superficial velocity and increased bed height, rather than an increase in superficial velocity and decrease in height, should be employed during scale-up of the WGFE ion-exchange system. However, if this alternative strategy is selected, the variation in superficial velocity and packed-bed height may compromise the pressure constraint on the system. With positive-displacement pumps being considered, this constraint is determined by the pressure rating of the chromatographic columns that will be employed in the production-scale facility. For a Pharmacia BPG 450/500 column, the pressure constraint is 3 bar. Part I of this thesis has estimated the pressure-drop behaviour of Sepharose Big Beads SP in this column for microfiltered whey at 20°C as a function of superficial velocity and packed-bed height. This was presented as a contour plot in Figure 4.19. The contour for 300 kPa in this Figure has been overlayed onto dimensionless costs displayed in Figure 9.8. It excludes only a small section of the visible domain in Figure 9.8 in its top right hand corner. Pressure-drop will not present an impediment to selection of superficial velocity and packed-bed height for optimisation of cost. In fact, Figure 4.19 indicates that the pressure drop in the system will be less than 25 to 50 kPa in the optimal region. This is much lower than 100 to 150 kPa at the proposed superficial velocity of 14

cm/min and bed height of 21 cm. A lower cost pump could be considered for scale-up of the WGFE ion-exchange system instead of an expensive-positive displacement pump. For example, a peristaltic-type pump can operate quite effectively in these lower pressure ranges.

9.13 Concluding Remarks

The non-linear multicomponent rate-equation model presented in Part II of this thesis has been employed to simulate the behaviour of the frontal-adsorption step in the WGFE ion-exchange system during scale-up. Lactoperoxidase and lactoferrin were employed to imitate the two key fractions in the microfiltered whey: the WGFE product and lactoferrin. The sensitivity of breakthrough during frontal adsorption to packed-bed height and superficial velocity was investigated. Intraparticle-diffusion limitations play an important role in determining the whey volume that can be sustained by the packed bed during frontal adsorption. This has an important impact on the cyclic WGFE yield. An increase in superficial velocity can result in a dramatic decline in WGFE yield per cycle.

Simulation results were combined with pilot-plant data for other steps in the WGFE ion-exchange system. Scale-up studies were performed to examine the impact of packed-bed height and frontal-adsorption superficial velocity on productivity. The results indicate that that an optimal region of productivity exists. This optimal superficial velocity rises from 5 cm/min at a bed height of 10 cm to nearly 20 cm/min at 30 cm. There are multiple scenarios for the superficial velocity in the frontal-adsorption step and the packed-bed height that will maximise productivity of the WGFE ion-exchange system. This is a direct result of intraparticle-diffusion limitations and the decline in cyclic WGFE yield it induces with an increase in superficial velocity. This has important implications for scale-up of other similar step-elution chromatographic. Many will employ a heuristic technique where arbitrary increases in linear flowrate are encouraged in order to improve productivity. This is designed to minimise resin volume required by the chromatographic system, and therefore, its cost. However, this study shows that an increase in flowrate does not always necessarily improve productivity.

A comprehensive design for the WGFE ion-exchange system in a proposed commercial-scale facility was developed. The design was correlated with an objective function

describing annualised dimensionless cost. The variation in annualised dimensionless cost with frontal-adsorption superficial velocity and packed-bed height was investigated. There is an optimal design for the WGFE ion-exchange system which will minimise cost. It is located at a superficial velocity and packed bed height of 2 to 6 cm/min and 25 to 30 cm, respectively. While the cost of chromatographic resin and columns were important, the cost of the WGFE ion-exchange system is dominated by consumable costs, in particular, those for eluent and sanitisation solutions. This reflects the increasing volumetric requirements of process solutions which are required to meet the increase in cycle frequency at higher superficial velocities and lower bed heights.

The current operating conditions employed for the WGFE ion-exchange system in the pilot-plant are therefore sub-optimal. They will result in annual scale-up costs more than 15 to 20% greater than if a superficial velocity and packed bed height in the optimal cost region are employed. Furthermore, the proposed increase in superficial velocity to 14 cm/min should be avoided. While it will improve system productivity, it will lead to an annual scale-up cost that exceeds its optimal counterpart by more than 50%.

CHAPTER 10

SUMMARY & FINAL REMARKS

The scale-up of an ion-exchange chromatographic system to separate WGFE from cheese whey has been investigated. A key impediment to successful scale-up has been identified. This was the compressibility of the chromatographic resin: Sepharose Big-Beads SP. For compressible chromatographic media, packed-bed pressure drop displays a functional dependence on column diameter. This is a result of wall friction effects. The pressure drop across a packed bed will inevitably increase during scale-up and may compromise the pressure constraint acting in the chromatographic system. This can have catastrophic financial consequences. A production-scale system may be forced to operate at a flowrate well below its design capacity. This presents an undesirable uncertainty for scale-up of the WGFE ion-exchange system. Some means of predicting the increase in pressure drop across compressible packed beds of Sepharose Big-Beads SP was required.

A review of literature revealed that techniques for prediction of packed bed pressure-drop during scale-up have been developed. However, they rely on empirical relationships and correlations. Genuine predictions can only be made over the experimental range for which they have been validated. Packed beds of compressible chromatography resin are similar to compressible packed beds of granular media encountered in other industries. Truly predictive models for pressure drop across compressible media have been developed. Many are based on a generalised theory: the volume-averaged continuum theory. Unfortunately these models cannot account for wall friction effects.

A new model for packed-bed pressure-drop prediction in compressible chromatographic media has been proposed. It combines the volume averaged-continuum theory with Janssen's method of differential slices. The method of differential slices is employed for prediction of stress fields in hoppers and silos where wall friction is a common phenomenon. This combination permits the volume-averaged continuum theory to predict the effect of variation in column diameter on packed-bed pressure drop. The new model consists of three ordinary differential equations:

$$\frac{dP}{dL} = -\mu v_z^{sup} \chi(\tau_{zz}^s) f_c(\tau_{zz}^s) \tag{4.3}$$

$$\frac{d\tau_{zz}^s}{dL} = \left(\mu v_z^{sup} \chi(\tau_{zz}^s) - \frac{4}{D} \tan\varphi_w \frac{1-\sin\varphi}{1+\sin\varphi} \tau_{zz}^s \right) f_c(\tau_{zz}^s) \tag{4.4}$$

$$\frac{dZ}{dL} = f_c(\tau_{zz}^s) \tag{4.2}$$

Equations 4.3 and 4.4 predict the variation in steady-state fluid pressure and compressive axial-stress field, respectively, in a packed bed. Equation 4.2 describes the variation in packed-bed height with compression. Simultaneous integration of the three equations over the initial bed height allow the pressure drop and compressed bed height of a packed bed to be determined.

The model consists of four key model parameters. These are φ, φ_w , $f_c(\tau_{zz}^s)$ and $\chi(\tau_{zz}^s)$. φ and φ_w are the internal angle of friction for the pulverulent material, and its angle of wall friction against the internal surface of a chromatographic column, respectively. $f_c(\tau_{zz}^s)$ is an empirical relationship which describes the variation in bed height with axial stress. $\chi(\tau_{zz}^s)$ is also an empirical relationship. It describes the variation in bed properties and their impact on fluid-pressure losses in the packed bed. It can be related to bed porosity, shape factor and (volume-mean) particle diameter by

$$\chi(\tau_{zz}^s) = \frac{200\varepsilon_s^2}{d_{pv}^2 \phi^2 \varepsilon_f^3} \tag{2.40}$$

The model parameters were determined for Sepharose Big-Beads SP. The internal angle of friction in water was 10.3°. The angle of wall friction of the resin against borosilicate glass in water was 8.0°. $f_c(\tau_{zz}^s)$ in water was measured and correlated to an empirical function (*eq.* 3.5). $\chi(\tau_{zz}^s)$ was also described by an empirical function (*eq.* 4.1). This function was determined by regression of the model against experimental pressure-drop data.

Model predictions of pressure-drop behaviour were made. These were validated against experimental pressure-drop data collected in Pharmacia XK 16/40, XK 50/60 and BPG 100/500 chromatographic columns. The internal surface in each column was borosilicate glass. Their column diameters were 1.6, 5.0 and 10 cm, respectively. The model can successfully predict pressure drop for packed beds of varying bed height in columns of different diameters, despite a inherent error in prediction of compressed bed height. Model predictions were also independent of solvent type.

However, despite extensive validation of the model, further investigation is required. Some key recommendations are as follows. First, only two test fluids were employed to gather experimental data for validation. Additional experiments to test the existing model parameters for Sepharose Big-Beads SP with other solvents should be considered.

Second, the values of model parameters φ, φ_w and $f_c(\tau_{zz}^s)$ were only determined for Sepharose Big-Beads SP in water. Further experiments should be conducted to examine if their values are subject to variation in other solvents

Third, Janssen's method of differential slices provides only an estimate of the stress field when wall effects are present. This results in a prediction error. For hopper and silos, this is error no more than 3% when compared against an exact solution generated by the method of characteristics. However, the prediction error is unquantified for its application to compressed packed beds in chromatographic systems.

Fourth, the influence of wall friction effects in chromatographic columns creates varying initial packing densities. The initial packed-bed heights in columns of different diameter do not correspond to model assumptions for $f_c(\tau_{zz}^s)$. A prediction error for compressed bed height is generated. This is an inherent limitation of the model and further model development should be considered to overcome this problem.

Fifth, model predictions are sensitive to variations in fluid viscosity. Original experimental pressure-drop data used to determine $\chi(\tau_{zz}^s)$ were subject to a ± 2°C temperature variation. This leads to a variation in viscosity of +5.1 and -4.7%, respectively, and therefore, a variation in recorded values of experimental pressure-drop data between ±5 to 20%. This

may have caused significant error in $\chi(\tau_{zz}^{s})$. This function should be re-determined using high integrity pressure-drop data measured under strict temperature control.

Finally, the model has been implemented and validated for Sepharose Big-Beads SP. The propensity of the model to predict the packed-bed pressure drop of other compressible chromatography resins is untested. Application of the model to other compressible chromatographic resin is necessary to confirm its true utility.

Further model predictions were made to examine the impact of column diameter on pressure drop during scale-up of the WGFE ion-exchange system. An increase in column diameter can lead to a dramatic increase in packed-bed pressure drop. The magnitude of this increase depends on the packed-bed height and superficial velocity. This represents a key conclusion of this study. It is not safe for a designer to assume that packed-bed pressure drop will remain constant during scale-up of the WGFE ion-exchange system.

Model predictions of pressure drop with superficial velocity and bed height for microfiltered whey in the proposed production-scale column: a Pharmacia BPG 450/500 column, for the WGFE ion-exchange system were performed. These were combined with an estimate of external column pressure losses from a Pharmacia BPG 300/500 column to determine the overall pressure-drop behaviour of the WGFE ion-exchange system during scale-up. The results were presented as a contour plot in Figure 4.19 of Chapter 4. The region below the contour at 300 kPa (*ie* the pressure rating of the BPG 450/300 column and the pressure constraint for the WGFE ion-exchange system) in Figure 4.19 is the feasible region for design during scale-up. The current pilot-plant operating conditions of v_{sup} and L at 8.5 cm/min and 21 cm, respectively, can be safely employed. Similarly, the proposed increase in superficial velocity 14 cm/min can be sustained.

However, the column pressure losses, rather than packed-bed pressure drop dominate the pressure-drop behaviour presented in Figure 4.17. If column pressure losses in the BPG 450/500 column are much higher than in the BPG 300/500 column (used to estimate column pressure losses), the contours in Figure 4.19 may not accurately reflect real-life scale-up conditions. The column pressure-loss behaviour of the Pharmacia BPG 450/500 column must be measured to eliminate this uncertainty.

Model predictions of the axial stress field for a packed beds in two different-sized columns of 2 and 20 cm internal-diameter were compared. The initial height of the packed bed was 20 cm and the superficial velocity was 35 cm/min. Equation 2.40 was used to estimate the variation in porosity within a packed bed during scale-up of the WGFE ion-exchange system. Values of 1 and 151 μm were employed to estimate the shape factor and volume-mean particle diameter, respectively, of resin particles in the bed. These parameters were assumed to be invariant with compression. The porosity of the packed bed before compression was 0.38. Compression was found to decrease porosity decrease, from top to bottom of the packed beds, by 8% and 35% in the 2 to 20 cm diameter columns, respectively. Scale-up of the WGFE ion-exchange system will result in a significant change in packed-bed porosity. This may create variations in WGFE ion-exchange system behaviour and affect its performance. To investigate this problem further, a modified version of the non-linear general rate equation chromatography model was formulated. The modifications account for the variation in porosity and Sauter-mean particle diameter that take place in a compressed packed bed. The modified model is described by three mathematical equations:

$$-\frac{\partial\left(\frac{1}{Pe_{Li}}\frac{\partial c_{bi}}{\partial z}\right)}{\partial z} + \frac{\partial c_{bi}}{\partial z} + \frac{v_o L}{L_o v}\frac{\partial c_{bi}}{\partial \tau} + \xi_i\,(c_{bi} - c_{pi,r=1}) = 0 \qquad (5.1b)$$

$$\frac{v_o}{L_o}\frac{L}{v}\frac{\partial}{\partial \tau}\left[(1-\varepsilon_p)c^s_{pi} + \varepsilon_p c_{pi}\right] - \eta_i\left[\frac{1}{r^2}\frac{\partial}{\partial r}\left(r^2\frac{\partial c_{pi}}{\partial r}\right)\right] = 0 \qquad (5.2b)$$

$$\frac{v_o}{L_o}\frac{L}{v}\frac{\partial c^s_{pi}}{\partial \tau} = Da^a_i\, c_{pi}\left(c^\infty_i - \sum_{j=1}^{N_s}\frac{C_{oj}}{C_{oi}}\theta_{ij}c^s_{pj}\right) - Da^d_i\, c^s_{pi} \qquad (5.3b)$$

An appropriate numerical solution strategy was developed to solve the model equations. This was validated against a numerical solution to the general non-linear multicomponent rate-equation model presented in the literature.

Compression effects in the WGFE ion-exchange system were investigated. Two major whey proteins, namely lactoperoxidase and lactoferrin were used to simulate the WGFE ion-exchange system behaviour. Many of the model parameters required for each protein were

provided by James (1994). Others were determined from common empirical correlations and some applied guesswork. To validate model predictions, model simulations were compared against experimental frontal-adsorption and step-elution data provided by James (1994). The results for frontal adsorption are presented in Figure 6.3. Step-elution simulations *vs.* experimental data are presented in Figure 6.4.

For model simulations, accurate selection of numerical parameters was important to ensure convergence of the numerical solution. In particular, at least 11 internal collocation points were required. To enable successful reconciliation of model predictions with experimental data, two apparently inconsistent sets of model parameters were used to describe multicomponent adsorption-desorption equilibria. Multicomponent Langmuir adsorption isotherms for were used frontal-adsorption and wash steps and single-component extended Langmuir-Freundlich adsorption isotherms for step-elutions. The multicomponent Langmuir adsorption isotherms and extended Langmuir-Freundlich adsorption isotherms used in this study where determined from experimental data provided by James (1994). This experimental data may have been flawed. Prediction errors in adsorption-desorption equilibria may have generated errors in other model parameters provided by James (1994). Further work is recommended in order to overcome this problem. A superior description of adsorption-desorption equilibria is essential to generate accurate predictions of lactoferrin and lactoperoxidase behaviour during frontal adsorption and elution in the WGFE ion-exchange system. Despite this, however, the model predictions of frontal adsorption and elution presented in Figures 6.3 and 6.4 compared exceptionally well with experimental data provided by James (1994).

The impact of compression on model parameters for the modified non-linear multicomponent rate-equation model during scale-up of the WGFE ion-exchange system was examined. The model for packed-bed pressure-drop prediction developed in this thesis was used to predict the axial stress field within a compressed packed bed for 2 and 20 cm (internal) diameter columns. The initial bed height was 20 cm and the superficial velocity was 35 cm/min. The axial stress field was used to determine $\chi(\tau^{s}_{zz})$, and in turn, the variation in porosity and particle diameter from

$$\chi(\tau_{zz}^{s}) = \frac{180\,(1-\varepsilon)^2}{d_{pS}^{\,2}\,\varepsilon^3} \qquad (7.2)$$

Equation 7.2 was created by comparing *eq.* 4.3 against the Carmen-Kozeny equation, an empirical correlation for pressure-drop prediction in incompressible packed beds. It has a single degree of freedom. Therefore, to determine bed porosity and Sauter-mean particle diameter through the compressed packed bed, an additional relationship between these variables, or with stress, was found. This was achieved by considering how resin particles deform in a packed bed. Each particle was assumed to remain a perfect ellipsoid during compression. Strain during particle deformation was restricted to the vertical semi-axis. Additionally, the variation in internal voidage with particle deformation was also calculated for each column.

Predicted variation in porosity, Sauter-mean particle diameter and internal voidage are presented in Figures 7.1, 7.2 and 7.4, respectively. The porosity variation from top to bottom of the compressed packed beds of the 2 and 20 cm diameter columns was 9% and 36%, respectively, from an initial porosity of 0.356. The variation in Sauter-mean particle diameter in each column equalled 2% and 5%, respectively, from an initial value of 167 μm. These seem moderate but can produce a 4% and 11 % increase, respectively, in the fluid pressure gradient during fluid flow in a packed bed. The variation in intraparticle porosity in each column from top to bottom was 0.2 an 1.0%, respectively, from an initial value of 0.94. These appear minor, but surprisingly correspond to a decrease in resin particle volume of 4 and 13%, respectively.

Variations in external-film mass transfer, retention time and axial dispersion were estimated from variation in porosity, particle diameter and internal voidage. These variations were automatically incorporated into model predictions. However, variation of D_p, ε_p, and adsorption-desorption equilibria could not be predicted with certainty. These considered constant, regardless of compression.

Model simulations of WGFE ion-exchange system behaviour for the compressed packed beds in the 2 and 20 cm diameter columns were performed. The results were compared. For both frontal adsorption and step elution, system behaviour was largely independent of

compression. Increasing compression generated only small and trivial variations in effluent concentration profiles. Two competing mechanisms appeared to influence these variations. Bed compression decreased void volume producing premature breakthrough and accelerated development of effluent concentration profiles. Compression-induced changes in external-film mass transfer caused delays. Decreasing particle diameter and superficial velocity did not markedly alter the influence of compression effects. It can be concluded that the impact of increased compression does not need to be considered during scale-up of the WGFE ion-exchange system.

However, it should be noted that compression effects on intraparticle diffusion, intraparticle voidage and adsorption capacity were not considered. Their contribution to WGFE ion-exchange system behaviour during scale-up is unquantified. Further investigation is recommended to determine whether compression effects on these parameters will influence system behaviour.

The general non-linear chromatography model used to simulate compression effects in the WGFE ion-exchange system can be also be used as a tool to optimise its scale-up. Model-adsorption simulations were employed to examine the sensitivity of system behaviour during frontal adsorption to superficial velocity and packed-bed height. Lactoperoxidase and lactoferrin were employed to imitate the two key fractions in the microfiltered whey: the WGFE product and lactoferrin. It was discovered that intraparticle-diffusion limitations play an important role in determining the whey volume that can be sustained by the packed bed during frontal adsorption. This has an important impact on the cyclic WGFE yield. An increase in superficial velocity can produce a dramatic decline WGFE yield per cycle.

Simulation results were combined with pilot-plant data for other steps in the WGFE ion-exchange system. Scale-up studies were performed to examine the impact of packed-bed height and frontal-adsorption superficial velocity on productivity. The results indicate that that an optimal region of productivity exists. This optimal superficial velocity rises from 5 cm/min at a bed height of 10 cm to nearly 20 cm/min at 30 cm. There are multiple optimal scenarios for the superficial velocity in the frontal adsorption step and the packed-bed height that will maximise productivity of the WGFE ion-exchange system. This is a direct result of intraparticle-diffusion limitations and the decline in cyclic WGFE yield it induces with an increase in superficial velocity. This has important implications for scale-up of

other step-elution chromatographic systems. Many will employ heuristic techniques where arbitrary increases in linear flowrate are encouraged to improve productivity. However, this study shows that an increase in flowrate does not always necessarily improve productivity.

The frontal-adsorption superficial velocity and packed-bed height which will optimise the cost of the WGFE ion-exchange system during scale-up was investigated. A comprehensive design for the WGFE ion-exchange system in a proposed commercial-scale facility was developed. The design was correlated with an objective function describing annualised dimensionless cost. The sensitivity of cost to frontal-adsorption superficial velocity and packed bed height was examined. There is an optimal design for scale-up of the WGFE ion-exchange system. It is located at a superficial velocity and packed bed height of 2 to 6 cm/min and 25 to 30 cm, respectively. While the cost of chromatographic resin and columns were important, the WGFE ion-exchange system cost was dominated by consumable costs, in particular, those for eluent and sanitisation solutions. This is an important observation. Existing heuristic techniques for chromatographic scale-up often use resin volume as an indicator of cost. This is not always the principal cost driver during scale-up of a chromatographic system. Furthermore, if this is the case, the preoccupation of existing heuristic techniques with increasing flowrate inadvertently act to increase consumable costs. This is a direct result of the rise in cycle frequency, which inevitably accompany higher superficial velocities, and increase the volumetric consumption of wash, buffer, eluent and/or sanitisation solutions.

The current operating conditions employed for the WGFE ion-exchange system in the pilot-plant are therefore sub-optimal. They will result in annual scale-up costs more than 15 to 20% greater than if a superficial velocity and packed-bed height in the optimal cost region are employed. Furthermore, the proposed increase in superficial velocity to 14 cm/min should be avoided. While it will improve system productivity, it will lead to an annual scale-up cost that exceeds its optimal counterpart by more than 50%.

An important observation was made during model simulations of WGFE ion-exchange system behaviour in this thesis. Inter-phase mass transfer in the WGFE ion-exchange system is intraparticle-diffusion limited. The impact of intraparticle-diffusion limitations on cyclic WGFE product yield were discussed above. It results in a dramatic decline in whey volume which can be sustained by the ion-exchange system during frontal adsorption.

Intraparticle-diffusion limitations are clearly the key impediment to improved performance in the WGFE ion-exchange system. However, a number of strategies can be employed to alleviate intraparticle-diffusion limitations, or even eliminate them. One recent development in resin technology is perfusion (Geisow, 1992) or macroporous resins (Frey *et al.*, 1993). Perfusion or macroporous chromatography resins use intraparticle convection to assist inter-phase mass transfer. In addition to conventional pores, the resin particle consists of artificially created gigapores which act as conduits for intraparticle fluid flow. Fluid flows through the gigapores from the bulk-phase and then diffuses through conventional pores to adsorption sites. Gigapores effectively reduce the intraparticle-diffusion distance in a resin particle that proteins must travel to reach adsorption sites.

Alternatively, a smaller particle size could be considered. This would immediately act to alleviate intraparticle-diffusion limitations. Compressed-bed simulations in this thesis where particle size was halved have already displayed variations in system behaviour that would be advantageous to scale-up of the WGFE ion-exchange system. For frontal adsorption, it increased the volume of whey which could be sustained by the ion-exchange system before breakthrough. During elution, it eliminated elution peak skew and peak tailing. It also isolated each protein in their respective step-elution peaks, and eliminated protein carry-over. Unfortunately, the reduction in particle size was accompanied by a decrease in superficial velocity. These results were inconclusive, and further investigation was not congruent with the objective of this study.

Clearly, further investigation should consider whether a smaller particle size or use of perfusion chromatography resin would be suitable for the WGFE ion-exchange system.

As an interesting note, the possibility of using a smaller particle size could almost be immediately considered. An alternative ion-exchange resin of smaller particle size is Sepharose Fast-Flow SP. This was the resin employed in the ion-exchange system prior to Sepharose Big-Beads SP. Sepharose Fast-Flow SP is a 6% cross-linked agarose resin like Sepharose Big-Beads SP. It therefore shares similar packed-bed properties, in particular those related to compression, except for its particle diameter. In fact, an empirical function, $\chi_s(\tau^s_{zz})$, which describes the variation in bed properties with τ^s_{zz} for Sepharose Fast-Flow SP can be estimated *per se*. Consider *eq.* 2.40:

$$\chi_s\left(\tau_{zz}^s\right)=\chi\left(\tau_{zz}^s\right)\times\left(\frac{d_{pv}}{d_{pv,s}}\right)^2=\frac{200\varepsilon_s^2}{d_{pv,s}^2\phi^2\varepsilon_f^3} \qquad (10.1)$$

where $d_{pv,s}$ is the volume-mean particle diameter for Sepharose Fast-Flow SP. This assumes that porosity, and its variations with compression for Sepharose Fast-Flow SP, are identical to Sepharose Big-Beads SP. Furthermore, it can be assumed that the relative magnitude in particle-diameter variation for both resins are identical, despite their different size. The particle-diameter ratio in *eq.* 10.1 therefore remains constant during compression and equal to the initial ratio prior to compression. Substituting *eq.* 10.1 into model equations (*eq.s* 4.3 and 4.4) gives

$$\frac{dP}{dL}=-\mu v_z^{sup}\chi\left(\tau_{zz}^s\right)\times\left(\frac{d_{pv}}{d_{pv,s}}\right)^2 f_c(\tau_{zz}^s) \qquad (10.2)$$

$$\frac{d\tau_{zz}^s}{dL}=\left(\mu v_z^{sup}\chi\left(\tau_{zz}^s\right)\times\left(\frac{d_{pv}}{d_{pv,s}}\right)^2-\frac{4}{D}\tan\varphi_w\frac{1+\sin\varphi}{1-\sin\varphi}\tau_{zz}^s\right)f_c(\tau_{zz}^s) \qquad (10.3)$$

Equations 10.2 and 10.3, along with *eq.* 4.2, can be used to make an estimate prediction of the packed-bed pressure-drop behaviour of Sepharose Fast-Flow SP.

The volume-mean particle diameter of Sepharose Fast-Flow SP has been measured by James (1994). Its value was 107 μm. The particle diameter ratio of Sepharose Big-Beads SP to Sepharose Fast-Flow SP is therefore 0.71.

Equations 10.1 and 10.2 were employed to predict the packed-bed pressure drop of microfiltered whey (at 20°C) for Sepharose Fast-Flow SP at various superficial velocities and bed heights. External pressure-loss data for the Pharmacia BPG 300/500 column with microfiltered whey (presented in Figure 4.16) were combined with model predictions. Figure 10.1 presents the result as a 300 kPa pressure-drop contour *vs.* superficial velocity and bed height. Figure 10.1 can be used to estimate the system pressure drop across a BPG 450/500 column with Sepharose Fast-Flow SP which might be used in a production-scale

WGFE ion-exchange system. The predicted 300 kPa contour for Sepharose Big-Beads SP with microfiltered whey in a BPG 450/500 column is also shown in Figure 10.1 for comparison.

Surprisingly, a large range of the feasible domain for design of the WGFE ion-exchange system with Sepharose Big-Beads SP is also available to Sepharose Fast-Flow SP. The current operating conditions of 21 cm and 8.5 cm/min for L and v_{sup}, respectively, could also be employed with Sepharose Fast-Flow SP. However, the proposed increase in superficial velocity to 14 cm/min cannot be sustained. Again, the reliability of these predictions in Figure 10.1 are unfortunately compromised by the use of external pressure-loss data for the Pharmacia BPG 300/500 column.

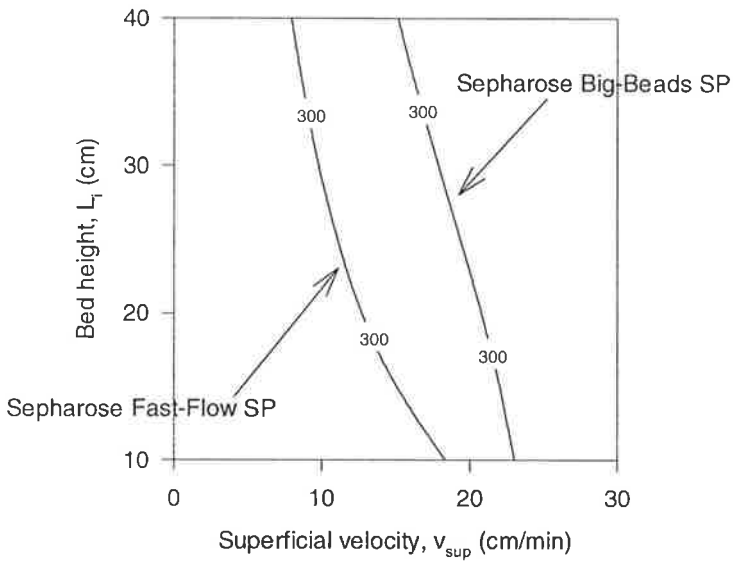

Figure 10.1: Column pressure-loss data for Sepharose-Fast Flow SP in a BPG 450/500 column with water at 20°C

Similarly, the general non-linear multicomponent rate-equation chromatography model could be employed to examine WGFE ion-exchange system behaviour during frontal adsorption with Sepharose Fast-Flow SP. James (1994) not only determined model parameters for Sepharose Big-Beads SP, but for Sepharose Fast-Flow S (Pharmacia, Uppsala, Sweden). Sepharose Fast-Flow S is a cation-exchange resin identical to Sepharose Fast-Flow SP, except for a slight variation in the spacer which attaches the ion-exchange functional group to the resin's internal surface (*ie* adsorption characteristics should be similar). The study in Chapter 9 could easily be repeated to determine the

optimal frontal-adsorption superficial velocity and packed-bed height for scale-up of the WGFE ion-exchange system with Sepharose Fast-Flow SP. The result would make an interesting comparison to the findings of this study, no doubt.

NOMENCLATURE

a	A measure of rigidity for a packing material in *eq.* 2.1, (min/cm^3). Major semi-horizontal axis of an ellipsoid resin particles in Chapter 7, (m).
a_i	Constant in Langmuir isotherm and extended Langmuir-Freundlich isotherms for component i, (m^3/m^3).
a_s	Specific particle-surface area, (m^2/m^3).
a_s^e	Specific particle-surface area at unstressed condition (*ie* top of cake), (m^2/m^3).
A_{col}	Column cross-sectional area, (m^2).
A_{pc}	Compressed-particle surface area, (m^2).
b	Minor semi-horizontal axis of an ellipsoid resin particle, (m).
b_1,b_2	Variable parameters in *eq.* 2.3, (–).
b_i	Constant in Multicomponent Langmuir and extended Langmuir-Freundlich isotherms, (M).
$b_{s,p}$	Constant in extended Langmuir-Freundlich isotherms for salt or protein, respectively, ($M^{-\eta_s}$ or $M^{-\eta_p}$).
B	Constant in Blake-Kozeny expression (refer *eq.* 2.9), (–).
Bi_i	Biot number for component i (= $k_i R_p/\varepsilon_p D_{pi}$), (–).
c_f	Polymer fiber concentration in *eq.* 7.16, (g/cm^3).
C_1	Empirical constant in *eq.* 2.2, (–).
$C_{bi,pi,\ pi}^{\ s}$	Bulk-, particle- and stationary-phase concentration of component i, respectively, (M).
C_{fi}	Feed concentration of component i, (M).
C_m	Modulator concentration, (M).
C_{oi}	Concentration used for non-dimensionalisation of component i (M).
C_s	Salt concentration, (M).
C_i^∞	Adsorption capacity for component i, (moles/m^3).
c_{bi}	Dimensionless bulk-phase concentration for component i (= C_{bi}/C_{oi}), (–).
c_{pi}	Dimensionless particle-phase concentration for component i (= C_{pi}/C_{oi}), (–).

c^{s}_{pi}	Dimensionless stationary-phase concentration for component ($i = C^{s}_{pi}/C_{oi}$), (–).
d_{pS}	Sauter-mean particle diameter of resin particle, (m).
d_{pv}	Volume-mean particle diameter of resin particle, (m).
D	Chromatographic column internal diameter, (m)
D_{bi}	Axial-dispersion coefficient of component i, (m^2/s).
D_{fi}	Bulk-phase diffusivity of component i, (m^2/s)
D_{pi}	Intraparticle diffusivity of component i, (m^2/s).
Da^{a}_{i} ,Da^{d}_{i}	Component i adsorption and desorption Damköhler numbers, respectively, (–).
e^{s}_{zz}	Axial solid-phase strain, (–).
F^{z}_{d}	Drag force acting on cake particles, (Pa/m).
g	Gravity acceleration, (m^2/s).
k_i	External-film mass transfer coefficient of component i, (s^{-1}).
k_o	Initial permeability constant in *eq.* 2.1, (–).
L	Bed height, (m).
L_i	Initial packed-bed height (*ie* prior to compression), (m).
m	Constant in *eq.* (5.9) (= ε/(1 - ε)), (–).
M	Constant parameter in *eq.* 2.12, (–).
MW	Molecular weight, (g/mole).
N_c	Number of chromatographic columns in Chapter 9 (refer *eq.* 9.7), (no.)
$N_{c,e,s}$	Number of collocation points, finite elements and species, respectively, in Part II (no.).
p	Distance from centre of Mohr circle to origin as defined in Figure 2.5, (Pa)
P	Fluid pressure, (Pa).
Pe_{Li}	Peclet number (dimensionless) in bulk fluid phase for component i (= vL/D_{bi}), (–).
PR_i	Production rate defined in *eq.* 9.1, (g/L.h).
Q	Volumetric flowrate, (m^3/h)
r	Cylindrical vessel radial coordinate, Part I, (m). Dimensionless particle radial coordinate, Parts II & III, (–).
r_s	Stokes radius of a protein, (cm).

r_f	Fiber radius of a protein, (cm).
R	Particle radial coordinate, (m).
R_N	Resolution ratio as defined in *eq.* 9.2, (–).
R^f	Drag-force resistance function in *eq.* 2.8, (Pa.s/m^2)
R_p	Particle radius, (m).
Re	Reynolds number (= $2\rho v_{sup}R_p/\mu$), (–).
Sc	Schmidt Number (= $\mu/\rho D_{fi}$), (–).
t	Time, (s).
t_{bk}	Time period before breakthrough during frontal adsorption, (h).
t_{cyc}	Cycle time of a chromatographic process as defined in *eq.* 9.1, (h).
T	Temperature, (K, ^oC).
TPV	Packed-bed total particle volume (refer *eq.* 7.15), (mL, L).
TPSV	Packed-bed total particle stationary-phase volume (refer *eq.* 7.16), (mL, L).
v, v_z^f	Fluid-phase interstitial velocity, (m/s).
v_o	Fluid-phase interstitial velocity prior to compression, (m/s).
v_{sup}	Superficial velocity, (m/s).
$v_{sup,cri}$	Critical superficial velocity (refer *eq.* 2.2), (m/s).
v_z^s	Solid-phase velocity, (m/s).
V_f	Feed volume defined in *eq.* 9.1, (L).
V_{col}	Empty column volume as defined in *eq.* 9.1, (L).
V_b	Resin bed volume (refer *eq.* 9.3), (L).
Y_i	Cyclic (product) yield in a chromatographic system in *eq.* 9.1 (g/g).
Y_p	Cyclic (product) yield in a chromatographic system in *eq.* 9.3 (g/L).
V_{pi}	Initial particle volume prior to compression, (m^3).
V_{pc}	Compressed particle volume, (m^3).
$\dot{V}_{res}$	Annual volumetric consumption of resin (refer *eq.* 9.14), (L/year).
z	Dimensionless axial coordinate, (–).
Z	Axial-coordinate variable, (m).
Z_c	Compressed packed-bed height, (m).

Greek Letters and Symbols

α, β	Cost-capacity parameters in Chapter 9.
α_i, β_i, γ_i	Empirical parameters as defined in *eq.* 5.10.
$\chi(\tau^s_{zz})$	Empirical function describing functional dependence of pressure gradient on variation in bed properties as defined in *eq.s* 2.37 and 2.40, (m^{-2}).
δ	Deflection, (mm).
	Strain, (–).
ε, ε_f	Porosity or interstitial void-volume fraction, (m^3/m^3).
ε_i	Porosity or interstitial void-volume fraction prior to compression, (m^3/m^3).
ε_p	Intraparticle porosity or internal particle voidage, (m^3/m^3).
ε_{pi}	Intraparticle porosity or internal voidage prior to compression, (m^3/m^3).
ε_s	Solid-phase volume fraction, (m^3/m^3).
ε^e_s	Solid-phase void fraction at unstressed condition (*ie* top of cake), (m^3/m^3).
ϕ	Particle shape factor, (–).
	Cost in Chapter 9, ($AUD).
ϕ^*	Dimensionless cost in Chapter 9, (–).
Φ	Empirical function defined by *eq.* 2.2, (–).
$f_c(\tau^s_{zz})$	Empirical parameter describing fractional variation in bed height as defined in *eq.* 2.42, (–).
$f_d(\tau^s_{zz})$	Empirical parameter describing fractional variation in particle size as defined in Section 3.8 - Chapter 3, (–).
$f_V(d_{pi})$	Volume particle-size distribution function, (m^3).
γ	Weight density of a pulverulent material in Chapter 2, (kg/m.s).
	Unit cost in costing equations of Chapter 9, ($AUD).
η_i	Dimensionless constant for component i ($= \varepsilon_p D_{pi} L/R^2_p v$), (–).
$\eta_{si,pi}$	Salt and protein constants, respectively, in multicomponent extended Langmuir-Freundlich isotherm, (–).
φ	Internal angle of friction for a pulverulent material, (degrees).
φ_w	Angle of wall friction for a pulverulent material, (degrees).

κ	Cohesion of a pulverulent material, (Pa).
κ_w	Cohesion of a pulverulent material at a hopper wall, (Pa).
μ	Fluid viscosity, (Pa.s).
θ	Anti-clockwise angle between horizontal x-axis and direction of major principal stress (refer Figure 2.5), (degrees).
θ_{ij}	Discount factor as defined in *eq.* 5.3a which accounts for uneven maximum adsorption capacities that can occur in multicomponent adsorption (Gu, 1995), (–).
ρ, ρ^f	Fluid-phase density, (kg/m^3).
ρ^s	Solid-phase density, (kg/m^3).
σ	Normal stress acting in a pulverulent material, (Pa).
σ^e	Solid-phase modulus at unstressed condition (refer *eq.* 2.12), (Pa).
σ_{maj}, σ_{min}	Major and minor principal stresses, respectively, (Pa).
σ^s	Solid-phase modulus in *eq.* 2.11, (Pa).
σ_w	Normal stress acting on a pulverulent material at a hopper wall, (Pa).
σ_{xx}, σ_{yy}	Normal stresses in Cartesian coordinates, (Pa).
σ_{zz}	Axial stress in Cylindrical coordinates, (Pa).
σ_{rr}	Radial stress in Cylindrical coordinates, (Pa).
τ	Shear stress acting in a pulverulent material in Chapter 2, (Pa).
	Dimensionless time in Parts II and III, (–).
τ_{bk}	Dimensionless time period at breakthrough during frontal adsorption, (–).
τ_{imp}	Dimensionless time period of concentration pulse, (–).
τ_{step}	Dimensionless time at a concentration step change, (–).
τ_{xy}, τ_{yx}	Shear stresses in Cartesian coordinates, (Pa).
τ_w	Shear stress acting on a pulverulent material at the hopper wall, (Pa).
τ^{s}_{zz}	Axial stress, (Pa).
ω	Angle defined by *eq.* 2.34, (degrees).
	Eccentricity of compressed particle in Chapter 7, (–).
ω_c	Daily cycle frequency of a chromatographic system (refer *eq.* 9.3), (no./day).
ξ_i	Dimensionless constant for component i (= $3Bi_i\eta_i(1 - \varepsilon)/\varepsilon$), (–).
Ψ	Productivity of a chromatographic system (refer *eq.* 9.3), (g/L.h)

REFERENCES

Akroyd. *Laboratory Testing in Soil Engineering, Geotechnical Monograph No. 1.* Soil Mechanics Ltd: Chelsea, London, England, 1957.

Amrad Pharmacia Biotech. 1994. *Personal Communication with Vanessa Wadell, Technical Services Coordinator: Inquiry regarding variation in particle size of Sepharose Big-Beads SP with solvent conditions.* Amrad Pharmacia Biotech, Sydney, Australia.

Amrad Pharmacia Biotech. 1996. *Personal Communication with Anne Harbours: Inquiry regarding Pharmacia BPG column design and construction and costing of production-scale chromatographic systems.* Amrad Pharmacia Biotech, Sydney, Australia.

Bernhinger, J.A.; Whitley, D.; Zhang, X.; Wang, N.H.L. 1991. A versatile model for simulation of reaction and nonequilibrium dynamics in multicomponent fixed-bed adsorption processes. *Comp. Chem. Engng.*, **15**(11), 749-768.

Boyer, P.M; Hsu, J.T. 1992. Experimental studies of restricted protein diffusion in an agarose matrix. *AIChE J.*, **38**(2), 259-271.

Carrére H.; Sochard, S.; Bascoul, A.; Wilhelm, A.M.; Delmas, H. 1994. Whey proteins extraction by fluidised ion exchange chromatography: Isotherms determination and process modelling. *Trans. IChemE*, **72**(Part C), 216-226.

Chase, H.A. 1984. Prediction of preparative affinity chromatography. *J. Chromat.*, **297**, 179-202.

Chase, G.G, Willis; M.S.; Kannel, J. 1990. Averaging volume size determination of electroconductive porosity probes. *Int. J. Multiphase Flow*, **16**(1), 103-112.

Chase, G.G; Willis, M.S. 1992. Compressive cake filtration. *Chem. Eng. Sci.*, **47**(6), 1373-1381.

Chung, S.F.; Wen, C.Y. 1965. Longitudinal dispersion of liquid flowing through fixed and fluidised beds. *AIChE J.*, **14**, 857-866.

Craig R.F. *Soil Mechanics.* Chapman and Hall: Boundary Row, London, 1981 (4th ed.); pp 99-112.

CSIRO. 1995. *Personal Communication with Janine Ortenburg: Inquiry regarding current operating and design conditions at the WGFE pilot-plant.* CSIRO Division of Food Science & Technology - Melbourne Laboratory: Melbourne, Australia.

CSIRO/DRL. 1990. *Protein Extraction from milk products.* Provisional specification for the invention entitled: Commonwealth Scientific and Industrial Research Organisation, Dairy Research and Development Corporation and State of Queensland as represented by the Department of Primary Industry, Australia.

Davey John Brown Pty Ltd. 1993. *Confidential Communication to Paul Donelly, Managing Director, Dairy Research & Development Corporation: CUJ:EC.* Davey John Brown Pty Ltd: Victoria, Australia.

Fellinger, A.; Guiochon, G. 1994. Optimising experimental conditions for minimum production cost in preparative chromatography. *AIChE J.*, **40**(4), 594-605.

Finlayson, B.A. *The Method of Weighted Residuals and Variational Principles.* Academic Press: New York and London, 1972; pp 96-107.

Foust, A.S.; Wenzel, L.A.; Clump, C.W.; Maus, L.; Andersen, L.B. *Principles of Unit Operations.* John Wiley & Sons: Toronto, 1980 (2nd ed.); pp 637-649, pp 699-714.

Francis, G.L.; Regester, G.O.; Webb, H.; Ballard, F.J. 1995. Extraction from cheese whey by cation-exchange chromatography of factors that stimulate the growth of mammalian cells. *J. Dairy Sci.*, **78**, 1209-1218.

Freitag, R.; Frey, D.; Horváth, C. 1994. Effect of bed compression on high performance liquid chromatography columns with gigaporous polymeric packings. *J. Chrom. A*, **686**(2), 165-177.

Frey, D.; Schweinheim, E.; Horváth, C. 1993. Effect of intraparticle convection of the chromatography of biomolecules. *Biotech. Prog.*, **9**, 273-284.

Gallant S.R.; Kundu, A.; Cramer, S.M. 1995. Optimisation of step gradient separations: Consideration of non-linear adsorption. *Biotechnology and Bioengineering*, **47**, 355-372.

Geisow, M.J. 1992. Pores for thought in bioseparation and bioassay matrices. *Trends in Biotechnology*, **10**, 373-375.

Gu, T.; Tsai, G.; Tsao, G.T. 1990. New approach to a general nonlinear multicomponent chromatography model. *AIChE J.*, **36**(5), 748-788.

Gu, T.; Truei, V.; Tsai, G.; Tsao, G.T. 1991. Modelling of gradient elution in multicomponent nonlinear chromatography. *Chem. Eng. Sci*, **47**(1), 253-262.

Gu, T. *Mathematical Modeling and Scale-up of Liquid Chromatography.* Springer-Verlag Berlin Heidelberg: Germany, 1995; pp 5-38.

Gupta, M.N.; Mattiasson, B. 1994. Novel technologies in Downstream processing. *Chemistry & Industry*, 5 September.

Hancock, A.W.; Nedderman, R.M. 1974. Prediction of stresses on vertical bunker walls. *Trans. IChemE*, **52**, 170-179.

Hassanizadeh, M; Gray, W.G. 1980. General conservation equations for multi-phase systems: 3. Constitutive theory for porous media flow. *Adv. Water Resour.*, **3**, 25-40.

Hodgson, J. 1990. Affinity innovations for bioprocessing. *Bio/Technology*, **8**, 864-865.

Horne, R.M.; Nedderman, R.M. 1976. Analysis of the stress distribution in two-dimensional bins by the method of characteristics. *Powder Technology*, **14**, 93-102.

James, E.A. *The Application of Multicomponent Adsorption Theory to an Ion-Exchange Chromatography System for Recovery of Whey Proteins*. Ph.D. Thesis: University of Queensland, 1994.

Janson, J; Hedman, P. 1987. On the optimization of process chromatography of proteins. *Biotech. Prog.*, **3**(1), 9-13.

Jönsson, K.A.; Jönsson, B.T.L. 1992. Fluid flow in compressible porous media: I: steady-state conditions. *AIChE J.*, **38**(9), 1340-1348.

Kaggwa, W. 1993. *Personal Communication*. Department of Civil & Environmental Engineering, University of Adelaide: Adelaide, Australia.

Kataoka, T.; Yoshida, H.; Yamada, T. 1973. Liquid phase mass transfer in ion-exchange based on the hydraulic radius model. *J. Chem. Engng. Japan*, **6**, 172-177.

Knight, P. 1989. Downstream processing. *Bio/Technology*, **7**(8), 777-782.

Kreyszig, E. *Advanced Engineering Mathematics*. John Wiley & Sons: New York, 1988 (6th ed.); pp 1068-1071.

Lambert, J.D. *Numerical Methods for Ordinary Differential Systems*. John Wiley & Sons Ltd: Chichester, England, 1991.

Ladisch, M.R.; Tsao, G.T. 1978. Theory and practice of rapid liquid chromatography at moderate pressure using water as eluent. *J. Chromatogr.*, **166**, 85-100.

Li, Q.; Grandmaison, E.; Hsu, C.C.; Taylor, D.; Goosen, M.F.A. 1995. Interparticle and intraparticle mass transfer in chromatographic separation. *Bioseparation*, **5**, 189-202.

Ma, A.; Guiochon G. 1991. Application of orthogonal collocation on finite elements in the simulation of non-linear chromatography. *Computers chem. Engng.*, **15**(6), 415-426.

Malvern Instruments Ltd. *System 2600 Instruction Manual*. Malvern Instruments Ltd: Malvern, England, 1991 (Issue 2.2).

Melander, W.R.; El Rassi, Z.; Horvath, C. 1989. Interplay of hydrophobic and electrostatic interactions in biopolymer chromatography. *J. Chromatography*, **469**, 3-27.

Middelberg, A.P.J. *A Model for Disruption of Escherichia coli. by High Pressure Homogenisation*. Ph.D. Thesis: University of Adelaide, South Australia, Australia, 1992.

Middelberg, A.P.J. 1995. The importance of accounting for bioprocess interactions. *Australasian Biotechnology*, **5**(2), 99-103.

Middelberg, A.P.J. 1996. The influence of protein refolding strategy on cost for competing reactions. *The Chemical Engineering Journal*, **61**, 41-52.

Mohammad, A.W.; Stevenson, D.G.; Wankat, P.C. 1992. Pressure-drop correlations and scale-up of size exclusion chromatography with compressible packings. *Ind. Eng. Chem. Res*, **31**, 549-561.

Nedderman, R.M. 1982. The theoretical prediction of stress distributions in hoppers. *Trans. IChemE*, **60**, 259-275.

Ogston, A.G.; Preston B.N.; Wells, J.D. 1973. On the transport of compact particles through solutions of chain-polymers. *Proc. Soc. Lond.*, **333**, 297.

PCT/AU91/00303. 1991. *Growth Promoting Agent*. Inventors: Ballard, F.J.; Francis, G.L.; G.O. Regester.

Perry, R.H.; Green, D. *Perry's Chemical Engineers Handbook*. McGraw-Hill: 1984 (6th ed.); pp 2-12 to 2-13, pp 5-53 to 5-56.

Petrides, D.P.; Cooney, C.L.; Evans, L.B. 1989. Bioprocess simulation: An integrated approach to process development. *Computers chem. Engng.*, **13**(4/5), 553-561.

Petrides, D.P. *Computer-Aided Design of Integrated Biochemical Processes; Development of Biodesigner*. Ph.D. Thesis: Massachusetts Institute of Technology, Massachusetts, USA, 1990.

Pharmacia Bioprocess Technology. 1995. *Q & SP Sepharose® Big Beads BioProcess™ Media- Data file Ion Exchange Media*. Pharmacia: Uppsala, Sweden.

Pharmacia Bioprocess Technology. 1996a. *SP Sepharose Fast Flow Ion Exchangers BioProcess ™ Media - Data file 3100*. Pharmacia: Uppsala, Sweden.

Pharmacia Bioprocess Technology. 1996b. *Bioprocess™ Glass Columns, BPG 300 series - Data file 5031*. Pharmacia: Uppsala, Sweden.

Pharmacia Bioprocess Technology. 1996c. *Bioprocess™ Glass Columns, BPG 100 and BPG 200 series - Data file 5030*. Pharmacia: Uppsala, Sweden.

Pharmacia LKB Technology. 1991. *Purification Center Course Notes: Chromatography in Biotechnology*. Pharmacia, Uppsala, Sweden.

Polson, A. 1950. Some aspects of diffusion in solution and a definition of a colloidal particle. *J. Phys. Colloid Chem.*, **54**, 649.

Regester, G.O. 1996. *Personal Communication.*

Rogers, M.L.; Goddard C.; Regester G.O.; Ballard, F.J.; Belford, D.A. 1996. Latent transforming growth factor-β activity in bovine milk: concentration, stability and molecular weight forms. *J. endocrinology*, In Press.

Ruth, B.F. 1946. Correlating filtration theory with industrial practice. *Ind. Eng. Chem.*, **38**(6), 564-571.

Ruthven, D.M. *Principles of adsorption and adsorption processes.* Wiley: New York, USA, 1984.

Sarker, M.; Guiochon, G. 1995. Study of the packing behaviour of axial compression columns. *J. Chrom. A*, **702**, 27-44.

Shirato, M.; Sambuichi, M.; Okamura, S. 1963. Filtration behaviour of a mixture of two slurries. *AIChE J.*, **9**(5), 599-605.

Skidmore, G.L.; Horstmann, B.J.; Chase, H.A. 1990. Modelling of single-component protein adsorption to the cation-exchanger S Sepharose® FF. *Journal of Chromatography*, **498**, 113-128.

Smithers, G. 1995. *Personal communication: Extract from Prospectus of Financial Overview for proposed WGFE bioprocessing facility.*

Snoswell, M.A. *Novel Approaches to Large-Scale Purification and Analysis.* Ph.D. Thesis: University of Adelaide, Australia, 1990.

Spalding, B.J. 1991. Downstream processing: Key to slashing production costs 100 fold. *Bio/Technology*, **9**(4), 229-233.

Sofer, G.K.; Nyström, L.E. *Process Chromatography - A Practical Guide.* Academic Press: 1989.

Stroud, A.H.; Secrest, D. *Gaussian Quadrature Formulas.* Prentice-Hall Inc.: 1966; pp 100-109.

Tiller, F.M.; Huang, C.J. 1961. Theory of filtration equipment. *Ind. Eng. Chem.*, **53**(7), 529-537.

Tsou, H.S.; Graham, E.E. 1985. Prediction of adsorption and desorption of protein on dextran based ion-exchange resin. *AIChE Journal*, **31**(12), 1959-1966.

van Brakel, J.; Kleizen, H.H. 1990. Problems in downstream processing. In *Chemical Engineering Problems in Biotechnology*, M.A. Winkler (-ed.), Chapt. 3, Elsevier Applied Science: London, pp 95-163.

Walters, J.K. 1973. A theoretical analysis of stresses in silos with vertical walls. *Chem. Eng. Sci.*, **28**, 13-21.

Wankat, P.C.; Koo, Y. 1988. Scaling rules for isocratic elution. *AIChE Journal*, **34**(6), 1006-1019.

Weast, R.C. *CRC Handbook of Chemistry and Physics.* CRC Press: Cleveland, Ohio, USA, 1974 (55th ed.).

Willis, M.S., and Tosun, I. 1980. A rigorous cake filtration theory. *Chem. Eng. Sci.*, **35**, 2427-2438.

Willis, M.S.; Collins, R.M.; Bridges, W.G. 1983. Analysis of non-parabolic filtration behaviour. *Chem. Eng. Res. Des.*, **61**, 96-109.

Willis, M.S.; Tosun, I.; Collins, R.M. 1985. Filtration mechanisms. *Chem. Eng. Res. Des.*, **63**, 175-183.

Whitley, R.D.; van Cott, K.E.; Wang, L. 1993. Analysis of non-equilibrium adsorption/desorption kinetics and implications for analytical and preparative chromatography. *Ind. Eng. Chem. Res.*, **32**(1), 149-158.

Yu, Q.; Wang, N.H.L. 1989. Computer simulations of the dynamics of multicomponent ion exchange and adsorption in fixed beds - Gradient-Directed Moving Finite Element Method. *Comp. Chem. Engng.*, **13**(8), 915-926.

Zienkiewicz, O.C. and Morgan, K. *Finite Elements and Approximation.* John Wiley & Sons, Inc.: New York, 1983.

APPENDIX 1: BPG 100/500 SCHEMATIC & PARTS LIST

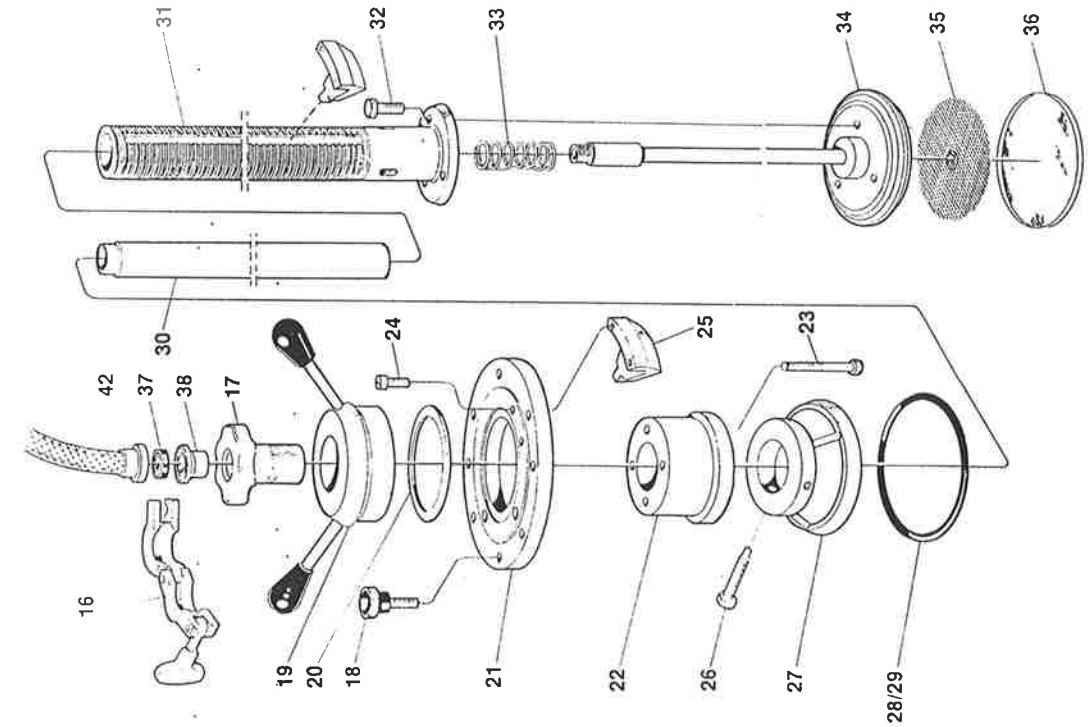

Fig. 11. Construction of the column adaptor. See Tables 9, 10 and 11 for parts and material identification.

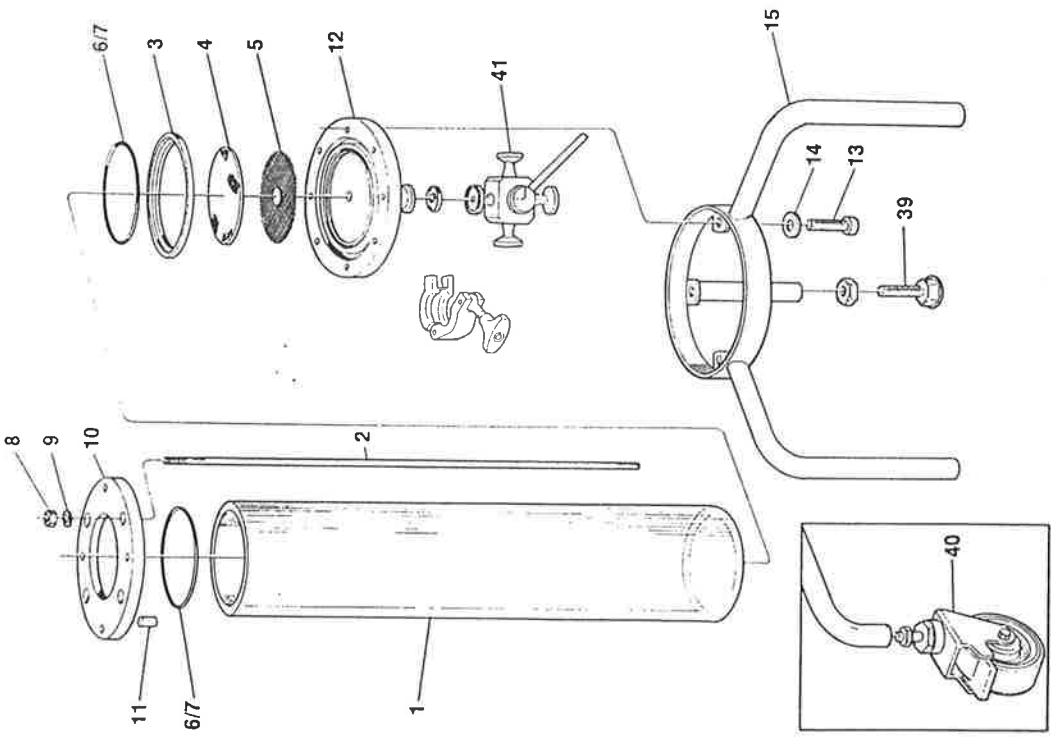

Fig. 12. Construction of the column tube and stand. See Tables 9, 10 and 11 for parts and material identification.

Figure A1.1: Photocopy of Schematic detailing parts and construction of Pharmacia BPG 100/500 column (Pharmacia Bioprocess Technology, 1996c).

Figure A1.2: Photocopy of Table containing parts list (Pharmacia Bioprocess Technology, 1996c) for Schematic presented in Figure A1.1.

Table 9. Identification and materials of component parts for BPG 100 columns (see Figs. 12 and 13 for part numbers). Components with code nos. are available as spare parts. See Table 11 for full listing of materials.

Part no.	Designation	Code no.	Materials[1]	Quantity per pack[2]
1	Column tube T 100/500 incl rods	18-0251-01	A	1
	Column tube T 100/750 incl rods	18-0251-02	A	1
	Column tube T 100/950 incl rods	18-0251-03	A	1
2	Rod for T 100/500	18-1001-94	D	1
	T 100/750	18-1001-95	D	1
	T 100/950	18-1001-96	D	1
3	Guide ring	18-0251-22	F	1
4	Net, 23 µm, end-piece	18-9252-01	E	2
	Net, 10 µm, end-piece	18-0251-77	H	2
5	Support net, end-piece	18-0251-55	E	2
6	Sealing O-ring	18-8494-01	C	2
7	Sealing O-ring	18-0019-41	M	1
8	Nut, M6	19-1582-01	D	5
9	Cup spring washer	18-8480-01	D	4
10	Flange		D	
11	Column centering dowel	18-1003-00	F	8
12	End piece		B	
13	Bolt, M6 x 20		D	
14	Washer		D	
15	Stand, complete	18-1001-32	D	1
16	Clamp, 25 mm	18-1001-31	P	1
17	Adjusting knob	18-9259-01	K	1
18	Bolts, complete, M6 x 20	19-8095-01	D	4
19	Adjuster nut, body		D	
20	Bushing ring	18-0264-01	L	1
21	Top Plate		D	
22	Adjuster nut, insert	18-0251-20	K	1
23	Allen screw, M8 x 45	19-6375-01	D	5
24	Allen screw, M4 x 14	19-6356-01	D	5
25	Stopper		D	
26	Adaptor head screw	18-8457-01	D	3
27	Sealing unit		D	
28	Adaptor O-ring	18-8475-01	C	2
29	Adaptor O-ring	18-0019-40	M	1
30	Inner adaptor tube		D	
31	Outer adaptor tube		D	
32	Screw, M6 x 12	19-8093-01	D	3
33	Spring	18-8491-01	D	1
34	Adaptor plate		B	
35	Support net, adaptor	18-0251-56	E	2
36	Net, 23 µm, adaptor	18-9251-01	E	2
	Net, 10 µm, adaptor	18-0251-76	H	2
37	Gasket, 25 mm	18-0019-27	C	5
38	Inlet connection, threaded	18-8484-01	L	1
39	Stand feet			
40	Wheel	18-1001-01	D,O,H	3
41	2-way valve, L-type manual	18-5757-01	B,F	1
42	Tubings		R	

[1] Materials are represented by letters as listed in Table 11.
[2] Refers to components available as spare parts.

APPENDIX 2: LITERATURE RESULT OF A NUMERICAL SIMULATION

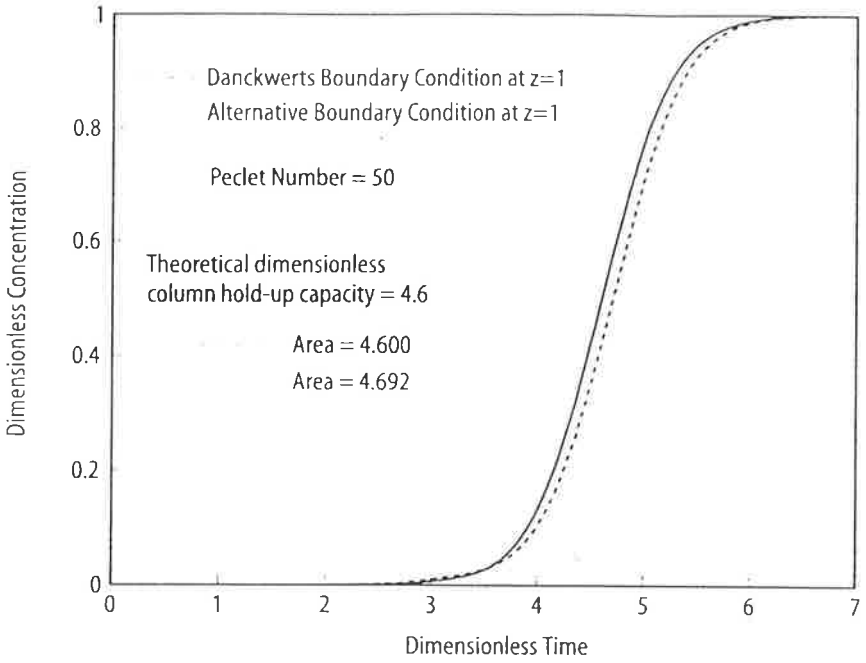

Fig. 3.8. Single-component breakthrough curves (Peclet number = 50)

Figure A2.1: Photocopy of general multicomponent rate-equation chromatography model single-component frontal adsorption simulation by Gu(1995).

Figure A2.2: Photocopy of Table presented by Gu(1995) containing model parameters for model simulation in Figure A2.1.

Table 3.1. Parameter values used for simulation in Chap. 3[a]

Figure(s)	Species	Physical Parameters					Numerical Parameters	
		$Pe_{L,i}$	η_i	Bi_i	a_i	$b_i \times C_{0i}$	Ne	N
3.3	1	300	4	20	1.2	1.5×0.1	7	2
	2	300	4	20	8	10×0.1		
3.4	1	400	6	10	2	4×0.1		
	2	400	6	10	7	12×0.1	10	2
	3	400	6	10	15	30×0.1		
3.5	1	300	4	20	1.2	1.5×0.1	7	2
	2	320	4.2	17	8	10×0.1		
	3	400	5.5	16	24	30×0.1		
	4	500	7	15	38.4	48×0.1		
3.6	1	600	6	5	3	6×0.1	12	2
	2	600	3	6	12	24×0.3		
3.8	1	50	2	10	8	7×0.2	4	2
3.9	1	50	2	10	8	7×0.2	20	2
3.10	1	50	10	4	4	3.5×0.2	8	2
	2	50	10	4	8	7×0.2		
3.11	1	200	2	10	8	7×0.2	5	2

[a] For Figs. 3.4 to 3.11, $\varepsilon_b=\varepsilon_p=0.4$. Sample size for Fig. 3.5 is $\tau_{imp}=0.1$; for Fig. 3.10, $\tau_{imp}=0.2$.